



Invited Talk, Oral & Poster Presentation Abstracts Guide

Table of Contents

Invited Talks

Invited Abstract #	Author	Title	Page #
1	Henrik Bruus	The acoustic body force in inhomogeneous fluids	7-8
2	Valeria Garbin	Acoustic manipulation of armored bubbles: shape oscillations, particle expulsion, and pattern formation	9-10
3	David J. Collins	A novel method for generating orientable self-aligned time-averaged acoustic fields in microchannels from surface acoustic waves	11-12
4	James Friend	Progress in novel rechargeable lithium metal batteries integrating acoustic wave recirculation of the liquid electrolyte	13-14
5	Virginie Daru	A numerical study of Rayleigh streaming at high acoustic level	15-16
6	Jean-Louis Thomas	Radiation pressure force and torque in single beam acoustical tweezers	17-18
7	Marco Cecchini	Ultra-High-Frequency Surface-Acoustic-Wave microfluidics and biosensors	19-20
8	Likun Zhang	Acoustic radiation forces for extraordinary manipulations from theoretical perspectives	21-22

Oral Abstracts

Oral Abstract #	Author	Title	Page #
003	Richard Y. Q. Fu	Flexible and wearable thin film acoustic wave sensing and acoustofluidic devices	24-25
004	Tan Dai Nguyen	The 3D patterning and manipulating microparticles inside millimeter- height of chamber using standing surface acoustic wave	26-27
005	Xuexin Duan	Biomolecule Manipulation Using Gigahertz Bulk Acoustic Waves for Enhanced Protein Sensing	28-29
008	Veikko Sariola	Controlling the motion of multiple objects on a Chladni plate	30-31
010	Luke Cox	Acoustic Lock: Single-axis Position and Orientation Trapping of NonSpherical Sub-wavelength Particles	32-33
012	Maxime Harazi	Oscillations of a cubic bubble	34-35
014	Côme Olivier	Dynamics of acoustic vaporization of encapsulated microdroplets	36
016	Kian-Meng Lim	Interactions Between Rigid Spheres Subjected to Bessel Beam	37-38
017	Adrian Neild	The Role of Diffraction on Particle Patterning using Travelling Surface Acoustic Waves	39-40
019	Thomas Combriat	The song of 2D micro-bubbles	41-42

020	Gergely Simon	Particle sorting in phase modulated surface acoustic fields: from theory to experiments	43-44
022	Thierry Baasch	Numerical Modelling of Viscous Damping for Acoustic Resonances of Suspended Microparticles	45-46
025	Ofer Manor	An Acousto-Gravitational Balance in Climbing Wetting Films	47-48
030	Ida Iranmanesh	Temperature-controlled acoustofluidic production of microbubble contrast agents with enhanced stability and monodispersity	49-50
031	Jinsoo Park	Acoustic in-droplet sample washing and enrichment	51-52
034	Douwe Kamsma	Single-Cell Acoustic Force Spectroscopy (scAFS): Resolving kinetics and strength of T-cell adhesion to a functionalized surface	53-54
037	Minji Kim	Investigation of Motile Algae Cells as Active Probes for Measurement of Acoustic Microfluidic Device Performance	55-56
038	Di Wu	Biogenic Nanostructures and Genetic Elements for Acoustic Trapping and Manipulation	57-59
044	Jacob S. Bach	Classification of acoustic streaming in three dimensions	60-61
046	Lorène Champougny	Ultrasound transmission through model liquid foams generated by microfluidics	62-63
047	Adrien Bussonnière	Sliding and climbing drops excited by surface acoustic waves on a tilted plane	64-65
049	Nicolas Chastrette Regis Wunenburger	Surface wave driven oscillatory instability of sessile droplets	66-67
050	Filip Plazonic	Basophil purification using a thin-reflector acoustic resonator	68-69
051	Gabriel Dumy	Parametric investigation of acoustic autopropulsion of metallic and polymer nanoobjects	70-71
052	Karl Olofsson	Ultrasonic tissue engineering in multi-well microplate enables layered co-culture tumor spheroids	72-73
053	Aleksandr Oseev	Integration of microacoustic sensor for the analysis of platelets-collagen interactions at physiological flow conditions of the whole blood.	74-75
054	Diego Baresch	Single bubble acoustic manipulation and actuation in complex environments	76-77
059	Glauber T. Silva	Deformation of vesicles with acoustic standing waves	78-79
060	Reza Rasouli	Integration of Sharp-edge and bubble acoustic microstreams for rapid mixing in Microfluidic platforms	80-81
063	Ghulam Destgeer	Self-assembly of micro particles driven by surface acoustic waves	82-83
068	Stefan Radel	Ultrasound enhanced PAT: increased sensitivity of an in-line Raman spectroscopy probe	84
071	Fabien Chauvet	Oscillation, coalescence and shape deformation of confined bubbles in an oscillating depth microchannel: application to the fragmentation of electro crystallized ramified branches for an alternative synthesis of colloidal metallic nanoparticles	85-86

075	Mauricio Hoyos	Bacteria manipulation in standing waves resonator, aggregation and dynamic structures	87-88
076	Tomohiro Hara	Measurement of flow resistance in the gap of a pump using ultrasonic transducer and opposing surface	89-90
082	Jay Mallinson	AcouWash: A standalone instrument for the washing, separation and enrichment of cells.	91-92
083	Thomas Franke	Surface acoustic wave actuated cell sorting using multilayer PDMS fluidics	93-94

Poster Abstracts

Poster Abstract #	Author	Title	Page #
007	Xinyi Guo	Gigahertz acoustic streaming induced cell membrane poration towards intracellular delivery	96-97
011	Amanda Franklin	Time domain multiplexing of single-beam acoustic fields for three-dimensional micro-particle manipulation in water	98-99
013	Greco Gina	Surface acoustic wave (SAW)-driven device for dynamic cell cultures	100-101
015	Camila Horvath	Acoustic “spoof plasmons” in an array of sound-soft inclusions	102-103
018	Andreas Winkler	Performance exploration of Acoustic force spectroscopy (AFS™) chips	104-105
021	Michael Gerlt	Silicon particle enrichment in flow conditions for the improvement of metal 3D printing resolution and material variability	106-107
023	Robert Weser	Tuning of the acoustic boundary conditions for SAW-driven microfluidics	108-109
026	Amihai Horesh	Acoustic Stabilization and Enhanced de-Stabilization of Single Bubbles in Microfluidics and the Connection to the Acoustic Landau-Levich Coating Problem	110-111
027	Peter Reichert	Design and Characterization of Thin Film Bulk Acoustic Wave Devices for Acoustophoresis	112-113
028	Zhixiong Gong	Reversals of acoustic radiation force and torque in a single Bessel beam: Acoustic Tweezers Numerical Toolbox	114-115
029	Seyed Amin Rahimzadeh	Characterization of surface waves on water films excited by ultrasonic vibration imposed on the substrate	116-117
032	Pierre Gelin	Acoustofluidics in multiphase reactors	118-119
033	Fabio Garofalo	A Methodology for the Quantification of Particle Separation and its Application to the Measurement of Device Effectivity and Particle Compressibility	120-121
035	Chanryeol Rhyou	Copatterning of micro particles using the continuously phase modulated standing surface acoustic waves	122-123

036	Naiqing Zhang	Optimized LiNbO cut and omnidirectional spiral surface acoustic waves for particles manipulation and multi-size particles separation in a microliter sessile drop	124-126
039	Antoine Riaud	In situ selective manipulation and seeding of human cells in a with micro-acoustic tweezers	127-128
041	Angelica Castro Jean-Luc Aider	Breakdown of acoustically levitating aggregates of fluorescent particles or living cells using specific illumination	129-130
043	Wei Qiu	Size-dependent steady-state motion of micro particles in acoustophoresis	131-132
045	Stephan Freitag	Ultrasound Manipulation of Bacteria in Drinking Water for Attenuated Total Reflection Infrared (ATR-IR) Spectroscopy	133-134
048	Nils Refstrup Skov	3D simulations of an acoustofluidic immersed-IDT SAW device	135-136
055	Nathan Jeger-Madiot	Spatial characterization of the acoustic field in a standing wave cavity to control the aggregate shape	137-138
057	Davood Saeidi	Investigation of Particle Interaction Forces in a standing acoustic wave field	139-140
058	Jing Bo Zhang	Acoustophoretic focusing in a microfluidic chip for rapid label-free identification of harmful microbial in water	141-142
061	Kedar C. Chitale	Particle Separation Using Bulk Angled Standing Waves	143-144
062	Chuanyu Zhang	Experimental study of acoustic induced streaming around sharp edges in a Y-type mixing channel	145-146
065	Itziar González	Aluminum-foil chip for ultrasonic particle manipulation	147-148
066	Rayisa P. Moiseyenko	Whole-system resonances enabling acoustophoresis in all-polymer microfluidic devices	149-150
067	Rui Tostoes Bart Lipkens	Acoustic Affinity Cell Selection for CAR T-Cell Manufacturing	151-152
069	Jeremy J. Hawkes	Building resonant cavities from multiple Lamé resonator units	153-154
072	William Connacher	Tunable control of atomized droplet size in a single thickness-mode acoustic device via signal modulation	155-156
077	S. Amir Bahrani	Boundary-layer streaming in viscoelastic fluids	157-158
078	Dan Zhao	Mesure de la force de pression de radiation exercée par une pince acoustique	159
079	Philippe Brunet	Unstationary contact-lines and oscillating drops	160-161
084	Amgad Rezk	Plug-and-actuate on demand: Fluid Actuation in 96-Well Plate using Hybrid Acoustic Waves	162-163
085	Haim Sazan	Microfabrication of Continuous Stable patterns Using Standing Surface acoustic waves in microfluidic systems	164-165
086	Clara Siber	Velocity field analysis of acoustophoretic focusing in a single-cell printing system	166-167

Invited Talk Abstracts



The acoustic body force in inhomogeneous fluids

Henrik Bruus

Department of Physics, Technical University of Denmark, Kongens Lyngby, Denmark
 E-mail: bruus@fysik.dtu.dk, URL: <http://www.fysik.dtu.dk/microfluidics>

Introduction. The vast majority of fundamental studies and applications of microscale acoustofluidic techniques reported in the literature, has involved homogeneous fluids. However, recent work have revealed some unexpected physical phenomena and exciting opportunities for the development of novel devices, when working with inhomogeneous fluids exposed to ultrasound in the MHz range. Here, a short review is presented of this so-called inhomogeneous acoustofluidics with special attention to the recently discovered acoustic body force.

An important early contribution to inhomogeneous acoustofluidics was the experimental discovery by Per Augustsson's team at Lund University in 2014 that a transverse standing 2-MHz-ultrasound half-wave is capable to relocate and stabilize an aqueous salt solution, a few percent heavier than surrounding co-flowing streams of pure water, in the central part of 375- μm -wide and 150- μm -high rectangular microchannel [1]. This discovery formed the basis of the subsequent development of iso-acoustic focusing in a Lund-MIT-DTU collaboration, again headed by Augustsson [2]. Here, a transverse standing ultrasound half-wave provided not only acoustic stabilization of an iodixanol solution in a central flow stream, but also gave rise to a radiation force acting on suspended cells. In contrast to conventional acoustofluidic systems, where suspended particles move to the central pressure nodal plane, the radiation force in the inhomogeneous system moves each cell to its iso-acoustic point, the position in space where the acoustic impedance of the inhomogeneous iodixanol solution equals that of the cell. Thus, remarkably, iso-acoustic focusing is a size-independent particle sorting method.

The acoustic body force of inhomogeneous fluids was treated by Karlsen, Augustsson, and Bruus in Ref. [3]. In summary, the inhomogeneity of the fluid is given by the solute concentration $s(\mathbf{r}, \tau)$, where τ is the slow (ms) hydrodynamic time scale, much slower than the fast (μs) acoustic time scale t . The density of the fluid has the form $\rho = \rho_0[s(\mathbf{r}, \tau)] + \rho_1(\mathbf{r})e^{-i\omega t}$, and similarly for the pressure p , velocity \mathbf{v} , viscosity η , and compressibility κ . The wave equation of the acoustic pressure has the form $-\omega^2\kappa_0 p_1 = \nabla \cdot (\frac{1}{\rho_0} \nabla p_1)$, while the acoustic velocity is given by $\mathbf{v}_1 = -\frac{i}{\omega\rho_0} \nabla p_1$. The slow-time-scale acoustic body force $\mathbf{f}_{ac}(\mathbf{r}, \tau)$ follows from an average over a single oscillation-period (angled brackets) of the fast-time-scale t of these acoustic fields,

$$\mathbf{f}_{ac} = -\nabla \cdot \left\langle \frac{1}{2} \kappa_0 |p_1|^2 + \frac{1}{2} \rho_0 |\mathbf{v}_1|^2 \right\rangle + \nabla \cdot \langle \rho_0 \mathbf{v}_1 \mathbf{v}_1 \rangle. \quad (1)$$

Given the acoustic and gravitational body forces \mathbf{f}_{ac} and $\rho_0 \mathbf{g}$, the governing equations on the slow-time τ for the solute concentration s and for the density ρ_0 and velocity \mathbf{v} of the fluid are

$$\partial_\tau \rho_0 = -\nabla \cdot (\rho_0 \mathbf{v}), \quad \partial_\tau (\rho_0 \mathbf{v}) = \nabla \cdot [\boldsymbol{\sigma} - \rho_0 \mathbf{v} \mathbf{v}] + \mathbf{f}_{ac} + \rho_0 \mathbf{g}, \quad (2a)$$

$$\partial_\tau s = -\nabla \cdot [\mathbf{v} s - D \nabla s], \quad \boldsymbol{\sigma} = -p \mathbf{I} + \eta_0 \left[\nabla \mathbf{v} + (\nabla \mathbf{v})^T \right] + (\eta_0^b - \frac{2}{3} \eta_0) (\nabla \cdot \mathbf{v}) \mathbf{I}. \quad (2b)$$

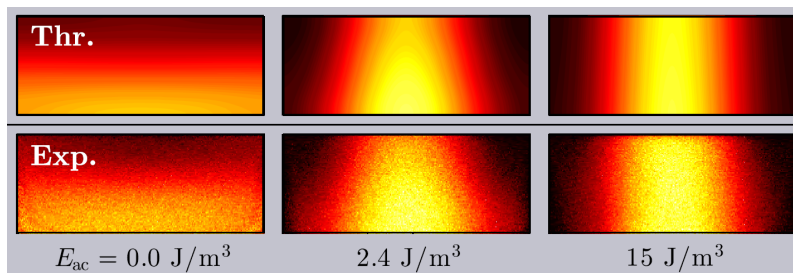


Figure 1: Simulation without fitting parameters (top) and experimental confocal image (bottom) of the iodixanol concentration in the vertical 375 $\mu\text{m} \times 150 \mu\text{m}$ cross section after 17 s for the acoustic energy density $E_{ac} = 0, 2.4, \text{ and } 15 \text{ J/m}^3$. Initially, the denser fluorescently marked fluid (36% iodixanol, white) is in the center and the less dense fluid (10% iodixanol, black) is at the sides. From Ref. [3].

Acoustic patterning of solute concentration fields. Based on Eqs. (1) and (2), and the setup shown in Fig. 1, Karlsen and Bruus performed a purely theoretical study of acoustic patterning of solute concentration fields [4]. In Fig. 2(a) simulations predict that by changing on the few-seconds time scale the acoustic actuation in the sequence 0 MHz \rightarrow 2 MHz \rightarrow 5 MHz \rightarrow 4 MHz \rightarrow 0 MHz \rightarrow , the iodixanol solution can be patterned remarkably fast, much faster than the one-minute diffusion time. Experimentally, using lithium niobate substrates with spiral-metal-electrodes and PDMS-defined microdevices as developed by the Lille-Paris team lead by Baudoin and Thomas, the first preliminary validation has been obtained by Baudoin and Gerbedoen at Lille in collaboration with Karlsen and Bruus, Fig. 2(b). Here, seen in a top view, an acoustic Bessel-1 vortex beam is created by the spiral electrode (black) and influencing an aqueous ficoll-solution (white) next to dyed water (dark gray). The color plot shows the corresponding simulation using Eqs. (1) and (2).

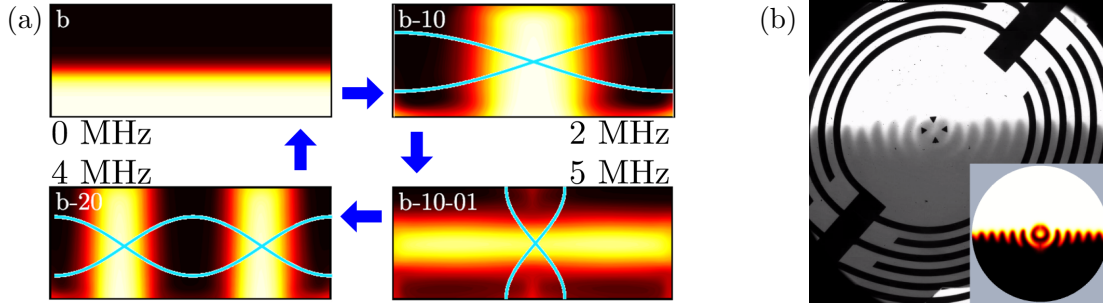


Figure 2: (a) Simulation of patterning on the 1-s time-scale of an iodixanol concentration field using four acoustic modes, switching faster than the 1-min diffusion time scale, Ref. [4]. (b) Preliminary comparison from the Lille-DTU collaboration between experimental (gray-scale image) and numerical simulation (color plot) of acoustic patterning of a ficoll-solution (white) next to dyed water (dark) using the acoustic vortex method [5].

Suppression of acoustic streaming in inhomogeneous fluids. From the first experiments [1, 2], see also Fig. 1(b), it is clear that acoustic streaming is suppressed in inhomogeneous fluids. The well-defined gradient from high to low solute concentrations is only smeared by diffusion and not by vortical streaming flows. This suppression phenomenon was studied in more detail by Karlsen, Bruus and Qiu at DTU in collaboration with Augustsson at Lund University, the first two theoretically and the latter two experimentally [6]. To correctly calculate the streaming and its spatial suppression shown in Fig. 3, it is necessary to include the full viscous stress tensor in the fast-time-scale acoustics that is the source of \mathbf{f}_{ac} in Eq. (1). In this case, the coupled acoustic equations for the velocity \mathbf{v}_1 , the pressure p_1 , and the density ρ_1 become

$$-i\omega\rho_0\mathbf{v}_1 = \nabla \cdot \boldsymbol{\sigma}_1, \quad -i\omega\kappa_0 p_1 = -\nabla \cdot \mathbf{v}_1, \quad -i\omega\rho_0\kappa_0 p_1 = -i\omega\rho_1 + \mathbf{v}_1 \cdot \nabla \rho_0. \quad (3)$$

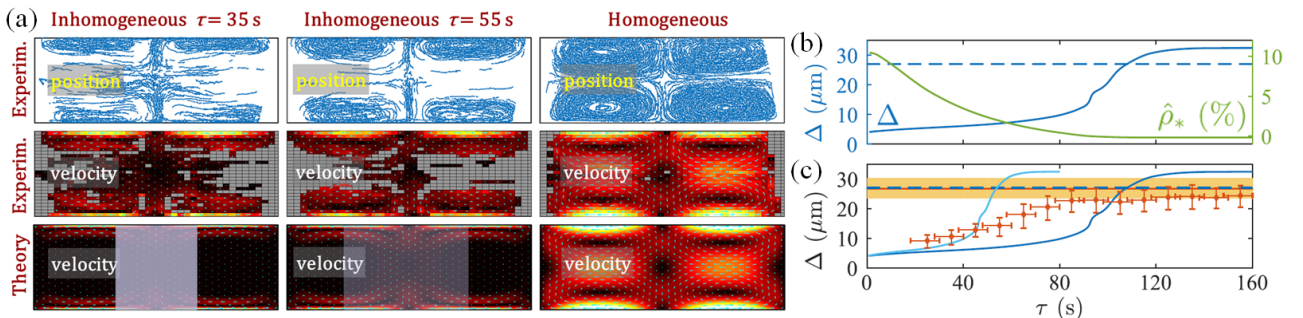


Figure 3: Adapted from Ref. [6]: Suppression of streaming by experiment and simulation in the same inhomogeneous system as in Fig. 1, using 1- μm -diameter polystyrene tracer beads. (a) Measured positions of the tracer beads at time $\tau = 35$ s and 55 s (top row); measured (middle row) and simulated (bottom row) particle velocities. (b) Distance Δ (blue) from the wall to the center of a given streaming roll vs. time τ , and the relative density difference $\hat{\rho}^*$ (green) between the center and the side of the channel. (c) Measured (red points) and simulated (blue lines) Δ versus τ . The streaming is suppressed until $\tau \approx 70$ s, after which time, the inhomogeneity has been smeared out sufficiently to render the system homogeneous, whereby \mathbf{f}_{ac} disappears.

References

- [1] S. Deshmukh, Z. Brzozka, T. Laurell, and P. Augustsson. *Lab Chip* **14**, 3394 (2014).
- [2] P. Augustsson, J. T. Karlsen, H.-W. Su, H. Bruus, and J. Voldman. *Nat. Commun.* **7**, 11556 (2016).
- [3] J. T. Karlsen, P. Augustsson, and H. Bruus. *Phys. Rev. Lett.* **117**, 114504 (2016).
- [4] J. T. Karlsen and H. Bruus. *Phys. Rev. Appl.* **7**, 034017 (2017).
- [5] A. Riaud, M. Baudoin, O. Bou Matar, L. Becerra, and J.-L. Thomas. *Phys. Rev. Appl.* **7**, 024007 (2017).
- [6] J. T. Karlsen, W. Qiu, P. Augustsson, and H. Bruus. *Phys. Rev. Lett.* **120**, 054501 (2018).

Acoustic manipulation of armored bubbles: shape oscillations, particle expulsion, and pattern formation

Valeria Garbin

Department of Chemical Engineering, Imperial College London, London SW7 2AZ, UK
E-mail: v.garbin@imperial.ac.uk, URL: <https://garbinlab.org/>

Introduction

Armored bubbles, covered by a monolayer of colloidal particles, exhibit outstanding stability against dissolution [1] and remarkable mechanical properties [2,3,4]. In this talk I will give an overview of the work in our group on acoustic manipulation of armored bubbles, and the intriguing phenomena we have observed: shape oscillations [5], particle expulsion [6], and pattern formation [7].

Shape oscillations

Armored bubbles respond to ultrasound by undergoing volumetric oscillations and, under the right conditions, they exhibit shape oscillations [5]. We investigated the shape oscillations of armored bubbles driven by ultrasound at 40 kHz. The bubbles (60-400 μm), stabilised by a monolayer of microparticles (1-5 μm), are made by mechanical agitation. We performed high-speed visualisation of the interface shape and of the particle distribution during ultrafast deformation at a rate of up to 10^4 s^{-1} . The shape oscillations exhibit period doubling but the mode of shape oscillations is found to not depend on the bubble size, in contrast with what has been reported for uncoated bubbles (Figure 1).

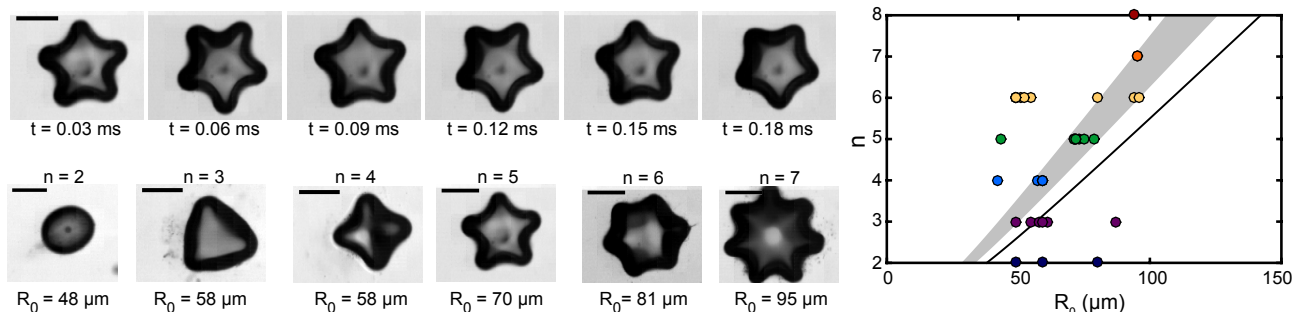


Figure 1: Shape oscillations of armored bubbles. The shape oscillations exhibit period doubling but do not exhibit mode selectivity. The solid line and the shaded area are the theoretical predictions for mode selectivity. The experimental data show no dependence of the mode n on the initial radius R_0 . Scale bars: 80 μm . Adapted from Ref. [5].

Particle expulsion

For large-amplitude ultrasonic forcing, we observed expulsion of colloids from the interface of armored bubbles. We uncovered different particle expulsion scenarios depending on the mode of bubble deformation, including highly directional patterns of particles release during shape oscillations. A decomposition of the non-spherical shape in spatial Fourier modes reveals that the interplay of different modes determines the locations of particle expulsion. The n -fold symmetry of the dominant mode does not always lead to desorption from all $2n$ antinodes, but only those where there is favourable alignment with the sub-dominant modes. Desorption from the antinodes of the shape oscillations is due to various mechanisms. Firstly, the radial acceleration of the interface at the antinodes can be up to 10^5 – 10^6 m.s^{-2} , hence there is a contribution from the inertia of the particles localised at the antinodes. The inertia of the particles can drive desorption through a collective effect at the points of high curvature. Secondly, the surface pressure is a maximum at the antinodes, where the rate of change of area is a maximum. The particles are pushed out of the interface because of the excluded volume constraint, i.e., the particles cannot overlap. In addition, our experiments revealed migration of particles to the

antinodes during shape oscillations. As a result, the accumulation of particles at the antinodes further enhances the contribution of the surface pressure in driving desorption.

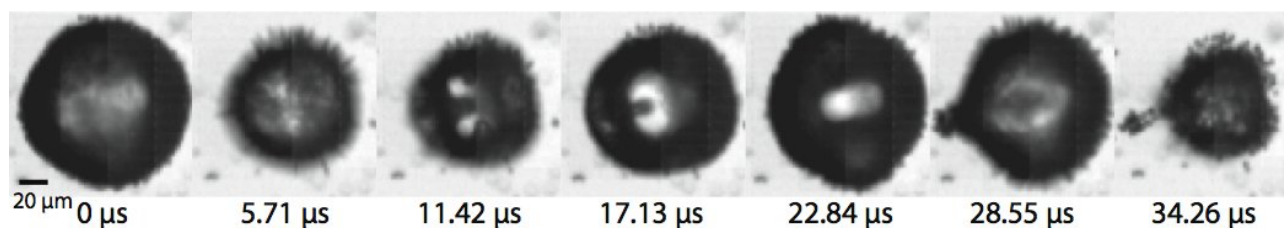


Figure 2: Directional particle expulsion from an armored bubble undergoing jetting. Adapted from Ref. [6].

Pattern formation

Monolayers of colloidal particles are a convenient two-dimensional model system to visualise emergent behaviors in soft matter, but previous studies have been limited to slow deformations. We have used ultrasonic driving of armoured bubbles to probe and visualise the evolution of a monolayer of colloids during high-rate deformation at 10^4 s^{-1} . We observed the emergence of a transient network of strings (Figure 3), which points to highly directional interparticle interactions during forcing. We used discrete particle simulations to show that it is caused by a delicate interplay of dynamic capillarity and hydrodynamic interactions between particles oscillating at high frequency. These results highlight again the importance of inertial effects, which are normally negligible in a colloidal system, caused by accelerations approaching $10,000g$ [7]. These phenomena have no counterpart at lower deformation rates, making armoured bubbles driven by ultrasound a promising platform to study extreme deformation of soft matter.

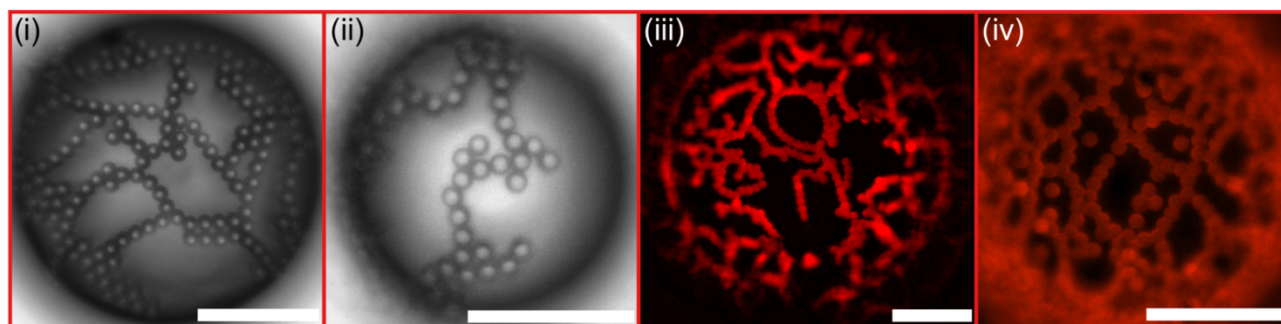


Figure 3: Pattern formation on ultrasound-driven armored bubbles. The colloids re-arrange into a network of strings. This is a transient microstructure, indicating that it is due to dynamic interactions. Scale bars: $40 \mu\text{m}$. Adapted from Ref. [7].

Conclusion

Bubbles stabilised by colloidal particles can find applications in advanced materials, catalysis and drug delivery. For applications in controlled release, it is desirable to remove the particles from the interface in a programmable fashion. We have shown that ultrasound is a precise temporal trigger for particle release, and directional release also seems to be within reach. The results on pattern formation also suggest that extreme deformation of soft matter offers new opportunities for dynamic self-assembly and tunable materials.

References

- [1] M. Abkarian et al., Dissolution arrest and stability of particle-covered bubbles. *Phys. Rev. Lett.* **99**, 188301 (2007).
- [2] N. Taccoen, F. Lequeux, D. Z. Gunes, C. N. Baroud, Probing the mechanical strength of an armored bubble and its implication to particle-stabilized foams. *Phys. Rev. X* **6**, 011010 (2016)
- [3] P. J. Beltramo et al., Arresting dissolution by interfacial rheology design. *PNAS* 05181 (2017).
- [4] G. Prabhudesai, I. Bihi, F. Zoueshtiagh, J. Jose, M. Baudoin, Nonspherical armoured bubble vibration, *Soft Matter* **13**, 3879-3884 (2017)
- [5] V. Poulichet, A. Huerre, V. Garbin, Shape oscillations of particle-coated bubbles and directional particle expulsion, *Soft Matter* **13**, 125 (2017)
- [6] V. Poulichet and V. Garbin, Ultrafast desorption of colloidal particles from fluid interfaces, *PNAS* **112**, 5932 (2015)
- [7] A. Huerre, M. De Corato, V. Garbin, Dynamic capillary assembly of colloids at interfaces with $10,000g$ accelerations, arXiv:1802.09318v1 [cond-mat.soft]

(termed “total internal reflection”)³. This corresponds to the red region on the substrate under the channel wall domain in Figure 1a.

We demonstrate here not only that this effect is substantial and robust for rapid particle, but also confirm that the periodicity of the pressure field can be predicted by a straightforward analytical model. This assumes that the effect of spatially limiting the transducer domain (a wavefront with phase φ_0 arising from the microchannel surface) is mathematically equivalent to the addition to a uniform wavefront of an oppositely phased ($\varphi = \varphi_0 - \pi$) domain just outside the channel region⁴. The patterning periodicity near a channel wall can then be predicted based on the intersection locations of these edge waves with SAW wavefronts, as shown in Figure 1b. The periodic spacing in the vicinity of a flat wall, a function of the angle of the channel wall relative to the SAW propagation direction (θ), is given by

$$\lambda_\theta = \lambda_l \sin(\theta) \csc\left(\theta - \sin^{-1}\left(\sin \theta \frac{c_l}{c_s}\right)\right), \quad (1)$$

where c_s and c_l are the sound speeds on the substrate and in the fluid, respectively, and λ_l is the acoustic wavelength in the fluid. Figure 2 shows the measured 1 μm particle pattern periodicity near flat polydimethylsiloxane (PDMS) walls exposed to a travelling SAW. Figure 2a shows the coordinate system for an example measurement, and Figure 2b shows the measured periodicity with respect to the SAW wavelength, $\lambda_\theta/\lambda_{\text{SAW}}$. For each of the measured angles in Figure 2 there is a clear correspondence to the predictions from Equation 1. Because the wavefront intersections will occur in a shorter time when they are counter-propagating, angles of the channel wall closer to 180° will result in smaller periodic spacings than will angles in which the reflected wavefront and substrate wave are co-propagating.

At $\theta=90^\circ$ a special case arises, where the periodic spacing from neighboring channel walls is equivalent². This permits the generation of time-averaged symmetric pressure fields along the channel. Figure 3a shows the simulated pressure field distribution when the width of a channel is equal to 0.5, 1 and 2 times λ_{90° . Interestingly, smaller channel dimensions ($w \lesssim \lambda_{90^\circ}$) results in acoustic fields that are highly atypical of acoustic resonators, where the minimum acoustic pressure locations are at the edges rather than at the channel center. This is demonstrated experimentally in Figure 3b and 3c, which shows a serpentine channel whose primary axis is along the SAW propagation direction. Changing the applied frequency, where higher applied frequencies correspond to smaller SAW and fluid wavelengths, results in an altered ratio of channel width to λ_{90° . Examining this ratio at the transition between the existence of one or two pressure maximums along the transverse axis, with $w = 1.63\lambda_{90^\circ}$ at 53.3 MHz ($\lambda_{\text{SAW}}=73.8 \mu\text{m}$) and $w = 1.42\lambda_{90^\circ}$ at 46.2 MHz ($\lambda_{\text{SAW}}=85.1 \mu\text{m}$), we demonstrate that we can control the number of nodal positions that develop across the channel, and thus dictate particle behavior in a continuous throughput microfluidic device.

Conclusions

We have demonstrated a novel method for producing time-averaged fields in microfluidic systems based on imposing finite transducer boundary conditions through the simple introduction of microchannel walls on a SAW substrate. Importantly, this permits particle patterning that can be at arbitrary orientations to the underlying SAW propagation directions (Figure 1c, Figure 2), and importantly can result in time-averaged nodal positions along channel edges rather than in the channel center (Figure 3). The flexibility of this channel-based patterning method will moreover expand the range of patterning activities that are possible on-chip.

References

- [1] C. Devendran, D. J. Collins, Y. Ai and A. Neild, *Phys. Rev. Lett.*, 118, 154501 (2017).
- [2] D. J. Collins, R. O’Rorke, C. Devendran, Z. Ma, J. Han, A. Neild and Y. Ai, *Phys. Rev. Lett.*, 120, 074502 (2018).
- [3] F. Kiebert, S. Wege, J. Massing, J. König, R. Weser, H. Schmidt and C. Cierpka, *Lab Chip*, 17, 2104-2114 (2017).
- [4] D. J. Collins, R. O’Rorke, J. Han and Y. Ai, *In Submission* (2018).

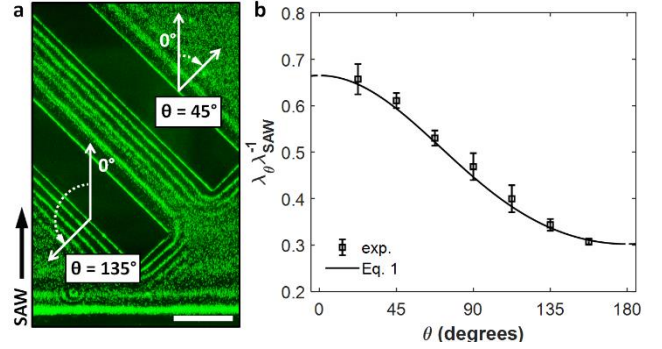


Figure 2: (a) Particle patterning in the vicinity of channel walls: coordinate system. Scale bar 200 μm . (b) Comparison of predicted spacings (Equation 1) and that measured at $\theta=22.5^\circ, 45^\circ, 77.5^\circ, 90^\circ, 112.5^\circ, 135^\circ$ and 157.5° .

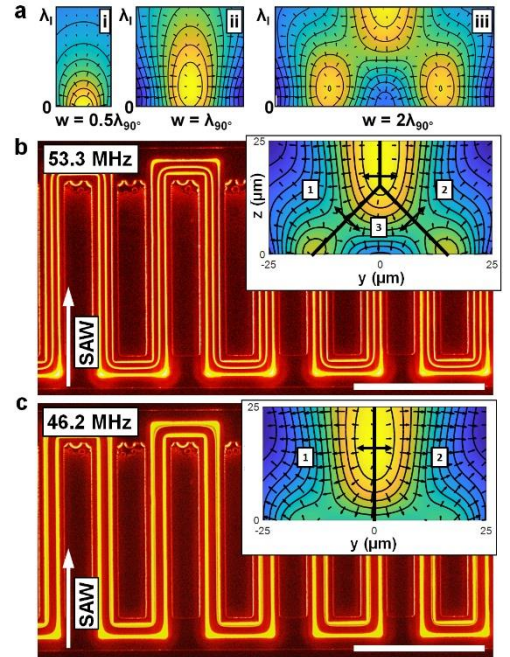


Figure 3: (a) Modelled pressure fields in a channel cross section for different widths. (b,c). Experimentally demonstrated focusing of fluorescent 2 μm particles in a continuous flow corresponds to modelled predictions. Scale bar is 500 μm .



Progress in novel rechargeable lithium metal batteries integrating acoustic wave recirculation of the liquid electrolyte

An Huang¹, Ping Liu² and James Friend¹

¹Medically Advanced Devices Laboratory, Departments of Mechanical and Aerospace Engineering and Materials Science and Engineering, University of California San Diego, San Diego, USA

²Nanoengineering, University of California San Diego, San Diego, USA

E-mail: jfriend@eng.ucsd.edu, URL: <http://friend.ucsd.edu/>

Introduction

We aim to overcome diffusion limitations in charging liquid electrolyte lithium ion batteries through inclusion of robust, fingernail-sized, and solid-state ~ 100 -MHz surface acoustic wave microdevices that produce turbulent acoustic streaming even through separator structures. These low-power (~ 10 mW of power per 1 cm^2 of electrode area) devices are fabricated from single crystal lithium niobate, and are compatible with lithium electrochemistry. Needed only during charging, the induced turbulent flow extends down to 100 -nm length scales, reducing the typically greater than $100 \mu\text{m}$ Li^+ ion depletion layer adjacent the anode to less than $1 \mu\text{m}$ during charging, and reducing the characteristic diffusion time of Li^+ ions by over three orders of magnitude. In crude prototype lithium metal batteries, this approach facilitates rapid recharging of up to 3 C (full charge in 20 min at 3.75 mA/cm^2) for greater than 250 cycles without dendrite formation with Li as an anode, LiFePO_4 as a cathode, and 1 M LiPF_6 in $1:1$ (w/w) EC/DEC as an electrolyte, maintaining charge capacities fully 90% of the theoretical 170 mAh/g that represent a doubling of the charge capacity possible in any commercially available battery today; we are now achieving 6 C charging rates and expect to demonstrate those results at the meeting. These same devices also serve as a means to detect morphological changes within the battery, providing a real-time determination of battery status and a significant improvement in safety.

Concept and underpinning mechanism

The performance of a LIB is mainly determined by its diffusion properties, which directly affect the battery's charge and discharge rate, capacity and cycling stability. The convection-diffusion equation is a useful representation for the transport of the ions responsible for charge within the battery, given by [1]

$$\frac{\partial C}{\partial t} + v \cdot (\nabla C) = \nabla \cdot (D_i \nabla C) - \frac{i \cdot \nabla t_+}{z_+ F}, \quad (1)$$

where the concentration of the relevant species, C , changes over time in the first term as determined by the fluid transport in the second term with fluid velocity v , the diffusivity or diffusion coefficient D_i in the third term, and the ionic migration in the last term either into or out of the solution on the electrodes. The variables in that term include t_+ as the Li^+ transport number, z_+ as the charge number, and i as the current density. In most batteries, the fluid transport is negligible and $v = 0$. [2] The ionic migration $\frac{i \cdot \nabla t_+}{z_+ F}$ is responsible for the depletion of Li^+ ions adjacent the anode during charging, and so the only physical mechanism acting to replace these ions lost to the anode must appear via diffusion. Unfortunately, diffusion is entirely too slow to overcome ion depletion in the electrolyte under rapid charging in many batteries. [3] Due to the loss of motive ions, resistance increases across this depletion layer, joule heating grows within the layer, increasing the battery temperature, and either the charge rate is reduced or the battery can be damaged.[4]

The diffusivity is therefore a key parameter that must be addressed to achieve a high charge rate battery. Either one acts to increase the diffusion rate D_i , reduce the distance between anode and cathode, or attempts to make the fluid velocity v non-zero and therefore a significant factor in ion transport in the battery. This is the point of inducing acoustic streaming: v is increased from zero to $\sim 1 \text{ m/s}$, and does so with bulk turbulence that underpins complete mixing phenomena observed to exist down to length scales that correspond to the Stokesian viscous boundary layer thickness, $\delta = 2\pi\sqrt{\mu/(\pi\rho f)} \sim 100 \text{ nm}$ for EC/DEC at 100 MHz . This fluid velocity and thorough mixing collectively increase the effective diffusion coefficient in a battery by two orders of magnitude, facilitating unprecedented rates of charge without a depletion layer and its unfortunate effects on the battery.

The SAW generated within the piezoelectric lithium niobate substrate is transmitted into the fluid electrolyte, giving rise to acoustic streaming. There are two attenuation length scales, one for the SAW in the lithium niobate substrate, which is $\sim 100 \mu\text{m}$ at 100 MHz, and another for the attenuation of the sound propagating in the fluid. Fortunately, the length scale of this attenuation is $\sim 1 \text{ cm}$ for 100 MHz,[5] ideal for a typical secondary battery cell used in EVs. This helps to generate the maximum possible electrolyte flow speed and mixing behavior in a thin region between the closely-spaced electrodes, all while avoiding acoustic wave reflection.

Uniquely, SAW generates extreme accelerations of 10^8 to 10^{10} m/s^2 in the fluid, driving *turbulent*[5] acoustic streaming—fluid flow at up to 1 m/s and exhibiting flow field vortices from centimeter-length scales down to $\sim 400 \text{ nm}$ length scales at 100 MHz.[6] By using such high frequencies, the acoustic wave also penetrates micro/nanoporous media such as the separator, having in the past been shown to drive rapid fluid flow through polymeric scaffolding with analogous pore sizes for tissue engineering.[7]

Results

Our latest results are shown in Fig. 1. A Swagelock battery was fabricated (Fig. 1 (a)) using a lithium metal anode, LiFePO_4 cathode, and EC/DEC in 1 M LiPF_6 as an electrolyte. It shows that no dendrite was formed after 280 cycles when the LMB is charged with SAW. On the other hand, clear lithium dendrite structure was formed (Fig. 1(e)) after 40 cycles for the traditional LMB (Fig. 1(d)).

Conclusions

We provide a technique for enabling rapid charging in batteries without having to make design compromises in materials and electrochemistry that hamper today’s technology, demonstrating a practical and inexpensive method for solving the 50-year dendrite growth problem that has long plagued rechargeable batteries. We also hint here at the physics underlying the development of the diffusion-dependent depletion layer and how the turbulent acoustically-induced electrolyte recirculation—even in the presence of a separator—can eliminate the depletion layer.

References

- [1] Newman, J. & Thomas-Alyea, K. E. *Electrochemical systems* (John Wiley & Sons, 2012).
- [2] Akolkar, R. *J Power Sources* **232**, 23–28 (2013).
- [3] Goodenough, J. B. & Park, K.-S. *JACS* **135**, 1167–1176 (2013).
- [4] Etacheri, V., Marom, R., Elazari, R., Salitra, G. & Aurbach, D. *Energy & Environmental Science* **4**, 3243–3262 (2011).
- [5] Dentry, M. B., Yeo, L. Y. & Friend, J. R. *Phys Rev E* **89**, 013203 (2014).
- [6] Friend, J. R. & Yeo, L. Y. *Rev Mod Phys* **83**, 647–704 (2011).
- [7] Li, H., Friend, J. R. & Yeo, L. Y. *Biomaterials* **9**, 647–656 (2007).

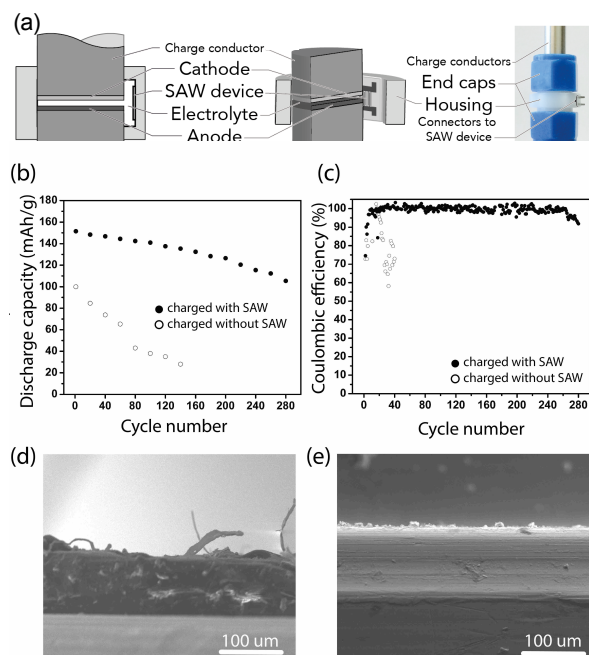


Figure 1: A prototype LMB with a SAW device to drive electrolyte recirculation; from left to right are: side view, cutaway view showing placement of SAW device, and photograph of assembled prototype battery. For scale, the charge conductors are 10 mm in diameter and the gap between the Li anode and LiFePO_4 cathode is $100 \mu\text{m}$. Applying 100 mW at 100 MHz to the lithium niobate SAW device produces an acoustic wave across its surface; this wave propagates into the adjacent fluid as intense sound that gives rise to acoustic streaming, fluid flow away from the SAW source. This forces recirculation in the gap between the anode and cathode that reduces the Li^+ ion concentration gradient’s depth during charging from over $100 \mu\text{m}$ to less than $1 \mu\text{m}$. (b) In a prototype prismatic lithium metal battery (LMB), charging and discharging at 1C causes rapid degradation to only 40% of the battery’s capacity in only 40 cycles **without SAW** (circles). **With SAW to recirculate the electrolyte, however, 70% of the battery’s capacity is preserved after 280 cycles.** Moreover, (c) the Coulombic efficiency is $\sim 98\%$ in the LMB when using SAW, far superior to the $\sim 70\%$ without SAW. Finally, dendrites are (d) clearly evident and over $100 \mu\text{m}$ in length in the LMB without SAW, but there are (e) **no dendrites even after 200 cycles when using SAW** (images taken using ex-situ scanning electron microscopy). We are able to suppress the effects of reasonably fast (3C) charging in LMB batteries where even slow charging ($\sim 0.1\text{C}$) would lead to an adverse outcome.



A numerical study of Rayleigh streaming at high acoustic level

Virginie Daru^{1,2}, Diana Baltean-Carlès^{2,3}, and Catherine Weisman^{2,3}

¹DynFluid Lab., ENSAM, 151 boulevard de l'hôpital, 75013 Paris, France.
E-mail: Virginie.Daru@ensam.eu

²LIMSI, CNRS, Université Paris-Saclay, F-91405 Orsay Cedex, France

³Sorbonne Université, Faculté des Sciences et Ingénierie, UFR d'Ingénierie, 4 place Jussieu, 75252 PARIS Cedex 05, France

Introduction

Rayleigh streaming is a steady flow generated by the interaction between an acoustic wave and a solid wall, generally assumed to be second order in a Mach number expansion. This motion was initially studied by Rayleigh [1] in the case of wide 2D channels. This streaming flow is characterized by four steady counter-rotating vortices in one-half wavelength of the standing wave outside the boundary layer, nowadays referred to as Rayleigh streaming. Along the central axis of the channel, the streaming motion is oriented from axial particle velocity nodes to antinodes. Inside the boundary layer four additional vortices are created simultaneously, with the streaming motion oriented from axial particle velocity antinodes to nodes along the inner walls of the channel [2].

In this work we present a numerical study of Rayleigh streaming associated with a standing acoustic wave initiated in a waveguide (2D channel or cylindrical tube). The numerical approach relies on the solution of the compressible Navier-Stokes equations, that enables the simultaneous computation of the acoustic field and the streaming flow. We focus here on the study of the nonlinear effects that are expected when the acoustic level is high. Numerical results show that harmonics develop in the acoustic flow, resulting in shock wave formation. The streaming flow is modified and additional streaming cells have been observed. This is consistent with experiments [3], but contradicts the results obtained by Menguy et al [4], in their analytical study of the effect of moderate nonlinearity on the streaming flow. In order to shed light on the different phenomena at work when the acoustic level becomes high, we have developed several numerical strategies.

Configuration and numerical model

We consider a rectangular channel or a tube of length L and half width y_0 (or radius R_0), initially filled with the working gas. In order to initiate an acoustic standing wave in the channel, it is shaken in the longitudinal direction, so that a harmonic velocity law is imposed, $V(t) = x_p \omega \cos(\omega t)$, ω being the angular frequency and x_p the amplitude of the channel displacement. The flow is solved based on a direct numerical simulation of the unsteady compressible Navier-Stokes equations expressed in the moving frame attached to it, so that a forcing source term is added. High order finite difference schemes developed in Daru and Tenaud [5] are used. The streaming flow is obtained throughout the calculation from calculating a simple mean value for each physical quantity over an acoustic period.

Resonant conditions are imposed, for which $L = \lambda/2$, $\lambda = c_0/f$ being the wavelength, c_0 the speed of sound for initial state and f the vibration frequency of the waveguide. Boundary layers develop along the walls, with thickness $\delta_\nu = \sqrt{2\nu/\omega}$, ν being the kinematic viscosity. The boundary layer is of small thickness and must be correctly meshed. We have determined that a value of 5 points per boundary layer thickness is sufficient for reasonable accuracy of the simulations. In the axial direction, 500 discretization points are used.

The non dimensional parameters governing this flow are the following : geometrical parameters y_0/δ_ν and y_0/L , the Mach number $M = U_{ac}/c_0$ where U_{ac} is the axial acoustic velocity amplitude, the Reynolds acoustic number $Re_{ac} = \frac{1}{2}\lambda/(\pi\delta_\nu)$, and the so-called nonlinear Reynolds number $Re_{NL} = (My_0/\delta_\nu)^2$ which corresponds to the Reynolds number of the streaming flow. This last parameter was introduced in [4] and is considered as representative of the nonlinear effects induced by high acoustic levels on the streaming flow.

Results

The vibration frequency is here fixed equal to 20000Hz, corresponding to fundamental resonant frequency of a waveguide of small length $L = 8.8125\text{mm}$. The working gas is air at standard atmospheric pressure. We have made a parametric study by considering Re_{NL} values varying from small ($\ll 1$) to large (≈ 100) values. Several observations were made concerning the corresponding streaming flow.

Firstly new vortices appear near the center of the resonator at the highest acoustic levels (see Fig. 1 a)-b) showing streamlines of the streaming flow for low and high acoustic level). Secondly, maximum axial velocity on the axis deviates from that predicted in the linear theory by Rayleigh. In Rayleigh's theory, this velocity has a second order power law dependency on the acoustic axial velocity amplitude. The numerical simulation at high acoustic level show that this dependency changes drastically and becomes linear at high acoustic level. This is illustrated in Fig. 1 c) presenting the maximum axial velocity on the axis, normalized by Rayleigh's theoretical prediction, according to the acoustic velocity. Finally it is also remarked that the acoustic and streaming flows have strong interaction on the transverse velocity components. At high acoustic levels, the streaming transverse (vertical or radial) velocity becomes greater than that of the acoustic flow. The acoustic field is thus strongly modified by streaming which is in turn also modified. It is worth noting that comparisons with experimental results, presented in [6], show excellent agreement with these numerical observations, although the size of the experimental apparatus is much larger than that of the numerical configuration.

Numerical strategies for studying the influence of different phenomena

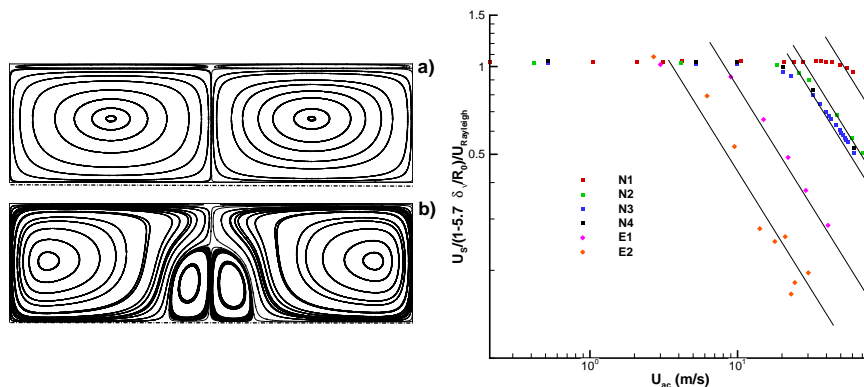
Understanding how the streaming flow is modified at high acoustic level, and trying to draw laws based on the appropriate parameters, is not an easy task since several phenomena that may be important are intricately related. These are: the harmonic content present in the acoustic field, temperature variation, inertia (characterized by Re_{NL}), nonlinear interaction between acoustics and streaming. In order to separate the effect of these phenomena, several strategies have been developed. Firstly the temperature effects were removed by considering an isentropic equation of state, resulting in similar behavior of the results. Secondly, to isolate inertial effects we developed a second numerical approach, where the streaming flow is calculated directly (again from the Navier-Stokes equations) from the Reynolds stresses source terms provided by direct numerical simulation in a low acoustic level case. Multiplying these source terms by a coefficient enables to calculate the flow at high acoustic level while keeping a monofrequency acoustic field. This is a strategy comparable to the one followed in [4]. The results obtained in this way compare well to those in [4], but not to those given by direct numerical simulations. This shows that inertia cannot be the only phenomenon at the origin of the evolution of the streaming flow at high acoustic levels. We also have studied the relative effects of inertia and momentum diffusion during the establishment of the streaming flow by analogy with the classical problem of the lid-driven cavity, since Rayleigh streaming is driven by the velocity at the edge of the boundary layer.

Conclusion

Numerical simulations were used to study the streaming flow in a resonator at high acoustic levels. It is shown that streaming is deeply modified with respect to Rayleigh's solution in the low level acoustic case. The numerical approach enables to have deep insight into the flow fields and the influence of different phenomena, and to develop strategies aimed at studying different aspects of the problem at hand. It is particularly well adapted for the study of flows at microscales, where Reynolds numbers are small, enabling to maintain the computational costs at affordable levels.

References

- [1] Lord Rayleigh. Philos. Trans. R. Soc. London **175**, 1-21 (1884).
- [2] W.L. Nyborg. *Physical Acoustics* W. P. Mason (ed), Academic Press, Vol. 2B 265-331 (New York, 1965).
- [3] I. Reynt, V. Daru, H. Bailliet, S. Moreau, J.-C. Valière, D. Baltean-Carlès, C. Weisman. J. Acoust. Soc. Am. **13**, **3**, 1791-1801 (2013).
- [4] L. Menguy, J. Gilbert. Acta Acustica, **86**, 249-259 (2000).
- [5] V. Daru, C. Tenaud. J. Comput. Physics, **193**, 563-594 (2004).
- [6] V. Daru, I. Reynt, H. Bailliet, C. Weisman, D. Baltean-Carlès. J. Acoust. Soc. Am. **141**, **563**, 563-574 (2017).



c) Figure 1: Left: Streamlines of the streaming flow at low (a) and high (b) acoustic level in the top half of the guide. Right: Normalized maximum axial streaming velocity vs acoustic velocity, for several values of the parameter R_0/δ_1 . Comparison between numerical results (labelled N1, N2, N3) and experimental results (labelled E1, E2).



Radiation pressure force and torque in single beam acoustical tweezers

Jean-Louis Thomas¹, Diego Baresch^{1,2}, Michaël Baudoin³, Régis Marchiano², Olivier B. Matar³, Antoine Riaud^{1,3}

¹Sorbonne Université, CNRS UMR 7588, Institut des NanoSciences de Paris, INSP, F-75005, Paris, France

²Sorbonne Université, CNRS UMR 7190, Institut Jean le Rond d'Alembert, F-75005 Paris, France

³Institut d'Electronique, de Microélectronique et Nanotechnologie (IEMN), LIA LEMAC/LICS, Université Lille 1, UMR CNRS 8520, 59652 Villeneuve d'Ascq, France

Introduction

Moving and positioning small objects without any mechanical contact is efficiently performed by different means as optical traps, magnetic traps, optical tweezers ... Optical tweezers[1] is however the most versatile and accurate tool to date. Here, a single laser beam focused by a high numerical aperture lens can trap relatively transparent dielectric beads at the beam focus. As the beam can easily be steered and the focal spot creates a single potential well, such a device can pick, push and pull, control both the position and the force on a single object selected among others. This combination of features are unique to optical tweezers that have become the tool of reference for contactless manipulation and led to many applications in biology for instance. They efficiently handle particles ranging in size from a few micrometers to hundreds of nanometers and apply forces in the range of tens of picoNewton. Their drawbacks is the weak force applied and the heating and photo-toxicity when light intensity is increased.

Acoustical traps

The physical force used in optical tweezers, the radiation pressure, is not specific to electromagnetic fields even if it was first observed and studied in optics. At equal incident beam power acoustical forces overtake by five orders of magnitude optical ones since radiation pressure is inversely proportional to the speed of propagation of the field. Furthermore, the large spectrum of frequencies covered by coherent piezoelectric ultrasonic sources provide a wide variety of manipulation possibilities from macro- to microscopic scales. Thus, acoustics radiation pressure was applied to the study of biological materials almost 40 years ago and levitation traps[2] for bubbles were devised even before. Acoustical levitation is an efficient technique for container-less processing and transportation of macroscopic matter in air, while acoustophoresis has provided a powerful strategy for on-chip manipulation, sorting and mixing of many microscopic particles and living organisms.

Acoustical tweezers

Although these ultrasonic techniques are becoming very popular, using standing wave systems have prohibited accurate manipulation of a single particle in three dimensions as can be done with optical tweezers. Indeed, the single-beam concept of optical tweezers is fascinating but challenging since one expects and in most situation, observes, that the radiation pressure tends to push a scatterer in the beam propagation direction. This pushing force can be understood as an exchange of wave pseudo-momentum when the incident beam is partially backscattered. In the single beam scheme of optical tweezers, another component of the radiation pressure force, called "gradient force", counterbalances the strong pushing force and is able to pull a scatterer located downstream from the focus.

Recently, we analyzed the radiation pressure on large elastic sphere or arbitrary size and devised a mean to get this pulling force in acoustics with an helicoidal beam, also named acoustical vortex[3]. These waves carry a phase singularity on the axis of propagation where the intensity is canceled. The object is trapped in this zone of silence that is surrounded by a ring of high intensity achieving the potential well needed to trap the particle. I will present the trapping of elastic particles by the large radiation force of a single acoustical beam in the three dimensions. As its optical counterpart, it can push, pull and accurately control the position of a unique particle[4]. Various features are promising for the development of a large variety of systems in biology, chemistry and physics where small particles play an important role, in particular, for single particle biophysical essays.

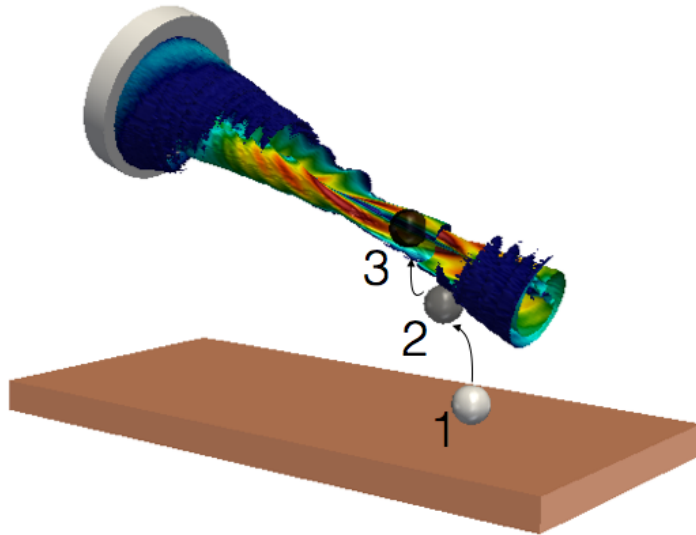


Figure 1: An acoustical single beam tweezers grabbing and then holding a sphere in its single position of equilibrium

Torque and sphere rotation for acoustical tweezers

Since the pulling and pushing radiation forces result from an exchange of wave pseudo-momentum when the medium is not homogeneous, one may expect a torque if the wave carry pseudo angular momentum or when the medium is not isotropic. And indeed, many experiments have demonstrated that an acoustic wave can induce rotation of non spherical objects[5]. One less expected effect is the torque applied on a sphere and this effect was predicted and analyzed when the sphere material absorbs part of the acoustic wave[6,7]. However, a torque and the resulting rotation was first observed for two orthogonal standing waves shifted in phase and this rotation was explained by inner streaming generated in the viscous boundary layers surrounding the sphere[8]. Recent advances on the modeling of inner streaming[10] allow to develop a model taking into account all the effects involved in the transfer of orbital pseudo-momentum. I will present some experiments and their comparisons with a quantitative modeling taking account these different mechanisms.

Conclusion

Acoustical tweezers have been designed and assessed, their miniaturization for the manipulation at the microscale is in development[10,11]. They are able to select, trap, move a single particle in the three dimensions. To these three degrees of freedom, one degree of rotation related to acoustic energy absorption is present and can be also dynamically controlled.

References

- [1] A. Ashkin, J. M. Dziedzic, J. E. Bjorkholm, and S. Chu, *Opt. Lett.* **11**, 288 (1986)
- [2] R. Apfel, *J. Acoust. Soc. Am.* **70**, 636 (1981)
- [3] D. Baresch, J.-L. Thomas, and R. Marchiano, *J. App. Phys.* **113**, 184901(2013)
- [4] D. Baresch, J.-L. Thomas, and R. Marchiano, *Phys. Rev. Lett.* **116**, 024301 (2016)
- [5] T. Schwarz, G. Petit-Pierre, and J. Dual, *J. Acoust. Soc. Am.* **133**, 1260 (2013)
- [6] L. Zhang and P. L. Marston, *J. Acoust. Soc. Am.* **136**, 2917 (2014)
- [7] G. T. Silva, *J. Acoust. Soc. Am.* **136**, 2405 (2014)
- [8] F. Busse and T. Wang, *J. Acoust. Soc. Am.* **69**, 1634 (1981)
- [9] M. Settnes and H. Bruus, *Phys. Rev. E* **85**, 016327 (2012)
- [10] A. Riaud, M. Baudoin, J.-L. Thomas, and O. B. Matar, *Phys. Rev. E* **90**, 013008 (2014)
- [11] A. Riaud, M. Baudoin, O. B. Matar, L. Becerra, and J.-L. Thomas, *Phys. Rev. App.* **7**, 024007 (2017)

Ultra-High-Frequency Surface-Acoustic-Wave microfluidics and biosensors

Marco Cecchini

NEST, Istituto Nanoscienze-CNR and Scuola Normale Superiore (Pisa, Italy)
E-mail: marco.cecchini@nano.cnr.it, URL: <http://web.nano.cnr.it/neurosens>

Introduction

Rayleigh Surface acoustic waves (SAWs) are an effective means to interact with fluids and activate a number of microfluidic phenomena, such as mixing, droplet actuation, microparticle manipulation, nebulization and micropumping, to name but a few. Moreover, in a different configuration, SAWs can also be exploited for sensing applications. The SAW operation frequency is a fundamental parameter that sets the relevant length-scales of the device, and that can importantly limit the miniaturization and portability of the devices, as well as multiplexing operation and the integration of many operational blocks on the same chip.

High-Frequency SAW microfluidics [1,2,3]

Here, I discuss the relevant length scales in sub-nanometer amplitude SAW-driven acoustic streaming and illustrate the absence of any physical limitations beyond fabrication capabilities preventing the downscaling of SAW-driven internal streaming to nanoliter microreactors and beyond. GHz-SAWs are experimentally shown to importantly allow the reduction of droplet volume in digital microfluidics, and of the microchannel size in case of acoustic counterflow. Moreover, droplet heating is discussed as a function of the SAW frequency.

(a)

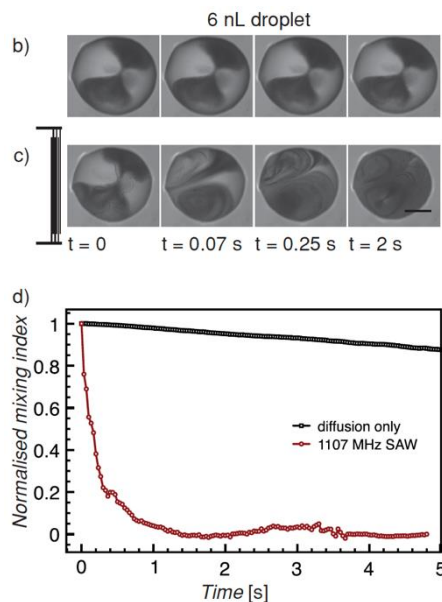
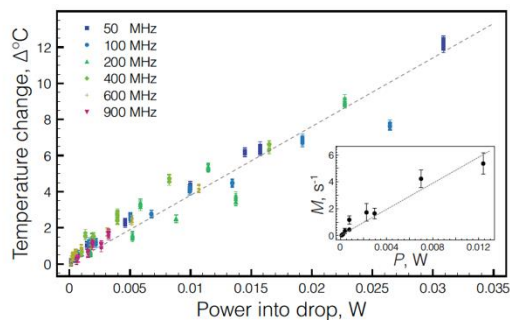


Figure 1. (a) Droplet heating across all devices is seen to be linear with SAW power into the fluid, akin to SAW-driven mixing efficiency, M (inset). (b,c,d) Active digital microfluidic mixing driven by ultra high frequency acoustic streaming. Mixing is shown for a ~ 6 nL droplet via (b) diffusion only, and actuated via a (c) 1107 MHz SAW. For nanoliter order droplets a shift to the UHF region is necessary to induce streaming. The normalized mixing of (b) and (c) are shown over time in (d), and shows a dramatic decrease in mixing time of over 100 times when the SAW is applied. Scale bar is 100 μm .

High-frequency SAW-resonator biosensor [4]

GHz-SAW acoustic resonators are fabricated and proposed for biosensing applications, demonstrating biomolecular detection in liquid after drying with a limit of detection far better than that of standard commercial gravimetric sensors (i.e., quartz-crystal-microbalances).

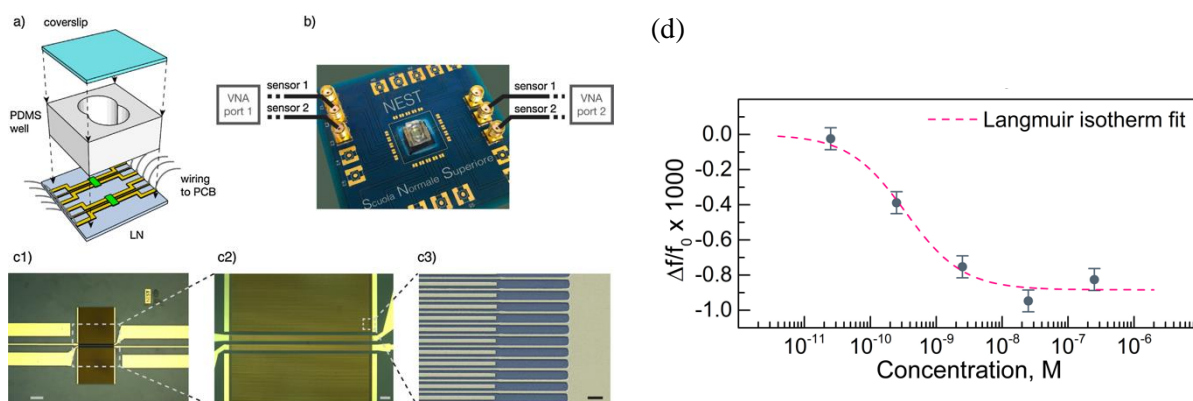


Figure 2. Chip and experimental setup. a) Exploded scheme of the biosensor chip. b) Photo of the mounted biosensor chip with external connections for electrical measurements. c1) and c2) Representative optical microscope images of a resonator. Scale bars are 200 μm (c1) and 40 μm (c2). c3) Representative scanning electron microscopy detail of a Positive Negative Reflector (scale bar is 2 μm). (d) Biosensor performance characterization: resonance shifts for different streptavidin concentrations. The sensor was functionalized with biotin-PEG-SH.

Conclusion

Here, the potential of high-frequency SAWs is shown and discussed for different applications. First, this regime allows many microfluidics operations (such as mixing, pumping and heating) for extremely small liquid volumes (of the order of 1-10 nL). Second, biosensors can be engineered with limit of detection much better than that reported for standard electrically-driven systems (such as commercial quartz crystal microbalances).

References

- [1] R.J. Shilton, M. Travagliati, F. Beltram, M. Cecchini. *Applied Physics Letters* 105 (7), 074106 (2014).
- [2] R.J. Shilton, M. Travagliati, F. Beltram, M. Cecchini. *Advanced Materials* 26 (29), 4941-4946 (2014).
- [3] R.J. Shilton, V. Mattoli, M. Travagliati, M. Agostini, A. Desii, F. Beltram, M. Cecchini. *Advanced Functional Materials* 25 (37), 5895-5901 (2015).
- [4] M. Agostini, G. Greco, M. Cecchini. *Sensors and Actuators B: Chemical*, 254, 1-7 (2018).



Acoustic radiation forces for extraordinary manipulations from theoretical perspectives

Likun Zhang¹

¹National Center for Physical Acoustics and Department of Physics and Astronomy, University of Mississippi, University, MS 38677, USA
E-mail: zhang@olemiss.edu, URL: <http://physics.olemiss.edu/zhang/>

Introduction

Acoustical radiation force analysis is essential for interpreting or finding special force conditions and for designing acoustic tweezers for well-controlled manipulations of particles. Since the force is a second-order effect, the analysis is complicated by interactions between incident and scattering fields and between different beam components. We consider three-dimensional radiation forces exerted by an arbitrary field and specific beams on an obstacle by momentum conservation that advances the flexible application of force superposition and gains insight. The analysis is particularly useful when considering the role of scattering and absorption on radiation forces as well as for selecting special beam parameters for extraordinary manipulations.

Force superposition and momentum conservation

In the early work in 1950s [1], acoustic radiation pressure was considered for the steady force exerted by a traveling plane wave on a plane reflector on which the wave is normally incident. The radiation pressure in this case, $E_i(1 + \gamma^2)$, might be thought as consisting of contributions from two parts: one part E_i by the incident wave only (where E_i is the time-averaged energy density of the incident wave) and the other part $E_r \equiv \gamma^2 E_i$ by the reflected wave (where γ is the amplitude reflection coefficient). In the view of momentum conservation, one might interpret that: the incident wave of energy density E_{in} is completely absorbed by the object, leading to a radiation pressure E_i on the reflector's surface, and meanwhile, the reflector re-emits a reflected wave of energy density E_r , resulting the reflector to experience a reactional radiation pressure $E_r = \gamma^2 E_i$. The phase between the incident and reflected waves doesn't play a role on the radiation pressure.

We implement this concept of force superposition to analyze three dimensional forces exerted by an arbitrary field on an obstacle. In this case, the total force is a sum of two parts associated with the traveling ingoing and outgoing spherical waves of the total field in a simple form as

$$\mathbf{F}_{tot} = \mathbf{F}_{in} + \mathbf{F}_{out}. \quad (1)$$

There is no net force due to interactions between the ingoing and outgoing waves. This superposition differs from considering the total field as a sum of incident and scattered fields whose interactions would always have contribution to the radiation force.

By considering the total field as a sum of the spherical ingoing and outgoing fields, one can again examine the force in the view of momentum conservation when evaluating at far fields in such as way that: the incident wave of energy density E_{in} is completely absorbed by the object, leading to a radiation pressure $-E_{in}\hat{\mathbf{r}}$ ($\hat{\mathbf{r}}$ is radially outwards at the far field), and meanwhile, the object re-emits a reflected wave of energy density E_{out} , resulting the object to experience a reactional radiation pressure $-E_{out}\hat{\mathbf{r}}$, leading to $\mathbf{F}_{in,out} = -\int E_{in,out}\hat{\mathbf{r}}dA$ (dA is surface element at far field; see Fig. 1). As a result, we relate the total force $\mathbf{F}_{tot} = \pi a^2(p_0^2/2\rho_0 c_0^2)\mathbf{Y}_{tot}$ to the angular functions $f_{in,out}(\theta, \phi)$ of the ingoing and outgoing waves in the far field form $p_{in,out} = p_0(a/2r)f_{in,out}(\theta, \phi)e^{i(\mp kr - \omega t)}$ as

$$\mathbf{Y}_{tot} = \mathbf{Y}_{in} + \mathbf{Y}_{out} \text{ with } \mathbf{Y}_{in,out} = -\frac{1}{4\pi} \int |f_{in,out}|^2 \hat{\mathbf{r}} d\Omega, \quad (2)$$

where the integral is over the whole solid angle Ω , a is a size scale of the obstacle, and ρ_0 and c_0 are density and sound speed of the surrounding media.

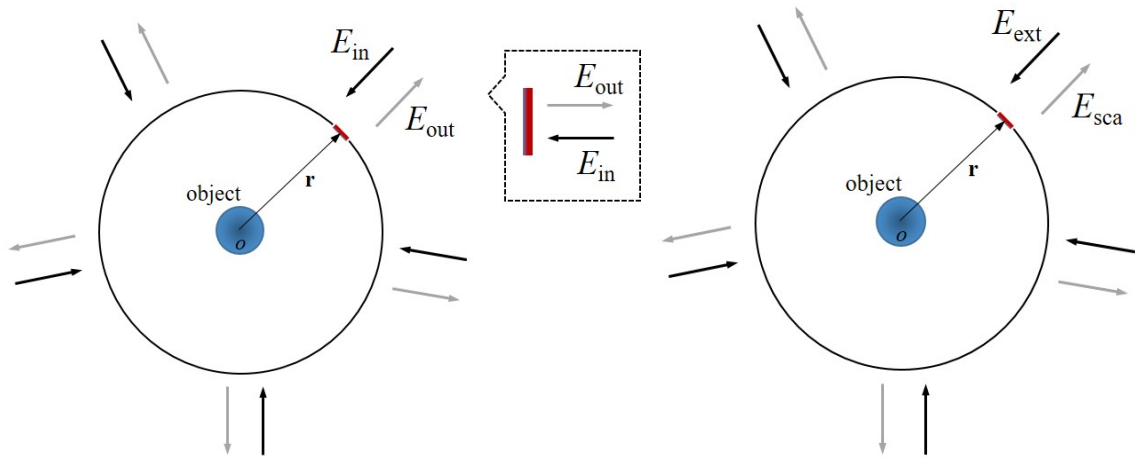


Figure 1: Illustration of analyzing three-dimensional radiation forces on an object in the pictures of spherical ingoing and outgoing wave fields (left) or momentum extinction and scattering (right) at far field.

Implement to special manipulations

The representation of force superposition and momentum conservation associated with far-field patterns of the traveling ingoing and outgoing spherical waves has a variety of applications for special manipulations of particles.

When considering an axisymmetric object like a spherical particle, the three-dimensional forces are as a function of the reflected partial wave coefficients s_n of the outgoing waves (which are partial wave scattering functions [2]) has the factor $(1 - s_n s_{n+1}^*)$ that is an analogue to the factor $(1 + \gamma^2)$ in the radiation pressure exerted by a plane traveling wave on a planar reflector, but with the coupling of adjacent partial waves as a result of momentum projections to the evaluated force directions. The adjacent partial wave coupling is related to momentum projections associated with scattering and extinction that relate to asymmetry of the ingoing and outgoing fields [3],

$$(Y_{\text{tot}})_i = Q_{\text{ext}} \mathcal{R}_{\text{ext},i} - Q_{\text{sca}} \mathcal{R}_{\text{sca},i}, \quad (3)$$

where $Q_{\text{ext},\text{sca}}$ are dimensionless efficiencies associated with extinction and scattering, and $\mathcal{R}_{\text{ext},i}$ and $\mathcal{R}_{\text{sca},i}$ are the factors taking momentum projection into the evaluated direction. Here $\mathcal{R}_{\text{ext},i} = 1$ when considering the axial radiation force exerted by a traveling plane wave [4]. For sound beams, the projection of momentum extinction from the wave fields can be manipulated for force reversal or for the absorption to increase or decrease the force along the evaluated direction [3].

The orthogonality of axial momentum between waves of different m -th order wave components (azimuthal order) allows the axial radiation force to be evaluated as a linear superposition of force contributions from different azimuthal components of the incident field. This has been found applications for analyzing forces on an arbitrarily located spherical particle by beam superposition as recently conducted for cylindrical Bessel beams [5]. The role of extinction and scattering by superposition is used to explore reversal of force direction and also radiation torque.

Conclusion

The examination of three-dimensional acoustic radiation forces exerted by arbitrary wave fields or specific beams on an obstacle via the view of momentum conservation and superposition relate the forces to far field patterns associated with beam and scattering parameters. The relation are useful for considering special forces and extraordinary manipulations of particles by special beams in the framework of momentum conservation associated with extinction and scattering.

References

- [1] F. E. Borgnis, Rev. Mod. Phys. **25**, 653-664 (1953).
- [2] L. Zhang and P. L. Marston, J. Acoust. Soc. Am. - Express Letters, **140**(2), EL178-EL183 (2017).
- [3] L. Zhang, J. Acoust. Soc. Am., submitted (2018).
- [4] P. J. Westervelt, J. Acoust. Soc. Am., **23**(3), 312-315 (1951).
- [5] L. Zhang, J. Acoust. Soc. Am., in press (2018).

Oral Abstracts



Flexible and wearable thin film acoustic wave sensing and acoustofluidic devices

Richard Y. Q. Fu,¹ Jack Luo²

¹Faculty of Engineering and Environment, Northumbria University, Newcastle, UK, NE1 8ST, UK

E-mail: richard.fu@northumbria.ac.uk; (<https://www.northumbria.ac.uk/about-us/our-staff/f/richard-fu/>)

²Institute for Materials Research and Innovation, University of Bolton, Deane Road, Bolton, BL3 5AB, UK

Introduction

Recently, piezoelectric thin films including zinc oxide (ZnO) and aluminium nitride (AlN) have found a broad range of lab-on-chip applications such as biosensing, particle/cell concentrating, sorting/patterning, pumping, mixing, nebulisation and jetting. Integrated acoustic wave sensing/microfluidic devices have been fabricated by depositing these piezoelectric films onto a number of substrates such as silicon, ceramics, diamond, quartz, glass, and more recently also polymer, metallic foils and bendable glass/silicon for making flexible devices. Such thin film acoustic wave devices have great potential for implementing integrated, disposable, or bendable/flexible lab-on-a-chip devices into various sensing and actuating applications. Compared with acoustic wave devices made of bulk piezoelectrics, the advantages of using thin film piezoelectrics include [1,2]: (1) potential integration with microelectronics and integrated circuits; (2) flexibility in applying substrates including those bendable, flexible or wearable ones; (3) flexibility to grow various oriented films for multiple wave mode generations; (4) reliability with less chances for device fracture.

Flexible and wearable thin film acoustic wave biosensors

Thin film acoustic wave devices have been used for detection of adsorbed biomolecules, viruses, bacteria and cells on surfaces through the interactions of DNA with complementary strands, antibody with antigen etc, and specific recognition of protein-ligands by immobilized receptors. This affinity-based detection concept can be utilised to diagnose early stages of diseases and cancers, allowing for early intervention and measures to be taken to prevent further development of illnesses and spreading of cancers. Recent developments in thin film acoustic devices have been focused on: (1) Sensors prepared on cheap and commonly used substrates to reduce the cost, or new substrate materials to introduce novel functionality, or flexible substrates for wearable and wireless applications; (2) High frequency sensing with improved sensitivity; (3) Shear-wave or Love mode based thin film devices for liquid sensing; (4) Development of various sensing layers/material systems; (5) Integration with acoustic streaming and microfluidics to form the LOC systems. Some of the flexible acoustic wave sensor designs are shown in Fig. 1.

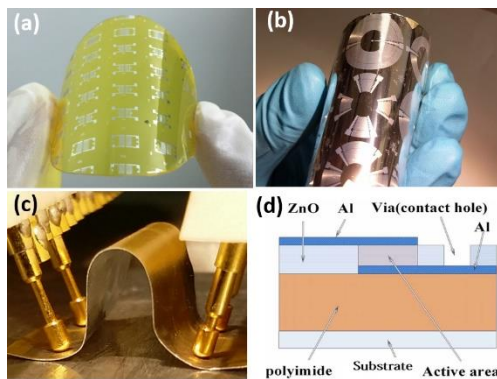


Fig. 1. Thin film flexible acoustic wave sensing devices: (a) ZnO/polyimide; (b) ZnO/Al foil; (c) Testing of ZnO/Al devices (d) flexible FBAR device

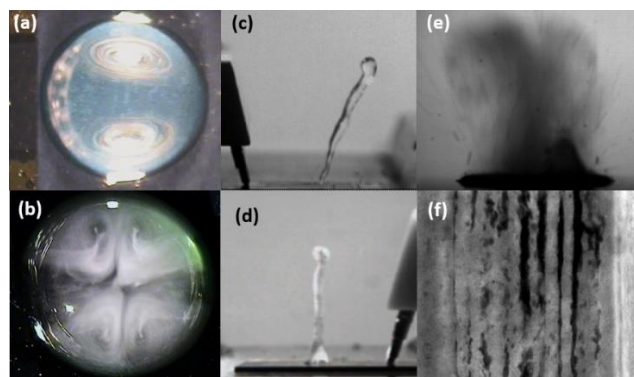


Fig. 2. ZnO/Si SAW based acoustofluidics: (a) Streaming from one IDT and (b) two IDTs; (c) vertical liquid jetting from one IDT; (d) jetting from a circular IDTs; (e) nebulization; (f) particle manipulation

Thin film SAW based flexible acoustofluidics

Recently, acoustic wave devices based on ZnO and AlN thin films have shown the same capability and better performance in some aspects and applications (for example in large RF power conditions). Substrates such as silicon, glass and polyimide (PI), on which the piezoelectric layer is deposited, play a significant role on the device performance in acoustofluidic applications. Fig. 2 shows the different acoustofluidic functions which can be generated from thin film SAW devices. Acoustic wave devices made of a ZnO film on Si typically generate Rayleigh and Sezawa modes, whereas those made with ZnO on glass only generate the Rayleigh mode due to the very close acoustic velocities of the glass substrate and the ZnO layer. Devices made from ZnO film on a flexible PI substrate produced Rayleigh and Lamb modes. Devices made of ZnO film on Si provide the best transmission properties, and the best microfluidic performance in term of acoustic streaming velocity among the devices on these three types of substrates. Compared to devices made on silicon and glass, the flexible devices based on PI have an inferior performance due to the large acoustic attenuation of the PI as well as the large mismatch in acoustic impedance at the interface between ZnO and PI. Thin film based flexible devices on Al foils show a better microfluidic performance compared to those made on polymers.

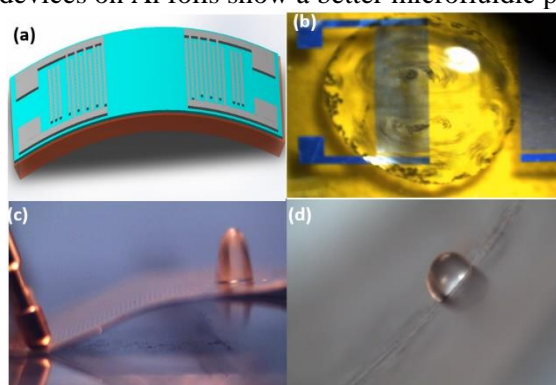


Fig. 3. (a) An illustration of flexible acoustic wave fluidic device designs; (b) Flexible SAW microfluidics on ZnO/PI substrate, showing a double vortex streaming pattern. (c) A snap shot of one example of droplet jetting behaviour on a ZnO/Al foil device with significant pre-bending of the Al foil, revealing the efficient microfluidic functions. (d) droplet pumping up on a bent and curved Al plates using SAW actuation

Flexible SAW devices would be ideal for the development of flexible and disposable lab-on-chip applications. Flexible SAW on PI substrate has demonstrated similar microfluidic functions such as streaming, mixing and particle concentration, with examples shown in Fig. 3. Flexible substrates such as polymers dissipate most of the energy from the acoustic source, leading to a major attenuation of the wave. Other problems associated with polymeric substrates are poor film crystallinity and poor adhesion of the thin piezoelectric film. A solution for this problem is to use a thin metal foil as the substrate. Flexible acoustofluidics based on aluminium foil could provide efficient microfluidic functions with the resonant frequencies from both the Lamb wave mode and Rayleigh wave mode. Fig. 3(c) shows one example of droplet jetting behaviour on a ZnO/Al foil device with significant pre-bending of the Al foil, revealing the efficient microfluidic functions. As the wave-liquid interaction is different from the conventional Rayleigh waves, liquid transportation on the ZnO/Al foil device generally leads to significant vibration and deformation of the droplets.

Summary

Both ZnO and AlN films are promising materials for the fabrication of fully automated and digitized microsystems with compactness, simple operation, precision, low cost, fast response, and reduced reagent requirement. This type of microsystem has multiple functions, yet it can be operated by a single acoustic wave mechanism, a unique characteristic no other microsystem can achieve. We foresee that such microsystems are capable of performing the complete task from delivering drops of bio-sample into the device through to the delivery of the detection results. Future directions should be focused on integration with new materials; integration with CMOS and other acoustic wave technologies; integration with other microfluidic and sensing technologies, and portable, wireless, flexible and remotely controlled devices

References

- [1] Y.Q. Fu, J.K. Luo, et al, Sens. Actuat. B. 143 (2010) 606-619.
- [2] Y.Q. Fu, J.K. Luo, et al, Prog. Mater Sci. 89 (2017) 31-91
- [3] G.H. Chen, Sci. Rep. 5 (2015) 9510.
- [4] W.P. Xuan, et al, nanoscale. 7 (2015) 7430-36.
- [5] H.Jin, et al, Sci. Rep. 3 (2013) 2140.
- [6] Y.Q. Fu, et al, Biomicrofluidics 6 (2012) 024105.
- [7] J. Zhou, et al, Sens Actuat B 202 (2014) 984-92A.
- [8] Y. Liu, et al, Sens Actuat B 221 (2015) 230-235.
- [9] C. Fu, et al, Appl. Phys Lett., 110 (2017) 173501.

The 3D patterning and manipulating microparticles inside millimeter-height of chamber using standing surface acoustic wave

Tan Dai Nguyen¹, Van Thai Tran², Yong Qing Fu³ and Hejun Du¹

¹School of Mechanical and Aerospace Engineering, Nanyang Technological University, 639798, Singapore

²Singapore Centre for 3D Printing, Nanyang Technological University, 639798, Singapore

³Faculty of Engineering & Environment, Northumbria University, Newcastle upon Tyne, NE1 8ST, UK

Introduction

In this study, we investigate the 3D motion of polystyrene microparticles in a large-sized chamber with the height of 1 millimetre under the presence of standing surface acoustic wave (SSAW). Recently, there were reports showed the trapping and manipulating of microparticles by the pressure nodes which is movable in two-dimensions [1] or three-dimensions with the short height of the chamber [2]. However, there is no study exploring the distribution of microparticles within the millimeter-scale of chamber height. In this work, we discovered that acoustic radiation force worked effectively with microparticles to form 3D lines or crystal-like patterns. In addition, the microparticles were well-positioned at a specific vertical location if there was a balance of forces including acoustic radiation force, drag force, buoyant force and gravity exerted onto the microparticles. Furthermore, both experimental results and numerical studies showed that the acoustic radiation force was increased gradually from the bottom to the top of the chamber, and microparticles could be levitated to a higher position or fallen to a lower position by simply adjusting the applied SAW power.

3D lines and patterns of microparticles using standing surface acoustic waves

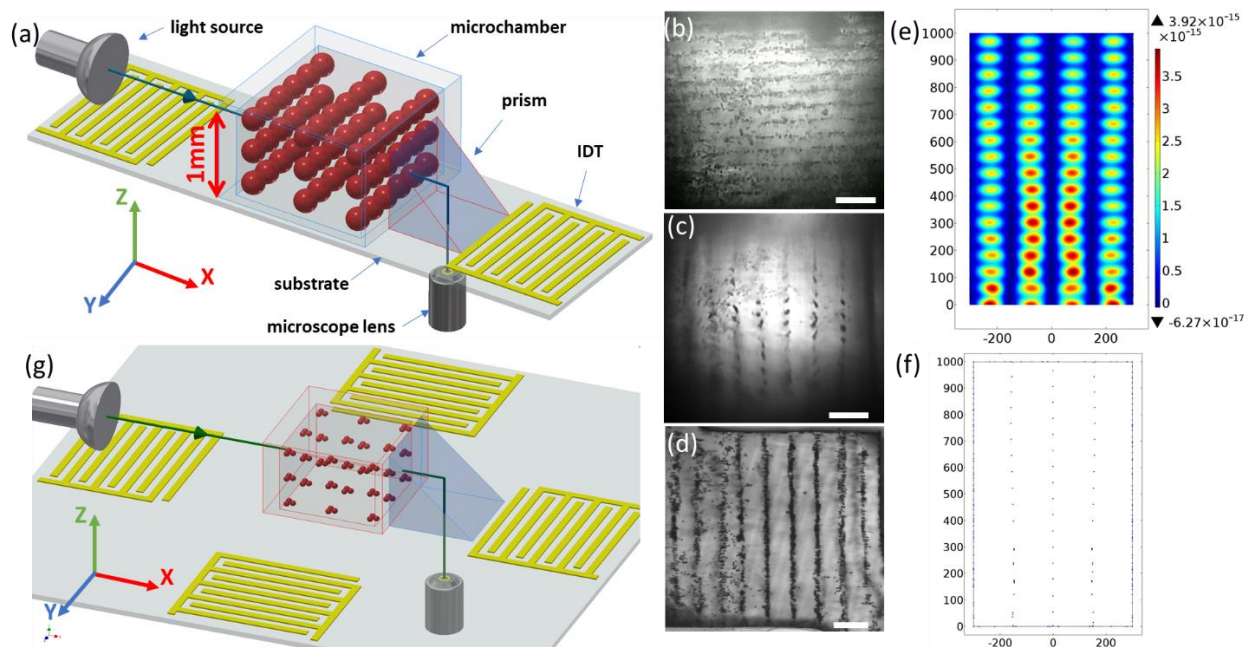


Figure 1: (a) Schematic of the experimental setup for the observation of the microparticle behavior from the side-view using a prism. (b), (c) and (d) are the microscopic images of the 10 μm -microparticles after the introduction of SSAWs with the input power of 3500 mW viewed from the direction of x, y, z, respectively (Scale bar: 200 μm). (e) Radiation force potential, magnitude shown as color range from $-6.27 \times 10^{-17}\text{J}$ (blue) to $3.92 \times 10^{-15}\text{J}$ (red). (f) Numerical results of 10 μm microparticles' motion after 10s, there are 1421 microparticles with the distance of two adjacent microparticles is 20 μm in the beginning (0s). (g) 3D patterning of 10 μm -microparticles using two pairs of IDTs.

Our experimental configuration includes a pair of interdigital transducers (IDTs) deposited on a piezoelectric substrate with a chamber bonded in the between of the two IDTs. The 10 μm microparticles dispersed uniformly in water were injected into the chamber. A prism was used for the side view observation (**Figure**

1a). After the RF signal was applied to the IDTs, the microparticles started moving, and they were trapped into 3D lines (red microparticles in **Figure 1a**). The experimental results from the x, y, and z-axis observation shown in **1b, c and d** confirm the present the 3D lines. We have also employed a numerical model to understand the mechanism of the acoustic radiation force in this higher chamber. Whereas, **Figure 1e and f** show the potential of acoustic radiation force and the microparticle's position after 10 s of activation, respectively. This simulation is well matched with the experimental results. In case of using two perpendicular IDTs, the microparticles were relocated, and they formed a 3D matrix structure with the nodes are composed of microparticles as shown in **Figure 1g**.

Force analysis and the dependence of microparticles' motion to input power

This phenomenon can be briefly explained by the interaction between SSAWs and the liquid in the chamber which leads to the generation of longitudinal leakage waves and pressure fluctuations inside the liquids along lateral and vertical direction. The acoustic radiation force raising from these pressure fluctuations together with gravity force and buoyant force pushed the microparticles into nodes and form the 3D lines (**Figure 1a**). **Figure 2a** describes all the force exerting on the microparticles at balance state in x-direction and z-direction. As previous discussion, we showed that the magnitude of acoustic radiation force increases gradually from the bottom to the top of the chamber (**Figure 1e**). Therefore, in the z-direction, the acoustic radiation force subjected an upward net force to the microparticles, while gravitational force combined with buoyant force resulting in a net downward force. In the x-direction, the total force was zero because the two opposite and equal acoustic radiation forces cancelled each other. Because the acoustic radiation force is significantly affected by the input power [2], the upward net force depends on the input power with the same size microparticles. **Figure 2b** shows the vertical position in layer order of a group of 10 μm microparticles when the input power was decreased from 954 mW down to 450 mW. In this figure, the fourteenth layer is the highest layer to be clearly identified, and the zeroth layer is the substrate. The microparticles linearly responded to the decrease of the input power by moving down to the lower layer. On the contrary, **Figure 2c** shows the rising of a single 10 μm microparticle from the bottom at the different periods with an input power of 4380 mW. After the RF signal was turned on, the single microparticle was gradually moving up and eventually reached the equilibrium position with a height of 524 μm after 31.4 s. From those observation, we proposed a new method to control the vertical position of 20 μm microparticle. In detail, the microparticle was let fall down to desire line by switching on/off the RF signal or the microparticle can be levitated to a higher position by turning the RF signal to a stronger power (**Figure 2d**).

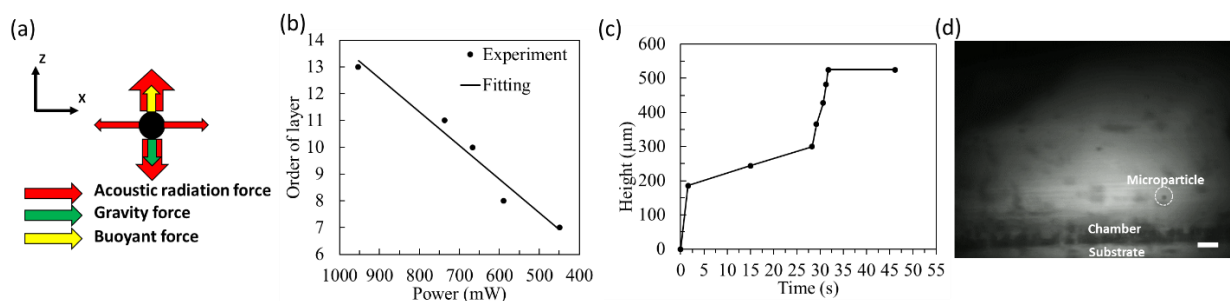


Figure 2: (a) Force analysis on single microparticle in radiation force potential in two directions of z and x-axis. (b) Changes of layer orders of 10 μm -microparticle when the input power is decreased (in the side-view of X-axis). (c) The levitation height of 10 μm -microparticles from the bottom layer at different moments with an input power of 4380 mW. (d) A single 20 μm -microparticle was trapped at 3D nodes by switching on the input power.

Conclusion

We have demonstrated the 3D lines and 3D lattice matrix of microparticles in millimeter-size of chamber using standing surface acoustic waves. We have investigated the mechanism of 3D lines through the numerical study which was then well-validated by experimental study. We found that the acoustic radiation force increases gradually from the bottom to top of the chamber, microparticles can be levitated by adjusting the power. Moreover, a large-sized single microparticle can be relocated to the desired height by switching on/off and turning the strength of the RF signal. The formation of 3D patterning of microparticles is a contactless process which is compatible with biological or cell applications (e.g., 3D cell-cell interaction). Furthermore, the lattice structure could have a wide range of applications in microfluidics and lab-on-chips. With these interesting results, we are looking forward to presenting for the international acoustofluidics community at *Acoustofluidics 2018* at sunny Lille, Université de Lille, Lille, France on 29–31 August 2018.

References

- Shi, J., et al., *Acoustic tweezers: patterning cells and microparticles using standing surface acoustic waves (SSAW)*. Lab on a Chip, 2009. **9**(20): p. 2890-2895.
- Guo, F., et al., *Three-dimensional manipulation of single cells using surface acoustic waves*. Proceedings of the National Academy of Sciences, 2016. **113**(6): p. 1522-1527.

Biomolecule Manipulation Using Gigahertz Bulk Acoustic Waves for Enhanced Protein Sensing

Xuexin Duan*, Shuting Pan, and Xian Chen

State Key Laboratory of Precision Measuring Technology & Instruments, Tianjin University, Tianjin, China
* E-mail: xduan@tju.edu.cn, URL: <http://www.tjumbios.com>

Introduction

Sensitive detection of low-abundance proteins (e.g. biomarkers) in complex biological samples is essential in biomedical diagnosis field. However, proteins detection is limited by the low diffusion rate, their surface binding affinity as well as nonspecific bindings (NSB).¹ Biomolecules manipulation techniques have been exploited to this end. Herein, we used a gigahertz bulk acoustic wave (BAW) resonator to realize biomolecules manipulation for enhancing protein sensing. A finite element model was built to simulate the flow motion of the acoustic streaming induced by BAW devices. Experimentally, we demonstrated that the BAW device could efficiently trapping biomolecules around the resonator as well as on other sensing surface. Such manipulation enhances the transportations of the targets and enriches analytes, thus improving the LOD of the biosensing. As BAW devices are miniature in size, we finally integrated this enhanced method into an optoelectronic bioassay.

The structure of the Lamb wave resonators

The device is fabricated using a complementary metal oxide semiconductor compatible technology. Briefly, thin layers of aluminum nitride (AlN) and silicon dioxide (SiO₂) were alternatively deposited on a silicon substrate to form Bragg reflector layers. Then, multi-layers of molybdenum and AlN were deposited to form the sandwich structures of the BAW device. Finally, a gold layer was sputtered and patterned to improve the conductivity of the electrodes. The schematic of the fabrication flow and SEM images are shown in Figure 1.

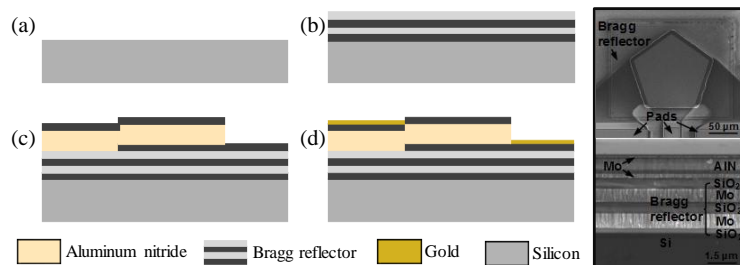


Figure 1: Fabrication process. (a) The silicon substrate. (b) The formation of acoustic Bragg reflector. (c) The formation of the sandwich structure. (d) The formation of a gold layer. Insets are pictures taken by SEM from top view and cross section view of BAW device where Bragg reflector can be clearly identified.

Theory and Simulations of the Microvortexes

When a BAW resonator is immersed in liquid, it experiences acoustic damping effect. The finite element analysis of the propagation of the acoustic waves in liquid is shown in Figure 2a, where we can conclude that the wave amplitude attenuates sharply near the device-liquid interface due to the high energy attenuation coefficient and the vertical vibration mode of BAW devices, then acoustic energy is efficiently transduced into liquid. The attenuation of acoustic waves introduces a body force within bulk liquid and the simulation of streamlines and velocity fields of the triggered fluid motion is shown Figure 2b. The vortexes streaming has been reported for many bio-applications due to their biocompatibility, controllability and low-power consumption.^{2,3}

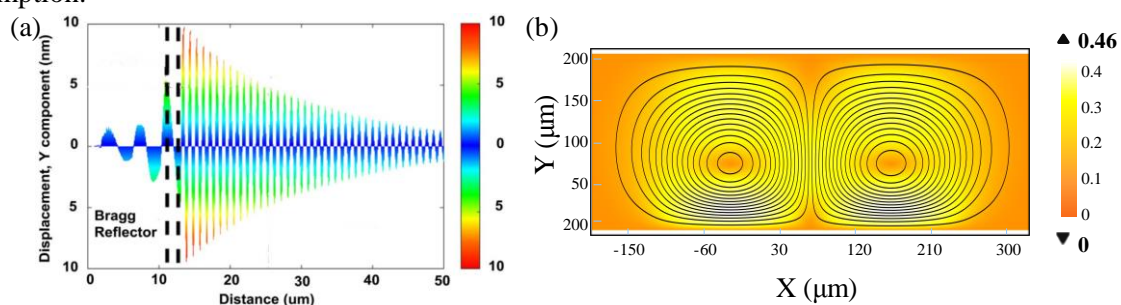


Figure 2: (a) Simulation of wave propagation when BAW resonators contacted with water. The color represents the acoustic wave amplitude. (c) Simulation of the fluid motion triggered by the BAW device.

Trapping biomolecules around BAW device and other sensing surface.

The biomolecular trapping effects are demonstrated by FITC labeled human IgGs. As schematically shown in Figure 3a, a 50 μm chamber is sealed on the BAW resonator to confine the vortexes motion. Such confined fluid breaks the diffusion limitation and highly enhances binding opportunities between probe molecules (modified on the resonator) to targets (human IgG), therefore the synergistic effect of physical flow motion/biochemical probe facilitated enriching biomolecules around the BAW resonator (Figure 3b). Besides, when we integrated BAW devices with other sensing surface (Figure 3c), the impulsive motion of microvortexes may dominate, and interesting, IgG proteins could be trapped on the most region of the sensing surface (also pre-modified by IgG antibody). Such results indicate that BAW trapping approach could be a promising and versatile sensing enhancement strategy.

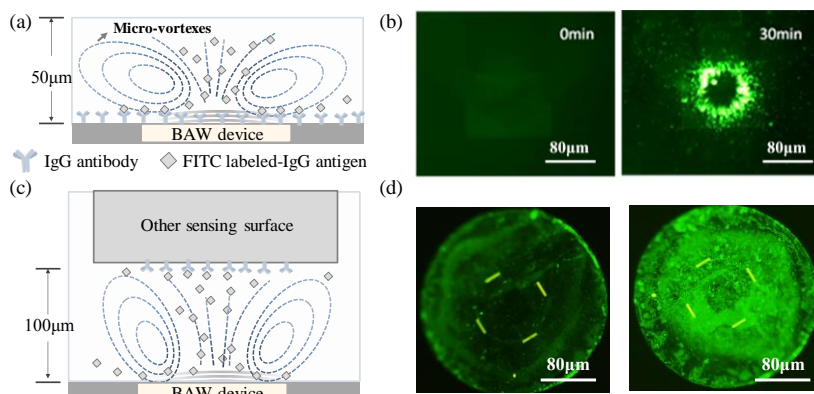


Figure 3: (a) Schematic of the micro-vortexes flow field which is highly confined by a 50 μm chamber and its application in biomolecules trapping around BAW resonator. (b) FITC labelled human IgGs are trapped around the BAW resonator at 0 min and 30 min. (c) Schematic of biomolecules trapping on other sensing surface. (d) FITC labelled human IgGs are trapped on the other sensing surface at 0 min and 30 min.

We finally integrated the microvortexes-enhanced method into an optic fiber. The real-time binding information can be quantitatively obtained by SPR. When applying low power (<200mw), acoustic streaming will accelerate the targets binding to the sensor surface. We compared different input power (Figure 4b) and the distance between the resonator to the sensor (Figure 4c). It turns out that the binding enhancement is optimized by applying 50 mW with 0.1 mm distance. It is interesting to note that when applying high power (500 mW), drag forces are generated which can be used to remove the nonspecific bindings (NSBs) (Figure 4d).

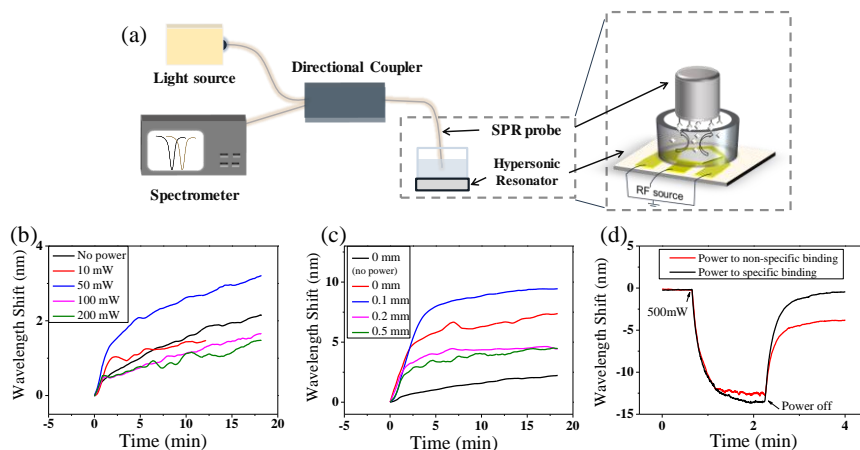


Figure 4: (a) Schematic of the micro-vortexes enhanced fiber optic SPR. Enhanced SPR results with different input power (b) and relative distance (c). (d) NSB removal.

Conclusion

We have investigated a hydrodynamic biomolecules manipulation approach for enhanced protein sensing using a gigahertz BAW resonator. Acoustic streaming improves the sensing performance by breaking the diffusion limitation and enriching biomolecules. Fluorescence immunoassay shows the efficiency and versatility of this approach. In addition, we demonstrated an enhanced fiber optic SPR based on the micro-vortexes mechanism. Moreover, by using high power of streaming, NSBs could be removed efficiently as well.

References

- [1] Duan, X., Rajan, N. K., Izadi, M. H., and Reed, M. A. *Nanomedicine*, **8(11)**, 1839-1851 (2013).
- [2] Zhang Z, Wang Y, Zhang H, et al. *Small*, **13(18)**, (2017).
- [3] Pan S, Zhang H, Liu W, et al. *ACS sensors*, **2(8)**, 1175-1183(2017).

Controlling the motion of multiple objects on a Chladni plate

Veikko Sariola¹, Quan Zhou²

¹Faculty of Biomedical Sciences and Engineering, Tampere University of Technology, Tampere, Finland
E-mail: veikko.sariola@tut.fi

²Department of Electrical Engineering and Automation, Aalto University, Espoo, Finland

Introduction

Ernst Chladni reported the accumulation of sand and particles to the nodal lines of transversely vibrating plate already in 1787. Following his ideas, even today many acoustic manipulation works focus on trapping objects at nodes, neglecting how the objects move before they reach the nodes. In this talk, we present our recent results [1] on modeling, predicting and controlling the motion of objects on a Chladni plate. By playing carefully selected sequences of musical notes – signals with finite duration and energy mostly around single frequency – we can control the position of multiple objects simultaneously and independently using a single acoustic actuator. In our method, the objects generally are not at the nodes. Our method allows independent trajectory following, pattern transformation and sorting of several different types of objects, including electronic components, water droplets on solid carriers, plant seeds, candy balls and metal parts. Our work is mainly experimental, supported by theory.

Methods

The schematic of our experimental platform is shown in Fig. 1a. The apparatus consists of a thin silicon plate (50 mm × 50 mm × 0.525 mm), actuated by a centrally mounted piezoelectric actuator (Piezomechanik/PSt 150/2x3/5). Objects on the plate are tracked by a camera and machine vision algorithms.

We first captured the motion of objects in response to different frequencies by placing ~ 130 solder balls (diameter: 600 μm) on the plate and actuating the plate with short (0.5 s) triangularly enveloped sinusoids in the frequency range 1.047 – 28.16 kHz. For 59 different frequencies, we tracked the positions of particles before and after playing a note. Each note was played 50 times, resulting in ~6,600 data points per note and ~390,000 data points in total. For each note n , we used LOESS-regression to find an approximate model of the data

$$\Delta \mathbf{x} \approx \mathbf{u}_n(\mathbf{x}) \quad (1)$$

where \mathbf{x} is the 2D-position of the object on the plate, \mathbf{u}_n is the regression model and $\Delta \mathbf{x}$ is the displacement after playing the note. During manipulation, we gave each object m having the position \mathbf{x}_m a desired displacement \mathbf{d}_m . By solving a linear programming problem (see [1] for details), we find scalar weights α_n :s such that

$$\mathbf{d}_m = \sum_n \alpha_n \mathbf{u}_n(\mathbf{x}_m) \quad (2)$$

for every m , with the additional condition of $\alpha_n \geq 0$. The condition $\alpha_n \geq 0$ simply states that the objects cannot move in opposition to \mathbf{u}_n . We then interpret α_n :s as what portion of *time* we should be playing note n . At each control cycle, we recompute α_n and then choose a note so that asymptotically the fraction of time allocated to note n is $\sim \alpha_n$. See [1] for more details. An alternative control strategy is discussed in [2].

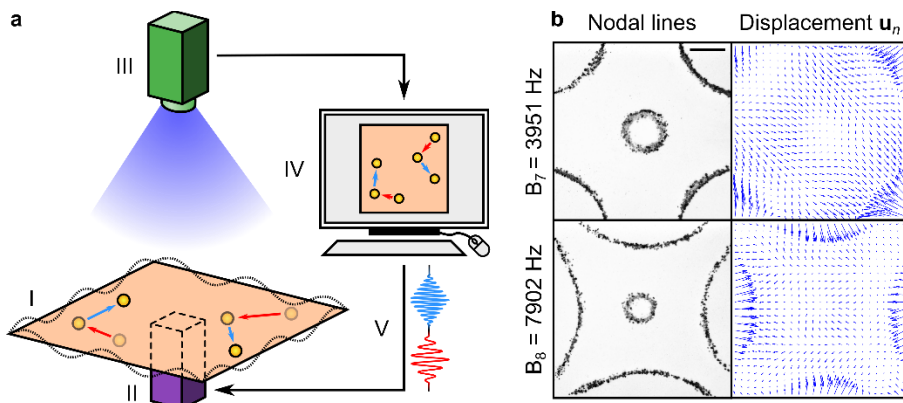


Figure 1: Concept of the manipulation method. (a) The experimental setup consists of a vibrating plate (I) with the manipulated objects on top, mounted on a piezoelectric actuator (II). The plate is imaged by a camera (III), and the locations of the objects are detected by a computer (IV). The computer chooses the signal (V) sent to the actuator. (b) Chladni figures and modelled displacement fields \mathbf{u}_n for two different frequencies.

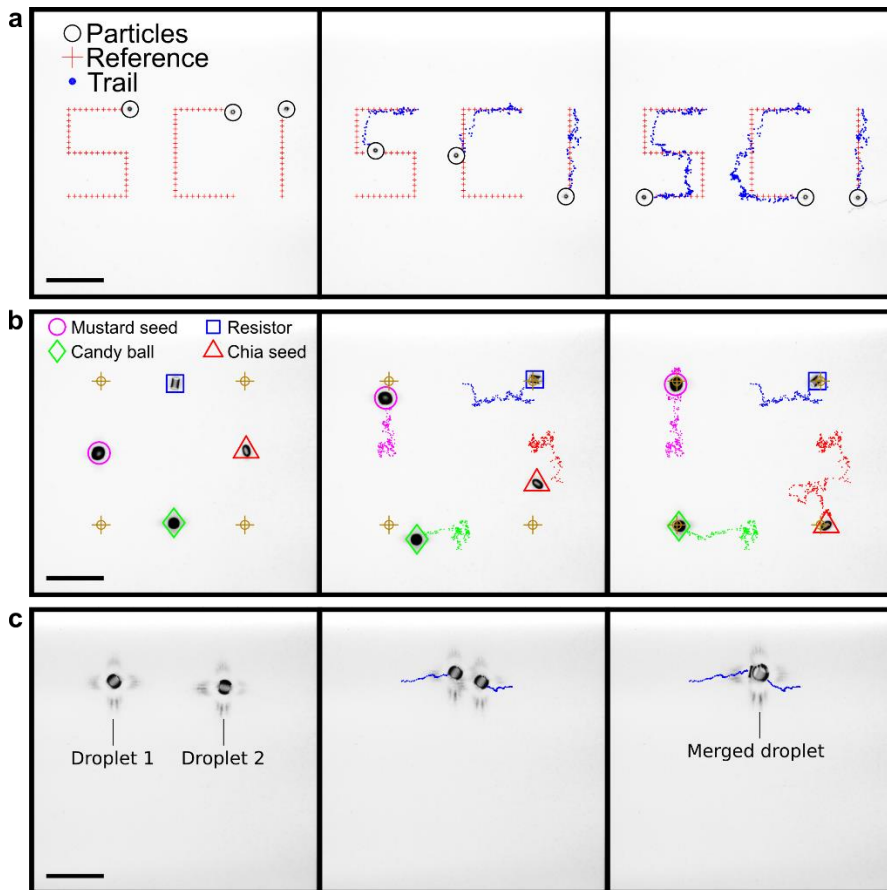


Figure 2: Demonstrations in manipulating multiple objects. (a) Simultaneous manipulation of three 600 μm solder balls. (b) Manipulating objects of different materials and shapes simultaneously. A diamond pattern of four objects – a SMT resistor, a mustard seed, a chia seed, and a candy ball – is transformed into a square pattern. (c) Droplet merging. Two 8 μl water droplets dispensed on flat carriers are brought together and merged into a single droplet. Scale bars: 1 cm.

Results

Our method can be applied to direct objects along trajectories. We split the trajectories into a set of waypoints and set the desired direction of each object towards its current waypoint. When the object is close enough to the waypoint, next waypoint along the trajectory is chosen. In this way, we have successfully performed trajectory following with three solder balls simultaneously (Fig. 2a).

Even though the model was developed for solder balls, the method can be applied to objects of various shapes and materials. Fig. 2b shows an experiment where we manipulate four different types of miniature objects are used: a mustard seed, a chia seed, a candy ball, and a surface mount technology (SMT) resistor. Besides solid objects, we have also transported water droplets on solid carriers (Fig. 2c and Supplementary Movie 7). Two carriers each loaded with an 8 μl water droplet were transported over a distance and finally merged into a single droplet. This paves way towards droplet-based lab-on-chip applications of the method.

Conclusions

In this work, we used transverse vibrations of a plate in air to move multiple objects. In comparison, most works in acoustofluidics [3-4] use bulk waves in liquid or surface acoustic waves. However, our control method is agnostic to the physical origins of the motion. As long as the motion is sufficiently predictable and a statistical model similar to (1) can be developed, the control method can be applied. Thus, we envision the control method to have multiple acoustofluidic applications, including lab-on-chips, cell/particle sorting and patterning of bio-, micro- and nanomaterials.

References

- [1] Q. Zhou, V. Sariola, K. Latifi, and V. Liimatainen. *Nature Communications* **7**, article number: 12764 (2016).
- [2] K. Latifi, H. Wijaya, Q. Zhou, in Proc. IEEE Conf. MARSS (2017).
- [3] J. Friend, L. Yeo, *Reviews of Modern Physics*. **83**, pp. 647 – 704 (2011).
- [4] H. Bruus et al. *Lab on a Chip* **11**, pp. 3579-3580 (2011).

Acoustic Lock: Single-axis Position and Orientation Trapping of Non-Spherical Sub-wavelength Particles

Luke Cox¹, Asier Marzo¹, Anthony Croxford¹ and Bruce Drinkwater¹

¹Department of Mechanical Engineering, University of Bristol, Bristol, UK
E-mail: luke.cox@bristol.ac.uk, URL: <http://www.bristol.ac.uk/engineering/research/ndt/>

Introduction

Single-axis standing wave levitators are the most widely used form of acoustic levitator in air [1] and a significant amount of work has been conducted on their use with spherical particles or droplets [2]. The rotation of non-spherical particles about the vertical axis is the only degree of freedom which has eluded control [3]. We present a technique in which position and orientation control by multiplexing in time between a) a pseudo-one-dimensional standing wave that provides vertical forces to counter gravity and b) a non-axisymmetric field known as a twin trap that provides asymmetric forces in the horizontal axis for rotational stabilization [4]. Stable trapping of non-spherical particles has previously been demonstrated only in 2D arrangements [10]. Previous studies have multiplexed between fields of the same type to achieve new capabilities such as vortex stabilization [6] and particle manipulation [7,11]. Here we multiplex between two different types of field to accurately and stably control the position and orientation of a trapped object.

The acoustic field of the device is predicted using a piston source model [5] and its impact on cuboidal objects modelled using a Finite Difference Time Domain (FDTD) simulation. The size stability region (the range of side lengths where the object hangs stationary in air without significant rotation or falling out of the trap) for a cube is identified experimentally and explained using the simulation. For example, the relationship between the torsional spring constant, K_T , and the multiplexing rate between standing wave and twin traps is identified. This technique creates a tunable method for levitation of non-spherical particles of varying sizes and densities for sample inspection or micro-scale manufacturing. Crucially, these results demonstrate the efficacy of multiplexing in time between entirely different fields to gain the net impact (in terms of force and torque) of a compound field.

Design and experimental stability

The device was designed as a larger version of the widely available “TinyLev” [5]. Due to the larger number of transducers (120 vs the original 72) it was called “HugeLev.” It operated at 40kHz and was capable of levitating acrylic particles of up to around 3.5mm. The transducer bowls at each end of the device are each connected in two halves with independent control, hence it requires 4 distinct input signals in total. This allows half of each bowl to be out of phase with the other, enabling the twin trap described above. This is illustrated in Figure 1a.

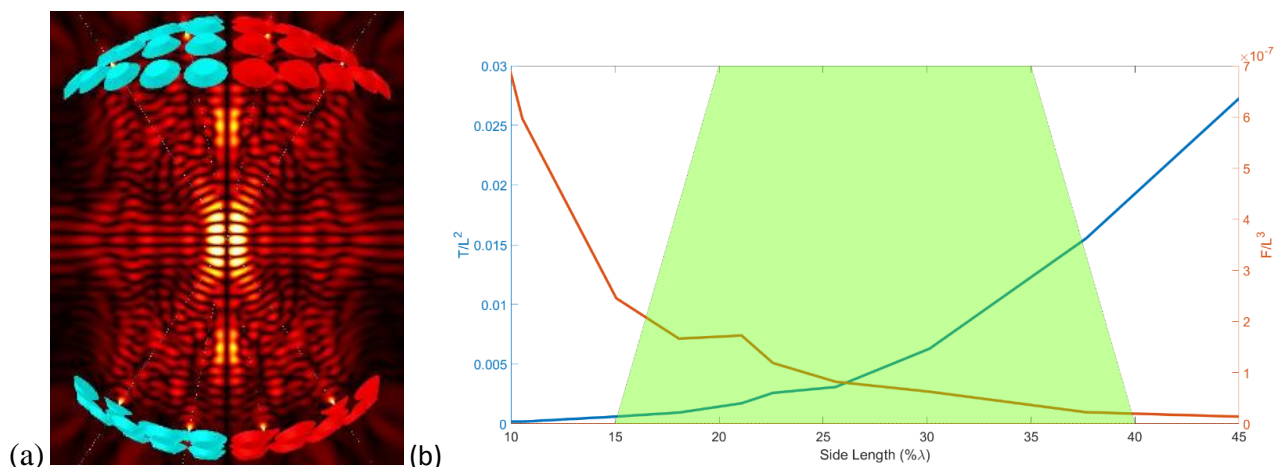


Figure 1: (a) A schematic representation of the HugeLev device and pressure field in the twin trap arrangement. Each bowl is excited with in two with independent input signals (i.e. the red and blue transducers). (b) The green region of stability, as found from experimental results. This is overlaid with the blue line representing Torque/Length², the condition that defines the lower size limit on stability, and the orange representing Force/Length³, the condition that defines the upper size limit on stability. When either of these conditions drops too low stability is lost.

For this device the optimal ratio for stability in all degrees of freedom of 100:50 standing:triple and the range of particles that could be stably trapped was found experimentally. The size stability region for a cube is 18-40% λ (percentage of the wavelength), as shown by the green region in Figure 1b. This could be explained by a reduction in the torque applied to the cube (as suggested by the simulation) relative to the lengths squared (which governs the moment of inertia) for small particles where the observed instability was due to rotation about vertical axis. The reduction of the force relative to the mass (which governed by the particle's volume) is the limiting factor as particle size increases where instability is due to a simple lack of levitation force or torque about the horizontal axis. This result agrees with observation and the existing literature, validating the model further [8,9].

Experimental and simulated determination of K_T

The torsional spring constant about the vertical axis, K_T , was determined experimentally and via simulation, with good agreement between the results. The experimental results were obtained by using video tracking of a dot on a disturbed acrylic cuboid. Here, K_T was calculated from the measured natural frequency, assuming known moment of inertia. This was compared with the K_T obtained from the FDTD simulations. The results from this comparison can be seen in Figure 2. There is excellent agreement in the gradients of the linear fits. There is a reduction in K_T by an offset for the experimental results, however this can be explained as a power loss from a real system, i.e. associated with the transients that occur when multiplexing.

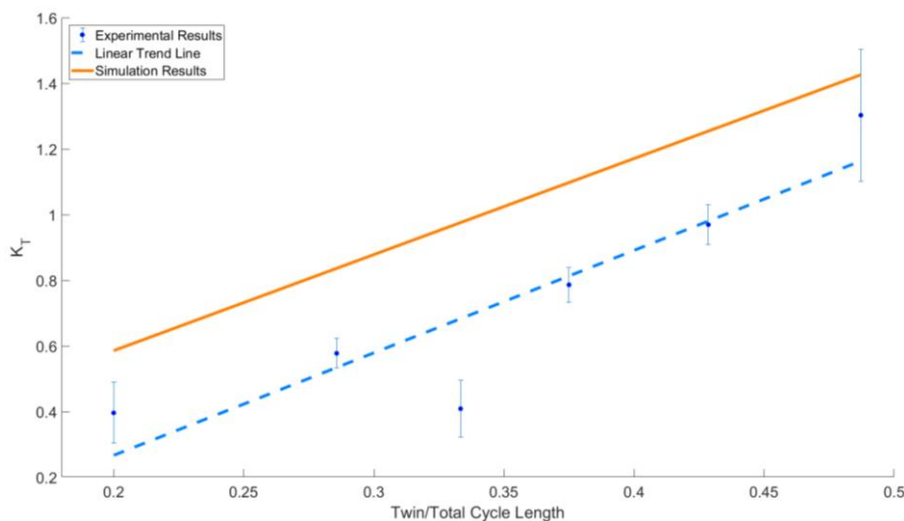


Figure 2: The comparison between the experimental and simulated results for the variation in K_T with varying cycle ratios.

Conclusion

We have demonstrated the feasibility of multiplexing in time different sound fields to create the desired control. In doing so we have gained control of the final degree of freedom previously uncontrolled in single-axis levitators and demonstrated the torsional trap stiffness to be linearly related to the time averaged sum of the force from the two fields.

References

- [1] R R Whymark. Acoustic field positioning for containerless processing. *Ultrasonics*, 13(6):251-261 (1975).
- [2] LV King. On the acoustic radiation pressure on spheres. *Proc. R. Soc. Lond. A*, 147(861):212-240 (1934).
- [3] V Vandaele, A Delchambre, and P Lambert. Acoustic wave levitation: Handling of components. *Journal of Applied Physics*, 109(12):124901 (2011).
- [4] A Marzo, S A Seah, B W Drinkwater, D R Sahoo, B Long, and S Subramanian. Holographic acoustic elements for manipulation of levitated objects. *Nature Communications*, 6:8661, (2015).
- [5] A Marzo, A Barnes, and B W Drinkwater. Tinglev: A multi-emitter single-axis acoustic levitator. *Review of Scientific Instruments*, 88(8):085105 (2017).
- [6] A Marzo, M Caleap, and B W Drinkwater. Acoustic virtual vortices with tunable orbital angular momentum for trapping of mie particles. *Physical Review Letters*, 120(4):044301 (2018).
- [7] D Foresti and D Poulikakos. Acoustophoretic contactless elevation, orbital transport and spinning of matter in air. *Physical Review Letters*, 112(2):024301 (2014).
- [8] P Glynne-Jones, P P Mishra, R J Boltryk, and M Hill. Efficient finite element modeling of radiation forces on elastic particles of arbitrary size and geometry. *The Journal of the Acoustical Society of America*, 133(4):1885-1893 (2013).
- [9] R Habibi, C Devendran, and A Neild. Trapping and patterning of large particles and cells in a 1d ultrasonic standing wave. *Lab on a Chip*, 17(19):3279-3290 (2017).
- [10] T Schwarz, P Hahn, G Petit-Pierre, and J Dual. Rotation of fibers and other non-spherical particles by the acoustic radiation torque. *Microfluidics and Nanofluidics*, 18(1):65-79 (2015).
- [11] P Glynne-Jones, R J Boltryk, N R Harris, AWJ Cranny, and M Hill. Mode-switching: A new technique for electronically varying the agglomeration position in an acoustic particle manipulator. *Ultrasonics*, 50(1):68-75 (2010).

Oscillations of a cubic bubble

Maxime Harazi, Matthieu Rupin, Olivier Stephan, Philippe Marmottant

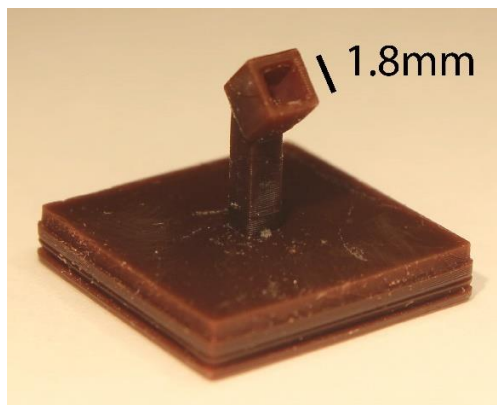
Laboratoire Interdisciplinaire de Physique (LIPhy), Université Grenoble Alpes, France

E-mail: maxime.harazi@univ-grenoble-alpes.fr, philippe.marmottant@univ-grenoble-alpes.fr

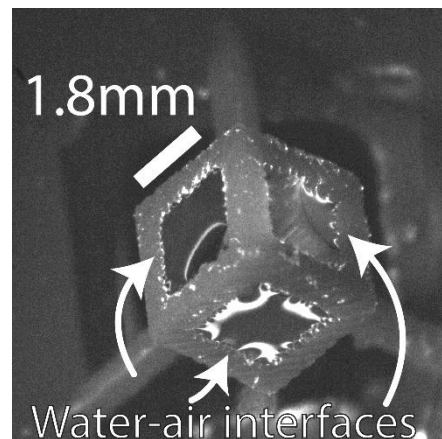
Introduction

Due to their great compressibility, bubbles are known to be excellent acoustic resonators and exhibit strong nonlinearities [1]. Furthermore, since the wavelength in the lowest frequency mode (Minnaert resonance) is way larger than the bubble size, they represent perfect candidates for building acoustic metamaterials [2]. One difficulty, though, is to create stable and precisely designed bubbly media. We propose to use 3D printing technique to overcome these two problems. We study experimentally the oscillations of a millimetric cubic cavity of air trapped in a 3D printed frame. In this configuration, the water-air interfaces are flat and attached to the printed frame, which increases the stability of the bubble. Furthermore, this new object does not behave as the usual spherical bubble, exhibiting for example a lower fundamental resonance frequency than the Minnaert frequency. Another interesting result is the possibility to shape the bubble frame in order to have different resonance frequencies for each side of the cube, giving the possibility to induce acoustic streaming in a specific chosen direction.

Description of the bubbles



(a)



(b)

Figure 1: (a) Example of a 3D printed cubic bubble with a single opening, in air. (b) Example of a 3D printed cubic bubble with six openings, in water. Air gets trapped in the bubble by capillarity, leading to the creation of six water-air interfaces on the faces of the cube (only three of them being visible on the picture).

The system we study consists of millimetric 3D printed cubes (figure 1a). The cubes have one or several faces opened in order to create water-air interfaces at each opening when put into water (figure 1b). One important thing to note is the possibility to create openings of *different* sizes on each face of one same cube (not shown here).

Description of the experiment

We study the acoustic and mechanical response of our cubic bubbles by putting them in a closed metallic cell filled with water (figure 2). An oscillating pressure is imposed on the water thanks to a shaker and the pressure is monitored thanks to a hydrophone. Finally, the displacements of the bubble interfaces are monitored and recorded thanks to a high speed camera. This closed cavity allows us to reach higher driving pressure compared to the pressure that would be reached in an open water tank with the same source amplitude – the rigidity of the system being mainly given by the one of the water – in the hope to reach easily a highly non-linear regime.

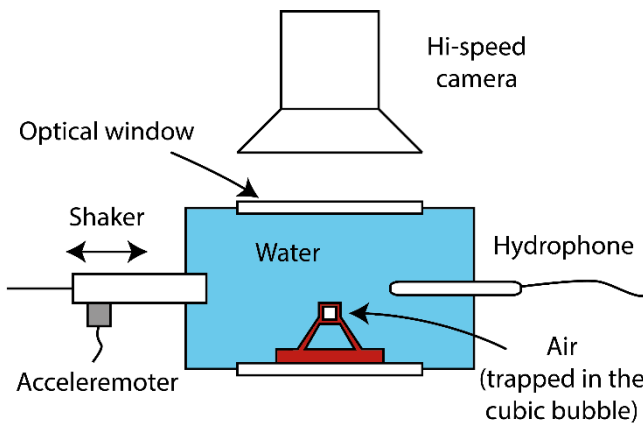


Figure 2: Schematic view of the experimental setup. The printed frame is put in a closed cell filled with water. A shaker exerts a hydrostatic pressure in the cell, which is monitored thanks to a hydrophone. The movements at the surface of the bubble are monitored thanks to a high speed camera.

Resonance and streaming

For a (unique) square orifice with fixed boundary, in the potential approximation with incompressible liquid motion, considering only capillary forces and neglecting air pressure, we find that the lowest mode for the water-air interface is

$$f_0 = \frac{1}{2\pi} \sqrt{\frac{\gamma 2^{3/2} \pi^3}{\rho L^3}} \approx 160 \text{ Hz}$$

With γ the surface tension, ρ the density and $L = 1.8 \text{ mm}$ the lateral size of the interface. It is important to note that for a spherical bubble with the same volume of air, the Minnaert frequency is around $f_M \approx 2.7 \text{ kHz}$. The extremely low value of the resonant frequency f_0 is well observed experimentally and corresponds to very high amplitude oscillation of a single interface. We still have to understand the effect of gas pressure in this oscillation.

Streaming is also observed (figure 3) and confirms the possibility to reach a non-linear regime and to induce a net flow right in front of the interface.

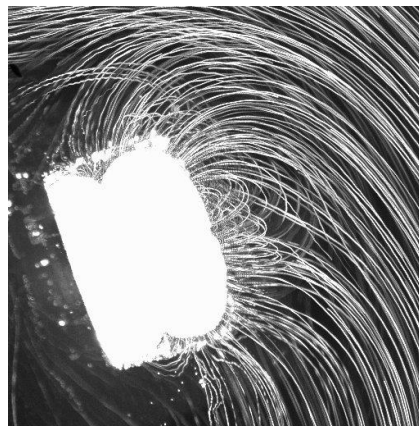


Figure 3: Observation of acoustic streaming in front of one vibrating air-water interface. The streaming is observed thanks to small beads and an extraction of the maximum luminosity on each pixel of the movie over time.

Conclusion

This study suggests that millimetric 3D printed frames could be used as efficient bubble holders. This technique seems interesting to stabilize bubbles and design complex 2D or 3D assembly of bubbles. We have shown that these new objects exhibit extremely low resonant frequency and acoustic streaming at high driving pressure. Furthermore, the use of 3D printing technique allows for the design of the bubbles themselves: as an example, we are currently working on bubbles with different acoustic properties assigned to each face.

Acknowledgement

This research has received funding from the European Research Council under the European Union's Seventh Framework Programme (FP7/2007-2013)/ERC Grant Agreement No. 614655 "Bubbleboost."

References

- [1] Leighton, T. *The Acoustic Bubble*. (Academic Press, 1997).
- [2] Leroy, V. *et al.* Design and characterization of bubble phononic crystals. *Appl. Phys. Lett.* **95**, 171904 (2009).



Dynamics of acoustic vaporization of encapsulated microdroplets

Come Olivier^{1,2}, Thomas Lacour², Jean-Louis Thomas¹, Alexey Podkovskiy^{3,4},
Vincent Faugeras^{3,4}, Wladimir Urbach^{3,4}, Nicolas Taulier³, and François Coulouvrat²

¹Sorbonne Université, CNRS, Institut des NanoSciences de Paris (INSP), F-75005 Paris, France
E-mail: come.olivier@insp.jussieu.fr

²Sorbonne Université, CNRS, Institut Jean Le Rond d'Alembert, F-75005 Paris, France

³Sorbonne Université, CNRS, Laboratoire d'Imagerie Biomédicale (LIB), F-75006 Paris, France

⁴Laboratoire de Physique Statistique, Ecole Normale Supérieure, PSL Research University, Sorbonne Université, École polytechnique, CNRS, F-75005 Paris, France

Background, Motivation and Objective

The use of encapsulated nanodroplets is currently largely investigated for medical applications, mainly because their reduced size allows them to enter targeted areas that cannot be reached by larger microbubbles. In particular, perfluorocarbon nanodroplets can be vaporized under the action of an ultrasonic field, in order either to turn them into echogeneous microbubbles (contrast agents), or to burst them to liberate a load (drug carriers). The optimization of acoustic droplet vaporization (ADV) will be enhanced by understanding its underlying physical mechanisms, which are currently not totally elucidated. Recent models [1,2] describes this phenomenon, paying particular attention to the finite size of the droplet and its encapsulation by a thin hyperelastic layer. Numerical simulations performed for droplets of micro- and nanometric radii and for frequencies of 1-5 MHz, reveal that droplet surface tension and shell rigidity are the main parameters in the determination of the acoustic droplet vaporization threshold.

Statement of the Contribution/Methods

To check the above theoretical results, the relationship between ADV and Inertial Cavitation (IC) is investigated in vitro for single micron-sized perfluorocarbon (PFC) droplets surrounded by a monolayer of fluorinated surfactant. Usual experimental setups consider vaporization of bubble either deposited at the surface of a gel phantom or captured inside it, or in acrylic tubing. In this study, vaporization of single droplets is carried out in free space with the droplet being held suspended acoustically at the focus of the transducer, in accordance to models established considering droplets in an infinite fluid medium. The threshold pressures required to induce ADV and IC are simultaneously determined for micron-sized PFC droplets as a function of droplet size and US parameters. For this purpose, the fast evolution of the bubble size is followed using a Mie scattering setup, where the light of a laser scattered by the forming bubble is collected over a large angle. The radius of the bubble can be shown proportional to the square root of the scattered intensity.

Results/Discussion

Depending on the parameters of the fluid, the bubble, and the acoustic excitation, various behaviors are observed for the evolution of the droplets after nucleation, including collapse with recondensation or “rebound”, and complete vaporization with shell burst. Distinguishing between this different regimes is crucial to maximize the load delivery by controlling and balancing effects such as extravasation enhanced by IC and the sonochemistry possibly denaturing the payload. Only by understanding the phenomena at stakes will one be able to accurately model and predict droplets and bubbles behavior.

References

- [1] Guédra, M. and Coulouvrat, F. The Journal of the Acoustical Society of America **138**, 3656-3667 (2015).
- [2] Lacour, T.; Guédra, M.; Valier-Brasier, T. and Coulouvrat, F. The Journal of the Acoustical Society of America **143**, 23-37 (2018).



Interactions Between Rigid Spheres Subjected to Bessel Beam

Shahrokh Sepehrirahnama ¹, Kian-Meng Lim¹

¹Department of Mechanical Engineering, National University of Singapore, Singapore
E-mail: mpeshse@nus.edu.sg, limkm@nus.edu.sg

Introduction

Pull-in effect of an acoustic Bessel beam is due to the negative axial force exerted on scatterers in the sound field [1]. It is known that factors such as conical angle of the Bessel beam, distance from the beam axis, and the size of the particle (denoted by ka where k is wave number and a the sphere radius) determine the operation range of the negative axial force for a single scatterer [1-3]. Previous studies were limited to the case of a single sphere, whereas, in an ensemble of particles, the interactions determine the resultant force acting on each individual particle, especially when the particles are close to each other. In this paper, it is demonstrated that component of interaction forces along the Bessel beam axis influences the total radiation force experienced by the particles. In addition, the partial force related only to particle's scattering field is studied with respect to the size factor ka .

Theory and Formulation

For a single particle, acoustic radiation force can be written as

$$F = F_{ii} + F_{is} + F_{ss}. \quad (1)$$

here, F_{ii} denotes the partial force obtained from stresses that are functions of the square of incident potential. It can be shown theoretically that F_{ii} is zero [4]. F_{is} denotes the acoustic primary force that is a function of the product of incident and scattering potentials. The last term F_{ss} denotes a partial force that depends on the square of scattering potential. This term is negligible for particles in Rayleigh limit, $ka \ll 1$, since it is proportional to $(ka)^6$, as compared to primary force F_{is} which is a function of $(ka)^3$. As ka increases, F_{ss} increases and finally overtakes the primary force F_{is} . Since negative axial force induced by a Bessel beam occurs at relatively large ka values, it is important to account for F_{ss} to calculate the resultant acoustic radiation force F . Figure 1 shows the particle size compared to the wave-front of a zero-order Bessel beam for different ka values. For a pair of particles (1 and 2), Equation (1) can be written as follows for the force acting on particle (1).

$$F_1 = F_{ii} + F_{i1} + F_{i2} + F_{11} + F_{22} + F_{21}, \quad (2)$$

where subscripts 1 and 2 denote the scattering potentials from particle (1) and particle (2), respectively. For particle (1) being the probe particle that the force is measured, F_{ii} , F_{i2} and F_{22} are zero since they contain no singularity in the probe particle. F_{i1} and F_{21} give the primary and interparticle radiation forces acting on the probe particle (1). For ka values beyond Rayleigh's limit, the self partial force F_{11} needs to be accounted for in the calculation of the total radiation force F_1 . The objective of this study is to investigate interparticle and self partial forces, particularly for a Bessel beam and a wide range of ka .

Results

A pair of rigid and immovable spheres of the same size (radius a) are placed along the axis of a Bessel beam, with their center-to-center distance set to $2.5a$ and sphere (2) downstream of sphere (1). Multipole series expansion was used to compute different terms of equation (2) [5]. The incident wave is a zero-order Bessel beam with cone angle $\beta = 60^\circ$ propagating in the positive z -direction.

Figure 2 shows the magnitudes of interparticle forces, F_{12} and F_{21} , and the self partial forces F_{11} and F_{22} . For this axisymmetric configuration, all the forces act in the z direction, which is the wave direction. A positive force denotes that the force acts in the positive z -direction, and a negative force is in the negative z -direction. It is noted that up to $ka = 1.3$, three of the forces, F_{21} , F_{11} , and F_{22} , act in the negative z -direction (as illustrated by the schematic of two spheres in Figure 2). In this range of $ka < 1.3$, it can be seen from the directions of F_{12} and F_{21} that the interaction force is repulsive. For the last four values of $ka = 1.30, 1.95, 2.92$, and 4.38 , there are changes in the directions of the forces; these are explicitly labeled in the Figure as + or - for each color to denote the force direction.

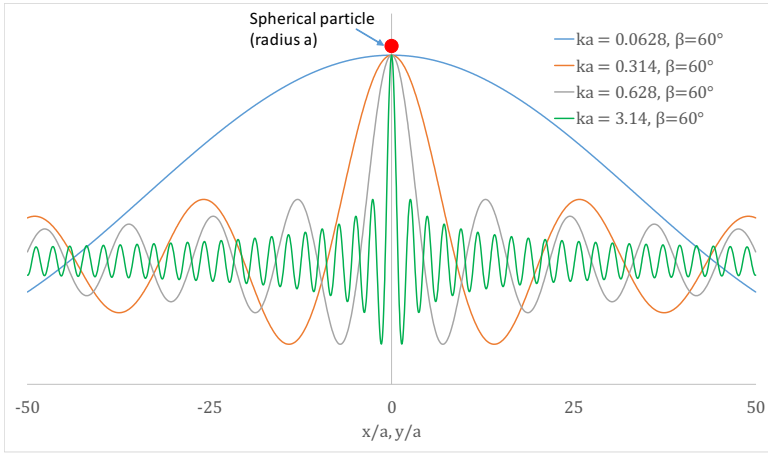


Figure 1: Illustration of particle size compared to the wave-front of a zero-order Bessel beam for ka values of 0.0628, 0.314, 0.628 and 3.14 which covers Rayleigh's limit and beyond.

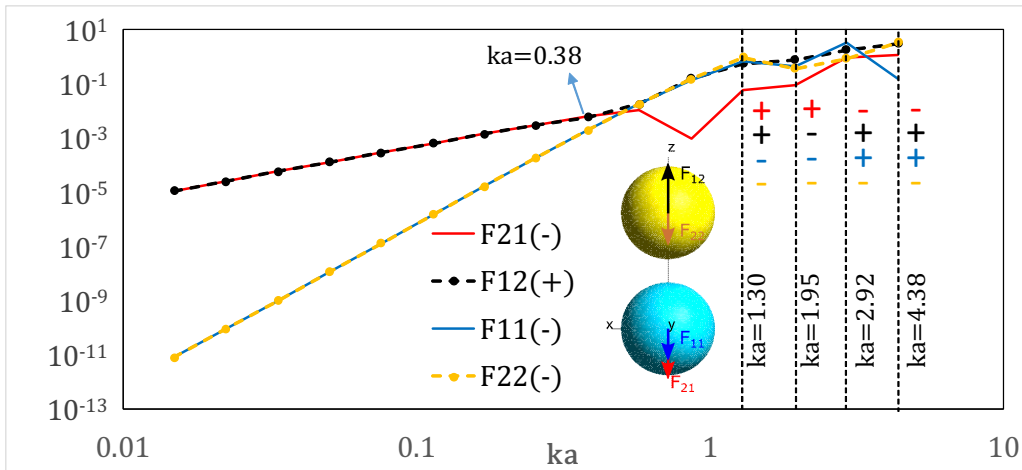


Figure 2: Magnitudes of F_{12} , F_{21} , F_{11} and F_{22} with respect to the size factor ka for two spheres aligned along the axis of a Bessel beam.

For small ka within Rayleigh's limit, the self partial forces (F_{11} and F_{22}) are much smaller than the interaction ones. At $ka \simeq 0.4$, these forces are of comparable order of magnitude, meaning that self partial forces should be included in computing the total radiation force for $ka > 0.4$. The interaction forces acting on the spherical particles are equal and opposite at small ka values. However, their magnitude starts to differ when $ka > 0.4$. Partial forces F_{11} and F_{22} also have the same magnitude up to $ka < 0.4$, but the magnitudes start to differ when $ka > 0.4$. For the last four ka values, changes in the force directions were observed. At $ka = 1.30$, the direction of the interaction force acting on sphere (1), F_{21} , changes to positive as compare to negative when $ka < 1.30$. At $ka = 1.95$, directions of both interaction forces (F_{12} and F_{21}) change from those of $ka < 1.30$, indicating attraction between the spheres. The direction change was also observed for F_{11} at $ka = 2.92$ and $ka = 4.38$. From the above results, it can be seen that interaction and self partial forces contribute to the resultant force on a particle and these contributions may be in the opposite direction (depending on ka) to the primary force due to the Bessel beam.

Conclusion

The interaction and self partial forces are reported for a pair of rigid spheres in a zero-order Bessel beam with respect to the size factor ka . The interaction and self partial forces may take on negative values depending on the size factor ka , hence they contribute to the negative axial force (pull-in effect) of a Bessel beam. Such contribution may be crucial when the Bessel beam is used to separate an ensemble of particles based on size. Finally, the self partial forces should be included in the calculation for the range of $ka > 0.4$, where these forces are no longer negligible.

References

- [1] P. L. Marston. J. Acoust. Soc. Am. **122**, 3162–3165 (2007).
- [2] F. G. Mitri. Journal of Physics A: Mathematical and Theoretical **42**, 245202 (2009).
- [3] G. T. Silva, J. H. Lopes, F. G. Mitri. IEEE trans. Ultrason. Ferroelec., Freq. Control **60**, 1207–1212 (2013).
- [4] S. Settnes, H. Bruus. Physical Review E **85**, 016327 (2012).
- [5] S. Sepehrihnam, K.-M. Lim, F. S. Chau. J. Acoust. Soc. Am. **137**, 2614–2622 (2015).



The Role of Diffraction on Particle Patterning using Travelling Surface Acoustic Waves

Adrian Neild¹, Armaghan Fakhfouri¹, Citsabehsan Devendran¹, Thomas Albrecht¹, David J. Collins^{2,3}, Andreas Winkler⁴ and Hagen Schmidt⁴

¹Department of Mechanical and Aerospace Engineering, Monash University, Clayton 3800, Victoria, Australia

E-mail: adrian.neild@monash.edu, URL: <https://www.labformicrosystems.com/>

²Pillar of Engineering Product Development, Singapore University of Technology and Design, Singapore 487372, Singapore

³Department of Biological Engineering, Massachusetts Institute of Technology, Cambridge, Massachusetts 02139, USA.

⁴SAWLab Saxony, IFW Dresden, Dresden, D-01069 Germany

Introduction

TSAW and SSAW are terms referring to travelling surface acoustic wave and standing surface acoustic wave systems respectively. In the former a single set of electrodes is excited on a piezoelectric substrate, forming an interdigital transducer (IDT), at the correct frequency of excitation, the result is a surface acoustic wave which travels away from the electrodes. In the latter, two opposing travelling waves, typically generated by a pair of opposing IDTs, interfere leading to a standing wave. In both cases the surface waves will couple efficiently into fluid placed on the vibrating substrate, making such excitation highly suitable for acoustofluidics.

Early theoretical work on acoustic radiation forces characterized the nature of forces obtained from planar travelling waves or planar standing waves [1]. Here, the former, causes particle motion across multiple wavelengths in the direction of propagation, whilst the latter induces movement of particles into patterns with a half wavelength periodicity. With travelling waves being synonymous with unidirectional migration, TSAW systems have been widely used to exploit this for particle sorting. Likewise, the link between standing waves and patterning has meant that SSAW devices have seen extensive use in patterning particles.

However, neither TSAW nor SSAW generate planar waves in the fluid, so the link between field type and particle behavior is more complex than in the ideal bulk acoustic fields described by Yosioka *et al* [1]. Additional possibilities exist. Indeed, previously, we have shown that features associated with travelling waves, namely migration across multiple wavelengths, can occur in SSAW systems due to attenuation effects [2]. Here, we offer a detailed analysis of the diffractive effects in a TSAW generate field, which gives rise to features more usually attributed to standing waves, namely particle patterning, here shown in two dimensions.

Characterisation of the sound field generated by TSAW

The vertical displacement magnitudes of the piezoelectric substrate, in which the TSAW is present, has been measured using an LDV. A set of IDTs with a pitch of 21 μm , and a width of 750 μm , was actuated at 180 MHz whilst a scan was performed using a 10.5 μm pitch. It can be seen from Figure 1(a) that the width of the beam decreases with distance away from the IDTs, and that within the beam there are fluctuations in displacement amplitude, Figure 1(b-d), both result from diffraction of the SAW. In Figure 1(e) a system depiction is shown. A cross-section through this system is modelled in COMSOL, Figure 1(f), yielding the absolute pressure amplitude distribution in a 2D plane. The SAW couples into a fluid volume measuring 100 μm wide (measured in the direction of TSAW propagation) and 46.5 μm high channel. The plot shows the time averaged absolute pressure, in an ideal travelling wave this would be uniform, instead variations are observed as the TSAW couples into the fluid at the Rayleigh angle. These fluctuations are due to diffraction and are typical of the lobes formed in an ultrasonic beam created by a finite source, in this case the limit of the source is the edge of the fluid volume.

Analysis of the resultant particle behavior

Figure 2 shows a set of experimental data on the particle behaviour due to exposure to a sound field generated by a TSAW. As the width of the IDTs increase, there is sufficient space, between the two large streaming swirls (the spacing of which can be linked to the width of the TSAW beam), for patterns to emerge. In the wider IDT sets considered (Figure 2 c and d) patterning is seen in two dimensions, both along the propagation

direction (parallel trapping) and perpendicular (orthogonal trapping) to it. The orthogonal trapping is due to the variations in amplitude across the TSAW beam caused by diffraction, as observed in Figure 1(b-d). To demonstrate this, channels were located at different distances from the IDT. When this was done, the location and interspacing in these patterns was altered, the characteristics of which agree with those seen in the TSAW profile. Namely, that at further distances from the IDT less features are seen and the spacing is greater.

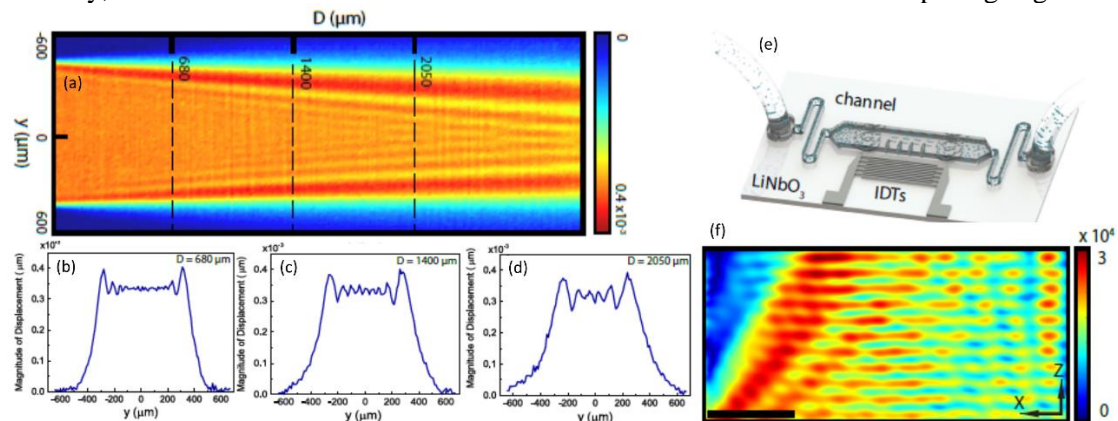


Figure 1: (a) An LDV scan of the out of plane displacement arising due to the propagation of a TSAW is shown as it propagates away from the $750 \mu\text{m}$ wide IDT. (b-d) Displacement magnitude across the beam at different distances, D , from the IDT. (e) A depiction of the substrate with a PDMS defined fluid channel attached. (f) Numerical results for the absolute pressure in a fluid excited by a TSAW (propagating left to right).

The parallel trapping is due to diffraction within the fluid [3]. Analysis of the spacing, Figure 2 (g and h) shows that the separation is consistently under a half wavelength, and as such can't be attributed to reflections within the system. In addition there is agreement between the spacing of the lobes seen in COMSOL simulations (like that shown in Figure 1(f)) and experimental data. Specifically we see that with channels of higher heights the spacing is larger, which is consistent with the angular spread seen in the areas of raised pressure in Figure 1(f).

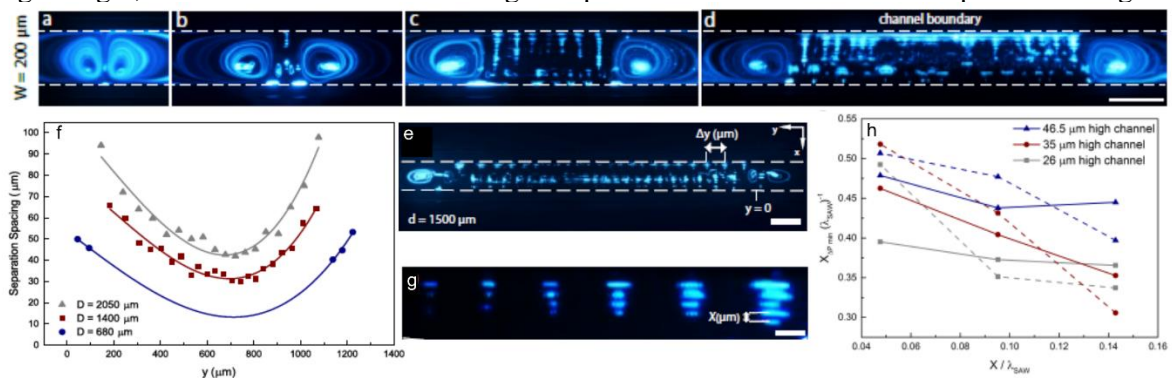


Figure 2: (a-d) Particle distribution during exposure to a TSAW for four different width IDTs: 187.5, 375, 750 and 1500 μm , particle patterning can clearly be observed. (e) Highlighting the patterning in the lateral direction, which is analysed in (f). (g) Patterning in the propagation direction, which is analysed in (h).

The data presented here is for a particle size of $1 \mu\text{m}$. When other particles sizes are examined, it becomes clear that size causes a transition between dominant mechanisms. In bulk acoustic standing wave systems a transition between streaming dominated to patterning is well known. For TSAW an additional regime is introduced, so that small particles are streaming dominated, larger ones exhibit patterning, and larger still migrate unidirectionally with the propagating waves.

Conclusion

We have identified the particle patterning capabilities of TSAW actuation. Showing that the travelling wave nature of excitation, yields a pressure distribution within the fluid which is significantly more complex than a planar travelling wave, hence we have access to effects beyond long scale migration of particles. Indeed patterning in two dimensions are observed and explained in terms of diffraction of the TSAW and of the resultant wave as it is coupled into the fluid.

References

- [1] K. Yosioka and Y. Kawasima. *Acustica* **5**, 167–173 (1955).
- [2] J. W. Ng, D. J. Collins, C. Devendran, Y. Ai and A. Neild. *Microfluid Nanofluid* **20**, 151 (2016)
- [3] C. Devendran, D. J. Collins, Y. Ai and A. Neild. *Physical Review Letters* **118**, 154501 (2017)

The song of 2D micro-bubbles

Thomas Combriat¹, PT ? AD ?¹, and Philippe Marmottant¹

¹LIPhy UMR 5588, CNRS/Université Grenoble-Alpes, Grenoble, France

E-mail: thomas.combriat@univ-grenoble-alpes.fr / philippe.marmottant@univ-grenoble-alpes.fr

Introduction

Sound and bubbles are closely related: because of their coupling with the surrounding fluid, they resonate at a frequency, given by Minnaert's formula $R_0 f_{Minn} \approx 3 \text{ m s}^{-1}$ for 3D bubbles, at a wavelength a lot greater than their own size [1]. Because of this property, an assembly of bubbles can show interesting properties when in interaction with an acoustic field which make them meta-materials [2]. Under acoustical excitation, a bubble will pulsate, thus enhancing or suppressing part of this excitation. Coupling effects can also come into place because of interactions between bubbles.

In this study, we try to understand the alteration of an acoustic wave by an assembly of *free pulsating* bubbles. Using microfluidics to produce assemblies of identical bubbles, we show that even low surface fractions of bubble can significantly decrease the transmission coefficient of the material.

Experiment

We use microfluidic chips to create and trap micro-bubbles (around 60 microns in diameter) using a flow focusing junction. As the microfluidic channel height (typically 25 microns) is smaller than the bubbles size, they are squeezed between the upper and lower walls and thus become a nearly 2-dimensional system. Bubbles can be trapped on beforehand known positions using capillary traps [3] as it can be seen on on Fig. 1 right or can be self-organised using a continuous ultrasonic "pump" wave before the pulsed measurements [4]. This setup is immersed onto a sound reflector in a water filled tank (see Fig. 1 left). A pulsed sound wave is produced by the transducer at the bottom of the tank and will propagate through the bubbly medium and will be measured on the other side by an hydrophone which position can be chosen in the whole tank. Finally a camera let us image the medium at the time of the acquisition.

The transmission coefficient of the bubbles is measured by doing the ratio between the Fourier transform of the signal with bubbles present over the Fourier transform of the signal without bubbles.

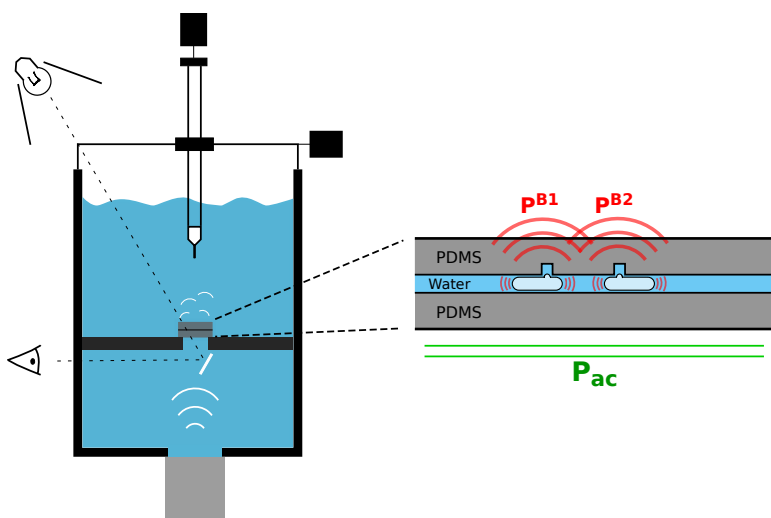


Figure 1: Experimental setup. Left: global sketch of the experiment featuring an ultrasonic transducer emitting a pulse in a water-filled tank. The microfluidic chip containing the bubbles (see right) is placed in the path of this travelling wave which is then measured using an hydrophone on the other side. Right: zoom on the microfluidic chip, showing two bubbles held by capillary traps under excitation by a sound wave.

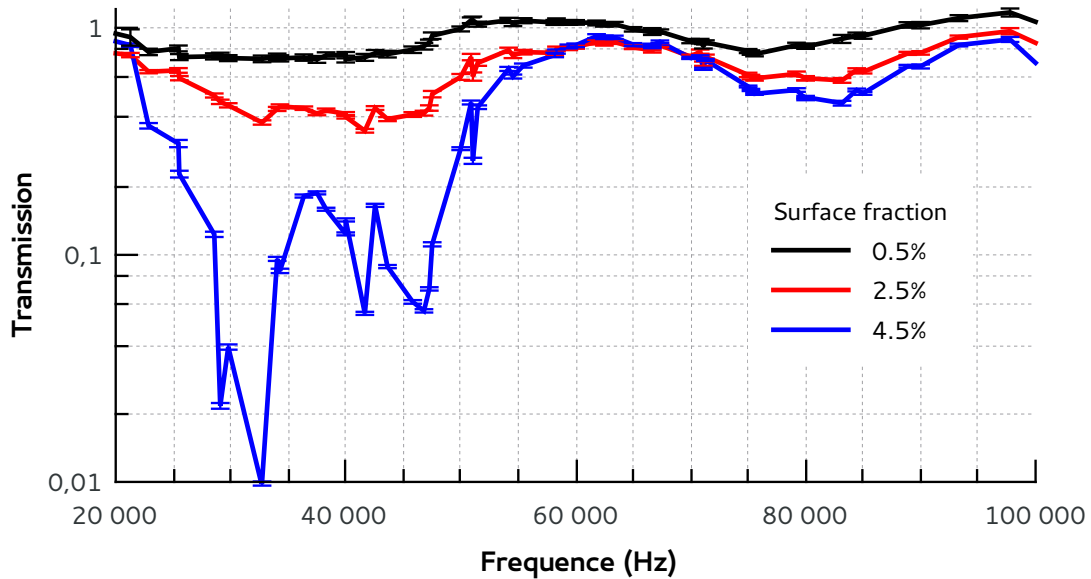


Figure 2: Transmission of an ultrasonic pulse through a single layer of bubbles for different surface fraction as a function of the frequency. The bubbles are approximately $40\ \mu\text{m}$ is radius, which agrees with the main absorption peak being at Minnaert’s frequency for 2D bubbles: $R_0 f_{Minn} \approx 2\ \text{m s}^{-1}$. The secondary absorption peak at approximately 85 kHz might be the result of non-linear vibration of the bubbles. For this experiment, the bubbles were neither attached to capillary traps nor organised using an ultrasonic pump.

Bubbles as an acoustic metamaterial

The transmission coefficient of an assembly of bubbles for different surface fraction of the microfluidic channel covered with bubbles is shown on Fig. 2. We can see that even quite small surface fractions of bubbles can significantly alter the transmission of a sound wave over a broad range of frequencies. The main absorption decrease, in the range of 30-35 kHz is very close the resonant frequency of the bubbles present in the system and may be due to bubbles pulsing with a great amplitude, dissipating energy from the sound wave inside the surrounding medium.

A second transmission decrease is also seen at approximately twice the Minnaert frequency. This effect is not fully understood yet but it might be due to non-linear effects occurring when the pulsing amplitude becomes high enough to trigger Navier-Stokes non-linearity.

Note that this absorption profile has different characteristics than the ones presented by Leroy *et al.* in [2] for a single layer of bubbles trapped in a yield stress fluid for which the absorption curve showed only one peak. The presence of several distincts low-transmission frequencies suggests that coupling of bubbles might comes into play.

Conclusion

In this abstract, we show preliminary results on the transmission of an acoustic wave through a layer of microfluidic bubbles. These results are encouraging for ongoing studies as they show a huge decrease of the acoustic intensity over a broad range of frequency. *In fine* this study could give us a better understanding of the coupling between bubbles and acoustic in order to expose more effects such as the acoustic SASER.

References

- [1] M. Minnaert. *Philos. Mag* **16**, 235 (1933).
- [2] V. Leroy, A. Strybulevych, M. G. Scanlon, J. H. Page. *Phys. Rev. Lett.* **29**, 123 (2009).
- [3] R. Dangla, S. Lee, C. Baroud. *Phys. Rev. Lett.* **107**, 12 (2011).
- [4] D. Rabaud, P. Thibault, M. Mathieu, P. Marmottant. *Phys. Rev. Lett.* **106**, 12 (2011).



Particle sorting in phase modulated surface acoustic fields: from theory to experiments

Gergely Simon¹, Marco A.B. Andrade², Julien Reboud³, Jose Marques-Hueso¹, Marc P.Y. Desmulliez¹, Mathis O. Riehle⁴, and Anne L. Bernassau¹

¹School of Engineering and Physical Sciences, Heriot-Watt University, Edinburgh, United Kingdom
E-mail: A.Bernassau@hw.ac.uk

²Institute of Physics, University of São Paulo, São Paulo, Brazil

³School of Engineering, University of Glasgow, Glasgow, United Kingdom

⁴Institute of Molecular Cell and Systems Biology, Centre for Cell Engineering, University of Glasgow, Glasgow, United Kingdom

Introduction

Sorting heterogeneous cell mixture has been of considerable interest in recent years for micro total analysis or lab-on-chip systems. Separation of particles or cells is crucial for various biological and biomedical applications as cancer [1] or sepsis diagnosis [2]. However, most of techniques developed are application based devices, and lack of adaption from cell to cell. Here we discuss a technique that allows sensitive and adaptive particle sorting based on modulated acoustic waves with surface acoustic wave device. In our previous work, we introduced an accurate form of acoustic radiation force for surface acoustic waves that differs from bulk acoustic waves [3]. The acoustic radiation force plays an important role on the particle trajectories. In this work, we present the importance of accurate acoustic radiation force in particle trajectories for adaptable particle sorting by size and density. An analytical prediction of particle behavior (dependent of acoustic radiation force) shows excellent agreement with COMSOL simulation and experimental data.

Device fabrication and experiments

The surface wave device was fabricated by standard processes [4] for 13.3 MHz operating frequency on lithium niobate 128° Y-cut wafer. A PDMS microchannel of width 240 μm and height 50 μm was bonded on top of the substrate. The width of the PDMS channel allows for two pressure nodes to be present within the device. Two inlets for sheath inflow and one particle inflow provide precise focusing of particles. To avoid stiction of particles to each other and device sidewalls, they were suspended in 0.1% w/v polyethylene glycol in DI water solution. For experiments carried out for density-based sorting, the particles were suspended in 30% OptiPrep to reduce sedimentation or lift. For the experiments, particle counts below 10^6 / ml were used to avoid interparticle effects.

Sorting method and theoretical framework

The modulated phase acoustic pattern and its effect on the particles' movement is illustrated in Fig. 1. To be able to predict the behavior of the particles within a phase modulated fields, we derived the equation describing the particle trajectories. The governing equation was a force balance of the accurate expression of the primary acoustic radiation and Stokes' drag. In this latter, wall effects were included. Utilizing the inertial approximation, i.e. the particles carry no inertia and can change momentum instantaneously, the particle trajectory equation was obtained.

Comsol simulation model

To reduce computational demand of the numerical simulation, we simulate a 2D cross section of the microchannel. Furthermore, instead of a complex coupled piezoelectric-acoustic-structure interaction model, we simulate the acoustic domain and describe the field by a pressure distribution. The acoustic radiation force

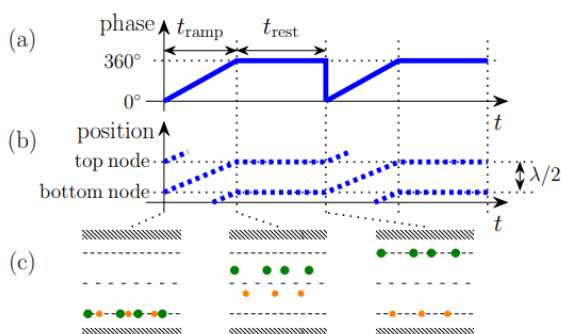


Figure 1: illustration of sorting. (a) The phase pattern used for sorting. (b) The resulting movement of the pressure nodes within the channel. (c) Particle position at different times.

The particles have a positive contract factor and are focused with the shear flow on the bottom nodal line. As the phase of one transducer is continuously modulated (from 0° to 360° , during t_{ramp}), the standing wave pattern moves laterally. The different sized particles experience different radiation and drag forces, resulting in different trajectories. With the right time parameters (t_{ramp}), the 2 types of particles are located at 2 different pressure nodes and relax at different spatial locations during the rest period (t_{rest}), where the phase is kept constant.

on the particles was calculated using Gorkov's potential approach [5]. As the acoustic radiation force is a second order time-averaged force, it is not possible to directly simulate the effect of continuous phase modulation. Instead, we decided to quantize the phase modulation as follows: start at 0° , then from 18° to 342° by steps of 36° (during the ramping), and finish at 360° , corresponding to the rest period. For each phase, the pressure field was resolved in a frequency dependent study, and this was passed onto the particle tracing module to allow calculation of the primary radiation force. In this investigation, interparticle forces were neglected [6].

Results

Figure 2 shows the influence of particle parameters on surface wave and bulk acoustic radiation forces. Two different material of particles were modelled: $10\ \mu\text{m}$ polystyrene (PS) and iron-oxide. It can be seen that for PS particle, not a large difference is expressed between the 2 acoustic radiation forces while for iron oxide, a difference of 50% in forces is noticed. To validate our theoretical model, we plotted the acoustic radiation force obtained from the Comsol simulation (Gorkov's potential) and excellent agreement to our model is shown (Fig. 2). We further utilized the model to anticipate the particle trajectories in sorting experiments. For simulation results, the only fitting parameter between the experiments and simulation/theory was the pressure amplitude (80 kPa). The OptiPrep solution was considered with density $\rho=1.2\ \text{g/cm}^3$, and its speed of sound was assumed to be the same as of water. The experimental results correspond to the average and standard deviation of 7 experiments. We carried out size-based separation of 10 and 15 μm diameter polystyrene particles, and density-based sorting of polystyrene ($\rho=1.05\ \text{g/cm}^3$) and iron-oxide ($\rho=1.5\ \text{g/cm}^3$) particles, $10\ \mu\text{m}$ in diameter. Fig. 3 shows simulations and experimental data. We believe the difference between the experimental and theoretical results can be attributed to the uncertainty of speed of sound of the medium. The simulation and theory have an excellent agreement, the small discrepancy comes from numerical errors and the discretization of the phase modulation.

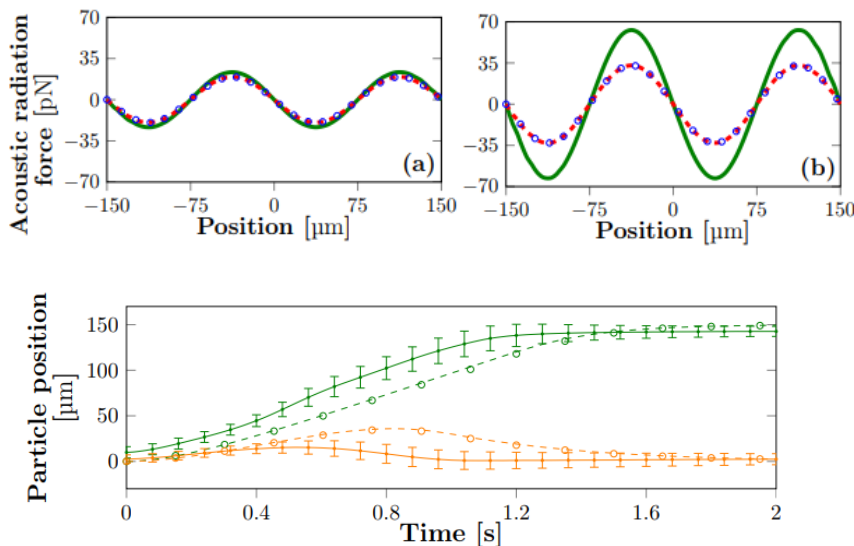


Figure 2: Comparison between bulk and surface acoustic wave radiation force: The primary radiation force using the standard theory (green, solid), our modified equation (red, dashed) and the derivative of the Gorkov potential from Comsol simulation (blue circles), for (a) a PS sphere (b) an iron-oxide sphere.

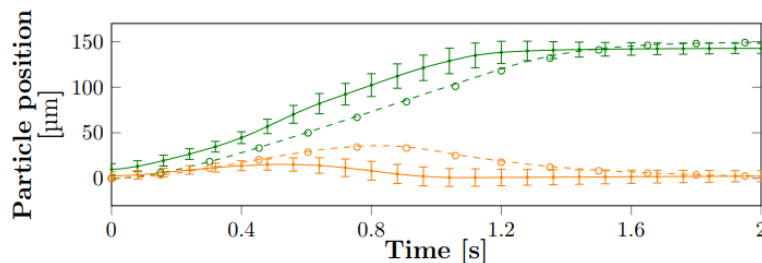


Figure 3: Density-based particle sorting: Particle trajectories for sorting of $10\ \mu\text{m}$ PS (in orange) and iron-oxide (in green) particles. Experimental (continuous line and error bars), COMSOL simulation (circles) and theoretical results (dashed lines) are shown.

Conclusion

We presented the importance of accurate primary acoustic radiation force in surface wave devices. We have shown excellent agreement between numerical simulations and our analytical equation. Particle trajectories from separation experiments were successfully validated by numerical and theoretical methods.

References

- [1] X. Y. Ding *et al.*, "Cell separation using tilted-angle standing surface acoustic waves," (in English), *Proceedings of the National Academy of Sciences of the United States of America*, vol. 111, no. 36, pp. 12992-12997, Sep 9 2014.
- [2] P. Ohlsson *et al.*, "Integrated Acoustic Separation, Enrichment, and Microchip Polymerase Chain Reaction Detection of Bacteria from Blood for Rapid Sepsis Diagnostics," *Anal Chem*, vol. 88, no. 19, pp. 9403-9411, Oct 4 2016.
- [3] G. Simon *et al.*, "Particle separation by phase modulated surface acoustic waves," *Biomicrofluidics*, vol. 11, no. 5, p. 054115, Sep 2017.
- [4] L. Y. Yeo and J. R. Friend, "Ultrafast microfluidics using surface acoustic waves," *Biomicrofluidics*, vol. 3, no. 1, p. 12002, 2009.
- [5] L. P. Gorkov, "On the forces acting on a small particle in an acoustic field in an ideal fluid," *Soviet Physics Doklady*, vol. 6, no. 9, pp. 773-775, 1962.
- [6] G. T. Silva and H. Bruus, "Acoustic interaction forces between small particles in an ideal fluid," *Phys Rev E Stat Nonlin Soft Matter Phys*, vol. 90, no. 6, p. 063007, Dec 2014.



Numerical Modelling of Viscous Damping for Acoustic Resonances of Suspended Microparticles

Thierry Baasch¹, Jonas Fankhauser¹, and Jürg Dual¹

¹Department of Mechanical and Process Engineering, Institute for Mechanical Systems, ETH Zurich, Zurich, Switzerland
E-mail: baasch@imes.mavt.ethz.ch, URL: www.expdyn.ethz.ch

Introduction

In this numerical, study we investigate the damping mechanisms of particle resonances in acoustofluidic systems. New applications such as the one-cell-per-well (OCPW) technology make use of frequencies higher than 100 MHz [1]. In this frequency range, it is possible to excite resonances of soft micrometer sized particles. To predict the particle trajectories under these conditions the acoustic radiation force needs to be computed. Under these conditions both the amplitude and direction of the acoustic radiation force can not be predicted using the Gorkov potential [2]. The amplitude of the resulting acoustic radiation force depends strongly on the damping and thus on the quality factor of the particle resonance. Numerically, this problem is rather difficult as the damping is inherently linked to the viscous boundary layer, which is very small at these high frequencies. Thus, a numerical discretization resolving the viscous boundary layer will lead to extremely expensive computations. Most generally the problem would require a full three dimensional simulation. However, symmetries can be exploited in the case of a single particle in a one-dimensional wave. Investigating this simple case provides some general insights into the damping mechanisms. Finally, we present a simplified approximate model, for which we derived an acoustofluidic damping factor semi-analytically similar to the work of Hahn et al. [3].

Methods and Results

In this work we use the finite element method (FEM) to numerically investigate the viscous and acoustic damping mechanisms of acoustically excited particle resonances. Neglecting intrinsic material damping and acoustic streaming, we chose the simple case of one single isolated 10 μm radius polystyrene particle in the pressure node of a one-dimensional standing wave in water (Fig. 1 I). This setup has a rotational symmetry and the full three-dimensional model can be reduced to two dimensions, improving the numerical cost. In order to fulfill the Sommerfeld radiation condition, we added a perfectly matched layer (PML) domain around the fluid domain (Fig. 1 II). Additionally, a viscous boundary layer of thickness $\delta = \sqrt{2\frac{\nu}{\omega}}$ will form in the full model, here ω and ν denote the angular frequency and kinematic viscosity, respectively. Typically, in acoustofluidics, the thickness of the viscous boundary is much smaller than the particle diameter. Thus in the fluid domain a very fine mesh is required close to the particle fluid boundary (Fig. 1 III). In total we used three FEM models:

- 1. Inviscid Model:** The fluid was modeled as inviscid, similar to [2]. Here the only contribution to the damping of the resonance is radiation damping. This model is computationally cheap but not very accurate.

- 2. Viscous Model:** The fluid was modeled as a viscous fluid. Both the radiation and the viscous boundary layer contribute to the energy losses. This method is exact but computationally expensive as the viscous boundary layer needs to be resolved.

- 3. Approximate Model:** We derived a semi-analytical expression for both the added mass and the loss factor, similar to the work of Hahn et al. [3]. This model is computationally cheap and approximates the more exact viscous model.

Figure 2 shows the energy spectrum of the first five resonances of the particle for our three models. The corresponding quality factors are summarized in table 1. It can be observed that the viscous boundary layer has a significant influence on the quality factor of the resonance and can thus not be neglected in calculations. Further, our computationally more efficient approximate method yielded good results; the error was in all cases in the range of a few percent.

Conclusion

We investigated the acoustically excited resonances of microparticles using different methods. So far

we found that the viscous boundary layer plays an important role and can generally not be neglected. We propose a simplified model that allows estimating the quality factor of the particle resonances using a semi-analytical expression. We plan to investigate other damping mechanisms such as thermal and material damping or damping due to acoustic streaming. Preliminary studies on two-dimensional models did, however, show that these additional effects are usually small and the main contributors to the energy losses are the viscous boundary layer and the radiation.

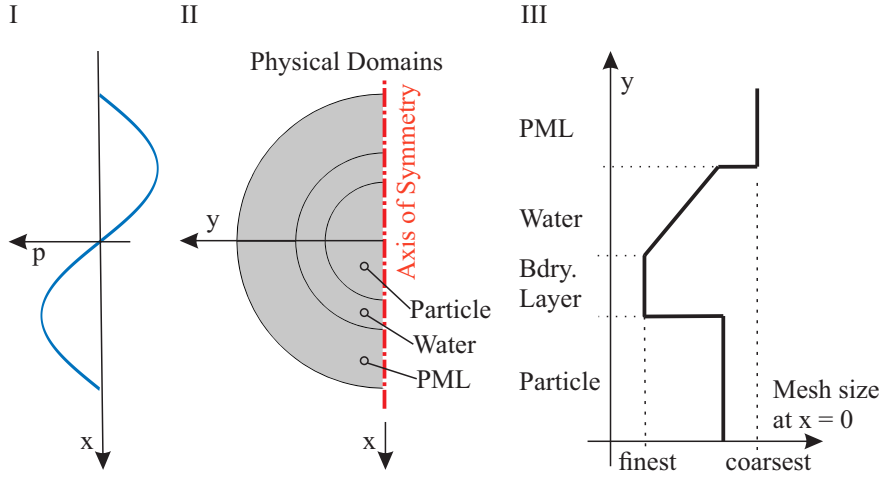


Figure 1: We used the finite element method to model a polystyrene particle placed at the pressure node of a one-dimensional standing wave. The whole model possesses a rotational symmetry and can thus be calculated in two dimensions. In I) the pressure distribution for 75 MHz is shown in I). II) shows the general setup, the perfectly matched layer assures that the Sommerfeld radiation condition is fulfilled. A very fine mesh is required at the particle fluid interface to resolve the viscous boundary layer, as shown in III).

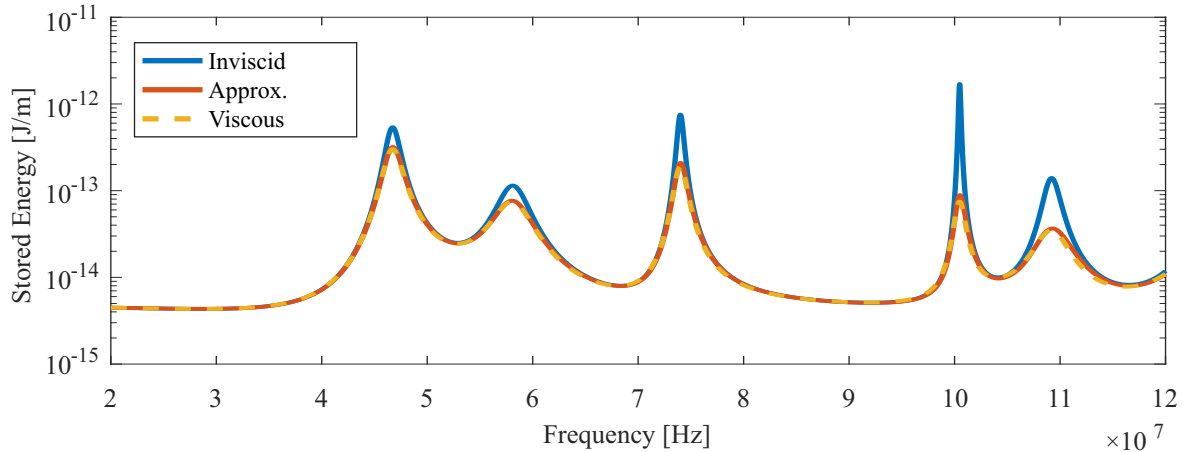


Figure 2: The energy spectrum of the particle is shown from 20 to 120 MHz for the inviscid, full viscous and approximative models. Every frequency sweep was divided into 6000 points, yielding a total of 18000 scattering simulations. The figure shows that the damping due to the viscous boundary layer influences the resonance amplitudes significantly. Furthermore, it can be observed that our approximative model underestimates the damping throughout the frequency range.

Method	Peak I	Peak II	Peak III	Peak IV	Peak V
Inviscid Model	30.8	16.9	111	430.6	65.5
Viscous Model	23.36	12.7	54.1	83.71	36.6
Approx. Model	23.37	12.8	56.2	91.4	38.8
Q Invi. / Q Visc.	1.31	1.33	2.05	5.14	1.79
Diff. Visc Vs Approx.	0.04	1.5	3.7	8.4	5.7

Table 1: The quality factors for the first five resonances of a 10 μm radius polystyrene particle placed in the pressure nodal plane of a one dimensional standing wave.

References

- [1] D. Collins, B. Morahan, J. Garcia Bustos, C. Doerig, M. Plebanski, and A. Neild. Nature Communications **6**, 8686, (2015).
- [2] R. Habibi, D. Citsabehsan, and A. Neild. Lab on a Chip **17.19**, 3279-3290, (2017).
- [3] P. Hahn, and J. Dual. Physics of Fluids **27.6**, 062005, (2015).



An Acousto-Gravitational Balance in Climbing Wetting Films

Ofer Manor, Daniel Khaikin, Amihai Horesh, and Anna Zigelman

Department of Chemical Engineering, Technion – Israel Institute of Technology, Haifa, Israel
E-mail: manoro@technion.ac.il, URL: <https://chemeng.technion.ac.il/ofer-manor/>

Introduction

The excitation of wetting liquid films by different forms of vibrations has been investigated for over thirty years now [1]. Recent studies on the excitation of oil films by MHz frequency surface acoustic waves (SAWs) found that oil may undergo dynamic wetting and may spread over a solid substrate under the influence of the acoustic excitation [2-4]. Further theoretical and experimental studies showed that the dynamic wetting of partially wetting liquid films of water is dependent on the magnitude of the finite three-phase contact angle between the water, vapor, and the solid substrate [5,6]. Here we study the balance between acoustical and gravitational forces in wetting films.

Experiment

The contribution of gravity to the acoustic wetting of liquid films was ignored to date. It appears that a balance between acoustical and gravitational forces will determine the extent in which partially wetting liquid films may climb over vertical SAW actuators. Moreover, the gravitational forcing in wetting films serves as an efficient and simple tool for the measurement of the level of acoustic forcing. We present new experimental and theoretical results on the climbing of a wetting liquid film atop a vertical SAW actuator from a reservoir of water or oil; see Fig 1. The experimental system is made from a 20 MHz SAW actuator, which is mounted on a vertical stage, so that its edge comes in contact with a reservoir of liquid. Upon the excitation of a propagating MHz SAW we observe a wetting liquid film, which is climbing atop the actuator.

Findings

Partially wetting water and surfactant solutions, which satisfy a finite three phase contact angle between the liquid, vapor, and the substrate of the actuator appear to reach a steady state height above the level of liquid in the reservoir. Theory predicts that the steady state height is a product of the balance between the acoustic pressure and gravitational stress in the film. In contrast, fully wetting films of oil are found to continuously wet and climb over the SAW device under the action of the propagating SAW. Theory shows that the vanishing contact angle renders the contribution of the gravitational stress to film dynamics small. In addition, the theory shows that such a film never reaches a steady state height. The film will continuously climb over the actuator as long as the SAW is excited.

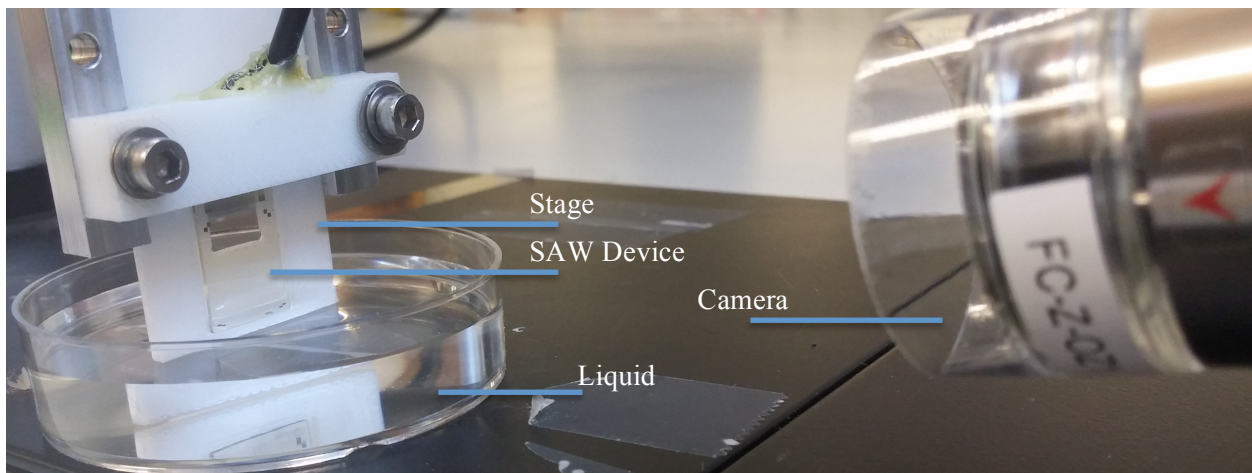


Fig 1. The experimental systems: (On the left) A SAW device mounted on a vertical stage and touching a reservoir of liquid below and (on the right) a USB camera

References

- [1] Morozov and Manor. *Curr. Opin. Colloid Interface Sci.*, 36 (37) 2018
- [2] Rezk, Manor, Friend and Yeo. *Nat. Commun.*, 3(1167) 2012
- [3] Rezk, Manor, Friend and Yeo. *Proc. Roy. Soc. A*, 470(20130765) 2014
- [4] Manor, Rezk, Friend and Yeo. *Phys. Rev. E* 91 (053015) 2015
- [5] Altshuler and Manor. *Phys. Fluids*, 27 (102103) 2015
- [6] Altshuler and Manor. *Phys. Fluids*, 28 (072102) 2016

Temperature-controlled acoustofluidic production of microbubble contrast agents with enhanced stability and monodispersity

Ida Iranmanesh¹, Shamit Shirvastava¹, Richard Browning¹, Dario Carugo^{1,2} and Eleanor Stride¹

¹Institute of Biomedical Engineering, University of Oxford, Oxford, UK

E-mail: ida.iranmanesh@eng.ox.ac.uk, URL: BUBBL

²Faculty of Engineering and Environment, University of Southampton, Southampton, UK

Introduction

Microbubble contrast agents have been vastly used in ultrasound imaging for over 30 years. In recent years, they have attracted considerable interest as carrier agents for drug delivery in cancer therapy and for permeabilising the blood-brain barrier non-invasively [1-2]. The resonance frequency of a microbubble mainly depends on its size. Thus, it is important to produce bubbles with a narrow size distribution. In addition, since the bubbles are injected intravenously and circulate in the blood stream, it is crucial to produce bubbles that are sufficiently stable to reach the target site within the body. Microfluidic techniques offer production of monodisperse microbubbles by scaling-down dimensions, however for the same reason they suffer from relatively low lifetime and production rates. Moreover, bubbles produced using microfluidic techniques have lower stability when compared to microbubbles produced by bulk sonication [3]. Here, we present a novel microfluidic device, based on the work by Carugo et al. [4], using a temperature-controlled microfluidic chip suitable for mass production of microbubbles with enhanced stability and narrow size distribution.

Experimental setup

The device consists of a 60 kHz power transducer operated using a compact built-in signal generator and amplifier with maximum power output of 200 W. A PDMS (Polydimethylsiloxane; 10:1 mass ratio) containing a T-Junction channel architecture was manufactured from a 3D printed mold (Formlabs, Form2 printer). The PDMS layer is then bonded to a glass substrate using plasma bonding, then coupled to the transducer and a PID-regulated Peltier element, using a small amount of conductive glue. A lipid mixture (DSPC: PEG-40S; 9:1 molar ratio) dispersed in water, propylene glycol and glycerol (8:1:1 volume ratio) is then injected (flow rate= 30 ml/h) into the chip using a syringe pump, as shown in Fig. 1.A. From the perpendicular inlet, Nitrogen gas is flown into the chip ($P \approx 80$ kPa). As a result, microbubbles are produced with mean diameter of 200 μm , without ultrasound exposure, see Fig. 1.B. When operating the transducer, these large microbubbles are broken-up into smaller ones due to ultrasonic cavitation, see Fig. 1.C.

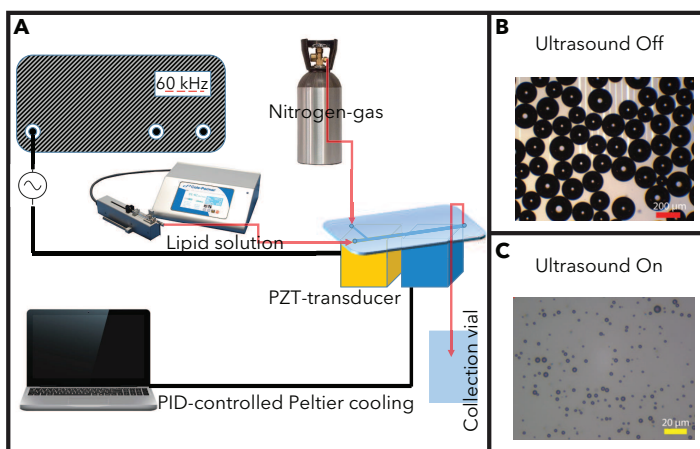


Figure 1: (A) experimental setup comprising: a compact signal generator and amplifier, PID-controlled Peltier unit and a PDMS microfluidic chip ($h = 50$ μm) which is filled by pumping lipid suspension from one inlet ($w_1 = 250$ μm) and Nitrogen gas from another inlet ($w_2 = 127$ μm). (B) Formation of large microbubbles ($D_{\text{mean}} = 200$ μm) in the absence of ultrasound exposure. (C) Continuous exposure to ultrasound leading to formation of clinically relevant sized microbubbles (1 to 4 μm).

Dimensional stability and concentration of microbubbles

The stability of microbubbles produced by acoustofluidic technique were compared with conventional bulk sonication method. The size and concentration of bubbles were measured over time and compared as it can be seen in Fig. 2.

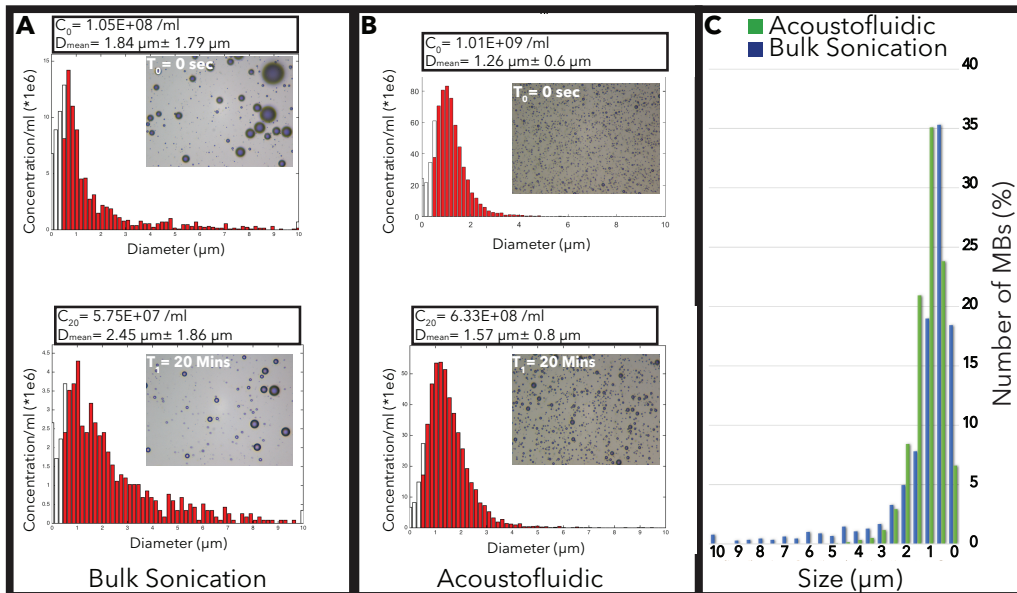


Figure 2: Size and concentration of microbubbles generated using (A) Bulk Sonication (BS), (B) acoustofluidic (AF) device within 20 minutes and (C) comparison of size distribution of microbubbles generated by the two methods. Microbubbles produced by (BS) have a wide size range from 1 to 10 μm , whereas bubbles generated using (AF) are ranged between 1-4 μm .

The effect of cooling on microbubble stability and lipid packing

Here, we use a PID-regulated Peltier element to cool the microbubbles right after production while flowing in the chip. As a result, the stability of microbubbles enhanced significantly as it can be seen in Fig. 3.A. In addition, to investigate a correlation between enhanced stability due to cooling and the change of lipid packing in the microbubbles shell, we used the method described in a paper by Shirvastava, et al [5]. In summary, a fluorometry technique is performed by incorporating Laurdan - an environment sensitive dye - in the lipid shell of the microbubble. Then, the emitted signal from the shell is detected and measured in two conditions: (a) cooling (from 16°C to 5°C) and (b) without cooling (from 16°C to 30°C), over 20 seconds of ultrasound exposure. As it can be seen in Fig. 3.B, the emitted signal increases over time when the bubbles are cooled immediately after production, indicating tighter lipid packing (which has been shown previously to increase the stability of microbubbles), when the temperature is decreased.

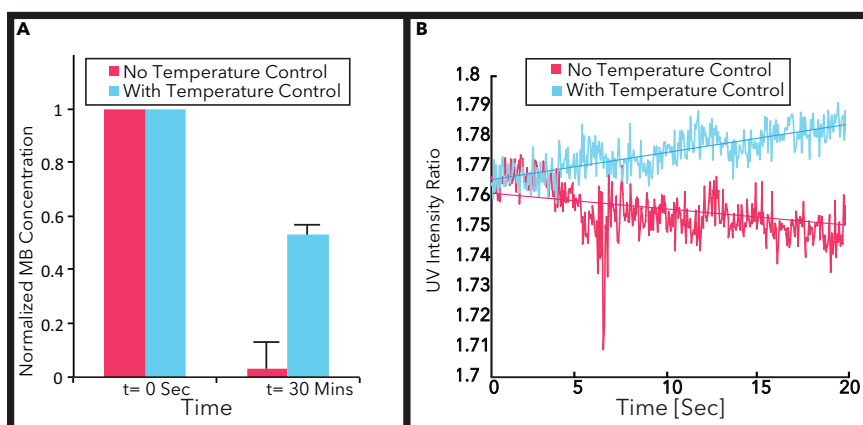


Figure 3: (A) The effect of cooling microbubble flow, from 16°C to 5°C, on concentration stability over time and (B) The effect of cooling on lipid shell compared to when no cooling is used and temperature is raising from from 16°C to 30°C, over 20 seconds.

Conclusion

In summary, we have presented a temperature-controlled acoustofluidic device to produce microbubble contrast agents with a significant improvement in stability and size distribution to overcome the limitations of both bulk sonication and conventional microfluidic platforms.

Acknowledgment

We would like to extend our gratitude to Estelle Beguin and Miles Aron for most helpful discussions.

References

- [1] Unger, E., et al., *Advanced Drug Delivery Reviews* **72**, 110-126 (2014).
- [2] Chu, p., et al., *Scientific Reports* **6**, 33264 (2016).
- [3] Talu, E., et al., *Langmuir* **24**, 1745-1749 (2008).
- [4] Carugo, D., et al., *The Journal of the Acoustical Society of America* **138**, no. 3, 1821-1821, (2015).
- [5] Shirvastava, Sh., et al., [arXiv:1612.06709](https://arxiv.org/abs/1612.06709),

Acoustic in-droplet sample washing and enrichment

Jinsoo Park, Ghulam Destgeer, Muhammad Afzal, and Hyung Jin Sung*

Mechanical Engineering, KAIST, Daejeon, Korea

*E-mail: hjsung@kaist.ac.kr, URL: <http://flow.kaist.ac.kr>

Introduction

Washing of beads and cells is an important experimental procedure for sample preparation in biomedical and biochemical assays. For example, a medium, in which functionalized beads are suspended, should be exchanged to change reagents in bead-based immunoassay [1]. Several biological analyses require cells and biomolecules to be washed for medium exchange [2]. Centrifugation is a conventional method for sample washing, but it depends strongly on skillfulness of technicians and thus may result in inconsistent samples. The centrifugation imparts high shear stress on the sample, and in-line integration and automation are difficult. As an alternative, microfluidic technologies have been introduced; various microfluidic methods based on hydrodynamics, microstructures, and external fields, such as magnetic and acoustic forces, have been utilized to realize in-line, automated system for sample washing. However, the continuous flow-based sample washing operation is subjected to sample contamination and Taylor dispersion, and it is not suitable for high-throughput screening and single-cell/bead analyses.

These limitations can be addressed by droplet-based microfluidic techniques. However, in-droplet sample washing has rarely been studied due to technological difficulties, despite the considerable potential and importance. Lee *et al.* [3] have recently reported a droplet microfluidic sample washing technique, but its operation is complicated with multiple steps: (i) synchronization of two trains of droplets, (ii) electric droplet coalescence; (iii) magnetic particle manipulation by a permanent magnet; (iv) asymmetric droplet splitting at a Y-junction. In the present study, we propose a surface acoustic wave (SAW)-based method for in-droplet microparticle washing. The proposed method is based on acoustic radiation force (ARF) for (i) droplet splitting, (ii) in-droplet particle concentration, and (iii) capturing. We further extend the capability of the proposed method to in-droplet sample enrichment.

Experimental

As shown in Fig. 1(a), a slanted finger interdigital transducer (SFIT), deposited on a lithium niobate (LiNbO_3) substrate, with its resonant frequency band of 100-130 MHz was used to generate 118 MHz travelling SAWs (TSAWs) with a Gaussian intensity distribution. A PDMS microfluidic chip was fabricated by a soft lithography process with its height $h = 50 \mu\text{m}$ and width $w = 150 \mu\text{m}$. It was then irreversibly bonded to the substrate by oxygen plasma bonding. For in-droplet sample washing and enrichment, alternating water-in-oil droplets were produced at a double T-junction (Fig. 1(b)). Fluorocarbon oil (NovecTM 7500, 3M) and heavy water (deuterium oxide, Sigma-Aldrich) were used as continuous and disperse phases, respectively. Two types of the droplets were alternately generated: one (A-type) with $6 \mu\text{m}$ polystyrene (PS) particles and the other (B-type) dyed with erioglaucine disodium salt (Sigma-Aldrich).

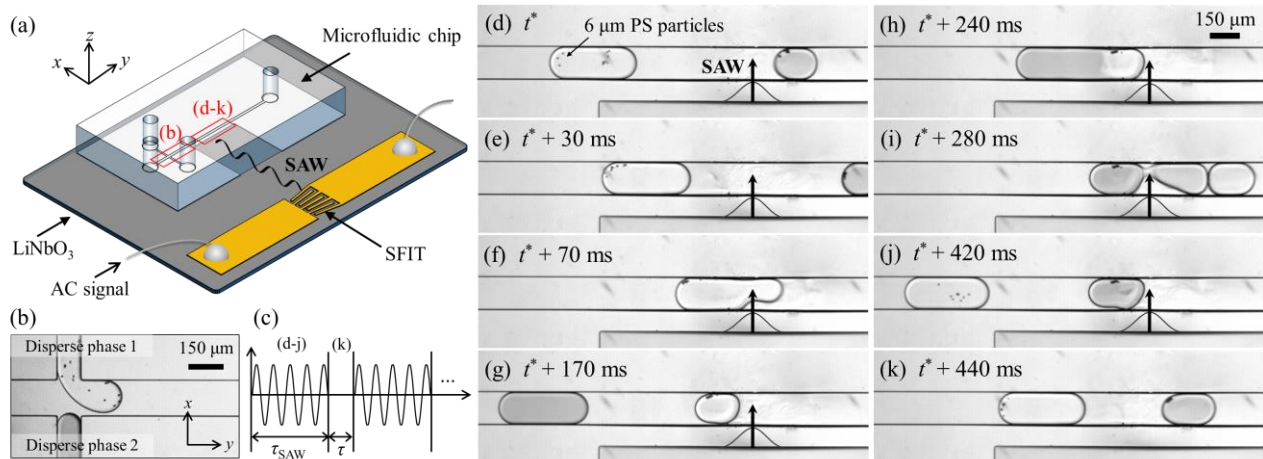


Figure 1: (a) Acousto-microfluidic platform for in-droplet microparticle washing and enrichment. (b) A double T-junction for alternating droplet production. (c) Periodic alternating current signal. (d-k) Sequential experimental images of the in-droplet sample washing operation.

In-droplet sample washing

For acoustic in-droplet sample washing, a 118 MHz AC signal (Fig. 1(c)) was periodically applied to the SFIT with $\tau_{\text{SAW}} = 440$ ms and $\tau = 10$ ms. Fig. 1(d-k) represents the sequential experimental images. As the plug-type droplets travelled in the microchannel, they experienced localized TSAWs and resultant ARF due to the acoustic impedance contrast between the continuous and disperse phases. The scattering component of ARF (F_{ts}) in the direction of the TSAW propagation was attributed to the droplet interface distortion, leading to acoustic droplet splitting (Fig. 1(e-g)). The gradient component of ARF in the perpendicular direction of the TSAW propagation captured a certain portion of the droplet while allowing the other portion of the droplet to pass the acoustic field-effective region. The volume of the captured droplet was decided by a force balance between the gradient component (F_{tg}) of ARF and the drag force (F_{d}) of the captured droplet, as reported in our previous study [4].

When 6 μm PS particles were exposed to the 118 MHz acoustic field, the Helmholtz number (κ) was approximately 1.5. Consequently, the suspended particles in the A-type droplets were concentrated in the captured droplet due to TSAW-based ARF acting on the particles. As the B-type droplet approached the captured A-type droplet, the two droplets were merged (Fig. 1(h)). Then, ARF-based droplet splitting occurred, and only a certain portion of the merged droplet, as well as the suspended particles, was captured by F_{tg} (Fig. 1(i-j)). The captured B-type droplet was then released during τ of the AC signal (Fig. 1(k)). As a result, the particles were washed with its medium exchanged from A-type to B-type droplets.

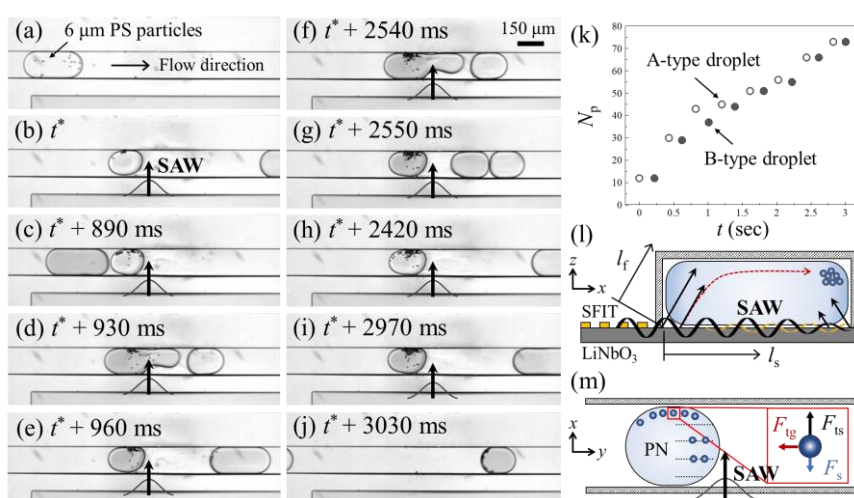


Figure 2: (a-j) Sequential experimental images for acoustic in-droplet sample enrichment. (k) The number of the microparticles within the captured droplet along with time. (l) A cross-sectional schematic of the acousto-microfluidic chip. (m) A top-view schematic of the acousto-microfluidic chip.

In-droplet sample enrichment

The ability of the proposed acoustic in-droplet sample washing method can be extended by modulating τ_{SAW} to in-droplet sample enrichment (Fig. 2(a-j)). With an increased $\tau_{\text{SAW}} = 3000$ ms, the particle population within the droplet was increased by eight-fold (Fig. 2(k)) while washing the sample into the B-type droplet. Under the acoustic field, the particles suspended in the droplet were pushed and thus concentrated in the periphery closed to the opposite wall. The acoustic wave attenuation length on the substrate ($l_s \cong 414$ μm) and in the fluid ($l_f \cong 4414$ μm) were much longer than the microchannel width ($w = 150$ μm) and height ($h = 50$ μm), respectively (Fig. 2(l)). Thus, standing SAWs (SSAWs) were formed within the fluid. However, since $\kappa > 1$, TSAW-based ARF (F_{tg} & F_{ts}) was dominant over ARF induced by SSAWs (F_{s}) (Fig. 2(m)). As a consequence, most of the PS particles were concentrated in the periphery of the droplet under the influence of TSAW-based ARF, while a few particles were trapped in the pressure nodes formed by SSAW-based ARF.

Conclusion

We have developed an acoustic in-droplet sample washing and enrichment method based on ARF-based droplet splitting and in-droplet microparticle concentration, which can provide a new route for in-droplet sample preparation in biomedical and biochemical analyses. We look forward to presenting in more detail at *Acoustofluidics 2018*.

Acknowledgment

This work was supported by the National Research Foundation of Korea (NRF) grant (No. 2018001483) and the Global Ph.D. Fellowship Program funded by the Korea government (MSIT), the KUSTAR-KAIST Institute, and the Korea Polar Research Institute (KOPRI).

References

- [1] A.H.C. Ng, U. Uddayasankar, and A.R. Wheeler, *Anal Bioanal Chem* **397**, 991-1007 (2010).
- [2] A. Hansen, Q. Yi, and J.P. Acker, *Transfusion*, **58**, 1772-1779 (2013).
- [3] H. Lee, L. Xu, and K.W. Oh, *Biomicrofluidics*, **8**, 044113 (2014).
- [4] J.H. Jung, G. Destgeer, B.H. Ha, J. Park, and H.J. Sung, *Lab Chip*, **16**, 3235-3243 (2016).



Single-Cell Acoustic Force Spectroscopy (scAFS): Resolving kinetics and strength of T-cell adhesion to a functionalized surface

Douwe Kamsma^{1,2,5}, Pascal Bochet^{3,4}, Felix Oswald⁵, Nander Ablas^{1,2,5}, Sophie Goyard³, Gijs J L Wuite^{1,2}, Erwin J G Peterman^{1,2}, Thierry Rose³.

¹Department of Physics and Astronomy, Vrije Universiteit Amsterdam, Amsterdam, The Netherlands.

²LaserLaB Amsterdam, Vrije Universiteit Amsterdam, Amsterdam, The Netherlands.

³Institut Pasteur, Center for Innovation and Technological Research, Networks & Signaling research group, Paris, France.

⁴CNRS UMR3691, Dynamique Cellulaire Physiologique Pathologique, Paris, France.

⁵LUMICKS b.v., Amsterdam, the Netherlands.

E-mail: d.kamsma@lumicks.com

Introduction

Assessing strength and kinetics of molecular interactions of cells with the extracellular matrix is fundamental to understand cell-adhesion processes. Given the relevance of these processes, there is a strong need for physical methods to quantitatively assess the mechanism of cell adhesion at the single-cell level, allowing discrimination of cells with different behaviors. Here we introduce single-cell Acoustic Force Spectroscopy (scAFS), an approach that makes use of bulk acoustic waves to exert controlled forces, up to 1 nN, to hundreds of individual cells in parallel. We demonstrate the potential of scAFS by measuring adhesion forces and kinetics of CD4+ T-lymphocytes (CD4) to a functionalized surface.

Manipulating cells with acoustic forces

CD4 cells are injected into the functionalized AFS chamber [1]. When a standing bulk acoustic wave is generated in the flow chamber, unbound cells move towards the nodal plane. Cells are live imaged using a standard inverted microscope and on the basis of their diffraction patterns the position of the cell position can be determined in 3 dimensions, with quadrant interpolation [2] and a look-up table [3]. A tracking accuracy of 2.0 nm in x and y, and 72 nm in z can be achieved.

Following the binding kinetics of CD4

We typically track several hundreds of cells simultaneously in three dimensions. By following the cell position over time, we could monitor the binding state of each cell. We found that cells can be classified in bound, binding and unbound states by monitoring the x and y position over time.

Measuring the acoustic force acting on the cells

When enough acoustic force is applied, the bonds between the bound cell and the functionalized surface can be broken. To determine the force applied when the CD4 ruptures from the functionalized surfaces, a calibration is required. To this end, we measured the Stokes' drag force from the upward velocity (in the z direction) of the CD4 when pushed towards the acoustic nodal plane. In order to measure the adhesion strengths of CD4 to the functionalized surface, we applied a voltage ramp and determined the rupture force of a large population of CD4 cells.

Conclusions

scAFS is a novel method that can be used to obtain insight in the cell adhesion process. We demonstrate that scAFS can be used to study the adhesion process of hundreds of cells in parallel in real time using well-controlled forces. Given, the relative simplicity and compactness of the system allows straightforward integration in advanced fluorescence microscopes. Taken together, this illustrates that acoustic forces can be applied directly to cells in order to quantitatively assess their interactions with their environment, opening up a wide range of potential applications in research and the clinic. We are looking forward to presenting these results for the international acoustofluidics community at *Acoustofluidics 2018* at sunny Lille, Universite de Lille, Lille, France on 29–31 August 2018.

References

- [1] D. Kamsma, R. Creyghton, G. Sitters, G. J. L. Wuite, and E. J. G. Peterman, "Tuning the Music: Acoustic Force Spectroscopy (AFS) 2.0," *Methods*, vol. 105, pp. 26–33, Aug. 2016.
- [2] M. T. J. van Loenhout, J. W. J. Kerssemakers, I. De Vlaminck, and C. Dekker, "Non-Bias-Limited Tracking of Spherical Particles, Enabling Nanometer Resolution at Low Magnification," *Biophys. J.*, vol. 102, no. 10, pp.

2362–2371, May 2012.

- [3] G. Sitters, D. Kamsma, G. Thalhammer, M. Ritsch-Marte, E. J. G. Peterman, and G. J. L. Wuite, “Acoustic force spectroscopy,” *Nat. Methods*, vol. 12, no. 1, pp. 47–50, Nov. 2014.

Investigation of Motile Algae Cells as Active Probes for Measurement of Acoustic Microfluidic Device Performance

Minji Kim¹, Emma Huff², Yicheng Zhao¹, Mathieu Bottier^{1,3}, Susan K. Dutcher³, Philip V. Bayly¹, and J. Mark Meacham¹

¹Department of Mechanical Engineering & Materials Science, Washington University in St. Louis, St. Louis, Missouri, USA, E-mail: meachamjm@wustl.edu

²Department of Biomedical Engineering, Washington University in St. Louis, St. Louis, Missouri, USA

³Department of Genetics, Washington University School of Medicine in St. Louis, St. Louis, Missouri, USA

Introduction

Accurate determination of the pressure field is critical to design and optimization of acoustic microfluidic devices; however, extant computational modeling and experimental methods that use passive microparticles do not adequately capture the pressure distributions in intricate chamber geometries. Here, we explore the feasibility of using calibrated, swimming microorganisms as active probes to assess the performance of complex device architectures. Two related approaches are described. In the first, an acoustic trap enables rapid measurement of swimming capability for a population of motile algae cells. In the second, these cells are used to investigate the pressure distribution within a fluid-filled chamber driven at resonance.

Characterization of the swimming behavior of a population of motile microorganisms

Use of motile cells to probe the pressure field within a device necessitates quantification of the inherent forces generated by the swimming cells. Conventional analyses involve capturing cell trajectories with a high-speed camera and using particle tracking software to analyze the swimming dynamics of individual cells. Individual-based characterization of a representative population is tedious, requiring substantial time and effort to reach acceptable statistical significance. To address this challenge, we introduce a rapid, population-based method that minimizes the statistical variation associated with individual measurements.

Our choice of microorganism is *Chlamydomonas reinhardtii* (CR), a motile unicellular alga with a $\sim 10\text{-}\mu\text{m}$ diameter body (Fig. 1A). A circular acoustic trapping chamber etched in glass is seeded with 4–5 million wild type (wt) CR cells per mL. The unimpeded random motion of the cells creates a uniform density. The glass microchip is actuated by a 0.75-mm thick bulk piezoelectric transducer (APC 880, American Piezo Ceramics). When the transducer is driven at a chamber resonant frequency, a standing wave field instantaneously develops, and suspended cells become confined within the nearest pressure node. An experimentally-determined resonant frequency of 1.15 MHz yields a cell aggregate of 48 ± 8 cells at the center of the chamber. Once the cell aggregate forms, the transducer signal is turned off, and the release of cells is recorded for ~ 1 s (Fig. 1B,C).

CR swimming can be described by a random walk model, i.e., cells proceed in a fixed direction for about one second before reorientation [1]. In the ballistic regime (the initial period before cells make the first turn), the mean square displacement (MSD) of an individual cell is expressed as $\text{MSD} \sim U^2 t^2$ where U is the velocity of cells and t is time [2]. Repeated analysis of individual free-swimming cell trajectories enables determination of the average behavior of a cell type. Conversely, for release from an acoustic pressure well, the ratio of polar

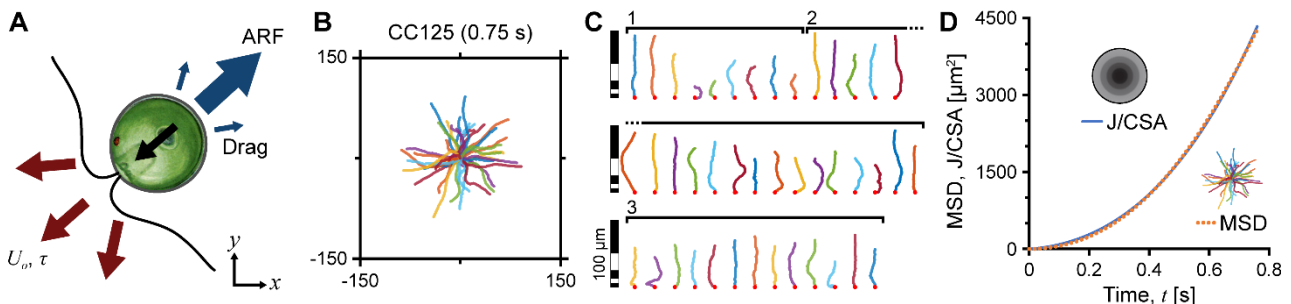


FIG. 1. use of an acoustic trap to characterize swimming of *Chlamydomonas reinhardtii* (CR): (a) balance of forces on an acoustically-confined CR cell, (b) trajectories of 42 wild type CR (CC125) over 0.75 s after release from an acoustic trap (axes in μm), (c) individual trajectories for the three experimental populations comprising panel b (total scale bar lengths are 100 μm), and (d) assessment of swimming using mean square displacement (MSD) and polar moment of inertia divided by total cell area (J/CSA) versus time t .

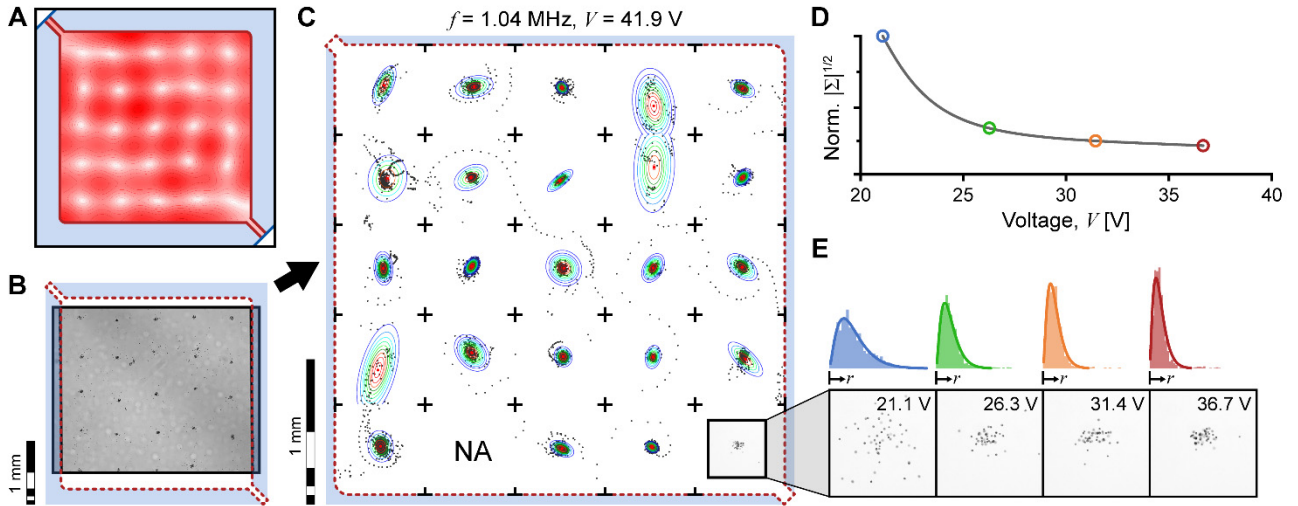


FIG. 2. use of swimming CR cells for determination of a pressure map: (a) computational model-predicted chamber resonance ($f = 1.02$ MHz), (b,c) bright-field image and bivariate Gaussian distributions for confined CR agglomerates ($f = 1.04$ MHz; $V = 41.9$ V; scale bars are 1 mm), (d) spread metric versus drive voltage for a representative well-behaved (circular) well, and (e) gamma distributions for confined cells under increasing drive voltage (same conditions as in d).

moment of inertia J and the cellular area CSA (evaluated using ImageJ) provides an equivalent measure of swimming performance for a large population in seconds ($J/CSA \sim MSD$, see Fig. 1D). The velocity of wt CR cells is then calculated to be $93 \pm 10 \mu\text{m/s}$, which is almost identical to the velocity of $90 \pm 24 \mu\text{m/s}$ obtained by tracking individual cell trajectories.

Correlation of CR cell spread metric and an observed pressure distribution

The motion of CR cells within an acoustic trap is constrained by the primary acoustic radiation force (ARF), which is a function of the local pressure field. Indeed, the performance of most acoustofluidic devices (e.g., for targeted cell and particle separation/enrichment or fluid pumping) is correlated with the pressure developed in such devices [3]. Analytical approaches, multi-domain computational models, and existing experimental methods are either difficult to implement or provide only limited information regarding the pressure distribution throughout an intricate chamber geometry [4]. Unlike passive particles (e.g., calibration beads) that reach terminal distributions at nodal locations, CR cells probe their environment and naturally swim against an imposed force field to fill complicated shapes and more completely describe the pressure field. Steady state distributions of swimming cells can be related to the field shape and strength. The balance of propulsive force (from earlier trap/release experiments), ARF, and drag on CR cells allows ARF (and thus pressure) to be accurately mapped. Further, CR cells continuously respond to their environment, enabling real-time monitoring while sweeping operating parameters (e.g., frequency and/or drive voltage).

Resonant frequencies of operation for a square, fluid-filled chamber are identified using the acoustics module of COMSOL Multiphysics. Fig. 2A is the predicted 5×5 well pressure field driven at a frequency $f = 1.02$ MHz. The device is modeled in three-dimensions and includes transducer, glass, and fluid domains to accurately describe the behavior of the real system. Pressure maxima (antinodes) and minima (nodes) are indicated by red and white regions of the contour plot, respectively. When a device assembly is actuated at a chamber resonance, cells are drawn to and confined within regions near these nodes (see Fig. 2B, brightfield image of cell aggregates held in a 5×5 array; $f = 1.04$ MHz; drive voltage $V = 41.9$ V). Corresponding bivariate Gaussian fits to each group of cells in the array exhibit similar structure to the wells of the model (Fig. 2C). A single, well-behaved (i.e., circular) nodal location is then used for further analysis of the response to varying drive voltage. The relationship between a spread metric (normalized determinant of the covariance) and transducer drive voltage suggests that CR cells explore a larger area in a relatively weak trap (~ 21 V) while reaching maximum confinement in a strong trap (~ 37 V). Results demonstrate the possibility to correlate the spread of motile microorganisms to the characteristics of complicated pressure fields.

Conclusion

Accurate experimental measurement of the pressure field within complex acoustic microfluidic devices is a significant challenge. Fast swimming cells like CR naturally fill their surroundings and maintain a spatial distribution during actuation. Application of CR cells as living, active probes to accurately map the acoustic pressure will lead to a better understanding of acoustic microfluidic device behavior.

References

- [1] M. Garcia, S. Berti, P. Peyla, and S. Rafai. Phys. Rev. E **83**, 035301 (2011).
- [2] S. Rafai, L. Jibuti, and P. Peyla. Phys. Rev. Lett. **104**, 098102 (2010).
- [3] A. Neild, S. Oberti, and J. Dual. Sens. Actuators B Chem. **121**, 452 (2007).
- [4] N. Nama, R. Barnkob, Z.M. Mao, C.J. Kahler, F. Costanzo, and T.J. Huang. Lab Chip **15**, 2700 (2015).



Biogenic Nanostructures and Genetic Elements for Acoustic Trapping and Manipulation

Di Wu¹, Diego Baresch², Dina Malounda³, Paulene Abundo³, David Maresca³, and Mikhail G. Shapiro^{3*}

¹Division of Engineering and Applied Sciences, California Institute of Technology, Pasadena, United States
E-mail: dwwu@caltech.edu, mikhail@caltech.edu URL: <http://shapirolab.caltech.edu/>

²Imperial College London, United Kingdom,

³Division of Chemistry and Chemical Engineering, California Institute of Technology, Pasadena, United States

Introduction

The ability to precisely position and apply force to biomolecules and engineered cells in microfluidic devices, inside mammalian organisms or within biologically-inspired living materials would have a large impact in multiple areas of medicine. Acoustic radiation force (ARF) provides a powerful means to effectuate such ability noninvasively, but most biomolecules and cells lack the appropriate acoustic properties to either experience strong ARF or distinguish themselves from their neighbors. Here, we describe a class of biomolecules and genetic elements that overcome these limitations, enabling acoustic manipulation. These biological constructs are based on gas vesicles (GVs), which are gas-filled protein nanostructures naturally found in cyanobacteria for buoyancy regulation. They have recently been repurposed as genetically engineered and encoded reporters for noninvasive imaging of cellular function.^{1,2} Here we report that, in addition to their uses in imaging, GV and their encoding genes can be used in ARF applications. We show that, due to their differential density and compressibility relative to aqueous media, GV experience the strongest reported ARF acting directly on a nanoparticle, to our knowledge. Furthermore, we demonstrate that the expression of GV genes in bacteria makes it possible to manipulate these cells acoustically in a selective manner. This work opens the door to potential applications in molecular and cellular navigation, patterning, and actuation in a broad range of *in vitro* and *in vivo* contexts.

Acoustic radiation force on purified GV

We hypothesized that GV would experience strong ARF due to their unique composition. These nanostructures, which self-assemble inside cells according to a genetic program, comprise a ~ 200 nm air interior surrounded by a 2 nm-thick protein shell. (Fig. 1a) This mostly gaseous composition gives rise to a large contrast in density and compressibility relative to aqueous fluid. To quantify the ARF acting on GV, we developed an acoustic device that facilitates simultaneous ultrasound insonation and fluorescence imaging (Fig. 1bi-ii). The ARF acting on the particles can be quantified from tracking single particle trajectories and applying a force balance with viscous drag force (Fig. 1biii). We tested intact and pressure-collapsed GV (Fig. 1c), as well as polystyrene control particles (PS), which have similar hydrodynamic radii as GV particles but should experience negligible ARF (Fig. 1d). During ultrasound insonation, intact GV particles are observed to move towards a trap location, while neither collapsed GV nor PS particles are moved by the sound wave (Fig. 1e). Importantly, the lack of motion of PS particles indicates a lack of streaming effects, and we can attribute the movement of intact GV to solely to direct ARF. A standing wave is generated inside the acoustic chamber, as confirmed by pressure measurements using a fiber optic hydrophone. Thus, we fitted the particle trajectory assuming a sinusoidal velocity profile³, and obtained an agreeable fit (Fig. 1e). We extended this analysis for all particles, and extracted the amplitude of their maximal velocity (Fig. 1f). We show that intact GV experience significantly higher trapping velocity compared to collapsed GV ($P < 0.0001$) and PS particles ($P < 0.0001$). For each particle, we additionally tracked their Brownian motion before insonation, and obtained their viscous drag characteristics. Finally, we estimated the ARF acting on a single intact GV particle within an acoustic gradient.

ARF manipulation with genetic specificity

If ARF manipulation could be coupled with genetic engineering, this could enable the use of acoustofluidics in a wide range of synthetic biology and cellular therapy applications. It has recently been demonstrated that acoustic reporter genes (ARG), when introduced to a bacterial host such as *E. coli*, can enable the expression of GV inside the bacteria, and can serve as the first reporter genes for ultrasound imaging². We hypothesized that the expression of ARG would allow the bacteria host to experience a unique ARF, due to changes to their density and compressibility. To test this, we constructed a similar acoustic device as before, but modified to accommodate multiple trapping bands at a high acoustic frequency (Fig. 2a). Bacteria expressing ARGs are compared to wildtype bacteria, and bacteria that have expressed GV but have undergone collapse (Fig 2b).

When low intensity acoustic trap is applied, we observe the formation of bacterial bands only with the cells expressing ARG, and not in the control cells (Fig. 2c). This demonstrates that ARG expression amplifies the ARF on cells, thus enabling acoustic manipulation with genetic specificity. Furthermore, when high intensity acoustic trap is applied to a mixed population of cells containing ARG bacteria and wildtype bacteria, the two populations form trap bands that are mutually non-overlapping (Fig. 2di). This suggests that ARG expression inverts the direction of ARF on the cells (i.e. from nodes to antinodes), providing additional genetic specificity for acoustic manipulation. In fact, the ARF acting on ARG-expressing cells is expected to be unique from all other biological cells, which exhibit similar acoustic properties as wildtype bacteria. We further show that the acoustic properties of ARG cells can be restored to normal by collapsing the GVs inside the cells, making them acoustically indistinguishable from wildtype bacteria (Fig. 2dii).

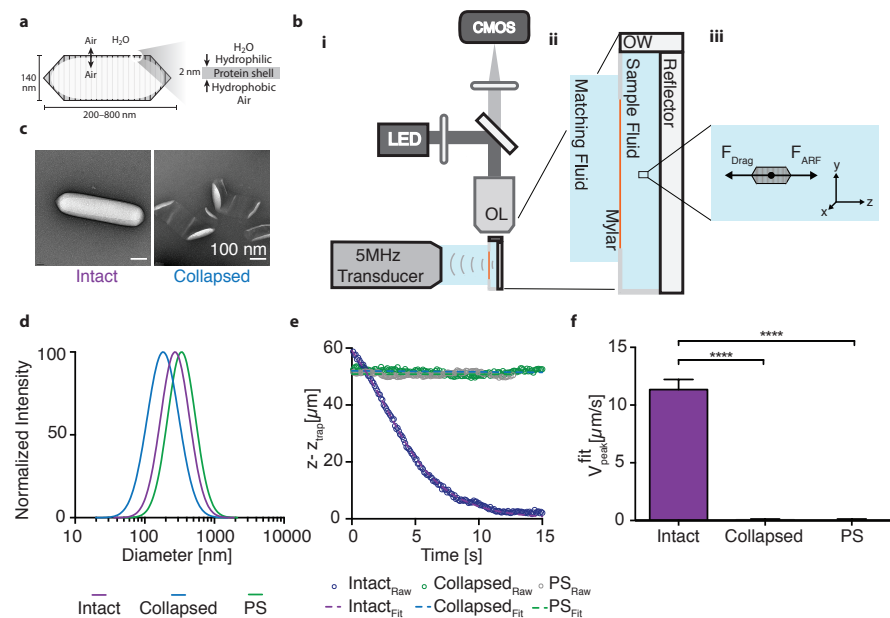


Figure 1: (a) Illustration of a gas vesicle. (b,i) The acoustic device integrates an ultrasound transducer, a sample chamber, and a fluorescence microscope with an objective lens (OL), a digital camera (CMOS) and a LED light source. (b,ii) The sample fluid is enclosed between an acoustic window made from Mylar film and an acoustic reflector made from glass. The sample chamber is submerged in an acoustic matching fluid, and is sealed from the top by a glass slide, creating an optical window (OW). (b,iii) Fluorescently labeled particles are imaged during ultrasound insonation, and acoustic radiation force is obtained from the force balance with viscous drag force. (c) TEM images of intact (left) and collapsed (right) GVs. (d) DLS size measurements of intact and collapsed GVs, and polystyrene beads (PS). (e) Measured and fitted particle trajectory during ultrasound insonation, fitted assuming a sinusoidal velocity profile. (f) Fitted peak velocity during ultrasound application for intact (N = 67) and collapsed (N = 54) GVs, and Polystyrene beads (N = 65). (****, P<0.0001, unpaired t-test with Welch's correction).

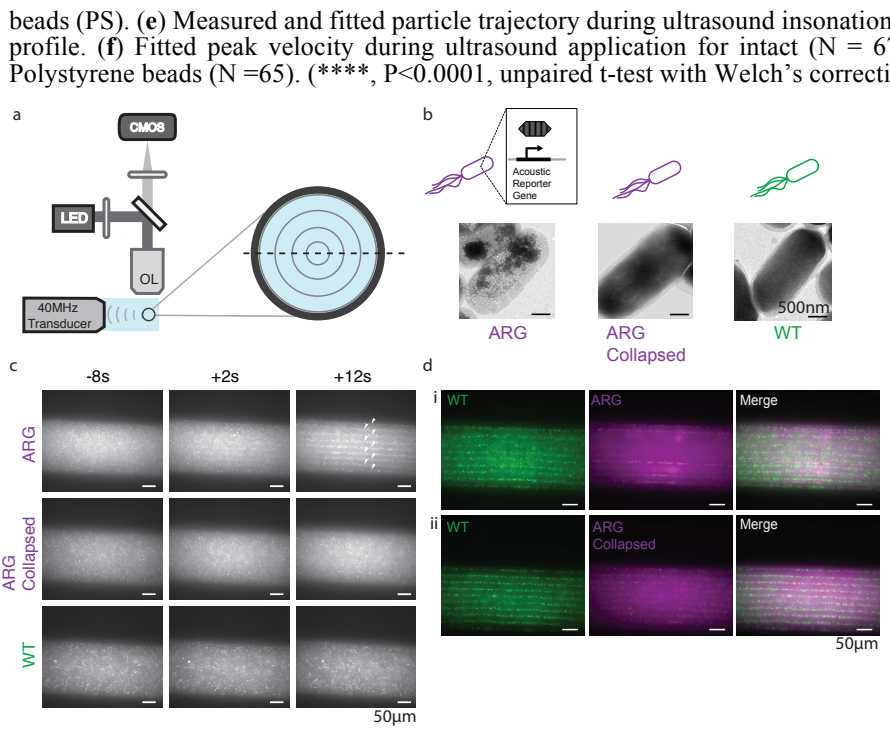


Figure 2: (a) The acoustic device integrates an ultrasound transducer, a sample tube, and a fluorescence microscope. Dashed line indicates the optical focal plane. (b) TEM images of *E.coli* expressing the acoustic reporter gene (left), after collapse (middle), and wildtype *E.coli* (right). (c) Fluorescence snapshots of fluorescently labeled *E.coli* taken at times relative to the start of low intensity acoustic trap. White arrows indicate locations of acoustic trap bands. (d) Fluorescence images of mixed populations of *E.coli*, during high intensity acoustic trap. (d,i) The mixture of wildtype bacteria and bacteria expressing ARG. (d,ii) the mixture of wildtype bacteria and bacteria that have expressed ARG and have undergone collapse.

Conclusion

Our study establishes GVs as a unique class of biologically constructed nanoparticles for ARF applications. Due to their density and compressibility relative to aqueous fluid, GVs enable ARF manipulation at unprecedented magnitudes and size-scales. We further establish ARG as the first genetic elements to couple to ARF manipulation. We believe this work could have broad impact in multiple areas of basic research and medicine, including targeted biomolecular and bacterial therapy, tissue engineering, high throughput screening and diagnostics, and noninvasive control of cellular function.

References

1. Shapiro, M. G. *et al.* Biogenic gas nanostructures as ultrasonic molecular reporters. *Nat. Nanotechnol.* **9**, 311–316 (2014).
2. Bourdeau, R. W. *et al.* Acoustic reporter genes for noninvasive imaging of microorganisms in mammalian hosts. *Nature* **553**, 86–90 (2018).
3. Bruus, H. Acoustofluidics 7: The acoustic radiation force on small particles. *Lab. Chip* **12**, 1014–1021 (2012).

Classification of acoustic streaming in three dimensions

Jacob S. Bach and Henrik Bruus

Department of Physics, Technical University of Denmark, Kongens Lyngby, Denmark
E-mail: jasoba@fysik.dtu.dk, URL: <http://fysik.dtu.dk/microfluidics>

Introduction

Acoustic streaming occurs in experiments in many different and complicated patterns. Based on our recently developed generalized effective model for acoustic fields and streaming [1], we have been able to make steps towards a classification of acoustic streaming in three dimensions. For a fluid with dynamic viscosity η_0 , acoustic damping coefficient Γ , acoustic angular frequency ω , and sound speed c_0 , the acoustic streaming velocity \mathbf{v}_2 and the associated excess pressure p_2 are in general described as a Stokes flow with a slip-velocity at the walls,

$$0 = \nabla \cdot \mathbf{v}_2, \quad \mathbf{0} = -\nabla p_2 + \eta_0 \nabla^2 \mathbf{v}_2 + \mathbf{f}_{\text{str}}, \quad \mathbf{v}_2 = \mathbf{v}_2^{\text{bc}} \text{ at walls}, \quad \mathbf{f}_{\text{str}} = \frac{\Gamma \omega}{c_0^2} \langle \mathbf{S}_{\text{ac}} \rangle. \quad (1)$$

Here, the force density \mathbf{f}_{str} expressed through the time-averaged acoustic intensity $\langle \mathbf{S}_{\text{ac}} \rangle = \langle p_1 \mathbf{v}_1 \rangle$ is responsible for *bulk-driven* streaming, while the slip-velocity \mathbf{v}_2^{bc} drives *boundary-driven* streaming. In micro-systems of size comparable to the acoustic wavelength, the importance of bulk-driven streaming is often overlooked, and only boundary-driven streaming is considered. Here, we present physical mechanisms that lead to bulk-driven streaming, which appears as flow rolls parallel to the actuator surface, and which is much larger than the boundary-driven streaming. One central mechanism is the rotation of the acoustic motion as measured by the acoustic angular momentum $\mathcal{L} = \langle \mathbf{r}_1 \times (\rho_0 \mathbf{v}_1) \rangle$ with mass density ρ_0 , acoustic velocity \mathbf{v}_1 and displacement $\mathbf{r}_1 = \frac{i}{\omega} \mathbf{v}_1$.

Bulk-driven acoustic streaming in the plane of the actuator

From our theory [1], we have found that bulk-driven streaming is important when \mathcal{L} is large. This is possible for almost any actuation, if the microchannel deviates slightly from perfect symmetry. Based on previous experimental observations [2], we have studied the acoustofluidic chamber shown in Fig. 1(a) of height $H = 200 \mu\text{m}$ and with a nearly quadratic bottom surface of aspect ratio $\Delta = \frac{W_y}{W_x} \approx 1$, where $W_x = W_y = 2000 \mu\text{m}$ for $\Delta = 1$. For different Δ , we actuate at the bottom xy surface in the perpendicular z direction with frequency $f = 0.7474 \text{ MHz}$ and excite pressure modes both in the x - and y -direction. If these two modes oscillate out of phase, a large angular momentum is introduced and \mathbf{f}_{str} in Eq. (1) will be important for the streaming [3]. As shown in Fig. 1(a), this effect drives mm/s-streaming in the actuator plane for pressure amplitudes of 1 MPa. In contrast to this case of parallel acoustic fields, we have also investigated perpendicular acoustic fields as shown in Fig. 1(b). Here, also the boundary-condition \mathbf{v}_2^{bc} rotates in the actuator plane but much slower

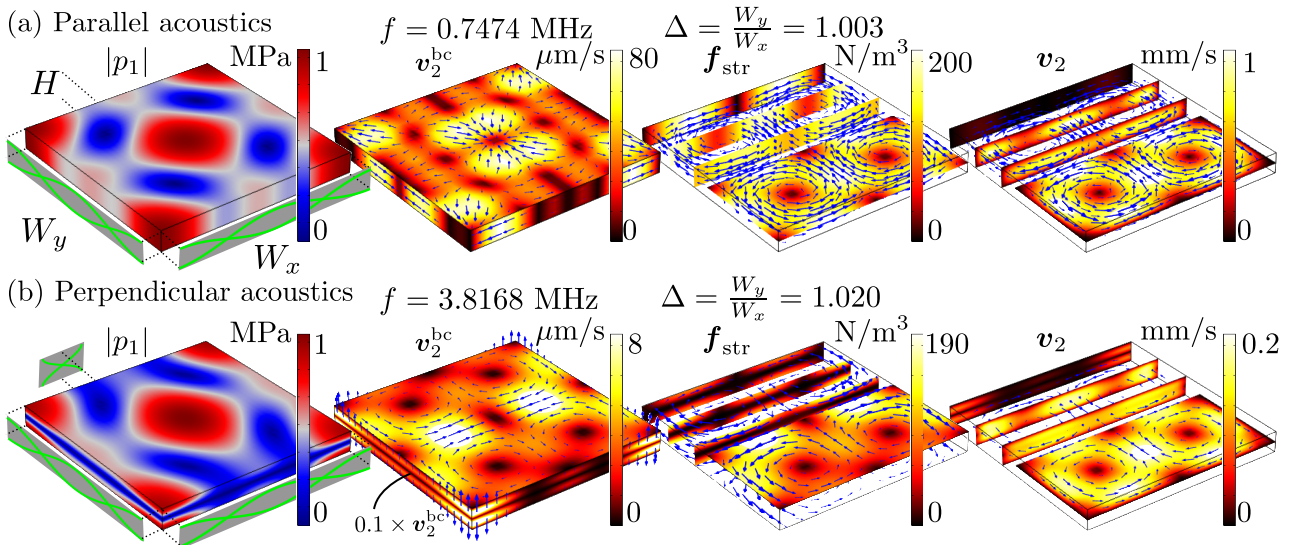


Figure 1: The pressure amplitude $|p_1|$ and the driving mechanisms \mathbf{v}_2^{bc} and \mathbf{f}_{str} of boundary- and bulk-driven streaming, together with the resulting streaming \mathbf{v}_2 for (a) parallel and (b) perpendicular acoustics.

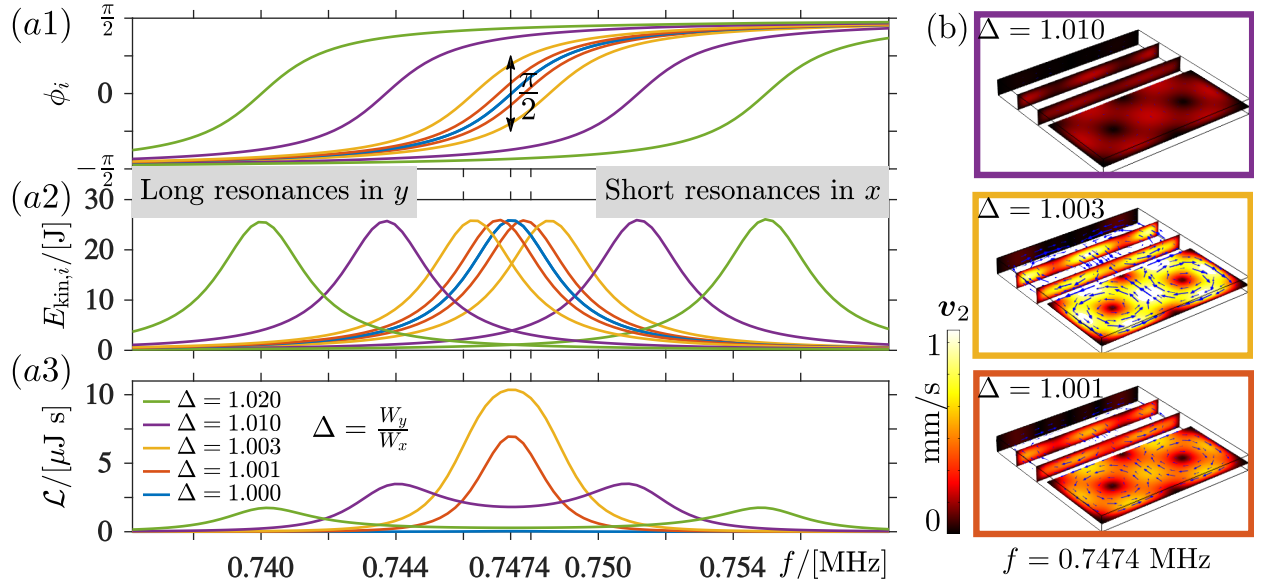


Figure 2: Parametric study in frequency f and aspect ratio Δ for the setup in Fig. 1(a). (a1) and (a2) Space-averaged phase ϕ_i and kinetic energy $E_{\text{kin},i}$ of y - (left lines) and x -resonances (right lines). (a3) Space-averaged angular momentum \mathcal{L} . (b) The acoustic streaming v_2 resulting from different aspect ratios Δ .

than the streaming produced by \mathbf{f}_{str} and, notably in the opposite direction. In Fig. 2 we show how the induced acoustic angular momentum is due to resonances out of phase. As the frequency is swept through a single resonance mode, the phase of this mode changes by π . Maximum angular momentum is obtained, when a single frequency excites two perpendicular modes having a relative phase difference of $\pi/2$. This occurs in Fig. 2 for $\Delta = 1.003$ (yellow lines). As shown in Fig. 2(b) this aspect ratio indeed gives the largest actuator-plane streaming as also shown in Fig. 1(a). In conclusion, rotating acoustics may be the governing mechanism of acoustic streaming in the actuator plane. We believe that a similar mechanism govern actuator-plane streaming in half-open capillaries which is currently investigated.

Boundary-driven streaming

The streaming slip velocity \mathbf{v}_2^{bc} in Eq. (1) is generally complicated but simplifications can be made in the important case of fluid resonance, where the fluid obtains much larger velocities than the surrounding wall. In this case, we distinguish between parallel and perpendicular acoustics denoting the main direction of velocity variations, and in these limits we find the simplified slip velocities,

$$\mathbf{v}_{2\parallel}^{\text{bc}} = \frac{1}{8\omega\rho_0} \nabla_{\parallel} (2\kappa_0 |p_1|^2 - \rho_0 |\mathbf{v}_{1\parallel}|^2) + \frac{\kappa_0}{2} \langle \mathbf{S}_{\text{ac}\parallel} \rangle \quad \text{parallel acoustics} \quad \nabla_{\parallel} \cdot \mathbf{v}_{1\parallel} \gg \partial_{\perp} v_{1\perp}, \quad (2a)$$

$$\mathbf{v}_{2\parallel}^{\text{bc}} = -\kappa_0 \langle \mathbf{S}_{\text{ac}\parallel} \rangle \quad \text{perpendicular acoustics} \quad \nabla_{\parallel} \cdot \mathbf{v}_{1\parallel} \ll \partial_{\perp} v_{1\perp}, \quad (2b)$$

with isentropic compressibility κ_0 . Fig. 1(a) exemplifies $\mathbf{v}_{2\parallel}^{\text{bc}}$ in the parallel limit, which is here dominated by the gradient-term in Eq. (2a), and therefore not rotating. Fig. 1(b) shows $\mathbf{v}_{2\parallel}^{\text{bc}}$ in the perpendicular limit, which here rotates opposite to $\mathbf{f}_{\text{str}} \propto \langle \mathbf{S}_{\text{ac}} \rangle$ as also predicted by Eq. (2b). Remarkably, the quantity $\langle \mathbf{S}_{\text{ac}\parallel} \rangle$ also plays an essential role for boundary-driven streaming. In general, a rotating $\mathbf{v}_{2\parallel}^{\text{bc}}$ in resonant devices is therefore accompanied by a rotating force density \mathbf{f}_{str} in the bulk and we emphasize, that the latter should not be overlooked as seen from Fig. 1.

Conclusion

We have presented a clarifying classification of the mechanisms leading to acoustic streaming, in particular relating to bulk- and surface driven streaming. Our goal is to systematically describe streaming classes based on the available resonance modes in both closed fluid chambers and open capillaries. We hope that our results will be helpful on the fundamental and applied level in creating insight and intuition for the complex phenomenon of acoustic streaming in microscale acoustofluidics.

References

- [1] J. S. Bach and H. Bruus, submitted (2018), ArXiv preprint arxiv.org/abs/1804.05802
- [2] S. M. Hagsäter, T. G. Jensen, H. Bruus and J. P. Kutter Lab Chip **7**, 1336-1344 (2007)
- [3] M. Antfolk, P.B. Muller, P. Augustsson, H. Bruus, and T. Laurell. Lab Chip **14**, 2791 (2014)

Ultrasound transmission through model liquid foams generated by microfluidics

Lorène Champougny¹, Juliette Pierre², Valentin Leroy³ and Marie-Caroline Jullien¹

¹Gulliver, CNRS, ESPCI Paris, PSL Research University, Paris, France

E-mail: lorene.champougny@espci.fr

²Institut Jean Le Rond d'Alembert, Université Pierre et Marie Curie, CNRS, Paris, France

³Laboratoire Matière et Systèmes Complexes, Université Paris-Diderot, CNRS, Paris, France

Introduction

While the acoustic properties of solid foams, which are frequently used for soundproofing purposes, have been abundantly characterized [1], sound propagation in liquid foams remains poorly understood. Recent studies have investigated the transmission of ultrasound through three-dimensional polydisperse liquid foams [2, 3]. However, further progress requires to investigate the acoustic response of better controlled foam structures. In this work, we study experimentally the transmission of ultrasounds through a single layer of monodisperse bubbles generated by microfluidic techniques. In such a material, we show that the acoustic wave undergoes a 'sieving' effect due to the liquid network, but that the sound velocity within the bubble monolayer is essentially sensitive to the gas phase.

Experimental setup and protocol

Building on the work of Pierre *et al.* [2], we implement a new experimental setup designed to study the transmission of air-born ultrasound (frequencies in the range 70 – 1000 kHz) through a single bubble layer. Gaussian shaped ultrasound pulses generated with broadband acoustic transducers (BATs) are propagated through bubble monolayers enclosed in a specifically designed cavity, as depicted in figure 1a.

The cavity being closed by flexible 1- μm -thick Mylar sheets, its thickness H can vary upon bubble injection and has to be measured independently using a laser telemetry setup. The monolayer itself is accurately characterized in terms of bubble size and liquid fraction, both of which are varied throughout the experiments (see figure 1c for an example of bubble monolayers with the same bubble size but varying liquid fractions).

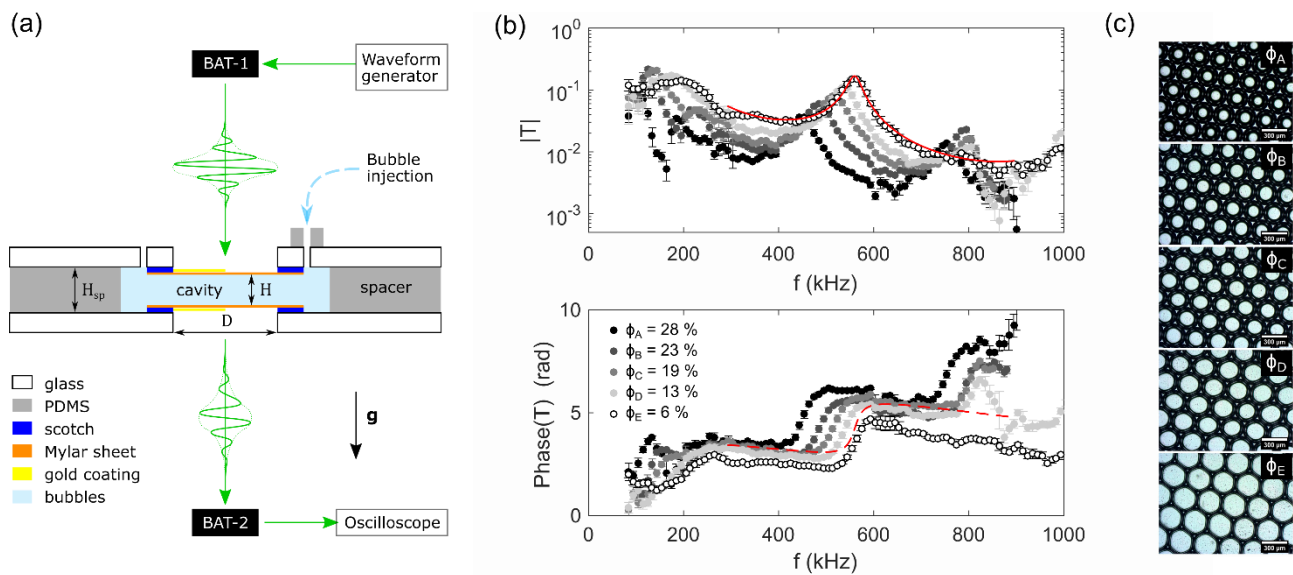


Figure 1: (a) Sketch of the simplified ultrasonic setup and microfluidic cell designed for ultrasonic transmission measurements through low acoustic impedance samples. The relative scales of the elements have been changed in order to ease reading. – (b) Modulus and phase of the acoustic transmission T as a function of the frequency f for a cavity filled with bubble monolayers of fixed hexagonal cell volume $V = 12$ nL and various liquid fractions ϕ (symbols). The solid red line is a fit using the five-layer model described below. – (c) Pictures of the corresponding monolayers.

Data analysis and discussion

The complex acoustic transmission T , which is essentially the Fourier transform of the pulse that has propagated through the sample, is obtained as a function of frequency f for each monolayer. As can be seen in figure 1b, the modulus and phase of the transmission T exhibit a clear resonant behavior, which is due to the cavity acting as a Fabry-Pérot resonator. We find that the frequency of the n^{th} resonance is consistent with the Fabry-Pérot resonance criterion $f_{\text{res},n} = n \times c/2H$, taking a sound velocity c equal to that in the gas phase alone, as shown in figure 2.

Building on that first approach, we compute the transmission through a five-layer system (outer medium / Mylar sheet / monolayer / Mylar sheet / outer medium), where the monolayer is assumed to have the density of the gas phase. The sound velocity and attenuation in the monolayer are determined by adjusting the experimental transmission curves (see figure 1b). In order to account for the heterogeneity of the monolayer (consisting in a network of high impedance ‘walls’ and low acoustic impedance ‘holes’) in the plane transverse to the wave vector, the sound velocity in the outer medium is also used as an adjustable parameter.

This ‘sieving’ parameter is found to scale convincingly with the surface ‘hole’ fraction in the monolayer, as expected from the literature on porous solids [4]. The sound velocity in the monolayer is again in good agreement with the one in the gas phase alone (see inset of figure 2) but the attenuation cannot be explained by thermal dissipation alone, hinting at additional dissipation mechanisms due to the presence of the bubbles, as suggested by Pierre *et al* [5].

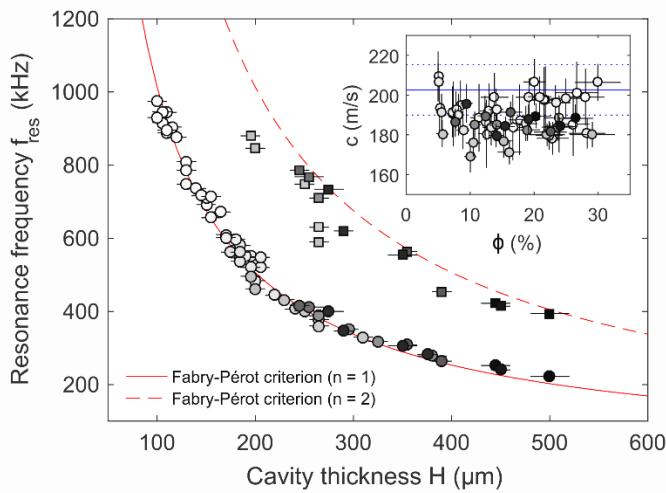


Figure 2: Main plot: frequencies of the first (circles) and second (squares) resonances in bubble monolayers as a function of the cavity thickness H . The solid and dashed lines show the Fabry-Pérot resonance criterion for $n = 1$ and 2 respectively, with a sound velocity $c = 203$ m/s corresponding to the gas phase alone. – Inset: sound velocity c in the cavity extracted from the fit of the transmission curves, as a function of the volume liquid fraction ϕ . The solid line shows the sound velocity in the gas phase alone. In both plots, the greyscale codes for the bubble volume V (the darker the symbol, the larger the bubble volume).

Conclusion

We implemented a new experimental setup to study the transmission of ultrasounds through single layers of monodisperse bubbles generated by microfluidics techniques. The fit of the experimental transmission data revealed that the sound velocity in the monolayer is insensitive to the monolayer structure, unlike the attenuation.

In the future, the study of bubble bilayers will likely show additional complexity, bearing the signature of the free liquid films separating the top and bottom bubbles. This discrete approach, allowing to isolate the signature of a single layer of free films in the acoustic response, will hopefully contribute to a better understanding of the dissipation in macroscopic liquid foams.

References

- [1] Attenborough, K., 1982. Acoustical characteristics of porous materials. *Physics Reports*, 82(3), pp. 179-227.
- [2] Pierre, J., Elias, F. & Leroy, V., 2013. A technique for measuring velocity and attenuation of ultrasound in liquid foams. *Ultrasonics*, Volume 53, pp. 622-629.
- [3] Pierre, J., Dollet, B. & Leroy, V., 2014. Resonant Acoustic Propagation and Negative Density in Liquid Foams. *Physical Review Letters*, 112(14).
- [4] Allard, J. and Atalla, N., 2009. *Propagation of sound in porous media: modelling sound absorbing materials 2e*. John Wiley & Sons
- [5] Pierre, J. and Gaulon, C. and Derec, C. and Elias, F. and Leroy, V., 2017. Investigating the origin of acoustic attenuation in liquid foams. *The European Physical Journal E*, Volume 40 (8).



Sliding and climbing drops excited by surface acoustic waves on a tilted plane

Adrien Bussonnière¹, Olivier Bou Matar² and Michaël Baudoin²

¹Institut de Physique de Rennes, UMR 6251 CNRS et Université Rennes 1, 35042 Rennes Cedex, France, E-mail: adrien.bussonniere@univ-rennes1.fr,

²Univ. Lille, CNRS, Centrale Lille, ISEN, Univ. Valenciennes, UMR 8520 - IEMN, International laboratory LIA/LICS, F-59000 Lille, France

Introduction

Surface acoustic waves (SAWs) are widely used to actuate droplets in digital microfluidic [1,2]. When submitted to a travelling SAW a sessile droplet undergoes complex dynamics coupling an inertio-capillary oscillation with a stick and slip translation in the wave propagation direction [3,4]. We recently explored the influence of gravity of this dynamic by comparing the motion of sessile and pendant drops [4]. We showed that gravity, although non-dominant at this length scale, strongly impacts the oscillation frequency and contact line mobility and pendant drops were significantly slowed down. In the present work, we experimentally investigated the competition between gravity and the SAW excitation when a drop moves on a tilted plane, with surface waves propagating upward. Under a low excitation drops undergo small oscillations able to intermittently overcome the contact angle hysteresis and the drop slips on the substrate. Therefore under such small vibrations the surface becomes slippery paving the way toward controllable slippery surfaces. At higher excitation, a reach variety of dynamics is revealed by varying the tilt angle.

Methods and materials

Rayleigh-type surface acoustic waves are generated on the surface of a 1.05 mm thick (Y-Cut 128 °) Lithium Niobate (LiNbO₃) piezoelectric substrate by interdigitated transducers (IDTs). The latter are fabricated by successively sputtering a titanium (Ti) layer (20 nm thick) and a gold (Au) layer (200 nm thick) on the substrate. The resonance frequency of such transducers is set by the width and spacing between interdigitated fingers according to the law $f_{saw} = \frac{c_s}{\lambda} = \frac{c_s}{4a}$ with f_{saw} the surface acoustic wave frequency, λ the wavelength, a the width and spacing and $c_s \approx 3484 \text{ m.s}^{-1}$ the Rayleigh wave speed in the z-direction. Here $a = 43.75 \mu\text{m}$ and the IDTs are powered with a 20 MHz signal generated by a high frequency generator (IFR 2023A) and amplified by Empower RF 1037 amplifier. The normal surface displacement is measured with a Mach-Zender interferometer.

The substrate is made hydrophobic using a self-assembled monolayer (SAM) of OTS (octadecyltrichlorosilane) leading to a static contact angle of 98° and contact angle hysteresis of 15°. The substrate is mounted on a tilted plane with controllable inclination α (ranging from 10° to 40°) shown in figure 1 a). Drops with calibrated volume (5, 10 and 15 μl) are deposited using a micropipette. Droplet dynamics are recorded with a high speed camera (Photron SA3) and analysed using ImageJ and Matlab software.

The variety of dynamics is analysed through the prism of two dimensionless numbers, the Bond and acoustic Weber number. The latter compares the acoustic radiation pressure to the capillary effects at the drop surface. As water-air interface behaves as acoustic mirror the acoustic Weber number can be calculated using $We_{ac} = \frac{\rho_l A_n^2 \omega_{ac}^2 R}{\sigma \cos^2 \theta_R}$ where ρ_l the liquid density, A_n the surface normal displacement, $\omega_{ac} = 2\pi f_{saw}$, σ the surface tension and $\theta_R = 23^\circ$ the Rayleigh angle [4]. We investigated the drop response for Weber number up to 2. In this regime, drops are strongly deformed by the acoustic radiation pressure. Therefore, the relevant length scale for the Bond number is not the initial drop radius but the maximum drop deformation h_{max} and the modified Bond number is given by $Bo_m = \frac{\rho_l g h_{max}^2}{\sigma}$ with g the gravity acceleration.

Results

The different regimes are summarised on the phase diagram (figure 1 b) which represents the observed dynamics as a function of the modified Bond number projected on the surface (characterizing the influence of gravity on the translation) and the acoustic Weber number (characterizing the ability

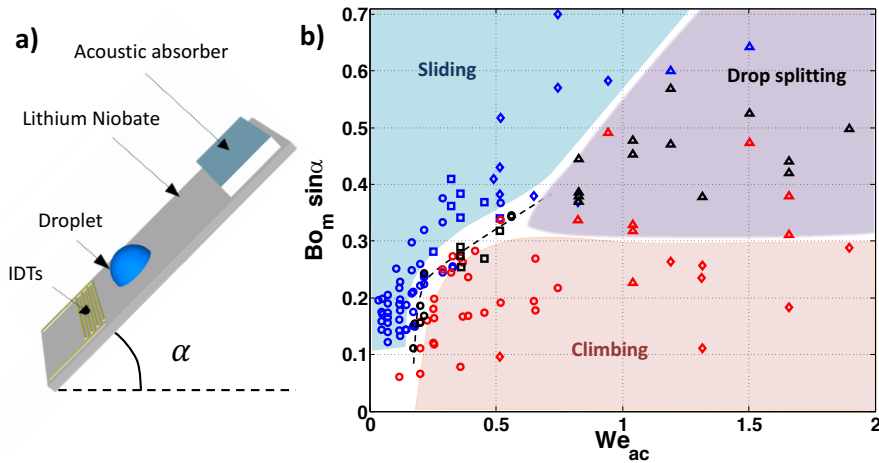


Figure 1: a) Sketch of the experimental setup. b) Phase diagram of the different observed dynamics in the $Bo_m \sin \alpha$ versus We_{ac} plan. Symbol in red correspond to a climbing dynamic, in blue to a sliding and in black to stagnation of the drop, i.e. the drop oscillates without global translation. Purple shaded area correspond to complex dynamics leading to a drop splitting.

of the acoustic wave to deform the drop). For low excitation ($We_{ac} < 0.2$), the acoustic radiation pressure is not sufficient to break the symmetry and drop exhibits small axisymmetric oscillations. As long as the gravity projection on the surface is small ($Bo_m \sin \alpha < 0.1$), drop oscillates without translation. However for higher tilt angle and/or drop volume ($Bo_m \sin \alpha > 0.1$) a new dynamic is observed where drops slide on the surface in a direction opposite to the SAW propagation. In this regime, the intermittent contact line depinning induced by the oscillation allows the drop to slide by gravity.

For intermediate excitation ($0.2 < We_{ac} < 0.7$) drop oscillates with an asymmetry in the SAW direction due to the radiation pressure. For low inclination, drops move upward in a similar manner as sessile drop. At high inclination, drop start to deform in the wave propagation direction due to the acoustic forcing but is pulled down during the elongation phase by gravity and the overall translation is directed downward. For intermediate inclination, an interesting dynamic arises where drop alternates between a climbing motion (similar to low inclination) and a sliding motion (similar to high inclination) and the drop stagnates on the surface. Finally, for higher excitation ($We_{ac} > 0.7$), drops are extremely deformed and exhibit complex dynamics leading to a drop splitting for $Bo_m \sin \alpha > 0.3$.

Conclusion

We experimentally studied the influence of the gravity on the drop dynamics excited by surface acoustic waves on tilted plane. The projection of the gravity on the substrate is in competition with the acoustic forcing directed upward. Due to this competition, new dynamics arise and drops can either slide, climb or stagnate. These dynamics can be summarised for different drop volumes, tilt angles and acoustic excitations into a single phase diagram based on a modified Bond number and the acoustic Weber number. Finally, for low excitation drop are able to slide offering a new way to make active slippery surfaces.

References

- [1] Ding, X., Li, P., Lin, S. C. S., Stratton, Z. S., Nama, N., Guo, F., Huang, T. J. Lab on a Chip, **18**, 3626-3649 (2013).
- [2] Friend, J., Yeo, L. Y. Reviews of Modern Physics, **83**, 647-704 (2011).
- [3] Brunet, P., Baudoin, M., Matar, O. B., Zoueshtiagh, F. Physical Review E, **81**, 036315 (2010).
- [4] Bussonnière, A., Baudoin, M., Brunet, P., Matar, O. B. Physical Review E, **93**, 053106 (2016).



Surface wave driven oscillatory instability of sessile droplets

Nicolas Chastrette^{1,2}, Michael Baudoin³, Olivier Bou-Matar³, Laurent Royon², Philippe Brunet², Régis Wunenburger¹

¹Sorbonne Université, Centre National de la Recherche Scientifique, UMR 7190, Institut Jean Le Rond d'Alembert, F-75005 Paris, France

²Laboratoire Matière et Systèmes Complexes, Université Paris-Diderot, CNRS UMR 7057, Paris, France

³International Associated Laboratory LEMAC, IEMN, CNRS UMR 8520, Université des Sciences et Technologies de Lille and EC Lille, 59652 Villeneuve d'Ascq Cedex, France

Introduction

Manipulation of sessile droplets with microliter typical volume can be achieved using surface acoustic waves (SAW). The conversion of SAW into bulk longitudinal waves inside the droplet results in various phenomena depending on the droplet size and viscosity and SAW frequency and intensity : droplet transport, oscillations, atomisation, streaming flows, mixing ... The most striking feature shared by all these hydrodynamic effects of acoustic waves is the large frequency gap between the acoustic frequency and the frequencies of hydrodynamic phenomena. Here we focus on the oscillations of the droplet free surface with typical frequencies 100 Hz occurring when the droplet is insonified at rather low acoustic excitation frequency ~ 1 MHz. We insonify a $10 \mu\text{l}$ water droplet using a Rayleigh wave with constant frequency $f_{\text{AE}} = 840$ kHz and modulated amplitude and we take advantage of the slow evaporation of the droplet, which allows a drifting acoustic eigenfrequency of the droplet f_{AR} to cross f_{AE} . Using high-speed imaging we evidence the spontaneous excitation of a surface eigenmode at well-defined values of the droplet height h_0 and acoustic excitation levels. We identify two narrow instability tongues on both sides of the droplet acoustic resonance. We propose and test an instability mechanism based on the delayed feedback of the radiation pressure exerted the intracavity field on the free surface deformations.

Experimental evidence of the oscillation instability

A sessile droplet is deposited on a 10 mm thick glass block. The tip of a needle hydrophone is immersed in the droplet, allowing the intra-cavity acoustic pressure to be measured during the droplet insonification. Due to slow evaporation, the droplet height h_0 decreases linearly with time t at a rate $\frac{1}{h_0} \frac{dh_0}{dt}$ typically equal to 60 min. Every 15 s, a harmonic voltage signal with constant frequency $f_{\text{AE}} = 840$ kHz, 5 s duration and amplitude slowly increasing from 0 V to 50 V as \sqrt{t} (sketched in figure 1 a) excites a high-power piezoelectric transducer mounted on a wedge in contact with the glass block. As a result, a Rayleigh wave propagates along the glass surface toward the droplet. As shown in figure 1 b, which displays the time-dependent altitude of a point of the droplet surface observed from the side, for some values of h_0 , the free surface of the droplet exhibits oscillations at frequency $f_{\text{SR}} \simeq 230$ Hz when the amplitude of the transducer excitation voltage exceeds a threshold value V_{th} . Independent image analysis based on the determination of the droplet surface shape from the deformation of the image of a grid observed through the droplet allowed to identify the excited surface eigen mode, whose pattern is shown in figure 2. The oscillation amplitude P_{AE} of the intra-cavity acoustic pressure at frequency f_{AE} and the closest droplet acoustic resonance frequency f_{AR} , which both vary with h_0 , are measured using the hydrophone by applying a chirp with 5 V amplitude and 20 ms duration just before the voltage ramp. The variations of P_{AE} and of V_{th} versus h_0 are shown in figure 3. P_{AE} exhibits a maximum for $h_0 = 1.63$ mm, corresponding to the coincidence of f_{AR} with f_{AE} . $V_{\text{th}}(h_0)$ exhibits two narrow instability tongues on both sides of the peak displayed by $P_{\text{AE}}(h_0)$.

Insight in the instability mechanism

As shown in figure 1 c, from the moment the surface oscillates, the intra-cavity pressure amplitude exhibits modulations at the frequency of oscillation of the droplet surface f_{SR} . This can be ascribed to the modulation of the effective length of the acoustic resonator by the surface deformation. As a consequence, the radiation pressure exerted by the intra-cavity acoustic field on the droplet surface $\Pi \simeq P_{\text{AE}}^2 / (\rho c^2)$ ρ is water density and c sound speed in water) is also modulated at frequency f_{SR} .

Given the large quality factor of the acoustic cavity $Q_{AR} \simeq 100$, measured independently, the intra-cavity acoustic field sets up after a time laps of the order of $\tau = Q_{AR}/f_{AR} \simeq 0.1$ ms. The corresponding phase delay expected between the resonator length modulation and the radiation pressure modulation is thus $\phi = -2\pi f_{SR}\tau \simeq -0.1$ rad.

The dynamics of the amplitude δh of the excited surface eigen mode can be described as the one of a harmonic oscillator forced by a time-delayed force f proportional to the radiation pressure. Linearising the radiation pressure variation against δh , in harmonic regime with angular frequency ω , $f = K \frac{d\Pi}{d\delta h}(0) \delta h \exp i(\omega t + \phi)$ (K positive constant) and δh satisfies:

$$\delta \ddot{h} + \left(\frac{\omega_{SR}}{Q_{RS}} - K \frac{d\Pi}{d\delta h}(0) \sin \phi \right) \delta \dot{h} + \left(\omega_{SR}^2 - K \frac{d\Pi}{d\delta h}(0) \cos \phi \right) \delta h = 0$$

where ω_{SR} is the eigen angular frequency of the excited surface mode, Q_{SR} its quality factor, and m its equivalent mass.

On the right side of the resonance in figure 2, P_{AE} decreases with h_0 , so $\frac{d\Pi}{d\delta h}(0) < 0$ and therefore the surface mode dissipation is decreased by the intra-cavity delayed feedback. Instability is thus expected if dissipation equals zero, i.e. at V_{th} such that :

$$\left. \frac{-K}{m} \frac{d\Pi}{d\delta h}(0) \right|_{V_{th}} \simeq \frac{\omega_{SR} \omega_{AR}}{Q_{SR} Q_{AR}}$$

Conclusion

As it will be shown during the conference, this instability model nicely fits the right-hand side instability tongue. Other considerations will allow to explain the left-hand side instability tongue.

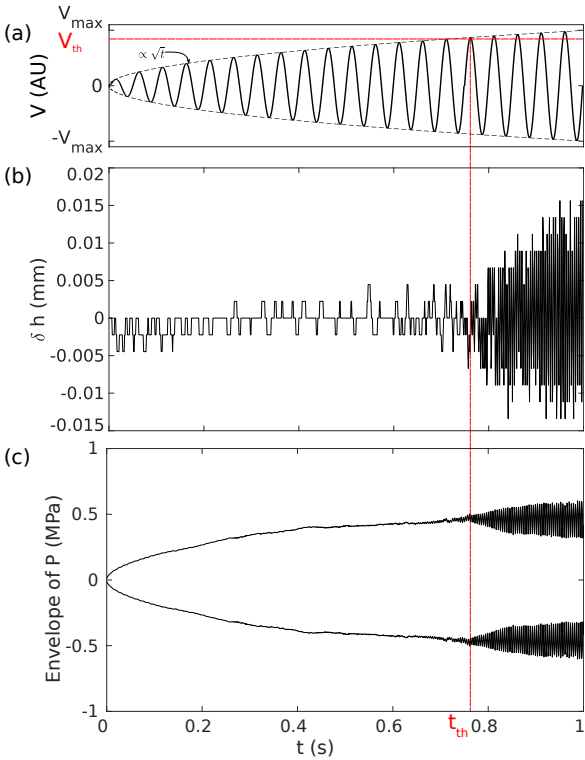


Figure 1: (a) Sketch of the harmonic voltage signal with frequency $f_{AE} = 840$ kHz, 5 s duration and amplitude slowly increasing from 0 V to 50 V as \sqrt{t} that excites the piezoelectric transducer emitting the SAW. (b) Time-dependent altitude of a point of the droplet surface observed from the side exhibiting oscillations at frequency $f_{SR} \simeq 230$ Hz when the amplitude of the transducer excitation voltage exceeds a threshold value V_{th} . (c) Intra-cavity pressure envelope exhibiting modulations at frequency f_{SR} .

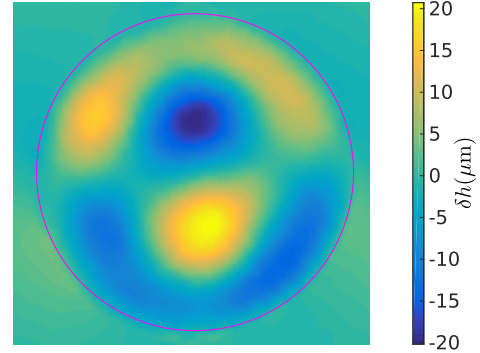


Figure 2: Pattern of the acoustically excited surface deformation eigen mode of frequency f_{SR} , determined using image analysis based on the determination of the droplet surface shape from the deformation of the image of a grid observed through the droplet.

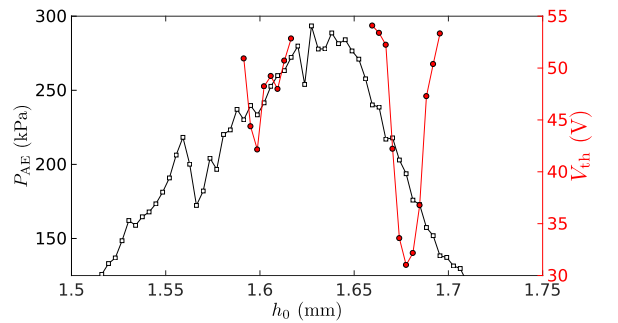


Figure 3: Oscillation amplitude P_{AE} of the intra-cavity acoustic pressure at frequency $f_{AE} = 840$ kHz and threshold value of the excitation voltage at the onset of the oscillation instability V_{th} as function of droplet height h_0 .



Basophil purification using a thin-reflector acoustic resonator

Filip Plazonic^{1*}, Chloe Rose^{1,2*}, Laurie Lau², Xunli Zhang¹, Andrew F. Walls², Dario Carugo¹, Martyn Hill¹, Peter Glynn-Jones¹

¹Engineering and the Environment/²Medicine, University of Southampton, Southampton, United Kingdom

* Authors have equally contributed to the work in this study.

Email: fp3g10@soton.ac.uk

Introduction

Allergic disease affects increasing proportions of the population worldwide, with foods, drugs and inhalant allergens implicated in conditions ranging from relatively mild rhinitis, to debilitating asthma or life-threatening anaphylactic shock [1]. For some patients, the accurate diagnosis of allergic sensitivity can represent a challenge, and there is a pressing need for better laboratory tests. A procedure that is showing great potential in diagnosis - and which avoids risks inherent in exposing a patient to allergens - involves collecting a blood sample and investigating the ability of basophils to respond to an allergen *in vitro*. Basophils are the rarest type of white blood cell, and the flow cytometric procedures currently employed to isolate them and detect allergen-induced cellular activation are time-intensive and require major capital expenditure and the availability of a trained technician [2]. As a consequence, basophil activation tests are seldom employed in routine diagnosis.

We have explored an alternative approach to the separation of basophils from other cell types which presents these cells in a way that will allow their activation to be assessed in response to allergens. Further work is necessary but initial results indicate that our method allows basophils in high purity to be immobilized on a surface. Combining this approach with automated imaging techniques offers important advantages over the technology currently available.

Device and acoustic background

The device is a layered resonator, designed to establish a “thin-reflector” standing wave field inside the fluid chamber. The thin-reflector mode is the first structural mode of the entire device, and has no pressure nodes within the fluid channel, instead relying on a potential energy gradient towards the outside of the reflector surface to push all cells (with positive contrast factor) towards the reflector layer [3].

The device consists of a 130 μm fluid layer constrained by a 170 μm glass cover slip (see below) acting as reflector layer on one side, and a 1000 μm stainless steel carrier layer on the other. The fluid layer thickness is determined by a cellulose acetate spacer and a PDMS gasket seals the chamber.

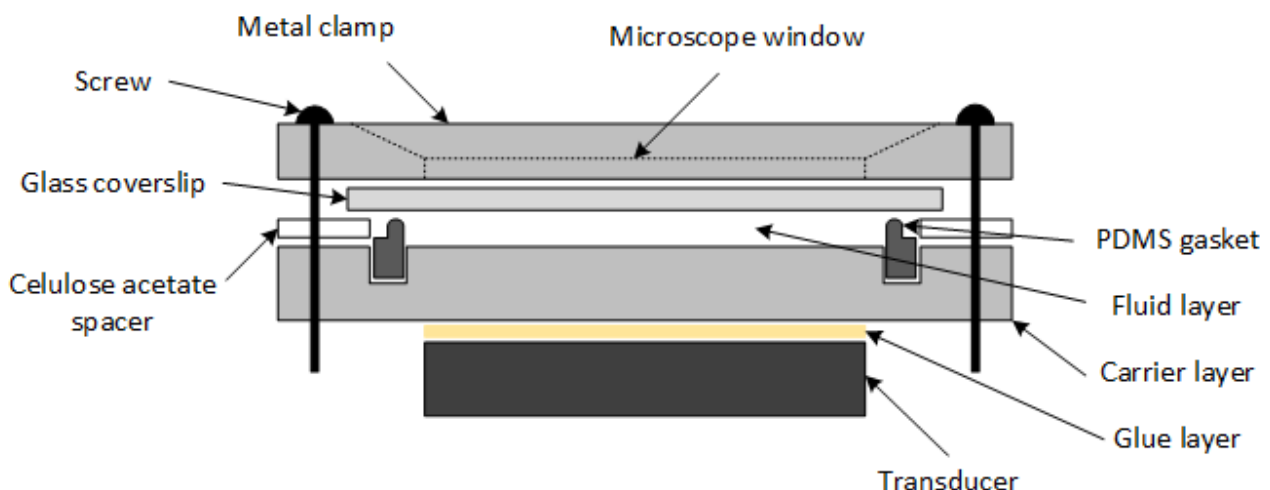


Figure 1: Cross-section schematic (taken perpendicular to the flow direction) of the thin-reflector device. Fluidic ports not shown.

The acoustic field is introduced via a 12 x 24 x 1 mm PZ26 transducer glued to the carrier layer. The device is held together by a clamp and bolts, which are adjusted to ensure planarity. Figure 1 shows the cross-section schematic of the device.

The clamp design means that the device can be disassembled so the coated coverslip that serves as the reflector layer can be taken for further analysis after basophil capture. Figure 1 shows a cross-section schematic of the device.

Method

The blood enters a fluidic port driven by a syringe pump. The thin reflector acoustic mode in the fluid channel causes cells within the sample to make contact with the functionalised glass surface that forms the upper channel wall as they flow through the device. The reflector layer is formed from a Schott Nexterion “slide-H” which presents a 3D hydrogel surface to the chamber to prevent non-specific binding, and also has amine reactive groups allowing a basophil specific antibody to be attached in the region above the transducer. A second fluid port takes the remaining fluid to waste. Aliquots of the waste flow are analysed by a fluorescent activated cell sorting (FACS) machine to measure the capture rate, as well as microscopy of the capture surface.

Experimental results

Initially, magnetically purified basophils were used to optimize the device function. Controls (No US+Ab and US with no Ab, both on plain glass) capture between 6 and 13 % of available basophils, but when both ultrasound and an antibody functionalisation are introduced the capture rises to 47% on average, further refinement of the acoustic field strength indicates that capture efficiencies as high as 94 % may be possible.

Initial experiments with whole blood proved unsatisfactory, likely due to obstruction of the surface. Instead, lysed blood was used; however, this work is still underway. Initial results indicate that capture levels will be comparable. Current challenges include working with the much lower cell numbers, as the number of basophils in the lysed blood is still only 3% of the total cell count.

Conclusion

With lysed blood, the captured basophils are immobilised (resist flushing) and histamine activation tests show that the basophils can still be activated after capture. The total processing time of the method is around 40 minutes, faster than the comparable magnetic purification method (taking around 150 minutes), and while the capture proportion is lower, this should still provide sufficient cells for subsequent allergy testing.

References

- [1] Warner J.O., Kaliner M.A., Crisci C.D., Del Giacco S., Frew A.J., Liu G.H., Maspero J., Moon H.-B., Nakagawa T., Potter P.C., Rosenwasser L.J., Singh A.B., Valovirta E., van Cauwenberge P., 2006, *Int Arch Allergy Immunol*, 139, Allergy Practice Worldwide: A Report by the World Allergy Organization Specialty and Training Council. Pp. 166-174
- [2] Boumiza, R., Debard, A. and Monneret, G.T., 2005, *Clinical Molecular Allergy*, 8, The basophil activation test by flow cytometry : recent developments in clinical studies, standardization and emerging perspectives, pp. 1-8.
- [3] Glynn-Jones, P., Boltryk, R.J., Hill, M., Harris, N.R., Baclet, P., 2009, *JASA*, 126(3), pp. 75-79

Parametric investigation of acoustic autopropulsion of metallic and polymer nanoobjects

Gabriel Dumy^{1,2}, Mauricio Hoyos¹, and Jean-Luc Aider¹

¹PMMH Lab, ESPCI Paris, Paris, France

E-mail: gabriel.dumy@espci.fr, URL: <https://www.pmmh.espci.fr>

²Paris Descartes, Sorbonne Paris Cité, Paris, France

Introduction

For a few decades now, acoustic manipulation of microscopic particles has been thoroughly investigated and described. A lot of theoretical work has been dedicated to derive the governing equations of the movement of spherical particles under the influence of standing or traveling waves [1], as well as their interactions with each other. Whether it be the experimental proofing with manipulation of synthetic and controlled beads, or to the applied manipulation of living cells [2] or bacteria, the phenomenon is quite well understood and exploited. But what happens when the spherical assumption breaks and the symmetry is lowered? As described in a previous work, cylinder shaped metallic micro objects are observed to propel themselves under acoustic field [3]. This work aims to experimentally explore a range of parameter influencing this motion, and to compare it with several developing theory [7,8].

Indeed, when an aspherical particle is submitted to a standing acoustic wave, we do not observe a stable aggregate anymore. For instance, if we observe metallic micro cylinders acoustically levitated, no stable aggregate are found, and instead a variety of motion is exhibited [3], as is described on Figure 1.

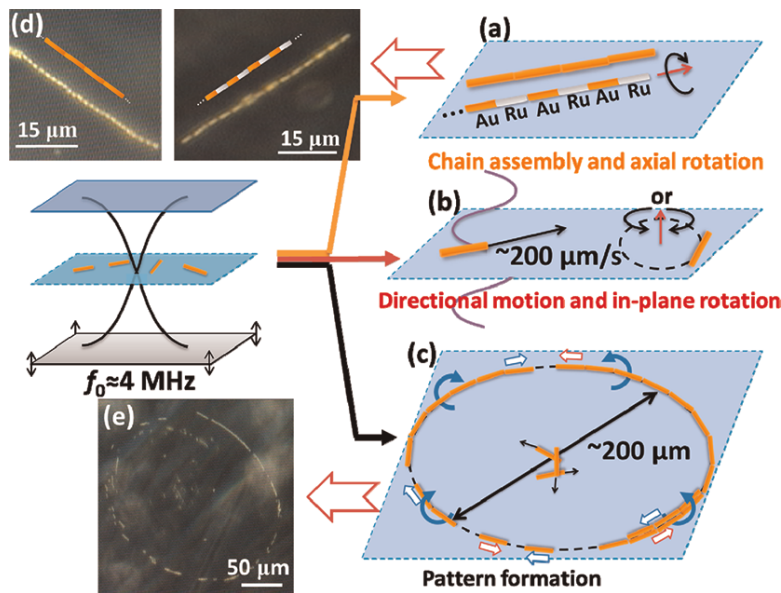


Figure 1: Description of the various modes of motion observed when metallic micro cylinders are suspended in a standing acoustic field (taken from [3]). As can be seen on (b), individual nanorods undergo translation going up to $200 \mu\text{m}\cdot\text{s}^{-1}$, and in plane rotation, staying in the nodal pressure plane of the acoustic field. Chain construction are observed, each nanorod locking itself behind a neighbor, creating long line structures such as in (d) or circular structures such as in (c) and (e).

The propulsion of cylindrical nanoparticles has been experimentally described: it has been observed that they are undergoing a translation motion which can go up to hundredths of micrometers per seconds, and are also experiencing a rotation along their symmetry axis that can go up to the kilohertz, translating to surface speeds of the cylinder up around the millimeter per second [5].

As a primary exploration of the influence of some geometrical and density factor has been done (exploration in length and density variation [4]), the influence of the geometrical parameters, frequency and acoustic contrast on the motion are not explored experimentally. It is important to do so since theory is really kicking in, as several groups are proposing promising theories to confront against the

experiment [7, 8].

Our setup and metallic nano cylinders

Using our own acoustic resonators and micro cylinders fabricated by Tom Mallouk's team in PennState University, we are exploring a variety of experimental conditions for the propulsion of these objects. Playing with acoustic contrast as well as with the acoustic Reynolds number, different regimes of motion are observed, allowing us to probe the different theories proposed (Figure 3).

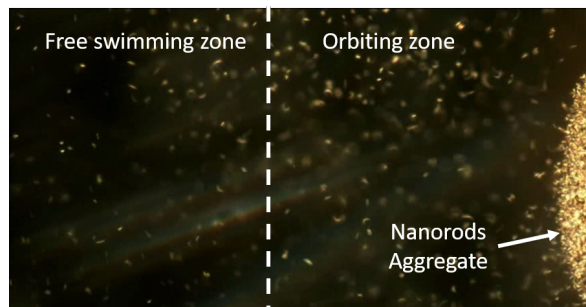


Figure 2: Picture taken from a video of acoustic propulsion, exhibiting the different zones of motion for a suspension of gold nanorods of $1\mu\text{m}$ average length, in a 4 MHz acoustic field.

Moreover, the motion of metallic nanorods submitted to a standing acoustic field can remind an observer of the typical trajectories of tracers dragged by acoustic streaming in a resonant cavity. We try to clear the role of acoustic streaming in the propulsion of microscale acoustic swimmers, by controlling the amplitude of this phenomenon as described in [6].

Exploration of geometrical and acoustical parameters

In order to investigate the geometry influence in the acoustic propulsion phenomenon, we are able to make in our lab custom micrometric structures (Figure 3). Made of polymer, these objects do not exhibit the same acoustic contrast as the metallic nano-cylinders, but the variety of shape obtained allows us to examine more precisely the impact of chirality on the acoustic motion for instance.

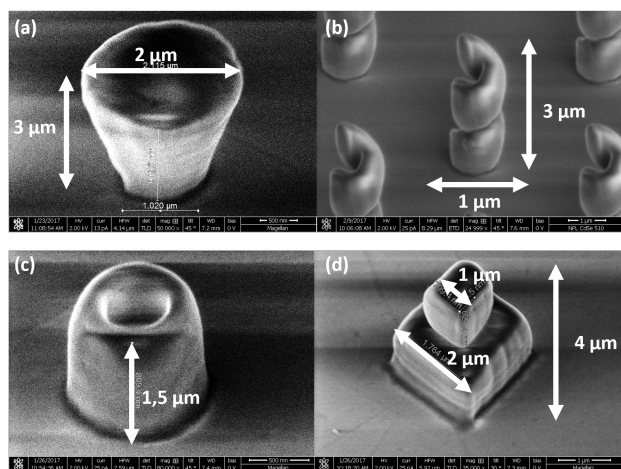


Figure 3: Micrometric structures produced in our team. These pictures illustrate the versatility of shapes that are available for the geometrical influence we aim to explore in acoustic propulsion. Whether it be axisymmetric shapes (a) and (c), with (c) being a hollow structure or chiral objects as illustrated with the (b) helix, we have a good control on shape and repeatability. More polygonal structures can also be produced, as the square base dumbbell on the bottom right picture (d) shows.

Conclusion

As will be more detailed during the conference, we have shown that several parameters influence the motion of structured microparticles under the effect of a standing acoustic wave. We tried to decouple the translational and rotational motion of the micro objects, and to relate it to the chirality and asymmetry of the shape employed. As more work is needed towards the experimental evidence of the motion frequency dependence, we are looking forward to explore the efficiency of propulsion by varying the composition of the micro objects constituting material.

References

- [1] G. Whitworth, M. Å. Grundy, W. T. Coakley. *Ultrasonics* **29**, 439-444 (1991).
- [2] J. Nilsson, M. Evander, B. Hammarström, T. Laurell. *Analytica chimica acta* **649**, 141-157 (2009).
- [3] W. Wang, A. Castro, M. Hoyos, T. Mallouk. *ACS Nano* **6**, 6122-6132 (2012).
- [4] S. Ahmed, W. Wang, L. Bai, D. T. Gentekos, M. Hoyos, T. Mallouk. *ACS Nano* **6**, 6122-6132 (2016).
- [5] A. Balk, L. Mair, P. Mathai, N. Patrone, W. Wang, S. Ahmed, T. Mallouk, A. Liddle, M. Stavis. *ACS Nano* **8**, 8300-8309 (2014).
- [6] M. Hoyos, A. Castro. *Ultrasonics* **53**, 70-76 (2013).
- [7] F. Nadal, E. Lauga, (2014). *Physics of Fluids* **26** (2014).
- [8] J. Collis, D. Chakraborty, J. Sader. *Journal of Fluid Mechanics* **825**, 29-48 (2017).

Ultrasonic tissue engineering in multi-well microplate enables layered co-culture tumor spheroids

Karl Olofsson¹, Valentina Carannante², Björn Önfelt^{1,2} and Martin Viklund¹

¹Department of Applied Physics, KTH Royal Institute of Technology, Stockholm, Sweden
E-mail: karlolo@kth.se

²Department of Microbiology, Tumor and Cell Biology, Karolinska Institute, Stockholm, Sweden

Introduction

Tissue micro-engineering is important for modelling 3D biological structures to bridge the gap between in vivo and in vitro in cellular and pharmaceutical research. Regular 2D in vitro cell cultures do not reproduce the complex 3D micro-environment of cells, extra cellular matrix and soluble factors which governs cell behavior and tissue function [2]. Many multicellular tumor spheroids (MCTS) culture methods has been developed based on either anchored-dependent (e.g. scaffolds) or anchored-independent (e.g. hanging drop, low-attachment surfaces) strategies [3] but few methods offer possibilities to control the spatial distribution of different cell types within the MCTS. Here we present the formation of scaffold-free and layered HepG2 hepatocellular carcinoma MCTS, opening up future possibilities for studying interaction cancer cell plasticity in the tumor-stroma interface [4] and more complex tissue modelling where the spatial distribution of cell types within the spheroid is important.

Layered HepG2 MCTS formation

In a previous study, we presented an ultrasonic standing wave (USW) 3D culture platform where immunotherapy of adherent HepG2 MCTS were investigated [1]. We further developed this platform with a protein repellent polymer coating (described in [5]) to produce un-anchored HepG2 MCTS [6] (Fig. 1). In this paper, we demonstrate culture and confocal imaging of layered HepG2 hepatocellular carcinoma MCTS. To culture layered MCTS, cells that will form the inner core of the MCTS were seeded into the multi-well microplate and incubated for 24 h during continuous 2D USW trapping that initiated cell-cell adhesion. The inner core MCTS was incubated passively (no USW) for 24 h to further develop stable cell-cell connections before cells intended for the outer layer were stained and seeded into the micro-wells. The seeded cells were focused onto the inner core MCTS and kept in place for 24 h to facilitate stable adhesion (Fig. 1C).

Staining and mounting in refractive index matching solution (RIMS)

To distinguish cells in the outer layer from the inner core, cells in the outer layer were stained with CFSE before seeding. CFSE is a cell tracking dye which is stable over multiple cell generations. 24 hours after the USW trapping of the outer layer, the MCTS were fixed and stained *in situ* with DAPI (both core and outer layer are DAPI positive). To overcome MCTS light scattering and facilitating on-chip whole MCTS imaging, the samples were mounted in a refractive index matching solution (RIMS) to remove all light scattering interfaces and enabling efficient capture of fluorophore signal.

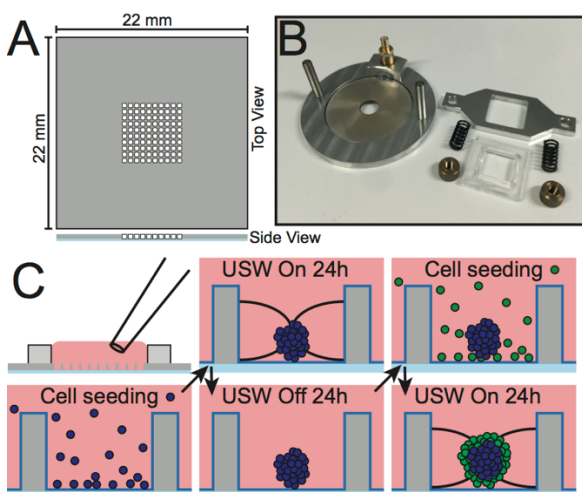


Figure 1 The silicon multi-well microplate is etched with 100 micro-wells (350 μm x 350 μm , 300 μm deep) is bonded to a glass plate (A) and mounted onto the transducers (B) by clamping it with a frame. To produce spheroids, a single cell suspension is seeded into the multi-well microplate reservoir with a standard pipette and the cells sediment into the micro-wells (C). When the piezo ceramic disk is actuated with frequency modulation (2.47 MHz \pm 50 kHz at 1 kHz sweep rate) the ultrasonic radiation forces, originating from USW, focus the seeded cells into all 100 micro-well centers. Spheroids that will serve as cores in the layered MCTS are then formed when incubated during continuous ultrasonic force focusing for 24 h followed by 24 h of passive incubation. After 48h, cells for the outer MCTS layer is seeded and focused onto the core MCTS with USW for 24h.

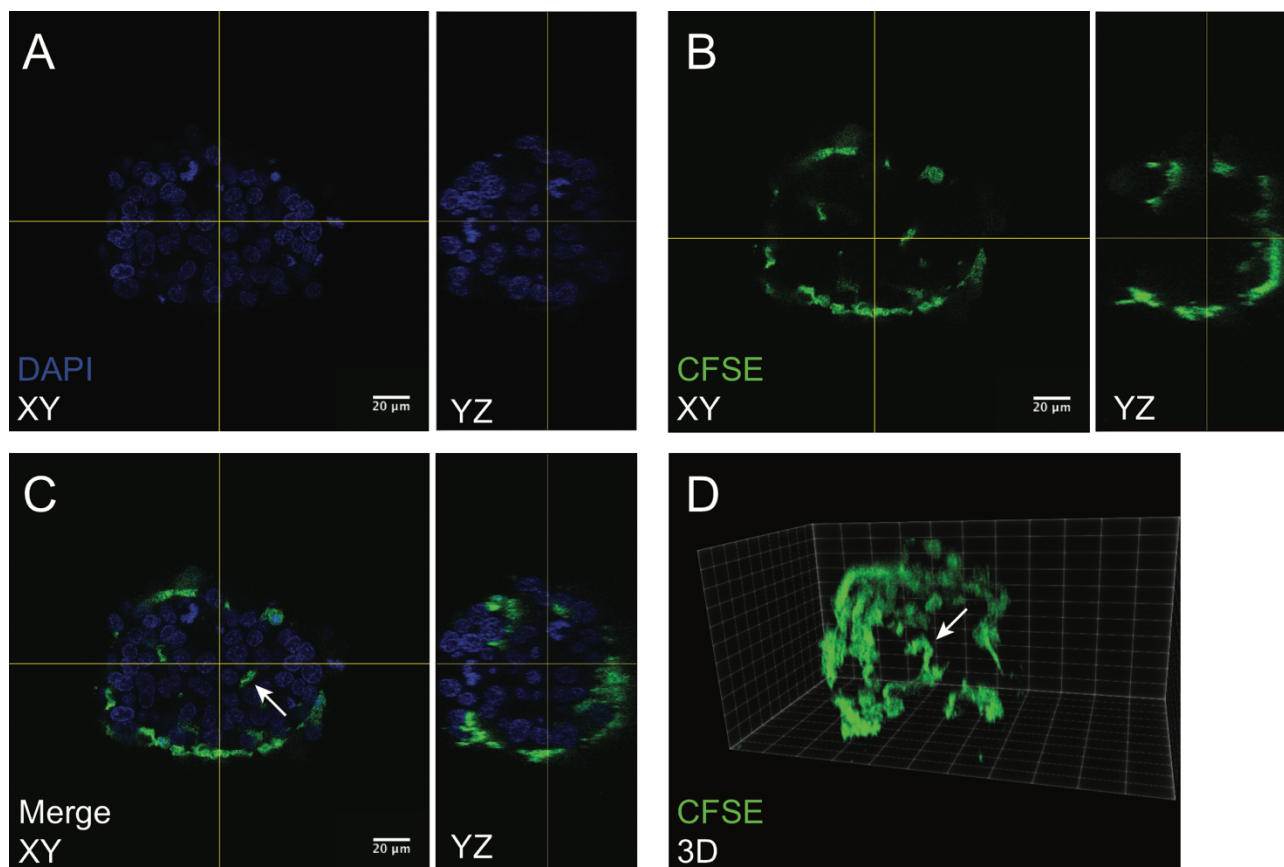


Figure 2: Confocal imaging of whole layered MCTS. Layered MCTS were formed by initial culturing of unstained cells for 48h before seeding and trapping of CFSE stained cells for 24h. Confocal imaging of the MCTS were performed after fixation, staining with DAPI and mounting in refractive index matching solution. DAPI (A) and CFSE (B) staining was visible throughout the sample. White arrow in the merged image (C) highlights CFSE signal from a cell sprouting into the core of the MCST. White arrow in the CFSE signal 3D rendering (D) shows that sprouting cell is still situated in the outer layer.

Confocal imaging of layered MCTS

The RIMS enabled on-chip whole MCTS confocal imaging and DAPI signal could readily be detected throughout the sample (Fig. 2A). Visual inspection showed equal cell density distribution within the MCTS and 24 hours were enough to facilitate cell adhesion between outer layer and inner core. The CFSE signal from the outer layer (Fig. 2B) showed that most of the cells were maintained at the outer boundary of the inner core. Small signs of cells from the outer layer sprouting into the inner core (highlighted by white arrow in merge image (Fig. 2C) and 3D rendering of CFSE signal (Fig. 2D)) was visible, but no cells completely infiltrated the inner core.

Conclusion

We have, to our knowledge, demonstrated the first scaffold-free layered MCTS which can be used for more advanced *in vitro* co-culture models compared to regular MCTS where spatial control of cells is not possible. Future work will be focused on further developing the protocol and including different cell lines for co-culture MCTS.

References

- [1] A. E. Christakou, M. Ohlin, B. Önfelt and M. Wiklund, *Lab Chip*, 2015, **15**, 3222-3231
- [2] C. J. Lovitt, T. B. Shelper and V. M. Avery, *Biology*, 2014, **3**, 345-367
- [3] C. R. Thoma, M. Zimmermann, I. Agarkova, J. Kelm and W. Krek, *Advanced Drug Delivery Reviews*, 2014, **69-70**, 29-41
- [4] M. Egeblad, E. S. Nakasone and Z. Werb, *Dev Cell*, 2010, **18**, 884-901
- [5] K. Nagahashi, Y. Teramura, M. Takai, *Colloids Surf B Biointerfaces*, 2015, **134**, 384-391
- [6] K. Olofsson, V. Carannante, T. Frisk, K. Kushiro, M. Takai, B. Önfelt and M. Wiklund, *The 20th International Conference on Miniaturized Systems for Chemistry and Life Sciences*, Dublin, 2016, p. 409-410

Integration of microacoustic sensor for the analysis of platelets-collagen interactions at physiological flow conditions of the whole blood.

Aleksandr Oseev¹, Benoît Le Roy de Boiseaumarié¹, Fabien Remy-Martin¹, Jean-François Manceau¹, Alain Rouleau¹, Franck Chollet¹, Wilfrid Boireau¹, Therese Leblois¹

¹FEMTO-ST institute, CNRS UMR-6174, Université de Bourgogne Franche-Comté, Besançon, France
E-mail: therese.leblois@femto-st.fr, URL: <http://teams.femto-st.fr/BioMicroDevices/>

Introduction

Analysis of primary haemostasis at rheological conditions of blood *in-vivo* is an important and demanding task in clinical practice. A number of parameters should be controlled in order to monitor the haemostasis: circulating platelets, the blood clotting proteins and the state of vascular walls [1]. Most of the currently available devices that are adapted for clinical practice have several limitations: they do not reproduce rheological conditions of blood; the reproducibility of measurements is insufficient; and a substantial amount of blood is required [2]. This contribution focuses on the development of microacoustic sensor solution integrated in a microfluidic platform for the monitoring of the whole blood coagulation properties by analyzing the whole blood platelets-immobilized collagen interactions at realistic rheological flow condition.

Results

The integrated microfluidic sensor platform is designed to satisfy following demands: microfluidic system replicates the rheological flow conditions of the whole blood under investigation; locally functionalization microfluidic channel interface mimics the blood vessel damage by exposing to the specific collagen. The microacoustic sensor is integrated without microfluidic structure disturbance and allows an in-flow detection of platelets-collagen interaction at predefined interface. Figure 1 shows the schematic representation of the integrated sensor platform and the preliminary microacoustic sensor structure simulation results.

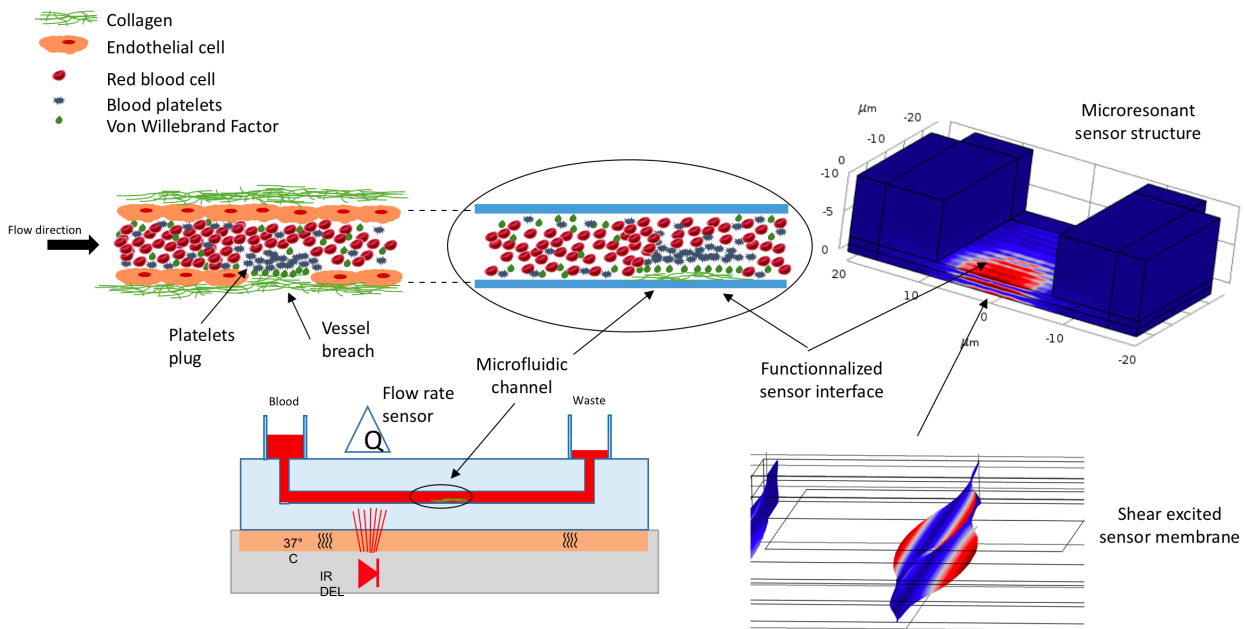


Figure 1: Schematic representation of sensor platform for the analysis of primary haemostasis integrating the microfluidic system mimicking the rheological blood flow conditions, functionalized interface for the localized platelets binding, integrated microacoustic sensor, flow rate and pressure control system. Displacement field distribution of FBAR structure was obtained using COMSOL Multiphysics® software.

The whole blood under arteriolar conditions should affect the platelets at the vessel wall with shear stress about 1500 s^{-1} . Replication of the shear stress within an artificial microfluidic channel with built-in microacoustic sensor, is one of the major aspects that ensures the validity of the detection process. The primary results obtained for the predefined shear rates and locally functionalized collagen interface demonstrate the specific binding of platelets within predetermined area, Figure 2.

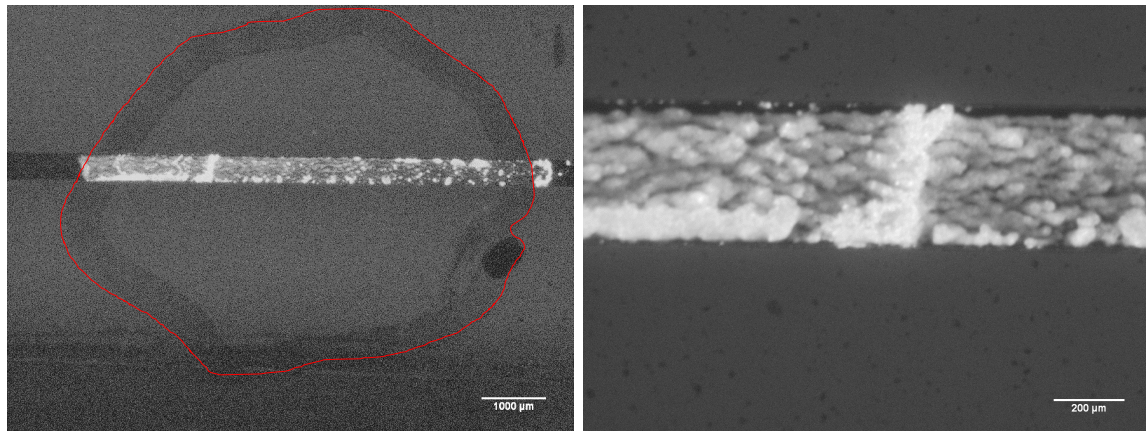


Figure 2: Pictures of fluorescent platelets thrombi formed on a collagen-coated channel (the collagen-coated area is shown in red). Whole blood was incubated with the fluorescence dye Calcein AM, perfused over collagen-coated channel and thrombi formation was recorded by fluorescence microscopy.

To ensure the measurement results it is required to keep stable the shear flow rate along the microfluidic channel. In order to prevent the blood flow disturbance, the microacoustic structure is designed to fit the collagen modified interface at sub-millimeter dimensions corresponding to a small blood vessel in which primary haemostasis occurs physiologically. The developed sensor is completed as a film bulk acoustic resonator (FBAR) operating at shear bulk acoustic mode [3]. The displacement field distribution and the deformation at the resonant frequency of 2.2 GHz are shown in Figure 1. The sensor design is taking into account the suppression of the normal components of the structure vibrations to diminish in-liquid radiation losses. The microacoustic sensor is integrated into predefined single side transparent microfluidic platform that enables simultaneous analysis of collagen-platelets interactions with acoustical and optical methods. The work specifically focuses on the technological challenges and solutions of integrated microacoustic sensor fabrication. Because of the necessity of the sensor structure integration with a predefined microfluidic arrangement, the fabrication process has to be reconsidered in comparison to conventional FBAR technology. In current work, we demonstrate the fabrication approach that enables the manufacture of designed integrated microfluidic sensor platform utilizing standard MEMS technology.

Conclusions

Contribution demonstrates a novel concept of the whole blood study with an integrated microacoustic sensor platform. It is intended to improve the pathology evaluation in order to manage patients with bleeding risk or under antiplatelets therapy. In particular, the work is focused on the in-flow analysis of platelets-collagen interactions at the rheological conditions of the whole blood *in-vivo*. The initial results demonstrate the microacoustic sensor design and the functionalization results enabling the selective detection of the platelets. Fabricated and experimentally verified microacoustic sensor structure will be presented in more details at the conference.

References

1. O. J. T. McCarty, D. Ku, M. Sugimoto, M.R. King, J.M.E.M Cosemans, and K.B. Neeves. *Journal of Thrombosis and Haemostasis* **14**(3), 619-622 (2016).
2. R. Paniccia, R. Priora, A. Liotta and R. Abbate. *Vascular health and risk management* **11**, 133 (2015).
3. J. Weber, W.M. Albers, J. Tuppurainen, M. Link, R. Gabl, W. Wersing, M. Schreiter. *Sensors and Actuators A: Physical* **128**(1), 84-88 (2006).

Single bubble acoustic manipulation and actuation in complex environments

Diego Baresch¹ and Valeria Garbin¹

¹ Department of Chemical Engineering, Imperial College London, London SW7 2AZ,
E-mail: d.baresch@imperial.ac.uk

Micron-sized gas bubbles are notoriously difficult to isolate, handle and remotely control. Their large buoyancy in common liquids will usually force them to rise and burst at any gas/liquid interface or remain trapped against a solid boundary until dissolution. While dissolution driven bubble instability has found numerous practical workarounds, the challenge remains at isolating and maneuvering a single bubble in free space to, for instance, perform precise single bubble dynamics experiments with applied ultrasound or to use them as active carriers for a specific payload deliverable on demand. Here we demonstrate that single-beam acoustical tweezers [1] can trap and manipulate in 3D a single bubble with the radiation pressure of helicoidal ultrasonic beams, or acoustical vortices (AVs). Contrary to the situation where bubbles are trapped in the antinodes of a standing wave [2], the trapping vortex beam does not require oscillating volume changes of the bubble to generate a force, *i.e.*, the trapping mechanisms cannot be explained in terms of Bjerknes forces.

We have successfully compared our observations with predictions for the average net force exerted by the trapping AV beam (**Figure 1**). The radiation pressure exerted by the AV on a bubble was predicted by using a full three-dimensional analytical framework [3]. In this model, the scattering coefficients of a free bubble can be calculated from the ECAH theory including thermo-viscous effects. By computing the scattered field for an incident AV we can finally derive the total acoustic force arising from the radiation pressure acting on the surface of the bubble.

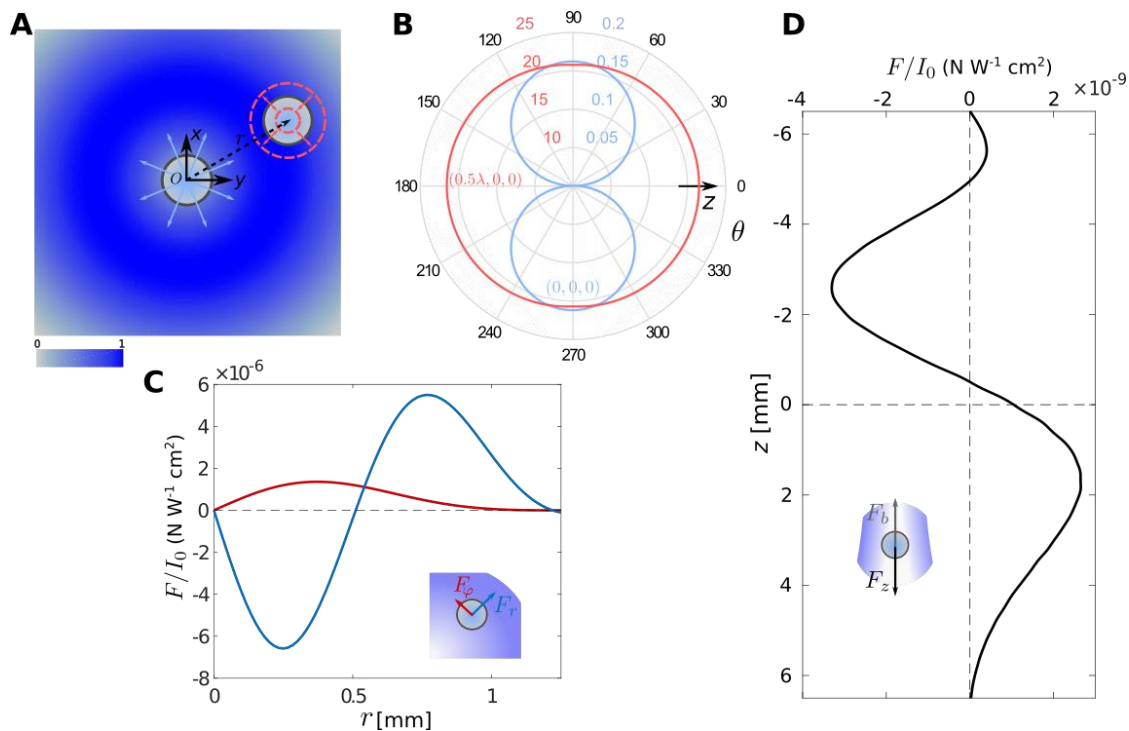


Figure 1: **A**, monopolar (red) and dipolar (blue) oscillations of a bubble located off and on-axis of the incident vortex beam (intensity in gray to blue color scale) respectively. **B**, consequent directivity patterns of the scattered field for a beam propagating along z . **C**, resulting lateral trapping force and azimuthal rotation force on a bubble of radius $a = 20\mu\text{m}$. **D**, axial pushing force (for $z > 0$) counteracting the bubble's buoyancy.

The experimental apparatus is based on an 8-element focused piezoelectric transducer operating at 2.25 MHz. It can generate a downward propagating focused AV in water. Bubbles are generated by a simple electrolysis setup and are released near the propagation axis of the AV. In our experiments, the bubble is trapped in the core of the incident AV and pushed away from the emitting source. If the bubble initially lies against an elastic gel layer (Figure 2 A), its position relative to this boundary can be controlled by adjusting the AV power. The pushing acoustic force was measured (Figure 2 B) by tracking the trajectory of bubbles at high frame rates (time-lapse in Figure 2 C). The driving acoustic force is derived from the complete force balance including buoyancy, Stokes' drag and the added mass force or the Basset Boussinesq Oseen equations. The predicted and observed forces are in good quantitative agreement for two independent experiments using bubbles of radii $a = 87 \mu\text{m}$ and $124 \mu\text{m}$. We have corrected the data points obtained to account for the observed streaming flow generated by acoustic absorption in the fluid bulk. Note that these bubbles are significantly out of the common long-wavelength assumption, $a/\lambda \ll 1$, leading to Bjerknes' expression of the acoustic force, justifying our use of a more general framework developed in Ref.[3].

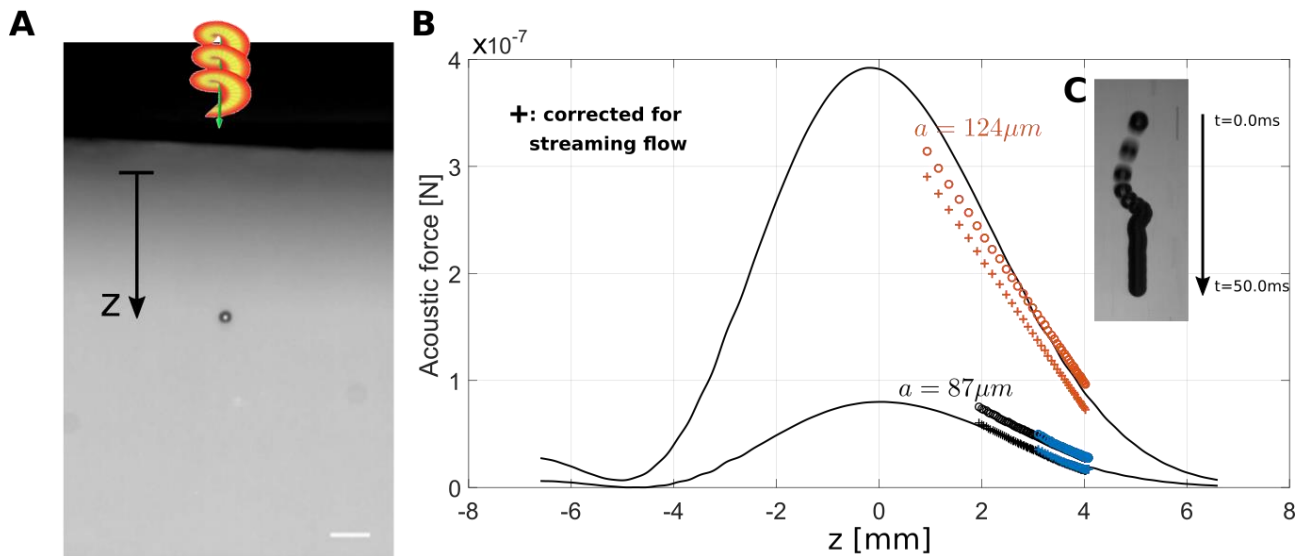


Figure 2: A, Photograph of a bubble (radius $a \sim 20 \mu\text{m}$) trapped through an elastic layer of Agarose gel ($200 \mu\text{m}$ scale bar). B-C, measurement and calculation of the acoustic pushing force for two independent bubbles ($a = 87$ and $124 \mu\text{m}$). The force is obtained from the observed trajectory (1000 fps) used to derive a force balance (C). The circles are the data points obtained without considering external acoustic streaming flows. The crosses correct the data for the influence of drag arising from the flow.

We will further investigate the extension of this experimental trapping platform to particle-coated bubbles [4-5], whose response to acoustic radiation forces have remained unexplored. These coated bubbles are toy models for future developments in the field of biomedical contrast agents and drug carriers that we envision to be dexterously maneuvered in 3D and acoustically actuated *in situ*.

Acknowledgments

Diego Baresch is funded by a Newton International Postdoc Fellowship (NF161558) and gratefully acknowledges the support of the Royal Society.

References

- [1] D. Baresch, J-L Thomas and R. Marchiano, 2016, *Phys. Rev. Lett.*, **116**, 024301
- [2] A. Eller, 1968, *Journ. Acoust. Soc. Am.*, **43**, 170
- [3] D. Baresch, J-L Thomas and R. Marchiano, 2013, *Journ. Acoust. Soc. Am.*, **133**, 25-36
- [4] V. Poulichet and V. Garbin, 2015, *PNAS*, **112** (19), 5932
- [5] V. Poulichet, A. Huerre and V. Garbin, 2017, *Soft Matter*, **13**, 125-133



Deformation of vesicles with acoustic standing waves

Glauber T. Silva¹, Liangfei Tian², and Bruce W. Drinkwater³

¹Physical Acoustics Group, Institute of Physics, Federal University of Alagoas, Maceió, Brazil
E-mail: glauber@pq.cnpq.br, URL: <http://www.if.ufal.br/~gaf>

²School of Chemistry, University of Bristol, Bristol, United Kingdom

³Department of Mechanical Engineering, University of Bristol, Bristol, United Kingdom

Introduction

It is well-known that acoustic waves carry linear momentum which can be transferred to a particle present in the wavepath. As a result, stress arises on the particle's surface that is referred to as the acoustic radiation stress. In turn, the overall contribution of the radiation stress yields the acoustic radiation force exerted on the particle. This effect has been put together with lab-on-a-chip technology to successfully manipulate, separate, and pattern biological cells and other microorganisms. A less explored phenomenon caused by the action of the acoustic radiation stress is the possibility of deforming the micro-particle's surface [1,2]. A controlled method based on acoustic deformation effect may quantitatively assess viscoelastic properties of cell membranes. Such assessment may open up an avenue of opportunities in mechanophenotyping of cells [3]. Acoustic deformation has at least two outstanding features: no contamination of the biological material occurs due to external mechanical contact, and dozens of cells can be investigated at once. Acoustic deformation poses as an alternative to contact methods used to measure mechanical properties of cells such as micropipette aspiration and atomic force microscopy. It also has an advantage over non-contact methods like optical stretchers which can only investigate one cell at the time.

Methods

We develop a theoretical model of the acoustic deformation caused by standing waves on a spherical vesicle much smaller than the wavelength, i.e., the so-called Rayleigh scattering limit. The vesicle is composed of a homogeneous liquid core encompassed by a thin elastic membrane. To calculate the acoustic radiation stress, we have to solve the corresponding scattering problem in the Rayleigh limit. After calculating this stress in the inviscid limit, we employ the shell deformation theory to obtain the vesicle's deformed radius as a function of the polar angle measured from standing wave distribution direction. Moreover, this radius depends inversely on the area elastic modulus $K_A = Eh$, where E is the membrane Young's modulus, and h is its thickness. It also depends quadratically with the vesicle's undeformed radius.

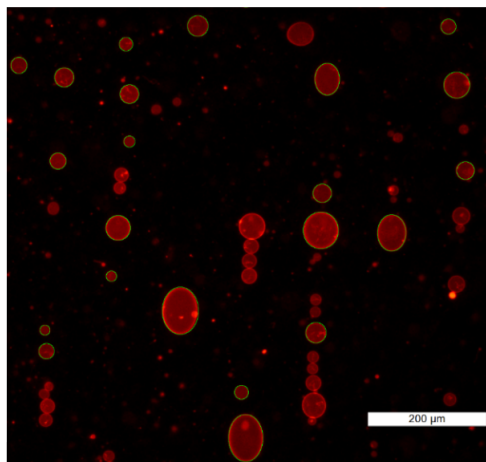


Figure 1: Image from a confocal microscope of the deformed giant unilamellar vesicles (GUVs) by a 6 MHz-acoustic standing wave. The observed diameters are smaller than 80 μm .

Results

Our theory is tested by estimating K for an acoustically deformed swollen red blood cell (sRBC) [1]. From measurements of deformed aspect ratio of the sRBC, we find $K_A = (42.1 \pm 5.6) \mu\text{N m}^{-1}$, which agrees with the optical stretcher result $K_A = 39 \mu\text{N m}^{-1}$ [4].

We are currently investigating the acoustic deformation of giant unilamellar vesicles (GUV) formed by a 4 nm-membrane enclosing a glucose aqueous solution. We have chosen GUVs because they are vesicles with no inner structure which is very close to our model assumptions. The GUVs are immersed in (2×2) cm-chamber filled with a sucrose solution. The standing waves are generated at 6 MHz by two opposing piezoelectric transducers placed in the border of the chamber. A confocal microscope image of the acoustically deformed GUVs is shown in Fig. 1. As theoretically predicted, larger vesicles are more prone to deformation.

Conclusion

We have developed a model for acoustic deformation of standing waves by combining scattering, radiation stress, and shell deformation theory. Good agreement has been found between our theory applied to sRBC and optical stretcher results. We are also investigating the acoustic deformation of GUVs. A preliminary result showing that larger GUVs are more prone to deformation is supported by our theory.

References

- [1] P. Mishra, M. Hill, and P. Glynne-Jones, *Biomicrofluidics* **8** 034109 (2014).
- [2] F. B. Wijaya, A. R. Mohapatra, S. Sepehrirahnama, and K. Lim, *Microfluid. Nanofluid.* **20** 69 (2016).
- [3] C. Alibert, B. Goud, and J.-B. Manneville, *Biol. Cell* **109** 167 (2017).
- [4] J. Guck, R. Ananthakrishnan, H. Mahmood, T. J. Moon, C. C. Cunningham, and J. Käs, *Biophys. J.* **81** 767 (2001).



Integration of Sharp-edge and bubble acoustic microstreams for rapid mixing in Microfluidic platforms

Reza Rasouli¹, Maryam Tabrizian^{1,2}

¹Department of Biomedical Engineering, Faculty of Medicine, McGill University, Montreal H3A 2B4, Canada

E-mail: Mohammadreza.Rasouli@mail.McGill.ca

² Faculty of Dentistry, McGill University

Introduction

Acoustic mixers have attracted significant interest in microfluidics, where mixing is still a challenge, due to their rapidity in achieving homogeneous environment. These mixers dissipate acoustic energy to generate acoustic micro-streams which disrupt one-directional flow pattern by adding normal advection and considerably modify the direction of mass transport [1]. Oscillatory sharp edges [2] and bubbles [1], excited by acoustic wave emanating from a piezo transducer, are shown to be two of the most efficient approaches to generate microvortices with reportedly close performance [3]. In this study, we integrate these two methods to induce a more vigorous acoustically-driven microstreams to enhance speed and homogeneity of the mixing. This integration lead to much stronger microvortices compared to sharp-edge mixers.

Material And Device Fabrication

A single-layer polydimethylsiloxane (PDMS) microchannel was fabricated by exploiting soft lithography and mold replica procedure. The PDMS was then bonded irreversibly to a glass slide, pre-treated with oxygen plasma. A piezoelectric transducer (SMBA4510T05M, Steminc) was then adhered to the glass adjacent to the channel by epoxy. The design is shown in Fig. 1, consists of sharp edges with room for bubble. When the channel is filled with solutions, the flow pass by the structure and leave a single bubble due to hydrophobic nature of PDMS and also surface tension. For repeatable bubble trapping, DI water was infused into the channel with a flow rate of 20 $\mu\text{l}/\text{min}$, though the system is not very sensitive. An acoustic transducer is adhered to the substrate of microchannel. The acoustic transducer is connected to a signal generator inducing vibration on the piezo transducer and consequently the PDMS. When driven by an acoustic transducer, the sharp edges begin to oscillate. Oscillations engender fluctuations in the flow field and pressure of the fluid, causing a strong vortex flow pattern in the channel.

Results

The piezoelectric transducer was agitated by the function generator with an amplitude of 10 V_{pp} and programmed by a square wave signal. The frequency was swept from 10 kHz to 110 kHz in 100 Hz increments while visually examining the acoustic streaming effect for a distinct prevalence of the vortices. Vigorous counter-rotating vortices were attained at the frequency of 43.7 kHz, while the deviation of more than 1 kHz from the peak exponentially reduces the vortices. To make the vortices visible, we infused DI water and food dye into the channel through two separate inlets. Upon the

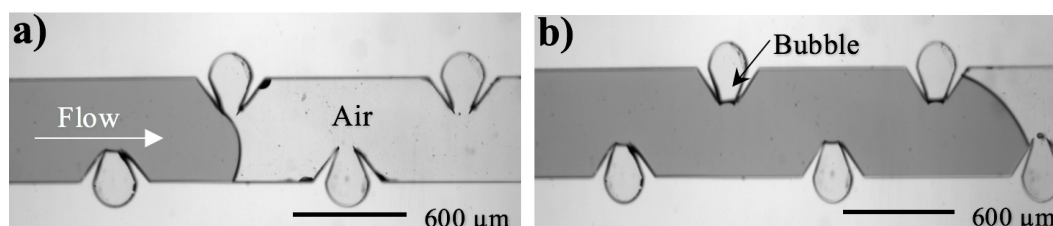


Figure 1: Formation of air bubbles in the acoustic structure. The flow is infused with flow rate of 20 $\mu\text{l}/\text{min}$ from left to right, leaving bubbles in the room between sharp edges.

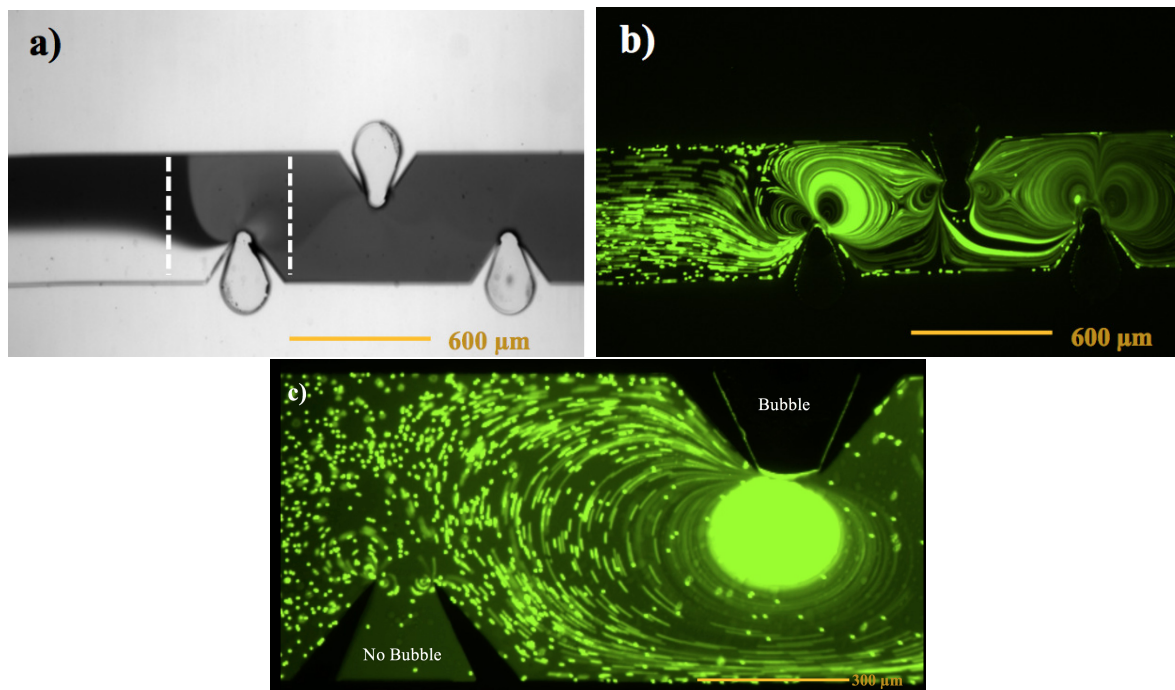


Figure 2: Mixing process in the new design a) mass transport before and after passing acoustic micro-streams b) Trajectory of 3-micron particles showing two counter rotating micro-streams c) Difference of Microstream intensity without bubble(left structure) and with bubble (right structure).

excitation of the piezoelectric transducer, the counter-rotating vortices drastically enhance the mass transport across the channel width by breaking the laminar streams and creating normal advection. With the use of this mixer, we were able to fully mix the two fluid with a flow rate of $18 \mu\text{l}/\text{m}$ which is faster than both bubble-based and sharp edge concepts, Fig. 2a. Also, 3-micron particles were infused to show the streamline of microstreams induced by acoustic streaming. As it is observable in Fig. 2b the microstreams cover the whole microchannel which shows its prevalence over infused laminar flow field and the ability to mix homogeneously. To show the impact of bubbles, we first treated half of the channel with ethanol to prevent the formation of bubbles, then we withdrew the ethanol and infused DI water and microparticles. The Fig. 2c represents the difference of microstreams intensity in the same device with and without a bubble. As it can be seen in the left structure with no bubble, the microstreams are substantially weaker than that of the structure with bubble.

Conclusion

We presented a new design for acoustic-based mixer for microfluidic platforms. When sharp edges are in the vicinity of bubbles, the acoustically-driven microstreams are substantially stronger. The intensity of microstreams is enough at the input voltage of 10 V_{pp} to prevail laminarity of an infused flow with the rate of $18 \mu\text{l}/\text{m}$.

Acknowledgments

The authors would like to acknowledge Natural Science and Engineering Council of Canada for their financial support through Discovery Grant and CREATE in Continuous Flow Synthesis.

References

- [1] Hashmi, Ali, et al. "Oscillating bubbles: a versatile tool for lab on a chip applications." *Lab on a Chip* 12.21 (2012): 4216-4227.
- [2] Huang, Po-Hsun, et al. "An acoustofluidic micromixer based on oscillating sidewall sharp-edges." *Lab on a Chip* 13.19 (2013): 3847-3852.
- [3] Nama, Nitesh, et al. "Investigation of acoustic streaming patterns around oscillating sharp edges." *Lab on a Chip* 14.15 (2014): 2824-2836.

Self-assembly of microparticles driven by surface acoustic waves

Ghulam Destgeer, Jinsoo Park, Husnain Ahmed, Muhammad Afzal, and Hyung Jin Sung

Department of Mechanical Engineering, KAIST, Daejeon 34141, Korea
E-mail: destgeer@kaist.ac.kr, URL: <http://www.flow.kaist.ac.kr>

Introduction

Self-assembly of microparticles leads to the bottom-up fabrication of ordered colloidal structures that are difficult to realize via a top-down approach. External fields such as, electric, magnetic[1] or acoustic[2], can be used to mediate the self-assembly process as the crystal structures form rapidly with better control compared to the passive techniques that are slow and tedious in operations. Acoustic methods, reported so far, to form colloidal crystals, rely on bulk acoustic standing waves.[3], [4] The colloidal particles are concentrated at the acoustic pressure nodes to generate a crystalline structure. The size of the crystal depends on the acoustic amplitude and the saturation limit of the acoustic pressure nodes. We present an experimental study of the on-demand assembly of microparticles into well-ordered structures, relying solely on travelling surface acoustic waves inside a microfluidic channel (see Fig. 1). The acoustic forces are combined with the hydrodynamic drag on the particles in a continuous flow to study the formation of colloidal crystals, their real-time rearrangement to fix the defects and the production of new cracks in the crystal.

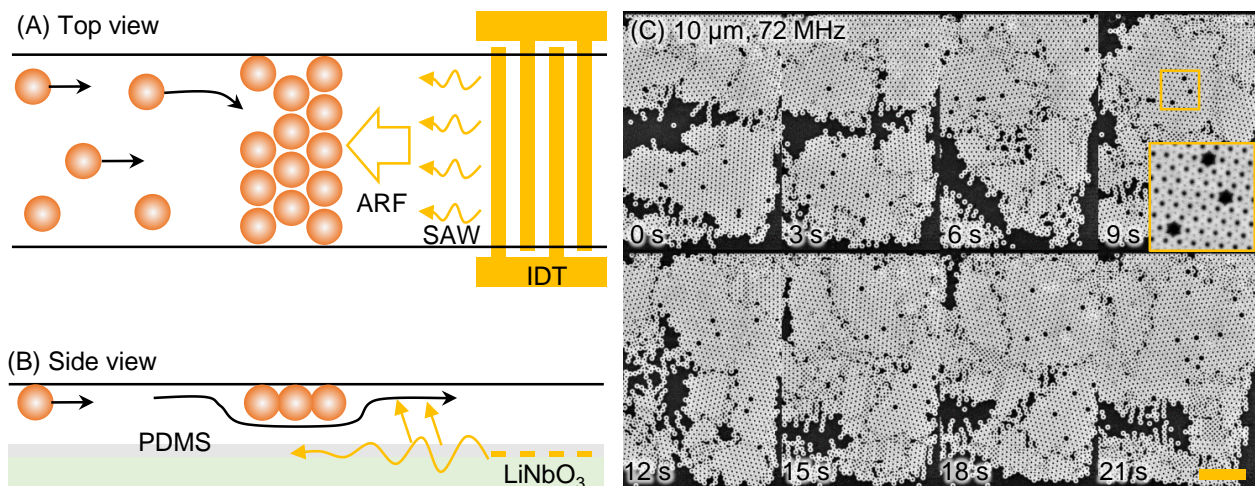


Figure 1: (A) Top view of the microfluidic channel placed on top of an interdigitated transducer (IDT). Surface acoustic waves (SAW) originate from the IDT to impart an acoustic radiation force (ARF) on the particles that is balanced with the Stokes' drag force to stop the particles and form crystals. (B) Side view of the microchannel shows a thin polydimethylsiloxane (PDMS) sealing membrane that separates the IDT from the fluid. (C) Experimental images of the trapped particles that form an ordered crystalline structure. The scale bar is 100 μm .

Experimental

The microfluidic platform used for the acoustics-driven self-assembly of the microparticles was constructed by a polydimethylsiloxane (PDMS) microchannel irreversibly bonded (oxygen plasma binding, COVANCE-MP, Femto Science, Korea) to a thin PDMS layer (90 μm) spin-coated on a salinized (1,1,3,3,5,5-Hexamethyltrisiloxane, Sigma Aldrich, Korea) silicon wafer. After punching the inlet and outlet ports, the sealed PDMS microchannel was reversibly bonded to a piezoelectric substrate (lithium niobate, 128° Y X cut LiNbO₃, MTI Korea, Korea) with a pair of interdigitated metal electrodes (width 12.5 μm , Cr/Au: 300 \AA /1000 \AA) that had been patterned using e-beam evaporation and lift-off processes (IAMD, SNU, Korea). The PDMS microchannel was fabricated by conventional soft lithography techniques where a thin layer (23 μm) of the patterned negative photoresist (SU-8, MicroChem, USA) was used as a mold. Once ready, the acoustofluidic device was mounted on a fluorescent microscope (BX53, Olympus, Korea) stage to observe microparticle trapping by the acoustic waves to form a crystalline structure inside the microchannel. The interdigitated transducer (IDT) on the piezoelectric substrate was excited by the resonance frequency AC signals produced by RF signal generators (N5181A, Keysight Technologies, USA), and the input signals were amplified by the power amplifiers (LZY-22+, Mini Circuits, USA) before feeding into the IDT. The experimental images were

recorded by a CCD camera (DP72, Olympus, Korea) attached to the microscope and an image acquisition software (CellSens Standard 1.6, Olympus, Korea). The acquired experimental images were analyzed using the ImageJ software (<http://imagej.nih.gov/ij/>) to create a montage of images captured at different time steps. The sample was prepared by introducing particles with the desired diameters in a density-matched mixture of deionized water (Sinhan Science Tech, Korea), deuterium oxide (D₂O, Sigma Aldrich, Korea) and surfactant (Photo-Flo 200 solution; Eastman Kodak Company, USA). A syringe pump (neMESYS Cetoni GmbH, Germany) was used to pump fluid through the microchannel. Fluorescent particles (Fluoro-Max™ polymer microspheres, Thermo Scientific, USA) with a nominal diameter of 10 μm (green, mean 9.9 μm) were used.

Results

Figure 1 (A) shows the schematic top view of the acoustofluidic platform used to form microparticles crystals. Surface acoustic waves (SAW) originating from the interdigitated transducer (IDT) impart an acoustic radiation force (ARF) on the particles to stop them in their path against the Stokes' drag force (see the side view in Fig. 1(B)). A thin PDMS membrane seals the microchannel and separates the IDT from the fluid. Figure 1(C) shows experimental images of the 10 μm particles that form an ordered crystalline structure when exposed to 72 MHz SAWs. The selected particles diameter and the acoustic frequency ensures that the particles experience a direct acoustic radiation force via travelling waves. Smaller crystals merge to repair a crack and form a bigger structure (0 s – 9 s). At 0 s, a big fissure at the center of the microchannel separates two crystalline bodies at top and bottom of the frame. The distance between the two crystalline bodies shortens at 3 s as the central crack nearly repairs itself at 6 s. As the crystals arrange themselves, particle holes are also formed at 9 s, where the inset shows a magnified view. From 12 s to 21 s, a new crack develops and grows near the bottom-left part of the frame as the particles adjust themselves between a crystalline and non-crystalline structure. Figure 2 shows a balance of different forces acting on the particles that are critical to the crystal formation. As the particles were continuously exposed to the acoustic waves, a crystalline structure had been gradually growing (see Fig. 1(A), 0.09 s). Crystalline form was distorted as soon as the waves were removed and the particles start to flow with the Poiseuille flow inside the microchannel (24.65 s). However, when the acoustic waves are imposed again, the particles arrange themselves in an ordered state (Fig. 2(B), 40.92 s).

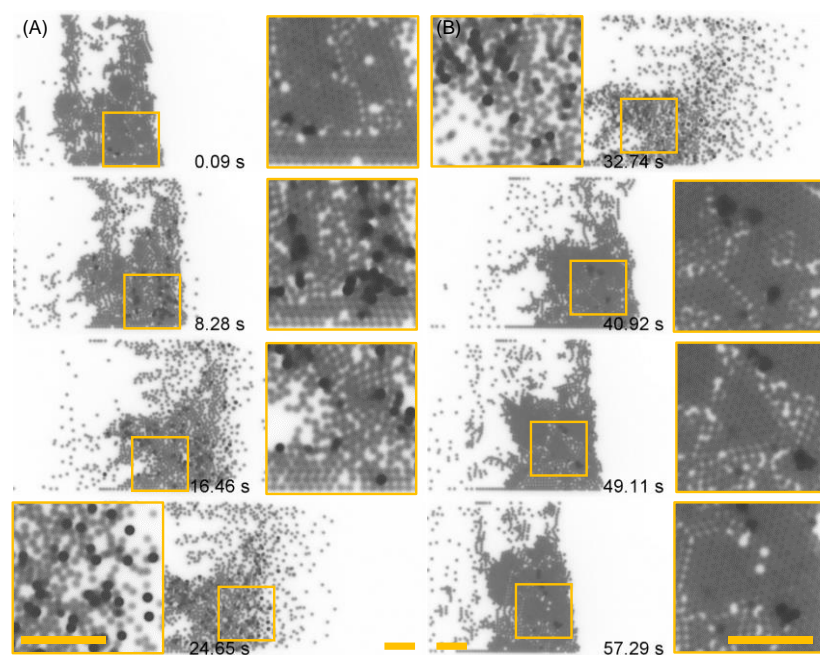


Figure 2: (A) When the particles had adopted a crystalline structure (0.09s) with the exposure to acoustic waves, the crystalline form was distorted as soon as the waves were removed and the particles started to flow with the Poiseuille flow inside the microchannel (24.65 s). The dark spots in the magnified windows indicate that the particles had moved out of the focal plan of the lens while the monolayer crystal structure disappeared. (B) Once the acoustic waves were turned back on, the dispersed particles (32.74 s) immediately arranged themselves in an ordered state again (40.92 s). Most of the dark spots merge with the monolayer crystal (49.11 s). The particles are pushed back to a position where the ARF balances the drag force on the particles clusters (57.29 s). Scale bars are 100 μm.

Conclusion

We have used traveling surface acoustic waves to trap microparticles against the interdigitated transducer. The particles gradually concentrate to form an ordered crystalline structure as the continuous flow inside the microchannel constantly exerts a drag force on the particles. The acoustic radiation force balances with the drag force to form the crystal. Once the acoustic waves are turned off, the crystalline structure disappears immediately because of the fluid flow.

References

- [1] J. Yan, S. C. Bae, and S. Granick, *Soft Matter*, vol. 11, no. 1, pp. 147–153, Dec. 2015.
- [2] Y. Yang, A. T. Pham, D. Cruz, C. Reyes, B. J. Wiley, G. P. Lopez, and B. B. Yellen, *Adv. Mater.*, vol. 27, no. 32, pp. 4725–4731, Aug. 2015.
- [3] M. Akella and J. J. Juárez, *ACS Omega*, vol. 3, no. 2, pp. 1425–1436, Feb. 2018.
- [4] C. E. Owens, C. W. Shields, D. F. Cruz, P. Charbonneau, and G. P. López, *Soft Matter*, vol. 12, no. 3, pp. 717–728, Jan. 2016.



Ultrasound enhanced PAT: increased sensitivity of an in-line Raman spectroscopy probe

Stefan Radel

Process Analytical Technology (PAT) is a modern approach when designing and controlling manufacturing processes. One main task is the definition and assessment of Critical Control Parameters (CPP). Novel instrumentation that allow for the in-line measurement, i.e. within the process itself, of CPPs are in development these days.

Raman spectroscopy is a method holding great promise for the in-line monitoring in production processes as it delivers rich information about the analyte, among which are the chemical composition but as well for instance the type of crystal forming (polymorphism). However, due to its quantum-mechanic nature, Raman spectroscopy is inherently low in respect to sensitivity. Only one of 10⁸ photons is scattered in-elastically and therefore affected by the chemical composition of the analyte and subsequently delivering the desired information. Therefore we set out to increase the sensitivity of an in-line Raman spectroscopy probe by the exploitation of the well-known radiation forces exerted on particles. These are used to increase the signal-to-noise ratio (SNR) of the measured Raman spectrum. Past work has shown, that the Raman signal of agglomerates brought about by the USW in a cuvette is comparable to the spectra of sediment.

Oscillation, coalescence and shape deformation of confined bubbles in an oscillating depth microchannel: application to the fragmentation of electrocrystallized ramified branches for an alternative synthesis of colloidal metallic nanoparticles

Fabien Chauvet¹

¹Laboratoire de Génie Chimique, CNRS-INPT-UT3, Toulouse, France
E-mail: fabien.chauvet@univ-tlse3.fr, URL: www.lgc.cnrs.fr

Introduction

This work focuses on the behavior of bubbles confined in an oscillating depth microchannel. This situation is encountered in a recently developed device, an “electrochemical and vibrating Hele-Shaw cell”, designed to synthesize colloidal metallic nanoparticles (cMnP) [1]. The principle is to make grow metallic ramified branches by galvanostatic electrolysis of a metal salt aqueous solution inside the cell, Fig. 1a. These fragile branches are composed of nanocrystals (the desired cMnP), whose the dissociation is achieved by the mechanical action resulting from the activation of a piezoelectric diaphragm (PZT) integrated into the cell as one of its largest side, Fig. 1a; the variations of the channel depth are induced by the bending of the PZT surface. In the case of the production of iron cMnP, the branches growth is accompanied by the formation of H₂ bubbles (co-reduction of H⁺), Fig. 1a. High speed visualizations of the fragmentation process highlight the key role of these bubbles whose the oscillations induce both microstreaming and branches fragmentation in close vicinity of their surface, Fig. 1b-c. An efficient fragmentation is obtained only when the PZT is driven with a square signal, Fig. 1c. The observed dependence of the bubbles behavior, to the waveform used, is analyzed with the support of specifically derived theoretical models for both breath oscillations (Rayleigh-Plesset like equation) and shape oscillations (stability analysis) of a single bubble in an oscillating depth microchannel. The specificity of the oscillating depth (the driving force), acting simultaneously on both the bubbles size and the liquid flow, is taken into account using a modified Darcy’s law adapted to small depth variations.

Experimental results

The images sequence of the fragmentation scene, using a sinusoidal signal ($f = 4$ kHz and $V_{pp} = 250$ V), Fig. 1b, shows that the branches are broken and the fragments are grouped into several blocks, set in a stationary rotational motion in the plane of the channel (red arrows in Fig. 1b), between the bubbles. These rotational motions are the signature of microstreaming induced by the bubbles oscillation. Nevertheless, these flows are not sufficiently fast to fragment the branches into small particles. It has to be noted that the bubbles network is unaffected by the PZT vibrations (no motions and no surface deformations). By performing the same experiment, but using a square signal, Fig. 1c, a more complex scene is visualized. Some of the initial bubbles coalesce to form larger bubbles which exhibit surface deformations, splitting/coalescence events and motions inside the channel. Microstreaming is also observed (red arrows in Fig. 1c) and the resulting flows break the branches and set them in motion. The fragments end up being “attracted” to the surface of unstable bubbles, where they are fragmented and ejected in the form of a cloud of particles, as it is shown in

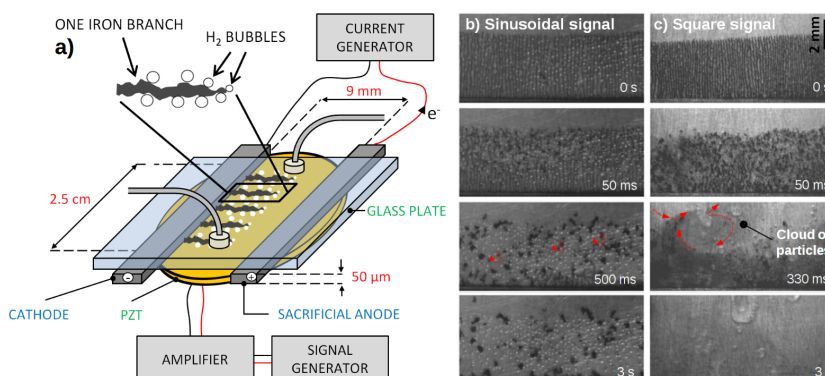


Figure 1: a) Sketch of the electrochemical and vibrating Hele-Shaw cell. b-c) Images sequences of the fragmentation process for sinusoidal b) and square c) signals, the arrows indicate the observed particles motions ($f = 4$ kHz, $V_{pp} = 250$ V, acquisition frequency = 1500 FPS; FeCl₂ 0.1 M, 80 mA/cm², growth duration = 300 s).

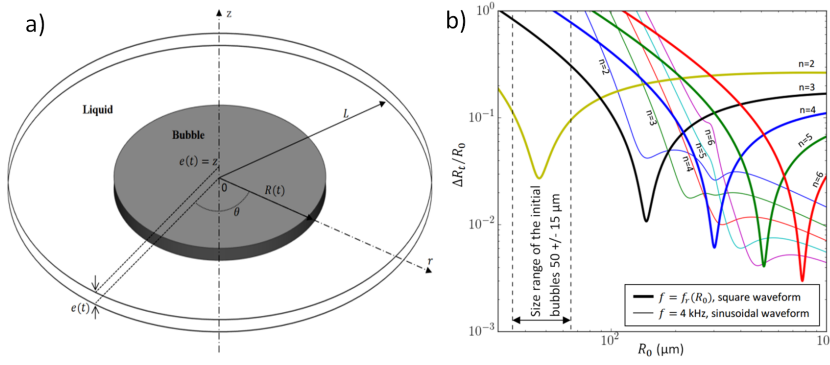


Figure 2: a) The model situation considered. b) Pulsation amplitude threshold for the onset of shape deformations as a function of the bubble size for several modes n and for both a sinusoidal waveform at 4 kHz (thin lines) and a square waveform at $f = f_r(R_0)$ (thick lines).

Fig. 1c. To sum-up, the fragmentation of the branches is observed only when large bubbles, formed by coalescence, oscillate with surface deformations when the PZT is driven with a square signal. To explain the appearance of the first coalescence events, and so the setting in motion of the initial bubbles, the assumption is made that using a square signal, bubbles pulsation amplitude is sufficiently high to induce the onset of shape deformations which lead to erratic bubbles motion, when different modes of shape oscillation interact; this phenomenon is known as “dancing bubbles” for spherical and unconfined bubbles [2].

Derivation of the pulsation amplitude threshold for the onset of shape deformations

The bubbles oscillation is considered in a simplified and model situation: a single confined bubble, of rest radius R_0 , located at the center of an oscillating thickness circular film as sketched in Fig. 2a. The oscillation of the bubble is driven by an imposed oscillation of the film thickness $e(t) = e_0 + \epsilon(t)$ which the fluctuation $\epsilon(t)$ is synchronized with the driving voltage. The modeling is based on the classical theory for the oscillations of unconfined bubbles aiming to derive a Rayleigh-Plesset equation, to describe the temporal evolution of the bubble radius $R(t)$, and an equation for the amplitude of surface fluctuations. The liquid flow is modeled by a modified Darcy’s law (taken into account inertia) adapted to small depth variations. This law is derived assuming the liquid velocity profile across the thickness is parabolic (this is valid for small Reynolds number [3] and so small $|\epsilon|$). First, breath oscillations (no shape deformations) are considered and after integration and linearization of the Darcy’s law, the equation of an equivalent forced and damped harmonic oscillator, providing the resonance frequency of the bubbles f_r (among other parameters), is obtained.

Next, the stability of the circular shape of the bubble is considered by authorizing small distortions of the surface $r_s(\theta, t) = R(t) + a(t)\Psi_n(\theta)$ (with $|a| \ll 1$ and Ψ_n is a circular harmonic of degree n) and assuming that the corresponding flow perturbation is the same as in the case of a long 2D bubble ($e \gg R$). The previous integrations are re-performed, to obtain a second order equation on a which is converted into the Mathieu’s equation, as classically done. Using the theory on the stability of the corresponding solutions, an expression for the threshold, $\Delta R_t/R_0$, is obtained. This result is easily applied to the case of a sinusoidal waveform but it cannot be directly applied to a square waveform. Nevertheless, since the resonance frequency of the initial bubbles $f_r = 30$ kHz ($R_0 = 50 \mu\text{m}$) is well higher than the applied frequency of 4 kHz, the bubbles should oscillate at their resonance frequency after a step (rise or fall) of the square signal. By considering these oscillations as stationary (low damping parameter), the threshold for the square waveform used can be estimated. The predicted thresholds are plotted as a function R_0 for several n in Fig. 2b. The developed theory shows that no shape deformations should occur for the initial bubbles when using a sinusoidal signal at 4 kHz whereas they should appear if pulsation amplitude exceeds $\sim 3\%$ when using a square signal. The pulsation amplitude has not been measured, but it has been verified that below a threshold voltage amplitude (~ 120 V), no coalescence events are observed. Additionally, keeping the same voltage amplitude of 250 V, but varying the frequency (0.1 - 4 kHz), coalescence and fragmentation events are always observed. These results are in agreement with the developed theory.

Conclusion

The observed coalescence of bubbles confined in an oscillating depth microchannel, occurring when using a square waveform, is required to dissociate the cMnP. This particular behavior is explained by the appearance of shape deformations leading to a dancing bubbles effect. The developed theoretical models can be applied to other acoustofluidics devices using a low-frequency piezoelectric diaphragm in direct contact of confined bubbles.

References

- [1] A. Iranzo, F. Chauvet and T. Tzedakis, *Electrochimica Acta* **250**, 348-358 (2017).
- [2] A. Doinikov. *Journal of Fluid Mechanics* **501**, 1-24 (2004).
- [3] C. Ruyer-Quil. *Comptes Rendus de l’Académie des Sciences - Series IIB - Mechanics* **329**, 337-342 (2001).

Bacteria manipulation in standing waves resonator, aggregation and dynamic structures

Mauricio Hoyos¹, Salomé Guttierrez-Ramos¹, Amie Wiesel², Elliott Varon¹, Jean-Luc Aider¹

¹ *Laboratoire PMMH, CNRS UMR7636, ESPCI Paris, PSL Research University, 1 rue Jussieu, 75005, Paris, France*

² *Institut Pasteur, 25-28 rue du Dr Roux, 75015, Paris, France*

E-mail: jean-luc.aider@espci.fr, mauricio.hoyos@espci.fr, URL: <http://www.acoustofluidics.org>

Introduction

Studies on Acoustic Manipulation of active biological objects like bacteria or microalgae are still rare because of the difficulties on the one hand of controlling biological parameters like motility, and reproducibility of experiments. In this work we present an study of bacteria levitation for understanding the process of aggregation or clustering in function. We describe the process of aggregation under acoustic field with frequencies between 1 and 2 MHz in an acoustic resonator. The manipulated volumes. We demonstrate differences in the aggregation process in function of bacteria motility and by using PIV measurements we observe dynamic structures forming in aggregates characterizing bacteria motility parameters.

Bacteria trapping

We designed a cylindrical acoustic trap of 180 μ m thick and 2cm diameter, where about 400 μ l volume, where bacteria suspension is poured. The ultrasonic standing wave, is generated by a cylindrical PZ26 transducer of frequency 1.69MHz. Voltages used ranges between 10 to 20 Vpp. Bacteria are then focused at the nodal plane as depicted in Figure 1 in a similar way compared to inert objects like micron-size particles. Bacteria are confined in layers of several bacteria size thickness and the cluster can be of several hundred of micrometres of characteristic size. Atypical experiment lasts 20 min, which is the replication time of the bacteria. The size and shape, are function of the acoustic energy distribution, acoustic average energy and on bacteria concentration. We consider in our experiments an acoustic energy large enough to confine the bacteria, i.e. the acoustic radial force is larger than the thrust induced by the swimming of each bacteria.

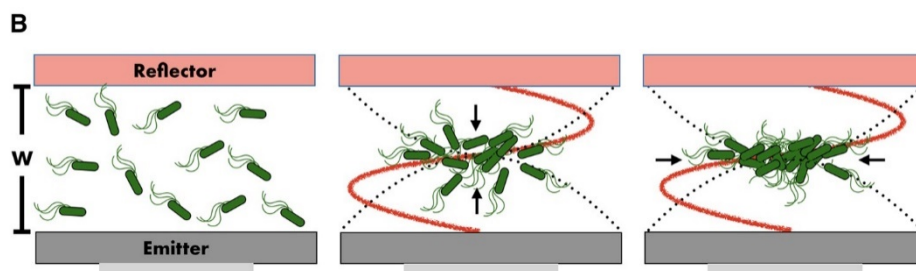


Figure 1: Principle used for the creation of a cluster of bacteria in acoustic levitation.

Creation and disaggregation of clusters of bacteria

The shape of the cluster formed at the levitation plane can be explained by an equilibrium established between the acoustic pressure and the swimming pressure exerted by bacteria motility, leading to a not well defined cluster boundary as shown in Fig 2. We will first present the aggregation and disaggregation dynamics of the clusters of bacteria as illustrated in Fig. 3. One can see that the disaggregation dynamics and the instantaneous organisation of the collective motion of the bacteria. We can control the aggregation and the disaggregation process by using different parameters like the voltage, initial concentration of bacteria, and also using pulsed mode acoustics. The control consists in modifying the aggregation and disaggregation time. We analysed several aggregates, in order to study the reproducibility. The difficulty is to have samples with the same concentration and the same mobility.

Large-scale and small scale velocity fluctuations into clusters of bacteria

The cluster formed at the levitation plane can be maintained in equilibrium for a few minutes. This is enough to study the instantaneous collective motion of the confined bacteria as well as the time-averaged

organization. A typical example is shown on Fig. 4 where one can see the large-scale coherent contra-rotating vortex created by the collective motion of the acoustically confined bacteria.

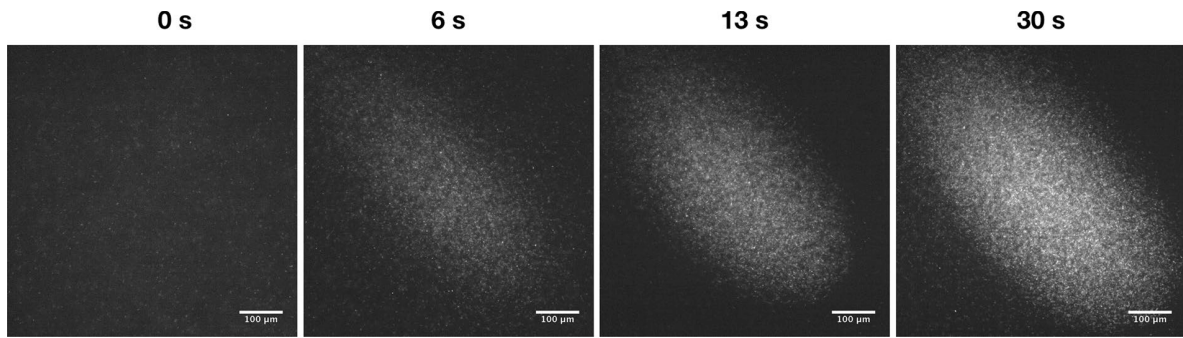


Figure 2: The bacteria clusters are created in 30s from a suspension initially homogeneously distributed in the volume. The elliptical shape of the cluster occurred with the same bacteria strand at the same place of the resonator..

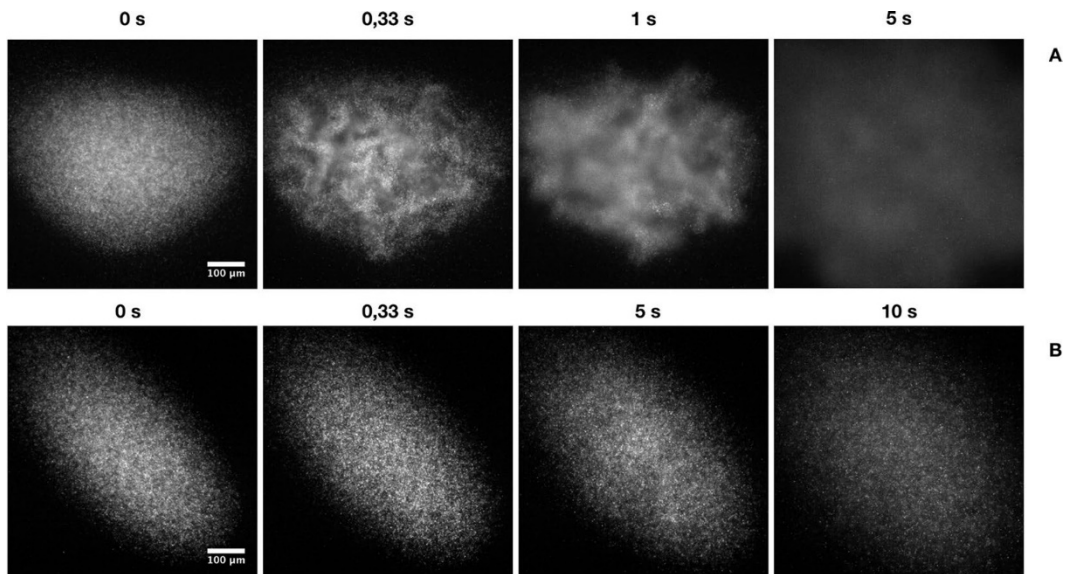


Figure 3: Two examples of disaggregation of a cluster of bacteria initially acoustically confined.

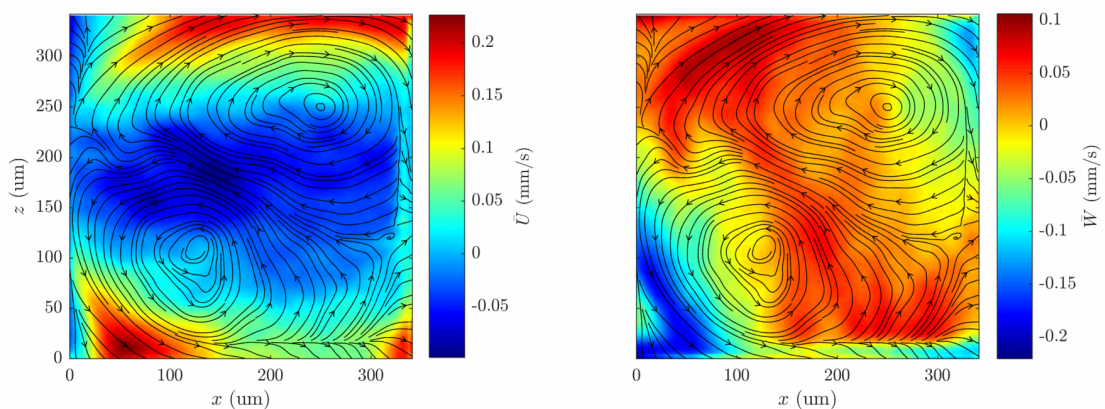


Figure 4: Creation of large-scale contra-rotating vortices induced by the collective motion of bacteria acoustically confined.

Conclusion

We have shown in this study that it is possible to create a large-scale aggregate of bacteria under acoustic levitation. The bacteria, despite their natural motility, can then be confined into the acoustic force field. This is a perfect tool to study collective motion of bacteria depending on the amplitude of the acoustic pressure applied to the colony of bacteria. We then discovered new type of collective motions in both the disaggregation process as well as in stable cluster in constant acoustic force field.

Measurement of flow resistance in the gap of a pump using ultrasonic transducer and opposing surface

Tomohiro Hara¹, Hiroaki Shinada¹, Masaya Takasaki¹, Yuji Ishino¹, Masayuki Hara¹, Daisuke Yamaguchi¹, Takeshi Mizuno¹

¹Department of Mechanical Engineering, Saitama University, Saitama, Japan
E-mail: t.hara.213@ms.saitama-u.ac.jp, URL: <http://control.mech.saitama-u.ac.jp>

Introduction

Pumps which supply air and liquid are used in various fields. These pumps usually have sliding parts and will be worn out as they drive. To solve this problem, pumps using ultrasonic vibration have been proposed. These pumps are more durable than the conventional ones because they don't have any sliding parts. Yun et al. proposed the pump using an ultrasonic vibrating pipe and flat surface faced at the end of the pipe [1]. Hasegawa et al. proposed the miniature ultrasonic pump using bending disk transducer [2]. We found an occurrence of pump effect for air when applying tapered surface for the block opposing the surface that is ultrasonically vibrating [3].

Ultrasonic transducer used for the pump

Fig.2 shows the schematic view of ultrasonic transducer used in the following experiments. A horn was attached to the top of the bolt-clamped Langevin transducer. This horn had a hole with a diameter of 4.2 mm inside to provide the path for fluid flow. The hole at the side was formed at the node of the vibration to reduce the influence of the vibration.

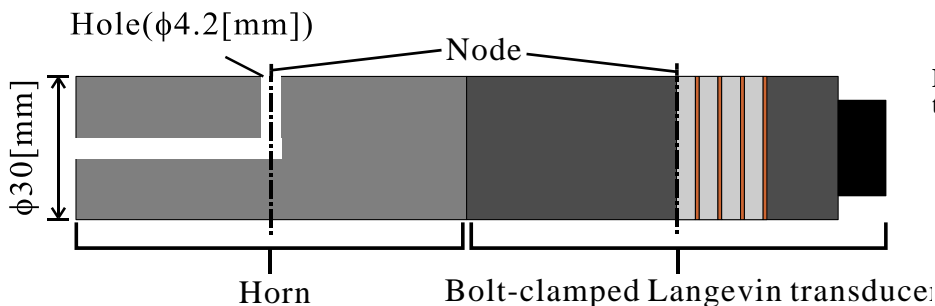


Figure 1: Schematic view of transducer

Principle of the pump effect

Fig. 2 shows the pump effect. Opposing block is an aluminum cylinder whose diameter is the same as that of the transducer, and this block has a tapered surface. In Fig. 2, α and β indicate the taper angle. A small gap is generated between the bottom of the transducer and the flat surface of the opposing block when the transducer vibrates at a resonant frequency of 28 kHz. This gap is induced by squeeze film effect. Fluid is discharged from the gap when circumference of the opposing block is tapered. On the other hand, fluid is sucked into the gap when center of the block is tapered.

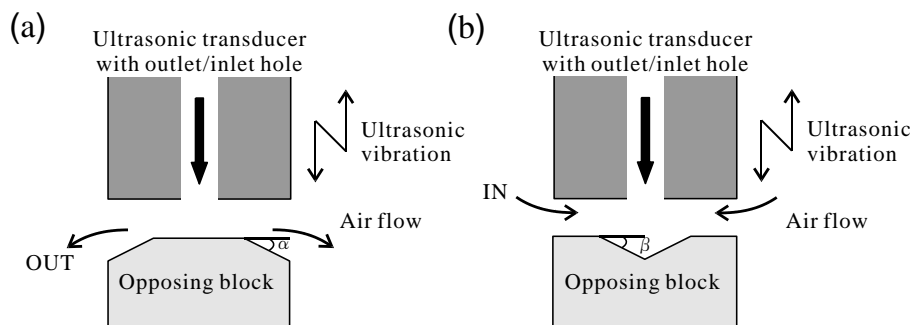


Figure 2: Principle of the pump effect (a) Air in the gap is discharged when circumference of the opposing block is tapered. (b) Air around the transducer is sucked into the gap when center of the block is tapered.

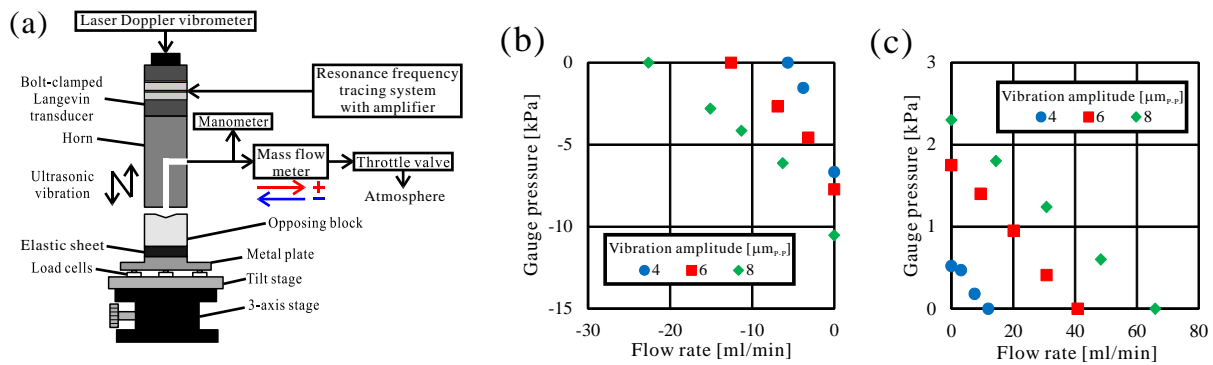


Figure 3: (a) Experimental setup. (b) Relationship between gauge pressure and flow rate of the pump with circumference taper surface. (c) The relationship with center taper surface.

Measurements of gauge pressure and flow rate

Fig. 3 (a) shows the experimental setup for observing the pump effect. The ultrasonic transducer was driven at its resonance frequency by using a resonance frequency tracing system [4] to obtain large vibration amplitude. Gauge pressure and flow rate were measured by a manometer and a mass flow meter, respectively. When the taper angle was 3° , the higher pump performance was observed for both taper shapes [3]. The performances with circumference configuration and center taper configuration are plotted on Fig. 3 (b) and (c) respectively. Gauge pressure of 10 kPa and flow rate of 60 ml/min were observed.

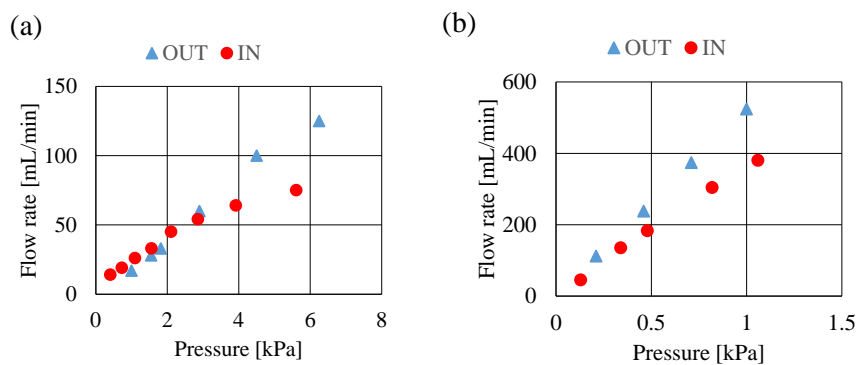


Figure 4: The measurements of flow resistance of the pump configuration without vibration (a) Relationship between pressure and flow rate with circumference taper surface. (b) The relationship with center taper surface.

The measurements of flow resistance of the pump

To discuss the principle of the effect, another experiment was carried out. Flow resistance of pump configuration was measured to investigate the reason why the flow direction is changed when the shape of the tapered surface is changed. Compressed air or vacuum was provided to the flow path of the experiment setup shown in Fig. 3 (a) without ultrasonic vibration, then air flow situations under pump effect were simulated. The gap between the bottom of the transducer and the opposing surface was set to $10\ \mu\text{m}$ constantly. Gauge pressure and flow rate were measured with change of pressure provided to the path. Measurement results are plotted on Fig. 4. Flow directions with change of pressure were same as those of Fig. 2. In both configuration, flow resistance in case of OUT flow was lower than case of IN.

Conclusion

We proposed an ultrasonic pump using an ultrasonic transducer with a hole inside and an opposing block with a tapered surface. It was found that the flow direction can be controlled by changing the shape of the opposing block. Gauge pressure of 10 kPa and flow rate of 60 ml/min were observed. Trial measurement of flow resistance under pump configuration was carried out.

References

- [1] C. Yun, T. Hasegawa, K. Hasegawa, and S. Ueha. An Ultrasonic Suction Pump with No Physically Moving Parts. Japanese Journal of Applied Physical Vol. 43. No. 5B pp. 2864–2868 (2004).
- [2] T. Hasegawa, D. Koyama, K. Nakamura, and S. Ueha. A Miniature Ultrasonic Pump using a Bending Disk Transducer. IEICE Tech. Rep. US2005-94, pp7-12 [in Japanese] (2005).
- [3] H. Shinada, Y. Ishino, M. Hara, D. Yamaguchi, M. Takasaki, and T. Mizuno. “Proposal of Pump Using Ultrasonic Transducer and Opposing Surface,” Physics Procedia 70. pp. 76 – 79, International Congress on Ultrasonics, 2015 ICU Metz, 2015
- [4] M. Takasaki, Y. Maruyama, and T. Mizuno. Proc. pp. 3817–3822, Resonance Frequency Tracing System for Langevin Ultrasonic Transducers, IEEE ICMA, 2007.

AcouWash: A standalone instrument for the washing, separation and enrichment of cells.

Jay Mallinson¹, Oskar Linander¹, Cecilia Magnusson^{1,2}, and Per Augustsson^{1,2}

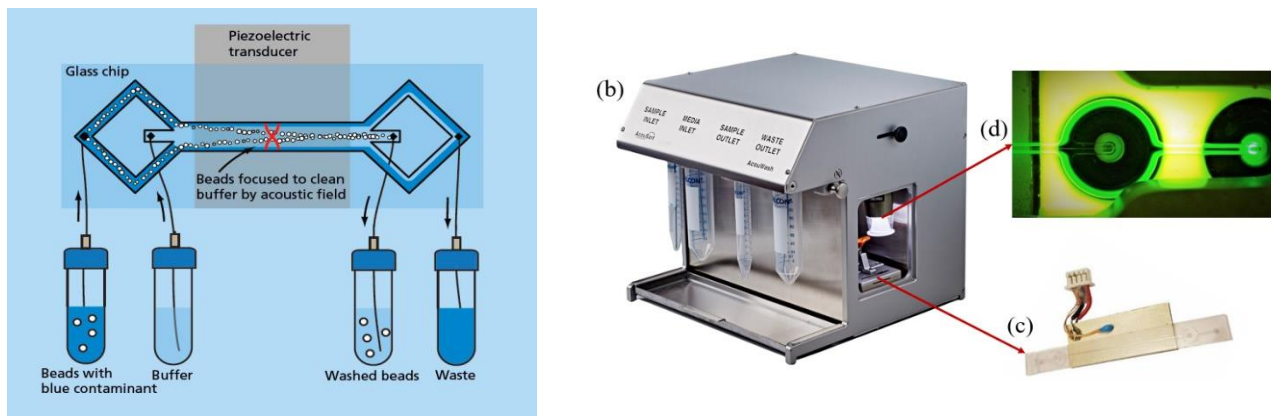
¹AcouSort AB, Lund, Sweden

E-mail: jay.mallinson@acousort.com, URL: <http://www.acousort.com>

²Department of Biomedical Engineering, Lund University, Lund, Sweden

Introduction

We developed AcouWash, a benchtop instrument for flow-through cell and particle separation by acoustophoresis. Building on previous research findings AcouWash can re-suspend cells in new medium, separate cells based on size or acoustic properties, or enrich cells [1-4]. While flowing through a glass microchannel, cells are pushed sideways into the center of the flow by an acoustic field generated by a piezoceramic transducer. AcouWash has inlets for cell sample and cell-free carrier media and a trifurcation inlet to position cells near the walls of the separation channel. At the end of the channel cells are collected in test tubes through a trifurcation outlet, Figure 1(a). By adjusting the flow velocity and the acoustic field amplitude the separation can be tuned to recover large particles (white circles) through the central outlet while small particles and dissolved molecules (dark blue) are routed to the side outlet branches.



(a)

Figure 1: (a) Schematic of the AcouWash process flow. The microfluidic chip has two inlets and two outlets and the flow rates are regulated through precise control of the air pressure within each sample container. Particles (white circles) initially suspended in blue dye contaminant are re-suspended in cell-free colorless medium (light blue). Due to the laminar flow and the short retention time in the chip there is a distinct boundary between the sample liquid and the cell-free medium. The Piezoelectric transducer, located underneath the glass chip, generates an acoustic standing wave (red curves) that exert acoustic radiation forces on the particles. This force pushes the particles across the boundary into the cell-free medium. The streams are separated in a trifurcation outlet and collected in their respective outlet containers. Photo showing (b) the bench top AcouWash system and (c) the microfluidic chip module, with piezo transducer, thermistor and ultrasound connector. (d) The output from the USB microscope, which is mounted above the micro fluidic chip. This image shows resuspension of 3-μm-diameter polystyrene particles from a fluorescein buffer into a cell- and fluorescein-free solution of phosphate buffered saline.

The AcouWash System

AcouWash is a stand-alone bench-top unit for automated, high recovery cell washing, separation and enrichment, developed as an alternative to standard centrifugation, Figure 1(b). AcouWash can handle low cell concentrations, small sample volumes, and is gentle to fragile cells. Unlike manual centrifugation and pipetting this acoustic separation technology is independent of operator skills. The acoustofluidic chip (Figure 1 (c)) measures 50 by 10 mm and may be fitted in line with other processes, enabling separation or washing in point of care analytical devices. Samples and wash medium are loaded onto the front of the instrument via customizable threaded ports. The liquid streams are pumped through the microfluidic chip using a precision flow control system, which can be monitored using the AcouWash dedicated software and USB microscope, Figures 1(d) and 2. Depending on the application AcouWash can be used in either enrichment mode (Figure 2(a)) or separation mode (Figure 2(b)).

Experimental Method

The focusing efficiency, recovery, and wash efficiency of the AcouWash system was evaluated by washing a 2.2 ml sample containing 5 μ m polystyrene particles in RPMI+PBS+Water media and resuspending the particles in PBS+1% FBS serum. The *focusing efficiency* is the number of particles recovered through the sample outlet (center) relative to all particles recovered from both outlets. The *recovery*, the number of particles recovered in the sample outlet divided by the number of particles in the input sample, accounts for all the particles that may remain in the system after processing. The *wash efficiency* measures how well the AcouWash can remove dissolved fluorescein molecules, initially present in the input sample, by transferring the polystyrene particles into new medium. This is calculated as a ratio of the number of fluorescein molecules in the waste outlet over the concentration in the input sample. Particles were counted using flow cytometry and fluorescein concentration was measured using a plate reader. During all repeats of the experiment, the sample processing rate was 100 μ l/min, and each sample took 27 minutes to process. All samples were processed using the AcouWash high recovery mode, which uses an automatic dilution sequence at the end of each sample to increase the amount of bead recovery in the outlet.

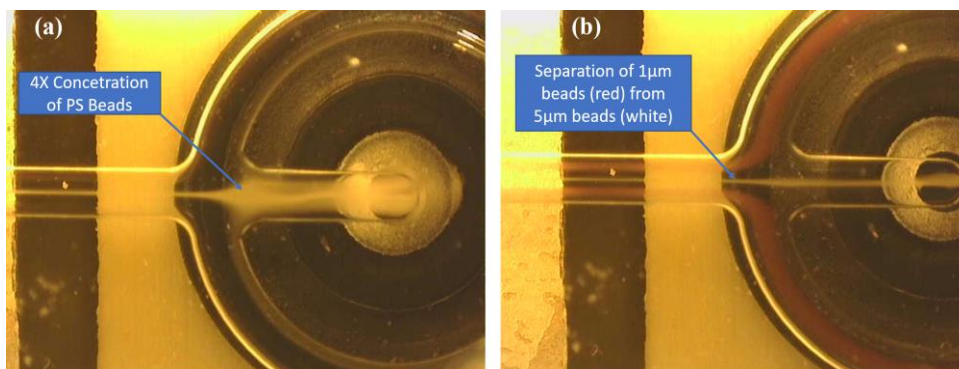


Figure 2: Screenshot images from the built-in USB microscope showing: (a) 4X concentration of 5 μ m polystyrene particles, by manipulation of inlet to outlet liquid flow ratios. (b) Separation of 1 μ m and 5 μ m polystyrene beads by adjusting the ultrasound amplitude.

Results and Discussion

Samples containing 4 \cdot 10⁵-6 \cdot 10⁵ polystyrene particles in 1ml PBS, 1ml RPMI and 200 μ l pure water were washed into PBS (+1% FBS) using the AcouWash system. In addition, samples of polystyrene beads in fluorescein solution were washed into a PBS (+1% FBS) solution and the fluorescein levels of the input sample and waste outlet were measured using a fluorescent reader to determine the washing efficiency. The pure water was added to lower the acoustic impedance of the sample stream preventing the sample stream to relocate to the central flow stream by acoustic body forces [5]. The results are shown in the figure 3.

A wash efficiency of 99.9 % is sufficient for many cell based assays and corresponds to 2-3 manual wash steps. The high recovery indicates that no particles remain inside the system after wash enabling several consecutive operations to be performed without any substantial particle loss. Separation of 5- and 1- μ m-diameter beads was found to be very good (no data). We conclude that AcouWash can wash and separate particles in a robust and reproducible manner with minimal loss of target particles and with high wash efficiency. In recent experiments, to be reported later, we have demonstrated successful medium resuspension of leukocytes and neurons and size based separation of algae with unaltered viability and function.

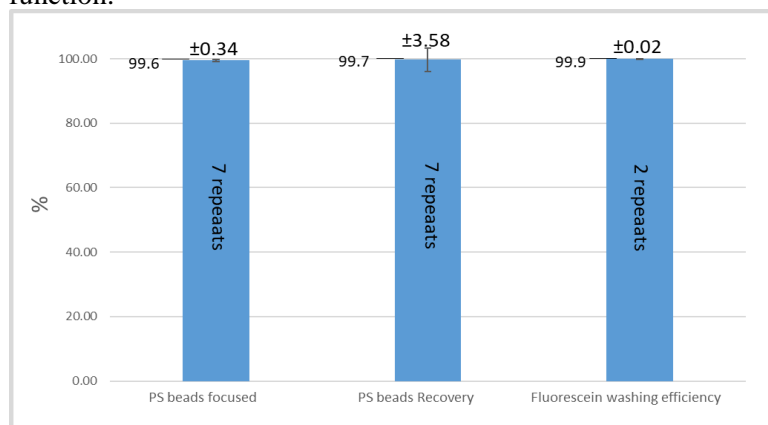


Figure 3: Bead focusing efficiency, total bead recovery and washing efficiency of the AcouWash system, after washing of polystyrene particles.

References

- [1] Hawkes, J.J., et al. Lab Chip **4**(5), 446-452 (2004).
- [2] Nordin, M. and T. Laurell. Lab Chip **12**(22), 4610-4616 (2012).
- [3] Petersson, F., et al. Anal Chem **77**(5), 1216-1221 (2005).
- [4] Petersson, F., et al. Anal Chem **79**(14), 5117-5123 (2007).
- [5] Deshmukh, S., et al. Lab Chip **14**(17), 3394-3400 (2014).



Surface acoustic wave actuated cell sorting using multilayer PDMS fluidics

T. Franke¹, K. Mustafopulos², P. Spink² and D. Weitz²

¹Biomedical Engineering, School of Engineering, University of Glasgow, Glasgow, G12 8QQ, United Kingdom. Email: Thomas.Franke@glasgow.ac.uk.

²Department of Physics and School of Engineering and Applied Sciences SEAS, Harvard University, Cambridge, MA, 02138, USA

Introduction

We summarize recent advances made on the acoustofluidic cell sorting platform that we have introduced earlier [1,2,3]. New significant experimental progress has been achieved by the combination of multilayer device fabrication with planar surface acoustic wave excitation. We harness the strong vertical component of the refracted acoustic wave to enhance cell actuation by using an asymmetric flow field to increase cell deflection. Precise control of the 3-dimensional flow is realized by topographical structures implemented on the top of the microchannel. The design attains cell sorting rates and purities approaching those of state of the art fluorescence-activated cell sorters with all the advantages of microfluidic cell sorting. In complementary and simple finite element simulations, we have been able to predict the cell trajectory by modelling the acoustic streaming in the microchannel.

Experiment

In our design, the microfluidic device is bonded directly onto a lithium niobate substrate adjacent to an interdigital transducer (IDT). When a RF signal is applied, the IDT generates travelling SAWs. Acoustic waves are excited in the channel adjacent to the IDT, in the sorting region of the device. Cells enter the sorting region of the device through the vertical flow-focusing nozzle. A slanted groove extends above the sorting region and enhances the deflection of cells by acoustic waves. Immediately after the sorting region, the device's main channel bifurcates: each cell either flows straight into the default outlet or acoustic waves actuate the cell into the sorting outlet. The design uses multi-layer features to create flows with vertical components. The vertical flow-focusing nozzle is a multi-layer feature formed at the intersection of the cell phase inlet with the channels containing the sheath flow. The cell inlet channel has a vertical constriction just prior to where it converges with the sheath channels, so the sheath flows focus the cell sample phase laterally and downward into a narrow thread at the bottom of the channel. This ensures that all cells flow along the bottom of the channel and are confined into a small region initially. If cells manage to reach the top of the channel by acoustic deflection, they interact with a different multi-layer feature, the slanted ceiling groove (see Fig.1). The slanted groove channels fluid along the groove, setting up a flow that carries cells laterally across the sorting region of the device. The magnitude of the lateral flow decreases with distance from the groove, and it is negligible at the bottom of the channel.

Results

To quantify the sorting success and to optimize devices with topographic structure, we measure the sorting performance using the tracks of moving cells. When a pulse of acoustic waves is applied to a cell, we use a high-speed camera to record the corresponding cell track; we combine the results from several cell tracks to determine a sorting success rate. Fig 1. shows the experimental cell trajectories of a cell flowing downstream a channel with a slanted groove obstacle implemented in the microchannel. The slanted groove enhances cell deflection using surface acoustic waves as observed in the experiments (right images). We analyse the sorter performance in terms of purity, efficiency and yield when varying the experimental sorting control parameters pulse length, intensity, flow rate and 3d-feature dimensions. In complementary finite element simulations we obtain cell trajectories that reproduce the experimental deflection precisely using only one fit parameter. The simulations turns out to be a useful tool to analyse more complex 3-d-features and predict cell deflection in multilayer PDMS devices.

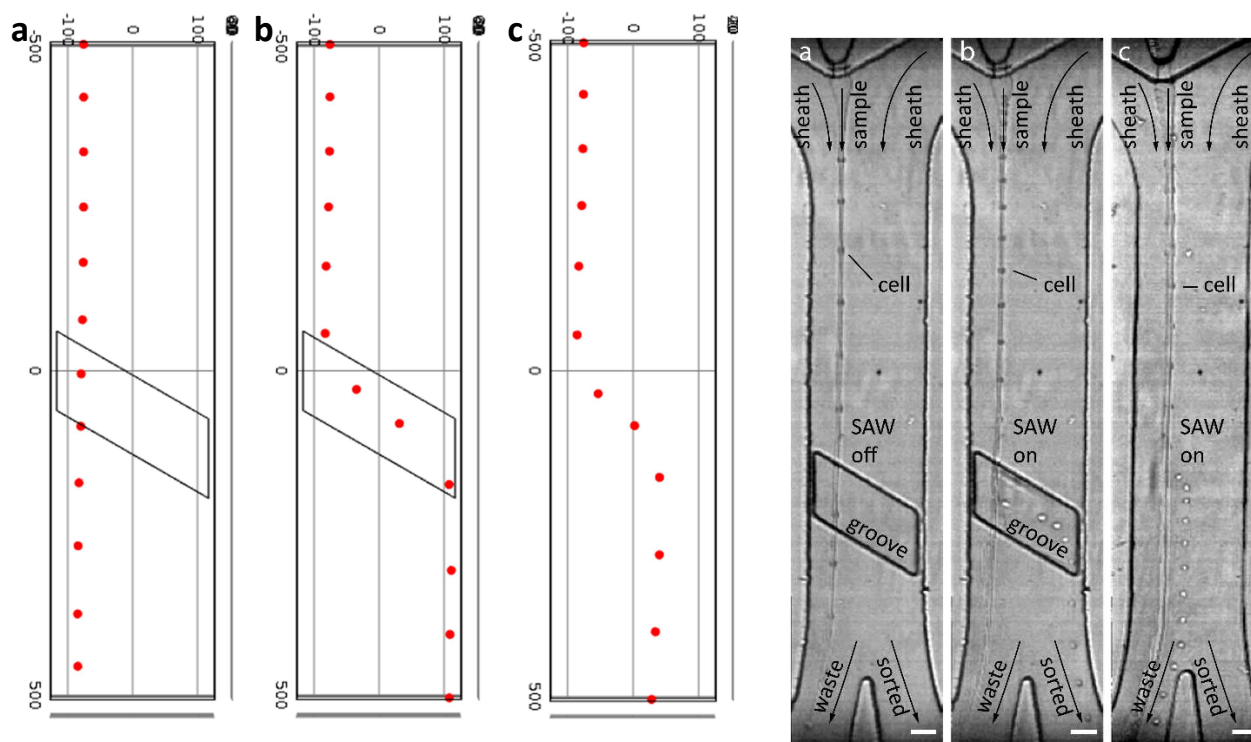


Figure 1: Simulation and experiments on lateral displacement of cells. (left) FEM simulations: Deflection of a particle flowing downstream in a microfluidic channel. (a) with a groove but no acoustic actuation the particle trajectory is straight along the channel, (b) with groove and acoustic actuation the particle is strongly deflected, and reaches the wall of the channel and (c) without a groove and acoustic actuation the particle is deflected but much less than with the groove included. (right micrographs): Fast camera movies are captured as cells flow through the sorting region of the slanted groove device. Multiple frames from a single cell transit event are superposed to create an image depicting the trajectory of a cell passing through the device (flow direction from top to bottom). (a) When no pulse is applied, the cell follows straight along the same trajectory as the bulk of the cell phase fluid. The cell passes through the sorting region and underneath the slanted groove without deflection and exits the device through the default outlet (waste outlet). (b) When a cell is detected, a radio frequency signal of 38.26 dBm is applied for 100 μ s to generate a surface acoustic wave pulse. In the device with a slanted groove, the refracted acoustic wave deflects the cell into the slanted groove, where it is carried across the sorting region of the channel by the flow of sheath fluid within the groove. The sorted cell moves laterally more than 150 μ m and exits the device through the sorting outlet. (c) For devices without a slanted groove, the sorted cell is still deflected by the acoustic wave, but the cell is only displaced about 50 μ m laterally under the same acoustic conditions. In all cases, the cell phase fluid is visible as a dark thread in the images, because of the index of refraction difference between the sheath fluid, phosphate-buffered saline, and the cell phase containing Optiprep. The cell tracks depicted here are projections of about 20 frames measured with a high-speed camera at 11,267 fps. The white scale bars correspond to 50 μ m.

Conclusion

Cell sorters with obstacles use traveling SAWs to sort cells rapidly to high levels of purity. The design features guide the vertically translated cells to isolate desired cells. The sorter operates at high rates, approaching those of commercial FACS instruments, and features a high purity mode for recovery of enriched samples. Moreover, the same SAW device platform is compatible with both cells and droplets, so a single instrument could provide users with both FACS and droplet sorting capabilities. The slanted groove devices demonstrated has been used to a variety of different adherent and non-adherent cell types demonstrating its versatile applicability.

References

- [1] L. Schmid, D. A. Weitz and T. Franke, *Lab Chip*, 2014, **14**, 3710–3718.
- [2] T. Franke, S. Braunmüller, L. Schmid, A. Wixforth and D. A. Weitz, *Lab Chip*, 2010, **10**, 789–794
- [3] W. L. Ung, K. Mutafulopulos, P. Spink, R.W. Rambach, T. Franke and D. A. Weitz, *Lab Chip*, 2017, **17**, 4059–4069.

Poster Abstracts

Gigahertz acoustic streaming induced cell membrane poration towards intracellular delivery

Xinyi Guo¹, Hongxiang Zhang², Mengjie Sun¹, Yang yang¹, Yanyan Wang¹, Wei Pang² and Xuexin Duan^{1*}

¹ State Key Laboratory of Precision Measuring Technology & Instruments, Tianjin University, Tianjin 300072, China

² College of Precision Instrument and Opto-electronics Engineering, Tianjin University, Tianjin 300072, China

* E-mail: xduan@tju.edu.cn, URL: <http://www.tjumbios.com>

Introduction

Efficient intracellular delivery of exogenous materials including anti-cancer drugs, genes, and other nanodevices remains a critical issue in fundamental biological researches and clinical applications [1]. Till now, numerous cell deformation and penetrating methods based on chemical or physical mechanisms have been developed for this purpose, and each of them keeps their respective strengths and deficiencies [2,3]. With the development of microsystems and nanotechnologies, acoustic devices based on piezoelectric effects have gained increasing attention from biomedical researchers due to their advantages such as miniaturization and batch manufacturing [4]. Based on this technology, we developed a novel chemical-free method for intracellular delivery enhancement using a designed gigahertz ultrasonic electromechanical resonator [5]. Under resonator stimulation, the propagating acoustic wave in liquid and its resultant acoustic streaming exerts strong pressure on cell membrane, thus cell poration and delivery of biomolecules can be achieved. Besides, QCM and AFM were applied in our work for the analysis of pressure generated by acoustic streaming, which provides a better understanding of the mechanisms for delivery and the interactions between fluid and cell membrane.

Intracellular delivery using acoustic streaming generated by a gigahertz resonator

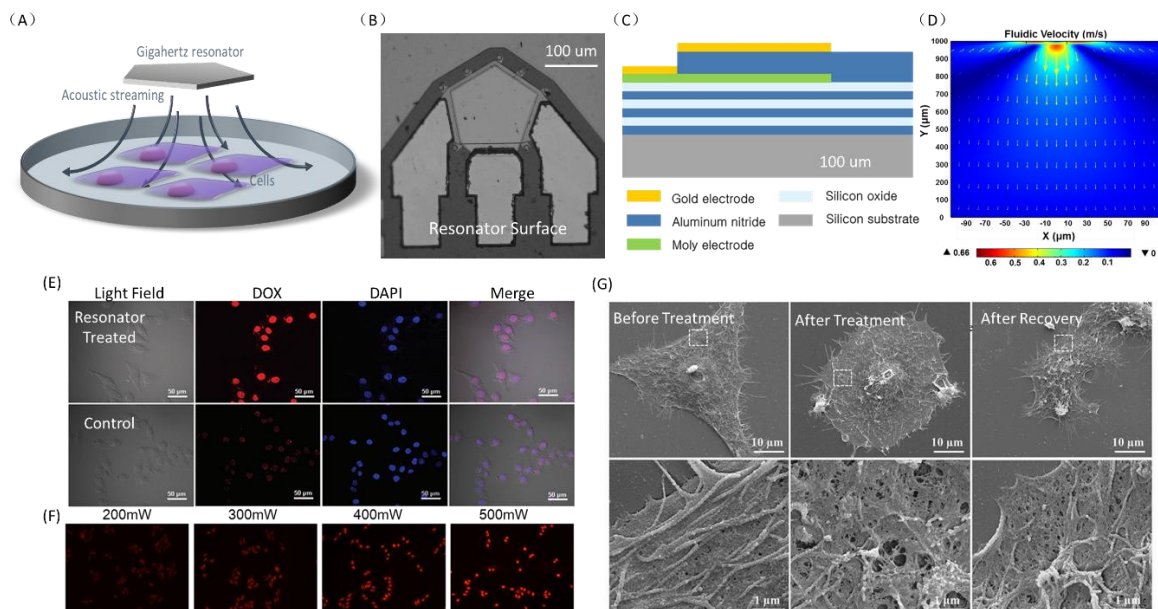


Figure 1: (A) Schematic of the intracellular delivery system. (B) SEM picture of gigahertz acoustic device surface. (C) Device structure. (D) 2D FEM analysis of acoustic streaming under resonator stimuli and its velocity distribution. (E) Results of DOX delivery, in which enhanced nucleus uptake can be seen. (F) Different delivery efficiency under different power. (G) Pores on membranes induced by acoustic streaming treatment observed by SEM.

Figure 1(A) shows the schematic of intracellular delivery system. A pentagonal-shaped electromechanical resonator with a working frequency of 1.6 GHz was designed and fabricated and is composed of a piezoelectric layer sandwiched between two metal electrodes (Figure 1(B) and 1(C)). When excited by a

sinusoidal electric signal, the propagation and attenuation of acoustic wave in liquid will generate high-speed acoustic streaming (Figure 1(D)). The liquid above the device working area will be accelerated and strike the substrate surface, thus generates pressure on cells, induces deformation and membrane poration, and finally realizes delivery of exogenous materials. To verify the intracellular delivery ability, DOX was selected as an example and its resulted intracellular distribution was recorded (Figure 1(E)). An enhanced fluorescence of DOX in cells exposed to resonator stimulation compared to control group can be seen, and cell nucleus stained by DAPI further indicated the ability to enhance nucleus uptake of this method. We also realized the delivery of fluorescent-labeled DNA strains and plasmids (data not shown here). Besides, different power applied to the resonator can induce different fluid velocity, thus generate different force intensity and control the deliver efficiency (Figure 1(F)). Pores on membranes induced by acoustic streaming treatment were observed by SEM (Figure 1(G)). Disrupted cell membranes and porous structures can be seen after treatment, and resealed after 10 min recovery, indicating a strong fluid force exerted on cells and the influence is temporary and reversible.

QCM and AFM analysis of acoustic streaming for mechanism study

To further study the intensity of acoustic streaming pressure exerted on cells, quartz crystal microbalance (QCM) was selected for analysis. Theoretically, the localized pressure generated by resonator on QCM chip surface will attenuate the resonance of chip center, split its lateral movement and increase wave number, thus increase its frequency and enable the pressure detection at the solid-liquid interface. Based on this theory, experiments for pressure detection were carried out. The results in Figure 2(A) indicate a positive correlation between resonator power and frequency shift, which correspond with the results from 3D FEM simulation. The simulated pressure distribution is given in Figure 2(B), and the calculated pressure is about several kPa.

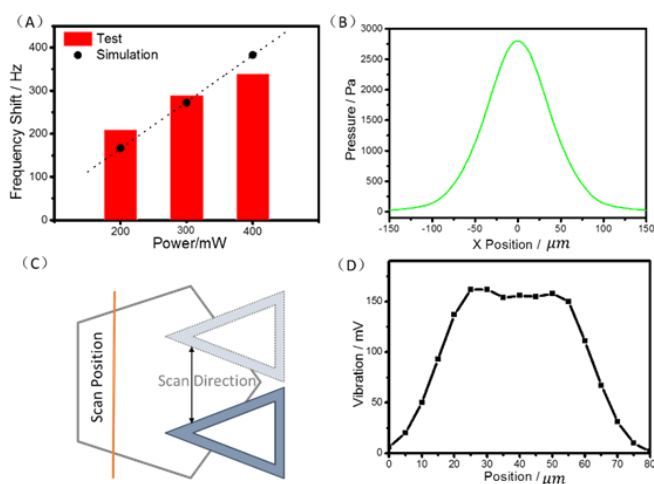


Figure 2: QCM and AFM detection of acoustic streaming. (A) QCM frequency shift given by experiments and 3D FEM simulations. (B) Pressure intensity and distribution of acoustic streaming calculated by 3D FEM analysis based on QCM frequency change. (C) Schematic of AFM detection of acoustic streaming. (D) Detected pressure distribution of acoustic streaming along one direction above the resonator surface. The most intense fluid movement occurs near the center of working area and decreases outwards. Vertical axis indicates tip deflection.

Since the sensing surface of QCM chip is much larger than resonator working area, QCM results can only tell the integral pressure in liquid environment. In order to thoroughly analyze the pressure distribution above the resonator surface, atomic force microscope (AFM) was further applied in our study. AFM probe was placed 200 μm away from resonator surface, and the pressure of the uplifting fluid during resonator stimuli bends the cantilever and thus provides pressure information (Figure 2(C)). Detected intensity along the resonator surface is given in Figure 2(D), indicating a more detailed pressure distribution inside and outside the resonator working area.

Conclusion

In this work, we successfully developed an intracellular delivery method using acoustic streaming generated by a gigahertz ultrasonic micro-resonator. All the results proved that the gigahertz hypersonic resonator has provided a versatile, well-controlled and promising way for intracellular delivery. The specific acoustic streaming pressure exerted on cells and its distribution was thoroughly studied by QCM and AFM, which very well explained the delivery mechanism, meanwhile providing a reference for pressure range that is suitable for in vitro cell stimulation.

References

- [1] MP Stewart, A Sharei, X Ding, G Sahay, R Langer, and KF Jensen. *Nature* **538**, 183-192 (2016).
- [2] D Mohanan, B Slütter, M Henriksen-Lacey, W Jiskoot, JA Bouwstra, Y Perrie, TM Kündig, B Gander, and P Johansen. *Journal of Controlled Release* **147**, 342-349 (2010).
- [3] V Sboros. *Advanced drug delivery reviews* **60**, 1117-1136 (2008).
- [4] H Zhao, X Guo, Y Wang, X Duan, H Qu, H Zhang, D Zhang, and W Pang. *Sensors and Actuators B* **223**, 83-88 (2016).
- [5] Z Zhang, Y Wang, H Zhang, Z Tang, W Liu, Y Lu, Z Wang, H Yang, W Pang, H Zhang, D Zhang, and X Duan. *Small* **13**, 1602962(2017).



Time domain multiplexing of single-beam acoustic fields for three-dimensional micro-particle manipulation in water

A Franklin¹, A Marzo¹, and B W Drinkwater¹

¹Department of Mechanical Engineering, University of Bristol, Bristol, UK
E-mail: a.franklin@bristol.ac.uk

Introduction

Ultrasonic manipulation is frequently used to give researchers the tools they need to accurately control the positions of small particles for a wide range of applications. These include bio-medical assays¹, micromanipulation of components² and additive manufacturing techniques³. Although in its relative infancy compared with optical tweezers, acoustical tweezers hold promise for tasks ranging from sub-micron to millimetric scales and have been shown to demonstrate four orders-of-magnitude higher forces than possible with optical tweezers on 200 μm particles⁴.

This paper concerns single-beam devices^{5,6} in water, which can be classified by a transducer or array emitting sound in a dominant direction. Such devices are necessary when the application does not facilitate access from multiple sides, for example flow devices under a microscope, inside the human body or within complex structures. The aim is to time domain modulate the three-dimensional acoustic forces on the trapped particles so that tailored force control for specific applications can be realised; for example, strengthening the field against the direction of gravity or flow-induced drag. Time domain multiplexing of the same field type has been previously employed to tune angular momentum in acoustic vortices⁷ and change the nodal position in a standing wave resonator⁸. The method presented achieves multiple field type multiplexing without high numbers of array elements or individually addressable electronics channels, making it portable and relatively simple to manufacture and thus more valuable to researchers and applications outside of the engineering field.

The study uses semi-analytical simulations of time domain multiplexing of different trapping force fields to achieve controllable 3D force profiles. The simulations are then used to inform experiments, including an experimental validation comparing measured and simulated pressure fields which evidences the use of the new force fields for practical application.

In demonstrating the adaptable nature of these devices and showing a single-beam transducer design capable of applying uniform and omnidirectional forcing it is hoped that a broader range of applications will be possible.

Three-dimensional acoustic force fields in trapping fields

The work by Marzo *et al.*⁹ established three optimal solutions for minimizing the Gor'kov acoustic radiation potential to create a three-dimensional trap for denser-than-host-medium particles. These solutions can be defined by their *holographic signature*: a map of phase delay required across the sound source. The three solutions do not provide equal forces along all axes, and therefore depending on the axis of greatest resistance- due to gravity, drag or other forces- in a given application different *holographic signatures* may be most suitable. Two of the *signatures* consist only of 0 or π phase delays; the so-called twin-trap and bottle-trap. For example, a twin-trap provides strong potential gradients (hence large forces) in one lateral direction where the potential is dominated by pressure amplitude effects, but produces orders-of-magnitude smaller forces in the other lateral and axial directions, where the force on the particle is dominated by velocity amplitude. Figure 1 shows the force magnitude as a 3D polar plot for (a) the twin-trap and (b) the bottle-trap at a radius of 0.35 mm from the focal point. The inhomogeneous forces are clearly shown by the irregular shape.

Although there is not a single *holographic signature* that can produce high forces in all axes, we show that omnidirectional forcing can be created by time domain multiplexing between the various *holographic signatures*. By rapidly switching between the different traps faster than the time constant associated with particle motion, more uniform forces from all axes can be achieved. This is illustrated in Figure 1(c) by a 3D polar plot of the force magnitude for a multiplexed field consisting of 6% twin-trap (3% each x and y orientation) and 94% bottle-trap. This is much more uniform than that of the single *holographic signatures*. Alternatively, the strength of the trap in different axes can be modulated depending on the real-time forces acting on a particle. Figure 1(d) shows how the maximum force magnitudes along the x, y and z axes change with varying duty cycles of the twin-traps and bottle-trap *holographic signatures*. Figure 1(e) shows a twin-trap force field with the 0.35 mm radius where the force magnitudes were calculated for (a-c) in red.

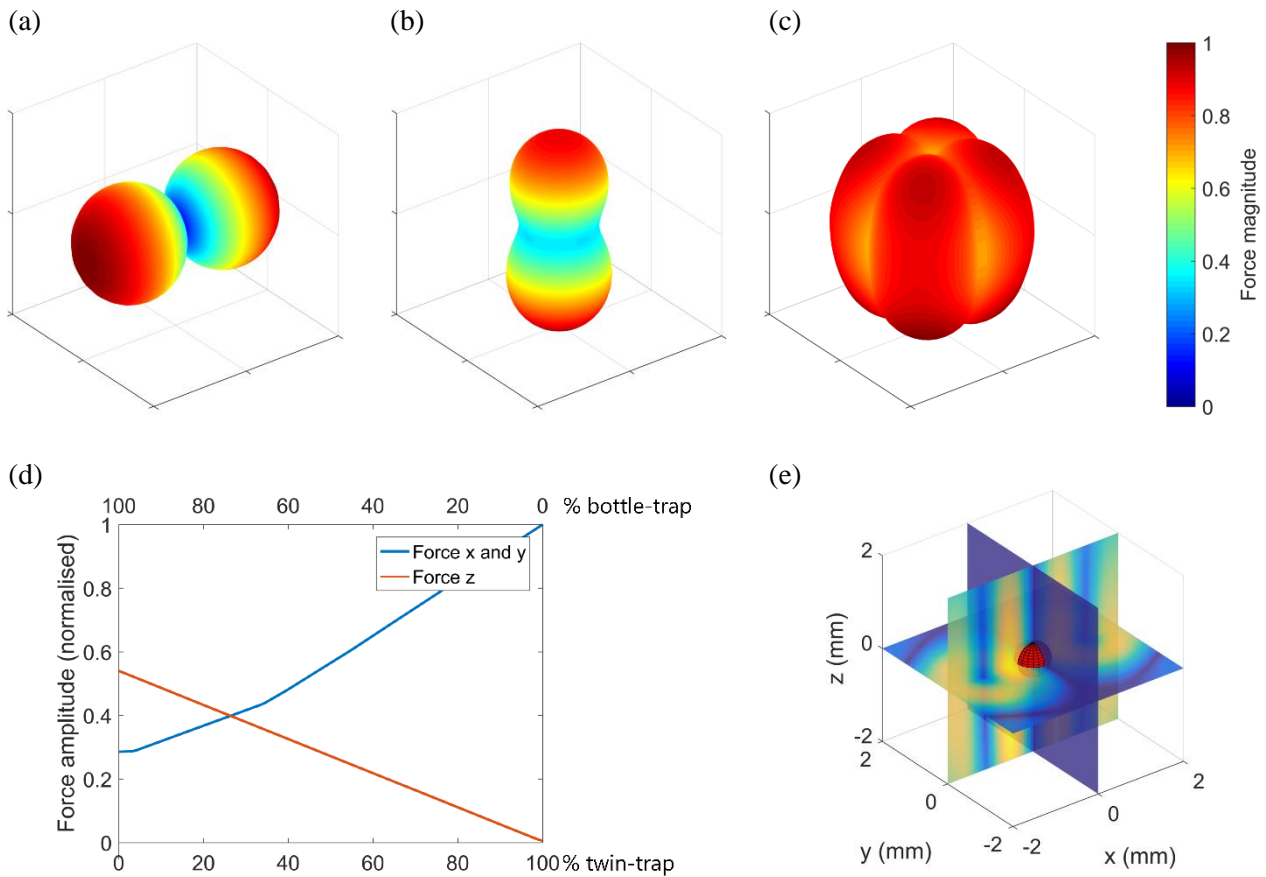


Figure 1. (a-c) 3D polar plots of the force magnitude at a distance of 0.35 mm in all directions from the trap centre (normalised) (a) Twin-trap (b) Bottle-trap (c) Time-domain multiplexed; (d) example of x, y and z axis forces for varying ratios of each trap type- the intersection point signifies the ratio which results in equal x, y, and x forces (e) example of a twin-trap force field with a 35 mm radius sphere from which the forces in (a-c) are taken shown in red.

Transducer design and validation

A transducer was designed and manufactured to form these time domain multiplexed fields. It consists of a PZT disk bonded to a 3D printed ABS acoustic lens¹⁰. The transducer is 50 mm in diameter and has a resonant frequency of 700 kHz ($\lambda_{\text{water}} = 2.1$ mm). The PZT disk is cut into sections to create the elements of the *holographic signatures*, and the sections are excited with a sine-wave of either 0 or π phase delay. The acoustic lens provides the focusing which is added to the *holographic signature* to provide the steep pressure gradients required to exert large forces. The transducer was immersed in a tank of water and a raster scan was performed with a fibre-optic hydrophone to record the pressure field. This allowed the transient fields to be characterised leading to an understanding of the maximum multiplexing speed achievable. The experimental field profiles were found to be in good agreement with the simulations.

Applications demonstration and discussion

The uniform and omnidirectional trap transducer demonstrated microparticle manipulation through an underwater ‘maze’, involving translation in all three axes. The microparticle was moved through the fluid to different positions by translating the transducer, controlled by high accuracy stage. By changing the duty cycle associated with each *holographic signature* we could strengthen/weaken the field in a chosen axis, for example, in the direction that the particle was being translated to counteract the drag forces.

References

- ¹ S.B.Q. Tran, P. Marmottant, and P. Thibault, Appl. Phys. Lett. **101**, 114103 (2012).
- ² S. Tsujino and T. Tomizaki, Sci. Rep. **6**, (2016).
- ³ K. Melde, E. Choi, Z. Wu, S. Palagi, T. Qiu, and P. Fischer, Adv. Mater. **30**, 1704507 (2018).
- ⁴ D. Baresch, J.-L. Thomas, and R. Marchiano, Phys. Rev. Lett. **116**, 24301 (2016).
- ⁵ A. Riaud, M. Baudoin, O. Bou Matar, L. Becerra, and J.-L. Thomas, Phys. Rev. Appl. **7**, 24007 (2017).
- ⁶ M.D. Brown, B.T. Cox, and B.E. Treeby, Cit. Appl. Phys. Lett **111**, (2017).
- ⁷ A. Marzo, M. Caleap, and B.W. Drinkwater, Phys. Rev. Lett. **120**, (2018).
- ⁸ P. Glynne-Jones, R.J. Boltryk, N.R. Harris, A.W.J. Cranny, and M. Hill, Ultrasonics **50**, 68 (2010).
- ⁹ A. Marzo, S.A. Seah, B.W. Drinkwater, D.R. Sahoo, B. Long, and S. Subramanian, Nat. Commun. **6**, 8661 (2015).
- ¹⁰ A. Franklin, A. Marzo, R. Malkin, and B.W. Drinkwater, Appl. Phys. Lett. **111**, 94101 (2017).



Surface acoustic wave (SAW)-driven device for dynamic cell cultures

Greco Gina¹, Matteo Agostini^{1,2}, Ilaria Tonazzini¹, Damiano Sallemi¹, Stefano Barone³ and Marco Cecchini¹

¹NEST, Istituto Nanoscienze-CNR and Scuola Normale Superiore, Piazza San Silvestro 12, 56127 Pisa, Italy
E-mail: gina.greco@sns.it, URL: <http://web.nano.cnr.it/neurosens/>

²Center for Nanotechnology Innovation@NEST, Istituto Italiano di Tecnologia, Piazza San Silvestro 12, 56127 Pisa, Italy;

³Centro Procreazione Assistita-Ospedale Versilia-USL Toscana Nordovest, Viareggio, Italy

Introduction

In the last decades new types of cell cultures have been introduced to provide better cell survival and development, and micro-environmental physico-chemical conditions aimed to mimic those present *in vivo*. Interestingly, dynamic cultures, *i.e.* those where the medium is in motion and shear stress (SS) is applied to cells, could enhance cell differentiation and metabolism or alter cell functions [1-3]. However, despite the efforts made, the systems available to date are often difficult to replicate and use. The widespread use of microfluidics in this context is indeed limited by the difficulty to adapt standard tissue culture protocols to these miniaturized biochips and because they are still typically based on bulky external pumping equipment. Here, we present an experimental study on an easy-to-use surface acoustic wave (SAW)-based platform for dynamic cell cultures, compatible with standard optical microscopes, incubators and cell culture dishes. The SAW chip is coupled to a standard Petri dish via a polydimethylsiloxane (PDMS) disk and consists of a lithium niobate (LN) substrate on which gold interdigital transducers (IDTs) are patterned to generate the SAWs and induce acoustic streaming in the dish. Excitation of SAWs is verified and characterized by laser Doppler vibrometry and the fluid dynamics is studied by micro particle image velocimetry (μ PIV). Heating is measured by an infrared (IR) thermal camera. We finally test this device with the U-937 monocyte cell line for viability/proliferation and cell morphological analysis. Data demonstrate that it is possible to induce significant fluid recirculation within the Petri dish while maintaining negligible heating. Remarkably, cell proliferation in this condition results enhanced with respect to standard static cultures. Finally, we show that cell death is not increased and cell morphology is not altered in presence of SAWs.

SAW chip and holder design

The SAW platform is composed by a microfabricated SAW-exciting chip, a chip/Petri holder and printed circuit boards (PCBs) for electrical connections (Fig. 1). The plastic holder, the PCB pogoes and the two clamps maintain the SAW-chip and the culture dish in a fixed position, ensuring the correct contact for optimal acoustic matching via the PDMS matching-disk. The working principle can be outlined as follows (orange inset in Fig. 1): the 48.8-MHz SAW that is generated by the IDT travels down to the center of the chip where a PDMS matching disk is placed. The SAW scatters through the PDMS matching disk (dark blue rectangle) into the culture medium (light blue rectangle) generating a longitudinal pressure wave that induces acoustic streaming. The net fluid motion inside the Petri dish is expected to lead to more efficient mixing and recirculation [4], and to beneficial effects for the cell cultures. The addition of a PDMS well in the culture dish (as depicted in Fig. 1) allowed the reduction of the liquid volume for the cell culture (220 μ L) and the confinement of the cells in the area overlying the matching-disk. The whole SAW platform is compact (it covers an area of about 10 cm²) and can be easily placed inside standard cell incubators. Moreover, it was designed to be compatible with standard 35-mm-diameter cell-culture dishes and standard inverted microscopes. Indeed, the optical window in the holder (see Fig. 1) is compatible with optical imaging of the cells without unmounting the culture dish from the plastic holder.

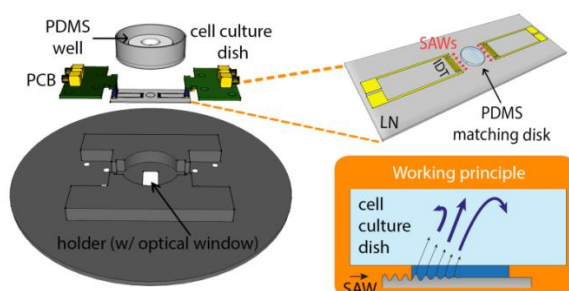


Figure 1: Exploded schematic of the SAW platform and working principle. The IDTs generate SAWs that travel down to the center of the chip where a PDMS matching disk is placed. The SAW scatters through the PDMS matching disk (dark blue rectangle) into the culture medium (light blue rectangle) generating a longitudinal pressure wave that induces acoustic streaming.

SAW activation/detection and fluid dynamics and thermal characterization

The IDTs were electrically tested by measuring the RF power reflection spectra by a VNA. A laser Doppler vibrometer (LDV) was used to map the SAW-amplitude spatial distribution and to measure the SAW-amplitude vs RF input power characteristics. Reflection spectra were quantitatively consistent among the different tested devices, showing a ≈ 10 dB dip centered at ≈ 48.8 MHz, corresponding to the expected SAW generation frequency. In general, devices showed good SAW homogeneity in the scanned area (amplitude standard deviation $SD_A \leq 15\%$). We chose to perform the experiments at two SAW amplitudes: low- and high- amplitude SAWs. We named SAW1, which corresponded to 1.1 nm amplitude, the minimum SAW amplitude at which streaming was detectable by visual observation. SAW2, found to have an amplitude of 1.7 nm, was chosen as the maximum SAW amplitude not leading to chip damage. The duty cycle $D = 2.5\%$ (500 ms SAW every 20 s) was then chosen such that in presence of SAW2 (and consequently SAW1) the heating of the culture medium was below 0.5°C (less than the typical temperature oscillations in a standard incubator upon normal operation - $\pm 1^\circ\text{C}$ -). A μPIV analysis was performed to map the fluid velocity field induced by acoustic streaming. The fluid flow was dominated by the presence of two main vortices in the planes parallel and perpendicular to the bottom of the culture dish. They were generated from a central jetting zone propagating from the bottom of the dish towards the surface of the culture medium. The resulting SS, considering a cell in suspension as a sphere of radius $10\ \mu\text{m}$, was $120 \pm 50\ \text{mN/m}^2$ and $280 \pm 120\ \text{mN/m}^2$ for SAW1 and SAW2, respectively.

Cell viability tests

In order to test the performance of our SAW-enhanced dynamic device on cell proliferation and vitality, we chose a cell model growing in suspension. U-937 monocyte cells were seeded on different devices and cultured for 48 h under standard static condition (control) or in presence of the described SAW excitations: “low-power” SAWs in case of SAW1 and “high-power” SAWs in case of SAW2. The results of these cell culture experiments ($n=3$) are plotted in Fig. 2, normalized to the control condition. Following SAW application, cell proliferation did not show statistically significant variations for SAW1, while we found enhanced proliferation in case of SAW2 ($136 \pm 12\%$; $P < 0.05$ SAW2 vs. Control, Student t-test), with respect to the control static conditions. The cells were also monitored with DAPI/propidium iodide staining, which confirmed the results of the proliferation assay and further provided insights about cell viability status. Finally, bright-field and fluorescence images of the cells stained for nuclei (blue) and actin (red) (Fig.2 a-f) were acquired in order to evaluate possible cell morphological differences among the three different culture conditions. U-937 cells cultured in presence of SAW-induced streaming did not show any marked morphological difference with respect to the control cells. Altogether, these data show that SAW dynamic devices are well suitable for cell culturing and in particular the SAW2 condition has beneficial effects on cell proliferation of U-937 monocytes.

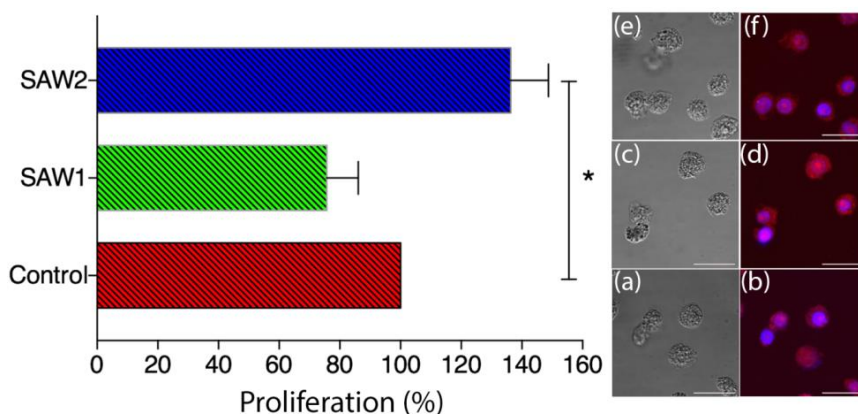


Figure 2: On the left, results of the cell proliferation assay performed on U937 cells after 48 h from seeding in case of U-937 cells cultured without SAW (red column, control), and in presence of SAWs (SAW1-green column- and SAW2-blue column-); $P < 0.05$ Control vs. SAW2, Student t-test. On the right, representative optical and fluorescence images of the cells cultured under standard control condition (a and b, respectively) and in case of SAW1 and SAW2 induced streaming (c,d and e,f, respectively).

Conclusion

We have demonstrated a novel SAW platform compatible with standard incubators, optical microscopes and standard cell culture dishes. The SAW-induced effects of fluid heating and streaming were fully characterized and controlled. Human monocyte cell proliferation in the presence of the high-amplitude SAW regime resulted to be $\approx 36\%$ higher than control. Our device is, to the authors' knowledge, the first attempt to exploit SAW-induced streaming to mechanically improve monocyte cell proliferation. We are looking forward to presenting our study for the international acoustofluidics community at *Acoustofluidics 2018* at sunny Lille, Université de Lille, Lille, France on 29–31 August 2018.

References

- [1] Datta, N. et al. Proc. Natl. Acad. Sci. 2006, 103 (8), 2488–2493.
- [2] Esch, M. B. et al. Lab Chip 2015, 15 (10), 2269–2277.
- [3] Greco, G.; Agostini, M.; Barone, S.; Cecchini, M. Sensors Actuators, B Chem. **250**, 525–532 (2017).
- [4] Shilton, R. J.; Travagliati, M.; Beltram, F.; Cecchini, M. Adv. Mater. **26**, 4941–4946 (2014).



Acoustic “spoo plasmons” in an array of sound-soft inclusions

Camila Horvath¹, María Luisa Cordero¹, Agnés Maurel²

¹LMFE, Department of physics, Universidad de Chile, Santiago, Chile

²Institut Langevin, CNRS, ESPCI ParisTech, Paris, France

E-mail: camila.horvath@ing.uchile.cl

Introduction

From a long time humans have been looking for new materials that present special characteristics, such as invisibility, negative refractive index, negative Poisson’s index, and others. Recently it has been discovered that it is possible, by building different structures with a “normal material”, to create a material that presents characteristics that aren’t found on nature. These new materials are known as metamaterials.

The concept of metamaterial is linked to different areas of physics, this work is centered on acoustics metamaterials and it’s sound-wave interaction. A beautiful and recurrent example of this kind of materials is the sculpture “Organo” of Eusebio Empere, placed in Madrid, Spain [1]. The sculpture is an acoustic crystal, able to block the propagation of sound waves of frequency around 1.6 kHz. In simple terms that means that, if we place a piano and try to hear it through the sculpture, we wouldn’t be able to hear when the pianist plays the keys 71 and 72 of the piano (*Sol*₅ and *Sol*₅[#]/*Lab*₅).

We are studying guided waves on the surface of a one-dimensional acoustic metamaterial (Figure 3, a). The metamaterial consists in a periodical array of rectangular cross section pillars, built in a sound-soft material, specifically, air structures on a polydimethylsiloxane medium. The metamaterial is excited by an incident wave whose wavelength is several orders of magnitude higher than the structure’s periodicity. The surface waves generated will be also known as “acoustic spoo plasmons”.

The problem it’s being studied experimentally, theoretically and numerically, using homogenization methods [2,3] to simulate the wave field on the array, excited by the incident wave, and comparing this results with the experimental measurements.

Numerical study of surface waves on a periodical array of penetrable scatterers [4]

Using two-scale homogenization techniques and multimodal methods, we studied a unidimensional array of air structures on a water media, showing that spoo plasmons can exist in a sound-soft array of inclusions (Figure 1). Furthermore, we demonstrated that when sound-soft inclusions are used, the wave excited on the surface has much lower wavelengths than using sound-hard inclusion. In addition, we showed that the wavelength of the acoustic spoo plasmon generated can be tuned by changing the impedance of the structures (Figure 2).

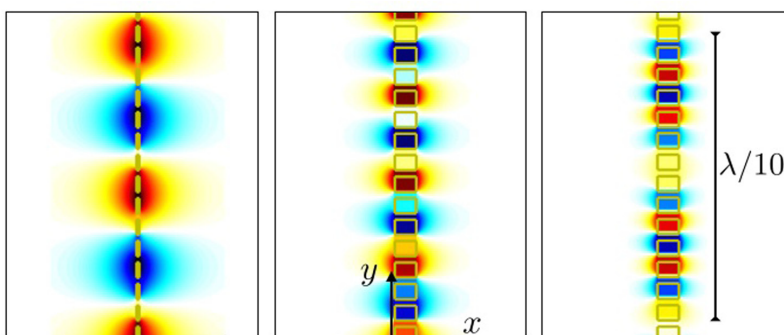


Figure 1: wavefield of the surface waves generated by an acoustic wave of wave length $\lambda = 7$ cm, for different geometries of the inclusions.

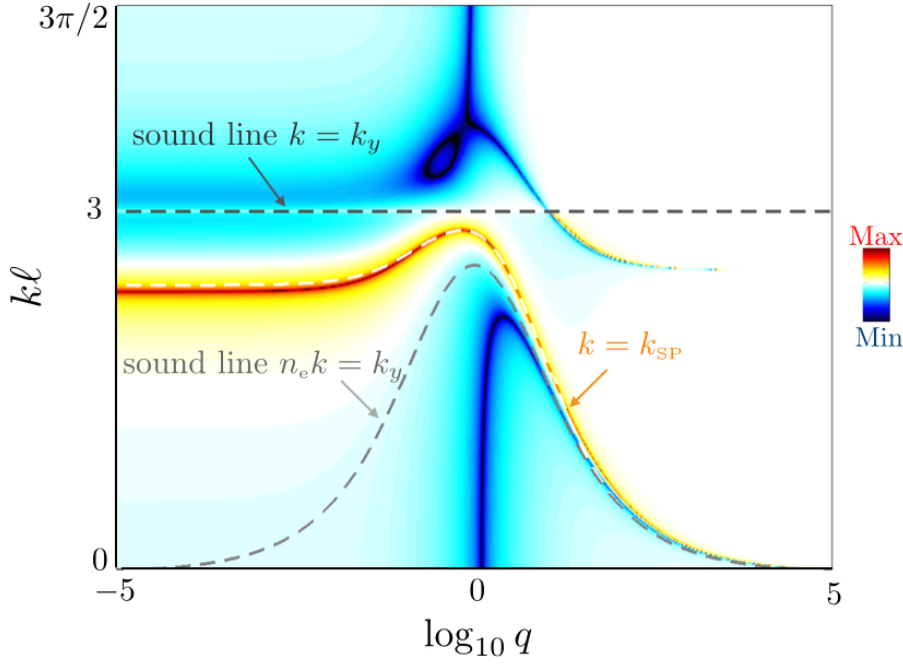
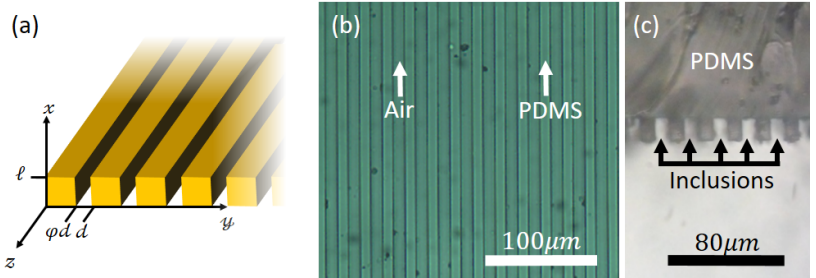


Figure 2: Dispersion relation as a function of the acoustic impedance contrast ratio q , evidenced by the divergence of the reflection coefficient (in color scale), for a fixed incident wavenumber. Meaning that the wavenumber of the Surface wave can be tuned by adjusting the impedance contrast ratio q

Experimental setup for generation and analysis of surface guided wave

We use optical lithography techniques to form the metamaterial’s air inclusions on a film of polydimethylsiloxane (PDMS) [5], with a global area of $9\text{ cm} \times 9\text{ cm}$ (Figure 3,b,c). The metamaterial is composed by thousands of parallel pillars, $10\text{ }\mu\text{m}$ high along the axis x , $18\text{ }\mu\text{m}$ wide along y and $\approx 10^5\text{ }\mu\text{m}$ long along z (Figure 3, a), separated by a $10\text{ }\mu\text{m}$ space between them. For measuring, it is encapsulated on a cylindrical media and excited using transducers at a frequency $\approx 200\text{ kHz}$.

Figure 3: (a) Air inclusions model used to study surface waves on a sound-soft inclusions array, the structures of width $\varphi d = 10\text{ }\mu\text{m}$ and height $\ell = 18\text{ }\mu\text{m}$ are distributed with a spacial periodicity d along y . (b) (y, z) plane view of the metamaterial produced in our laboratory. (c) (x, y) plane view of the air inclusions on a 3 mm thick PDMS film.



Conclusion

We have theoretically demonstrated the possibility of tuning the frequency of the spoof plasmons by changing the acoustic impedance contrast between the inclusions and the medium [4]. We successfully fabricated a $9\text{ cm} \times 9\text{ cm}$ metamaterial consisting in an array of micrometric air bubbles encapsulated in a PDMS matrix and we are conducting experiments to verify the numerical results.

References

- [1] R. Martínez-Sala, J. Sancho, J. V. Sánchez, V. Gómez, J. Llinares, and F. Meseguer. Nature **378**, 241-242 (1995).
- [2] J. J. Marigo, A. Maurel, K. Pham, A. Sbitti J. Elast. **128**, 265-289 (2017).
- [3] A. Maurel, J. F. Mercier and S. Félix. ASA **135**, 165-174 (2014).
- [4] M. L. Cordero, A. Maurel, J.-F. Mercier, S. Félix, and F. Barra. Appl. Phys. Lett. **107**, 084104 (2015).
- [5] V. Leroy, A. Strybulevych, M. Lanoy, F. Lemoult, A. Tourin, and J. H. Page. Phy. Rev. B **91**, 020301 (2015).

Acknowledgement

PhD. student finance by CONICYT National PhD-fellowship: Beca Nacional (2016) N°21161479. Samples were fabricated using the microfabrication facility funded by project FONDEQUIP EQM140055.



Performance exploration of Acoustic force spectroscopy (AFS™) chips

Andreas Winkler¹, Cynthia Richard¹, Felix Oswald², Douwe Kamsma², Siegfried Menzel¹ and Thomas Gemming¹

¹SAWLab Saxony, Leibniz Institute for Solid State and Materials Research (IFW) Dresden, Germany

E-mail: a.winkler@ifw-dresden.de, URL: <http://www.SAWLab-Saxony.de>

²Lumicks B.V., Amsterdam, The Netherlands URL: <http://www.lumicks.com>

Introduction

Acoustic Force Spectroscopy (AFS™) is a novel, commercially-available acoustofluidic technique that enables scientists to investigate mechanical properties of biological systems which may either be molecules attached to synthetic microspheres or cells in a label-free setup. These experiments can be performed in a highly parallel fashion, making AFS™ an ideal tool for a wide variety of biological investigations, including, but not limited to studies on DNA, antibody - antigen affinity, protein unfolding, cell manipulation, microrheology, lipid membrane interactions, enzymatic activity and DNA-protein interactions.^{[1][2]}

AFS™ chips utilize resonant bulk acoustic wave (BAW) modes excited by a piezoelectric plate mounted on a glass biochip with interior microfluidic channel. For high efficiency, accuracy and reproducibility, AFS™ relies on a homogeneous amplitude distribution in the active region of the biochip, i.e. on the lower side of the microfluidic channel. However, BAWs show a complex acoustic behavior with very narrow frequency bandwidths and a strong dependency on the acoustically relevant boundary conditions, including setup geometry and electrical signaling. Due to acoustic diffraction and refraction, disturbances in the wave field, i.e. the lateral distribution of amplitude and phase, can occur, leading to parasitic effects and unwanted behavior of the micro-acoustofluidic system.

In this combined experimental and numerical study, we investigated AFS™ chips in respect to their geometry, their electrical behavior and the excitable acoustic wave modes. Various analytic techniques, including Laser Doppler vibrometry (LDV), 3D stylus topography measurement, high-resolution large-area digital microscopy, computer tomography (CT) and vectorial network analysis (VNA), were applied. Furthermore, based on the gained knowledge of the device dimensions, we modelled the electric and acoustic behavior using the finite element method (FEM). As will be presented, our comprehensive approach results in a deep understanding of the frequency-dependent evolution of the complex acoustic wave field in AFS™ and the origins of possible wave field disturbances, e.g. wave-structure interactions.

Experimental and Simulation

The exact 3D geometry of AFS™ chip setup was determined by a combination of digital video microscopy (VHX 6000, Keyence GmbH, 3D stitching with 100x magnification), surface profilometry (Dektak XT-A, Bruker Co.) and X-ray absorption computer tomography (Nanotom M, General Electric). The resistivity of the ITO contact electrodes on the piezo was determined via van-der-Pauw method. The electrical radio-frequency behavior was investigated with a vectorial network analyzer (VNA E5070B, Agilent Technologies) regarding the complex scattering (S-)parameters, which were used to calculate the corresponding impedance/admittance curves and the time-domain behavior.

The lateral distribution of amplitude (the surface normal component u_3 , only) and phase of the oscillation was determined via Laser Doppler vibrometry (UHF 120, Polytec GmbH) using large scan fields ($> 10.000 \text{ Px}^2$) and broad multi-carrier sinus signals (> 100 Fourier lines) at the lower chip surface. Lateral standing waves resulting from diffraction and refraction were visualized with an aqueous dispersion of $10 \mu\text{m}$ Polystyrene particles inserted in the AFS channel via a syringe pump (neMESYS, Cetoni GmbH) during the excitation at chosen frequencies.

The measured 3D geometry as well as known and measured material properties were used to create a model in Comsol Multiphysics 5.3a (Comsol Multiphysics GmbH) in a 3D slice model. On the one hand, the impedance spectrum was simulated and compared to the measured ones. On the other hand, the displacement amplitudes (mode shape) and the transient acoustic excitation was simulated for chosen frequencies of operation.

Results & Discussion

The comprehensive experimental approach to analyze AFS™ chips combined with numerical FEM simulation carried out in this study enabled deep insights into the device function. Thereby, (1) geometry-related issues (e.g. geometry of glass chip, piezo placement and deformation), (2) the ideal (FEM) and real (VNA) electrical rf behavior of the chips (e.g. Fig. 1), (3) frequency-related amplitude and phase distributions, i.e. the excitable

wave modes (e.g. Fig. 2) and (4) their transient evolution were revealed. With this knowledge, the origin of local (chip internal) scattering and diffraction, as well as their influence on the stationary wave field can be determined. On the one side, this enables the choice of an ideal driving frequency to achieve a homogeneous amplitude and phase distribution over a large area of the microchannel. On the other side, it makes the search for an improved device layout possible. The results of the study will be discussed in detail.

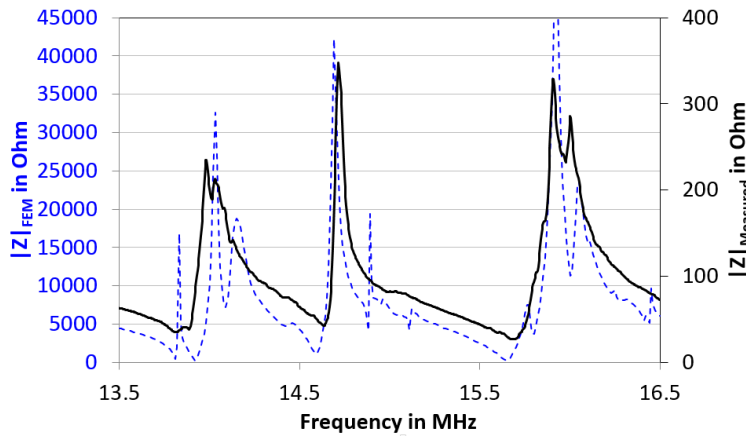


Figure 1: Measured and FEM-simulated spectra of the electrical impedance of an AFSTTM chip under investigation in the dry state

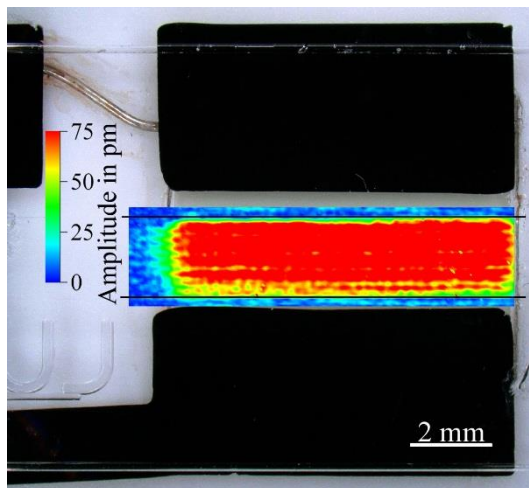


Figure 2: Acoustic Force Spectroscopy (AFSTTM) chip layout under investigation (view on lower chip side) with overlay of a measured amplitude distribution (surface normal component $u_{3,max}$); channel location indicated by black horizontal lines

Conclusion

Here, we studied acoustic force spectroscopy chip devices using advanced analytic techniques dedicated to their electrical and acoustic behavior as well as their geometric and material-related, acoustically-relevant boundary conditions. Using a comprehensive approach, we are able to investigate the frequency-dependent evolution of the complex acoustic wave field to better understand and control the origin of parasitic effects based on wave diffraction and refraction as well as material and geometry properties.

References

- [1] G. Sitters, D. Kamsma, G. Thalhammer, M. Ritsch-Martel, E. Peterman and G. Wuite, *Nature Methods* **12**, 47-50 (2015).
- [2] D. Kamsma, R. Creyton, G. Sitters, G. Wuite and E. Peterman, *Methods* **105**, 26-30 (2016).

Silicon particle enrichment in flow conditions for the improvement of metal 3D printing resolution and material variability

Michael Gerlt¹, Miriam Müller¹, Jürg Dual¹

¹Department of Mechanical and Process Engineering, Institute for Mechanical Systems, ETH Zurich, Zurich
E-mail: gerlt@imes.mavt.ethz.ch, URL: www.zfm.ethz.ch/e/exp-dyn

Introduction

Laser Powder Deposition (LPD) is one of the most flexible technologies for metal, alloy and composite material 3D printing [1]. However, the resolution is not precise enough to meet all needs of e.g. the watchmaking and med-tech industry. To be able to overcome this limit, a new approach has been proposed by a consortium consisting of Swiss research institutions which is based on a combination of particle enrichment in continuous flow conditions, electrostatic droplet ejection, microwave drying and laser melting, Fig. 1. In this experimental study, the first step of this revolutionary approach - silicon particle enrichment in continuous flow conditions by means of Acoustophoresis - is evaluated.

System design

To achieve a higher resolution in metal 3D printing, smaller particles need to be used. When the particle size drops below a critical limit, van der Waals forces start to dominate and the particles tend to form clumps. Clumped particles cannot be melted or sintered in a reproducible manner. Therefore, small particles (< 5µm) need to be dispersed in a solution. However, dispersed particles have a much lower packing density than solid material. To achieve a print speed that is comparable to state of the art methods, the concentration of the particles need to be increased in continuous flow. Furthermore, to impede the abrasion of the nozzle tip, the particles should be focused in the center of the device.

We designed two systems that are capable of achieving the before mentioned demands. The first system is based on a combination of capillaries with different geometries as suggested by [2]. A round capillary with tapered tip is inserted into a square shaped capillary. The particles are focused in the center of the square-shaped capillary and transmitted to the round capillary. A high percentage of the liquid is extracted at the side of the square capillary, Fig. 2a. Therefore, the particle concentration in the round capillary is much higher than in the square-shaped capillary. The desired enrichment is achieved.

The second system is based on silicon chips. They are fabricated using standard clean room fabrication techniques. The chip designs are based on experiments that have been performed in literature, Fig.2b [3]–[6]. A combination of all the tested techniques is tested to optimize the increase in concentration.

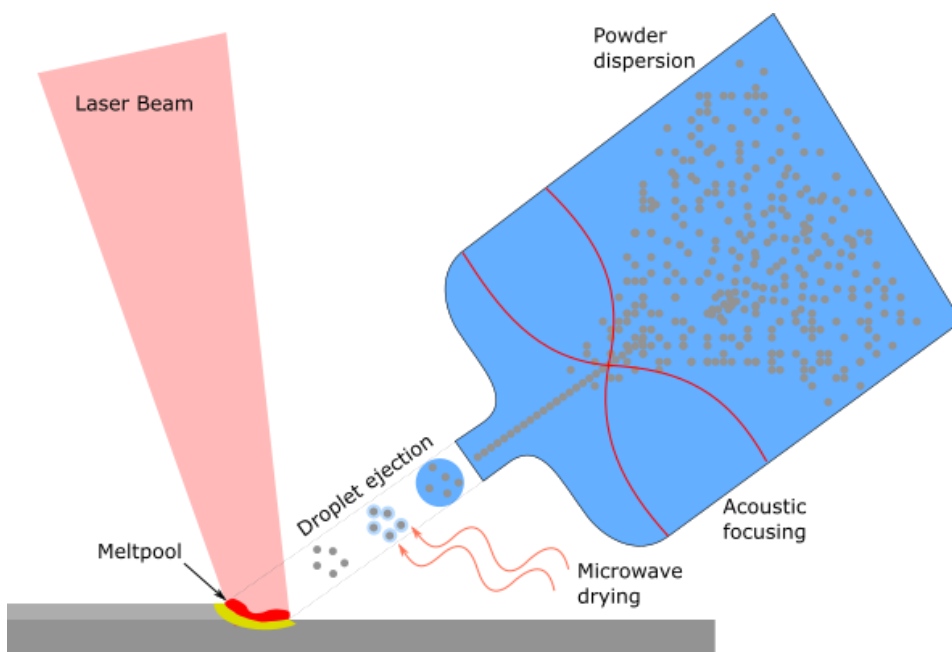


Figure 1: Sketch of the planned setup for an increase in precision of metal, alloy and composite material 3D printing. Small particles (~5-10 µm diameter) are dispersed in a solution, inserted into a nozzle, focused in the center of the nozzle by Acoustophoresis. This is followed by electrostatic droplet ejection, microwave drying and finally melting of the metal particles in a meltpool to form a solid layer.

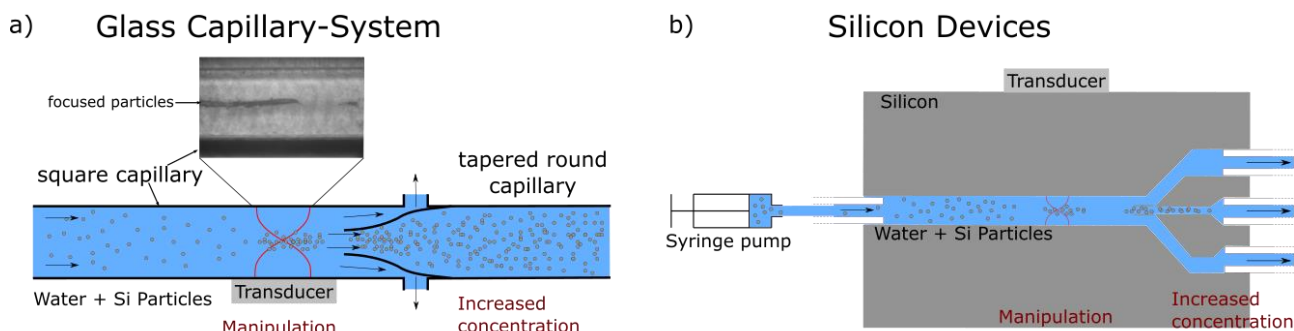


Figure 2: Sketch of the two systems that have been evaluated for the silicon particle enrichment in flow conditions. a) A tapered round glass capillary is glued into a square-shaped glass capillary. Liquid is extracted from holes on the side of the square-shaped capillary. A piezo is attached to the side of the square-shaped capillary to focus the particles in the center of the capillary. Thereby, a high percentage of the particles is transferred into the tapered round glass capillary. b) Microfluidic channels are etched into a silicon wafer. Particles are focused in the center of the microfluidic channels by means of acoustic forces. After the trifurcation, the particle concentration is increased depending on geometries and flow rates.

Device fabrication

Silicon devices:

Standard silicon wafers (thickness: 500 μm) are dry etched using deep reactive-ion etching (DRIE). After the etching step, glass (thickness: 700 μm) is anodically bonded to the silicon enabling a visual inspection of the acoustic forces on the particles. A Piezo (PZT, dimensions: 10 mm x 2 mm x 1 mm) is glued to the backside of the Silicon chip using conductive polymer (H20E, EPO-TEK). Capillaries (TSP-250350, Polymicro TechnologiesTM) are inserted to the sides of the chip and then glued to achieve a stable position and impede leaking of the devices.

Glass capillary system:

Round glass capillaries (900 μm OD, VWR International) are pulled in a laser-based micropipette puller (P-2000, Sutter Instruments) to get tapered round glass capillaries with a tip diameter of ~ 300 μm . Holes are drilled into square shaped glass capillaries (1 mm ID, VitroCom, Inc.) by electrochemical discharge machining. The tapered round glass capillaries are inserted into the square shaped glass capillaries and fixed using a two component epoxy glue. A Piezo (PZT, dimensions: 10 mm x 2 mm x 1 mm) is glued to one sidewall of the square shaped glass capillary using the same glue as for the silicon chips.

Experiments

Enrichment of silicon particles in continuous flow conditions with the before mentioned systems is examined. Depending on the flow rate and specific design parameters, different increases in concentration are determined. Key parameter for the glass capillary-system is the tip diameter of the round capillary. For the silicon chips, the width of the trifurcation in combination with the channel width is most important. We plan to show a concentration increase from 1% solid particle content at the inlet to more than 10% solid particle content at the outlet. Such a high enrichment is needed to be compatible with the throughput of state-of-the-art 3d printing methods.

Conclusion

In this work enrichment of silicon particles in continuous flow conditions is shown by the use of two completely different systems. The first step for a much higher precision in metal, alloy and composite material 3D printing has been taken.

References

- [1] L. Costa and R. Vilar, "Laser powder deposition," *Rapid Prototyp. J.*, vol. 15, no. 4, pp. 264–279, 2009.
- [2] H. Onoe *et al.*, "Metre-long cell-laden microfibres exhibit tissue morphologies and functions.," *Nat. Mater.*, vol. 12, no. 6, pp. 584–90, 2013.
- [3] M. Antfolk, P. B. Muller, P. Augustsson, H. Bruus, and T. Laurell, "Focusing of sub-micrometer particles and bacteria enabled by two-dimensional acoustophoresis.," *Lab Chip*, vol. 14, no. 15, pp. 2791–9, 2014.
- [4] M. Antfolk, C. Magnusson, P. Augustsson, H. Lilja, and T. Laurell, "Acoustofluidic, Label-Free Separation and Simultaneous Concentration of Rare Tumor Cells from White Blood Cells," *Anal. Chem.*, vol. 87, no. 18, pp. 9322–9328, 2015.
- [5] M. Nordin and T. Laurell, "Two-hundredfold volume concentration of dilute cell and particle suspensions using chip integrated multistage acoustophoresis," *Lab Chip*, vol. 12, no. 22, p. 4610, 2012.
- [6] M. Antfolk, C. Antfolk, H. Lilja, T. Laurell, and P. Augustsson, "A single inlet two-stage acoustophoresis chip enabling tumor cell enrichment from white blood cells," *Lab Chip*, vol. 15, no. 9, pp. 2102–2109, 2015.



Tuning of the acoustic boundary conditions for SAW-driven microfluidics

R. Weser^{*}, A. Winkler[†], S. Menzel and H. Schmidt

Leibniz Institute for Solid State and Materials Research Dresden, SAWLab Saxony

E-mail: r.weser@ifw-dresden.de, URL: <http://www.sawlab-saxony.de>

^{*}Corresponding author, [†]Presenting author

Introduction

Using surface acoustic waves (SAW) for fluid agitation or manipulation of immersed particles and cells at microscale is state of the art for several years [1, 2]. However, special attention has to be paid to the acoustic boundary conditions since they are significant for the intended use of SAW-driven microfluidic devices. Here, we present extensive experimental results for SAW devices using travelling SAW (tSAW) excited by single iIDT, standing SAW excited between two IDTs (1DsSAW, 1D acoustic tweezers) and between two pairs of IDTs with different angular alignment (2DsSAW, 2D acoustic tweezers). For these basic configurations, that are typically used to drive microfluidics, the influence of beam steering, coupling coefficient and diffraction on the acoustic behavior is investigated. Therefore, electrical parameters as well as the lateral distribution of complex displacement amplitude are evaluated in order to obtain profound knowledge of the influence of acoustic boundary conditions that need to be well-tuned in order to achieve the desired microfluidic behavior.

Experiments

Experimental investigations were carried out for different IDT arrangements on the surface of 128°Y LiNbO₃ (128° rotated Y-cut lithium niobate), which is a commonly used piezoelectric substrate for microfluidics. Each arrangement (SAW chip) contains up to four equal IDTs (solid finger, 150 μm wavelength, 2 mm aperture, 33 electrode pairs) with two IDTs arranged face-to-face to each other with 3 mm distance. Two pairs of IDTs are oriented at $\theta = \pm 45^\circ$, $\theta = \pm 52.8^\circ$ and $\theta = 0^\circ/90^\circ$ related to the X-propagation direction. Excitation and propagation of SAW under these different angles θ is accompanied with varying phase velocity and coupling coefficient [3]. Furthermore, beam steering occurs for the non-pure Rayleigh mode direction of $\theta = 45^\circ$. Characterization of the electrical behavior is carried out via complex electrical S-parameters measured by a vector network analyzer (VNA, Agilent E5071C). The wave field, i.e. the lateral distribution of surface normal displacement component and the associated phase, is measured with a scanning laser Doppler vibrometer (LDV, Polytec UHF 120) at high resolution by long-term stabilized measurements.

Results

Travelling SAW encountering a microchannel

Travelling SAW (tSAW), excited by a single IDT, are typically used to induce forces within the fluid in a microchannel, i.e. for active mixing. Fig. 1 shows the amplitude distribution (left) and three extracted beam profiles (right) of tSAW in front of the IDT.

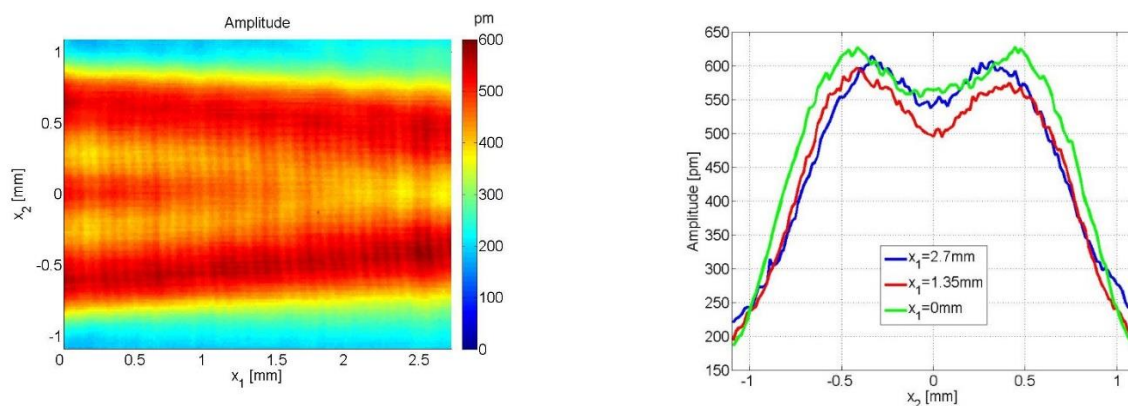


Figure 1: Surface normal displacement amplitude for a travelling SAW excited by single IDT oriented parallel to X-propagation direction ($\theta=0^\circ$) at a frequency $f=26.0$ MHz: lateral distribution (wave field, left) and beam profiles at different distances to the IDT (right). Right edge of IDT is located at $x_1=0$ with center of aperture at $x_2=0$ (propagation direction is from left to right).

The wave field is symmetric with respect to $x_2=0$, which is expected for a pure Rayleigh mode direction as no beam steering occurs. The width of beam profile slightly decreases with increasing distance to the IDT. Moreover, the beam profile considerably deviates from the rectangular shape often assumed for simplicity, as the position and height of characteristic local minimum and both-sided maxima also vary with distance to the IDT. These effects arise for IDTs with an aperture-to-wavelength ratio (here: $w/\lambda = 13.3$) of below ~ 100 , which are typical for acoustofluidics. They originate from SAW diffraction, as well as from beam steering for other IDT orientation angles differing from the pure mode direction and they are frequency dependent. We present more experimental results illustrating the influence of these parameters on the wave field and beam profile of tSAW. The width and shape of beam profile are of special importance for the acoustofluidic interaction within the microchannel since the spatial distribution of induced forces are substantially influenced by them [4].

Standing SAW used for acoustic tweezers

Standing SAW (sSAW) arising from the superposition of counter-propagating travelling SAW (tSAW), are often applied to acoustic tweezers within microfluidic setups. Fig. 2 shows the lateral amplitude distribution of sSAW for two pairs of IDTs (each consisting two opposing IDT) rotated by $\theta = 0^\circ$ and $\theta = 90^\circ$ relative to X-propagation direction. The maximum amplitude of sSAW in one dimension (1DsSAW) arises at different frequencies ($f = 24.4$ MHz for $\theta = 0^\circ$, $f = 23.75$ MHz for $\theta = 90^\circ$) due to the different phase velocities for these directions (Fig. 2, left and center). Hence, the superposition of both 1DsSAW at particular frequencies features a non-steady state of 2DsSAW because variant frequencies cause beating, i.e. transient modulation of the local amplitude. Driving both sSAW at the same frequency (i.e. $f = 25.35$ MHz) yields a steady state wave field but with a comparably low amplitude and a non-ideal lateral distribution for microfluidic actuation purposes (Fig. 2, right).

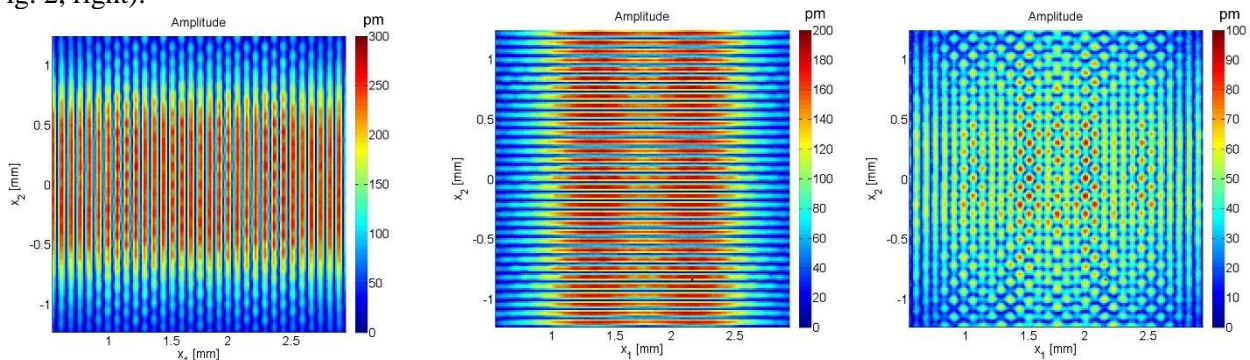


Figure 2: Lateral distribution of surface normal displacement amplitude for standing SAWs excited by two IDT pairs oriented at $\theta = 0^\circ$ and $\theta = 90^\circ$ relative to X-propagation direction at different driving frequencies: $f=25.75$ MHz (left), $f=24.4$ MHz (center), $f=25.35$ MHz (right). Note the different color bar scaling.

To overcome this drawback, alternative IDT arrangements can be used. We present results for two IDT pairs rotated by $\theta = \pm 45^\circ$ and $\theta = \pm 52.8^\circ$. Both setups exhibit the same phase velocity for all four IDTs eliminating the beating issue and ensuring steady state wave fields with lateral amplitude distribution more suitable to drive microfluidics. However, as will be shown, the 45° alignment leads to asymmetric beam profiles, while the 52.8° alignment leads to non-square acoustic wells. Other alignments are possible, but feature all effects of wave field distortion, beating and asymmetry at once.

Conclusion

The electrical characterization of IDTs or IDT arrangements by means of S-parameter measurements is simple to carry out, but also delivers only minimal information on the excited acoustic wave field. Effects including diffraction, asymmetry or beating cannot be determined with this technique without additional high effort. The determination of the lateral distribution of surface normal displacement and phase via laser Doppler vibrometry, however, gives significant information on the propagation and superposition of SAW. The layout of the SAW chip (design, orientation and position of IDT), the position of the microfluidic container (channel, chamber) and the driving frequency have to be properly chosen in order to realize the desired functionality of SAW-driven microfluidic devices. Finally, the intended usage determines the necessary wave field properties and the suitable IDT setup. Furthermore, experimentally obtained information about electroacoustic behavior of SAW devices can help to improve acoustofluidic simulations based on wave field characteristics as input parameters.

References

- [1] T.-D. Luong and N.-T. Hguyen. *Micro and Nanosystems* **2**, 217-225 (2010).
- [2] G. Destgeer and H. J. Sung. *Lab on a Chip* **15**, 2722-2738 (2015).
- [3] K.K. Wong. *Properties of Lithium Niobate*, Institution of Electrical Engineers (London, 2002).
- [4] F. Kiebert et al. *Lab on a Chip* **17**, 2104-2114 (2014).

Acoustic Stabilization and Enhanced de-Stabilization of Single Bubbles in Microfluidics and the Connection to the Acoustic Landau-Levich Coating Problem

Amihai Horesh and Ofer Manor

Department of Chemical Engineering, Technion – Israel Institute of Technology, Haifa, Israel
E-mail: amihaih@technion.ac.il, URL: manoro@technion.ac.il

Introduction

The manipulation of liquid films over a solid substrate, which support different forms of vibrations, have been investigated for over thirty years [1]. It was recently found that oil and water may spread over a solid substrate that supports a propagating surface acoustic wave [2-4] (SAW). Further theoretical and experimental studies showed the connection between acoustic spreading and the three-phase contact angle between the liquid, vapor, and solid substrate [5, 6]. Moreover, an important system in both industry and academia, which supports the formation of free liquid films, is the interaction between bubbles and solid substrates at close proximity. Examples of applications for the attachment of bubbles to solids are floatation unit operations [7], the intense purification of water [8], drug delivery and cancer treatment [9] and microfluidics [10].

We recently showed that the excitation of SAWs in a microfluidic channel might destabilize the micron thick film of liquid between a bubble and a solid substrate at close proximity, rendering attachment [11]. Our results correlated very well with a model for the Landau–Levich type coating of a solid substrate by a liquid film under the action of a propagating MHz frequency SAW [12]. We were able to show that the conditions that rendered the acoustic Landau–Levich coating film unstable in theory further supported the enhanced destabilization of the micron thick liquid film, which resulted in the fast attachment of the bubble to the substrate (figure 1a).

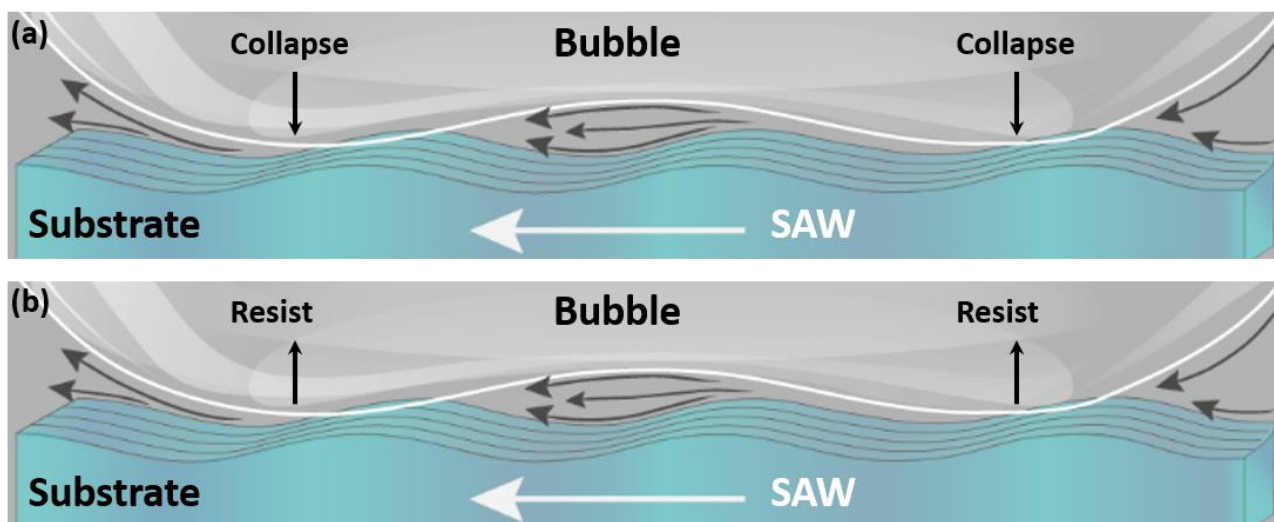


Figure 1: A cross-section of a liquid film between a bubble and the substrate of a microchannel: Excited by a propagating SAW, the film will (a) collapse faster than in the absence of the SAW, causing film breakage and the fast attachment of the bubble to the substrate or (b) resist collapse and the attachment of the bubble to the substrate.

Experiment

Briefly, we show results for an acoustically stabilized film of water, which intermediates a quiescent bubble and the solid substrate of a 500-micron thick channel. We use monochromatic light microscopy to capture the spatiotemporal variations in the geometry of the micron thick film between the bubble and the substrate. The light diffracts in the liquid film, supporting the formation of light fringes of equal chromatic order (FECO)

along the air/water interface. We convert the FECO to local variations in the film thickness and extract the dynamic film geometry under the influence of the SAW.

Conclusions

We present new experimental results in which the conditions that render the acoustic Landau–Levich coating film stable in theory further supporting the stabilization of the micron liquid film between a bubble and a solid substrate. The film remains stable, resisting thinning, destabilization, and breakage, which will naturally occur in the absence of the SAW excitation (figure 1b).

References

- [1] Morozov et al. Colloid Interface Sci., 36 (37) 2018
- [2] Rezk et al. Nat. Commun., 3 (1167) 2012
- [3] Rezk et al. Proc. Roy. Soc. A, 470(20130765) 2014
- [4] Manor et al. Phys. Rev. E 91 (053015) 2015
- [5] Altshuler et al. Phys. Fluids, 27 (102103) 2015
- [6] Altshuler et al. Phys. Fluids, 28 (072102) 2016
- [7] Edzwald. Wat. Sci. Tech., 31 (3) 1995
- [8] Soler, et al., ACS Nano, 7 (11) 2013
- [9] Lentacker, et al., Adv. Funct. Mater, 17 (12) 2007
- [10] Zhang, et al. Langmuir, 24 (9) 2008
- [11] Horesh et al. Phys. Rev. E 95 (052803), 2017
- [12] Morozov et al. JFM, 810 (307) 2017

Design and Characterization of Thin Film Bulk Acoustic Wave Devices for Acoustophoresis

Peter Reichert¹, Dhananjay Deshmukh¹, Lukas Lebovitz¹ and Jürg Dual¹

¹Department of Mechanical and Process Engineering, Institute for Mechanical Systems, Swiss Federal Institute of Technology Zurich, Zurich, Switzerland
E-mail: reichert@imes.mavt.ethz.ch, URL: www.expdyn.ethz.ch

Introduction

Thin film bulk acoustic wave (TFBAW) devices use a thin piezoelectric film as actuation source for BAW acoustophoresis. A TFBAW device consists of a microfluidic silicon/glass chip where one side of the channel is sealed by a silicon plate and a thin piezoelectric layer. The piezoelectric layer drives the silicon plate to a coupled plate-fluid resonance [1]. In common BAW devices, vibrations are typically more complex than plate resonances and optimization algorithms are required for the design prediction [2]. Moreover, the experimental verification is not straightforward. In this study we characterize the plate mode shapes of TFBAW devices using experiments and simulations.

Device characterization - experiment and simulation

In BAW acoustophoresis the devices are operated typically close to a multiple of half a wavelength ($\lambda/2$) of the standing wave formed in the microfluidic channel. Here, we characterize TFBAW devices and identify mode shapes suitable for acoustophoresis. The TFBAW cross section is sketched in figure 1a and consists of a glass wafer, a SiO_2 (yellow)/silicon (grey) wafer surrounding a microfluidic channel and a piezoelectric layer (blue). The microfluidic channel has a length larger than 4 mm, a height of $t_c=86 \mu\text{m}$ and a width of $w_c=100\text{-}400 \mu\text{m}$. The passive silicon plate and the piezoelectric layer have a thickness of $t_m=13 \mu\text{m}$ and of $t_p=2 \mu\text{m}$, respectively.

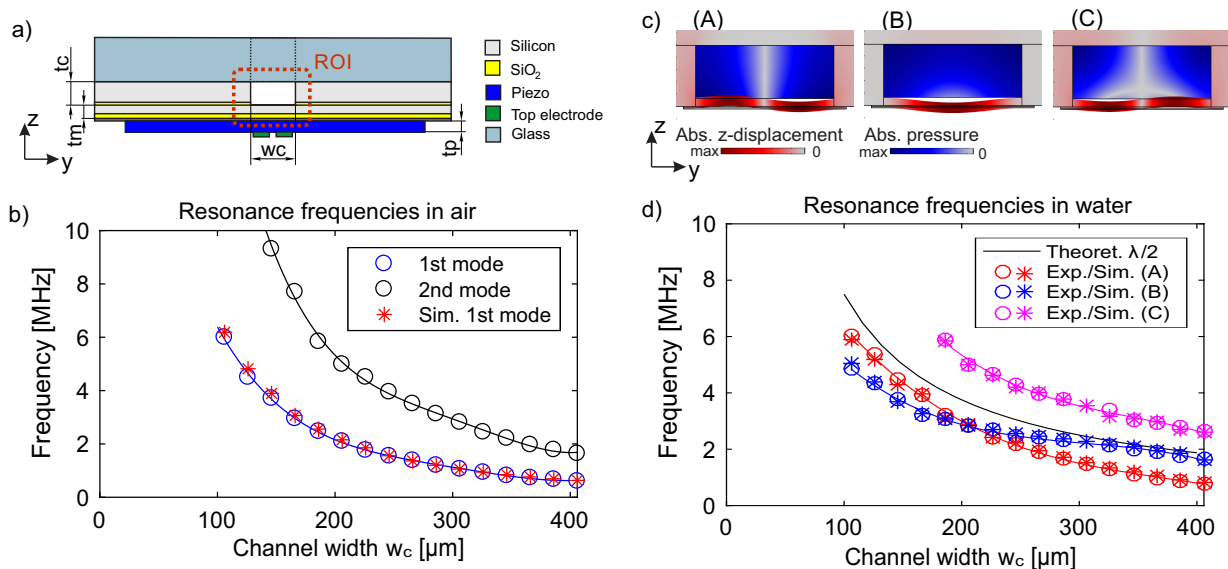


Figure 1: (a) TFBAW device cross section with an indication of the materials and the device dimensions. (b) Experimental (circles) and simulated (red stars) resonance frequencies for an air filled channel with width w_c . The first resonance (symmetric) and the second resonance (antisymmetric) are plotted in blue and black, respectively. (c) and (d) show the TFBAW device characterization for three different mode shapes for a water filled channel. (c) Simulated mode shapes (A), (B) and (C) in the region of interest (ROI) of a) for a channel width of $w_c=220 \mu\text{m}$. (d) Experimental (circles) and simulated (stars) resonance frequencies in water for a variation in channel width w_c for the mode shapes (A), (B) and (C). The solid black line shows the frequency for a theoretical 1D half-wavelength pressure wave in y-direction.

A 2D FEM simulation was used to model the TFBAB device. For the TFBAB device characterization we measured the resonance frequencies of the device with a laser vibrometer for both with and without water inside the microfluidic channel and for varying channel widths. Fig. ??b shows the plate resonance frequencies in air for the first (symmetric) and second (antisymmetric) resonance mode. A good agreement between simulation and experiment is shown for the first resonance mode in air. Fig. ??c and d show the characterization results for a water filled microfluidic channel. We could identify three resonance mode shapes close to the theoretical $\lambda/2$ fluid resonance. Mode (A) has a pressure node in the channel middle, mode (B) has a pressure node at the plate surface and mode (C) has a more complex 2D pressure field. For all three modes the resonance frequencies are varied over the channel width w_c in fig. ??d. When comparing fig. ??b and d, the fluid inside the microfluidic channel is not acting solely as an additional mass loading as the plate mode shapes are coupled to the fluid resonance inside the channel. Interestingly, mode (A) and (B) scale differently over the channel width w_c and the curves of mode (A) and (B) intersect for a channel width of $w_c=200 \mu\text{m}$.

Damping effects in a TFBAB device

A measurement in vacuum was used to determine the material properties for our FEM simulation. In a next step, damping effects for a water loaded channel and from varying boundary conditions could be identified. In table ??, the quality factor is listed for different boundary conditions. From vacuum to air the Q factor drops for the unsealed channel. After injecting water into the device the Q factor further dropped and a variation between mode (A) and (B), as shown in fig. ??c, could be investigated. The damping effect is different for both modes as the formation of a viscous boundary layer and losses to the bulk material is varying. In a further step, we changed the boundary condition by gluing a bulk piezoelectric transducer to the side of the device and found a further reduction of the Q factor.

Table 1: Damping effects on a TFBAB device in vacuum, air, with a water filled channel and for a variation in external boundary conditions. The 1st mode was evaluated in vacuum and air. Mode (A) and (B) were evaluated for the water filled channel.

Device boundary condition	f_{res} [MHz]	Q [-]
1 st mode in vacuum	1.79	444
1 st mode in air	1.79	262
Mode (A) in water	2.46	209
Mode (B) in water	2.69	244
Mode (A) with glued parts	2.49	126
Mode (B) with glued parts	2.73	148

Further characterization results

We tested mode (A) in fig. ??c for acoustophoresis and observed a strong particle alignment in the channel middle and extracted a pressure amplitude of 0.55 MPa at only 1 V_{pp} excitation amplitude. For a channel width of $w_c=220 \mu\text{m}$ and a frequency of 6 MHz we found a plate mode shape which is able to excite a pressure field with two nodal planes, similar to a full-wavelength λ -mode. This mode can be used to move particles to the nodal lines of the λ mode and together with mode (A) enable an acoustophoretic particle sorting.

Conclusion

We evaluated the major mode shapes for TFBAB devices, identified suitable modes for acoustophoresis and pointed out damping contributions. Results of a 2D FEM simulation matched well with experimental results. With these results, a design approach is presented for the development of acoustophoretic lab-on-a-chip devices, that produces high acoustic pressures even at a low excitation voltage.

References

- [1] P. Reichert, D. Deshmukh, L. Lebovitz and J. Dual. *Procs. pp. 87-88, Acoustofluidics 2017*, San Diego, 28 - 29 August 2017.
- [2] P. Hahn, O. Schwab and J. Dual. *Lab on a Chip* **14**, 3937 (2014).



Reversals of acoustic radiation force and torque in a single Bessel beam: Acoustic Tweezers Numerical Toolbox

Zhixiong Gong, Yingbin Chai, and Wei Li

Department of Ocean Engineering, Huazhong University of Science and Technology, Wuhan City, 430074, P.R. China

E-mail: hustgzx@hust.edu.cn; cybhust@hust.edu.cn; hustliw@hust.edu.cn

Introduction

Acoustic radiation force (ARF) and torque (ART) are important for particle manipulations in nearly ideal fluids, which correspond to the transfer of linear and angular momenta in acoustic scattering instead of streaming. The ARF and ART in arbitrary fields are derived in terms of incident and scattered beam shape coefficients that could be calculated with both theoretical and numerical methods. Bessel beam is promising in acoustophoresis for its novel properties and could result in reversals of ARF and ART under certain conditions. Physical mechanisms of reversals are discussed.

Methods

The partial-wave series (PWS) solution and T-matrix method (TMM) are employed in this work. It has been demonstrated that the PWS and TMM are efficient to calculate the scattering of Bessel beam^{1,2}. According to the physical mechanisms of the ARF and ART, it is anticipated that the ARF and ART are associated with the incident and scattered fields. In this study, we derived the expressions of ARF and ART in arbitrary fields in terms of incident (a_{nm}) and scattered (s_{nm}) beam-shape coefficients as follows:

$$\mathbf{F} = \frac{1}{2} \rho_0 k^2 \psi_0^2 \iint_{S_0} \text{Re} \left\{ - \sum_{nm} \sum_{n'm'} \frac{i^{n'-n}}{(kr)^2} (a_{nm} + s_{nm}) s_{n'm'}^* Y_{nm}(\theta, \varphi) Y_{n'm'}^*(\theta, \varphi) \right\} \mathbf{n} dS \quad (1)$$

$$\Gamma = - \frac{\rho_0 \psi_0^2}{2k} \text{Re} \iint_{S_0} \frac{1}{r^2} \left\{ \sum_{nm} \sum_{n'm'} i^{n-n'} (a_{nm}^* + s_{nm}^*) s_{n'm'} (Y_{nm}^* \mathbf{L} Y_{n'm'}) \right\} dS \quad (2)$$

where \mathbf{L} is the angular momentum operator from the definition of the quantum mechanics. Other quantities are denoted by conventional symbols. As observed, the ARF and ART could be obtained once the scattered coefficients are computed with the PWS or TMM. To conduct the numerical experiments, the ARF and ART in (1) and (2) need to be projected in three directions of Cartesian coordinates. Taking the ARF as an example³, the Cartesian component could be obtained by eliminating the surface integral with the orthogonal relationship of spherical harmonic functions, and be finally expressed only with a_{nm} and s_{nm} .

Results: Bessel beam example

Both the ARF and ART in Bessel beams are studied with the schematic in Fig. 1(a). The incident coefficients of Bessel beam with arbitrary order and location are calculated based on the multipole expansion method². The axial ARFs of a rigid oblate spheroid (aspect ratio $a/b=1/2$) placed on the axis of the first-order helicoidal Bessel beam with different half cone angles are shown in Fig. 1(b). The reversal of ARF occurs in the frequency region with the enlarged figure on the top right corner. It implies that larger cone angle tend to induce the ARF reversal (See $\beta=80^\circ$) since there is no reversal for $\beta=30^\circ$. The Physical interpretation of negative axial ARF for an object without absorption was derived by Zhang and Maston⁴: $F_z = P_{\text{sca}} c_0 (\cos\beta - \langle \cos\theta \rangle)$, where P_{sca} is the scattered energy from the object, c_0 is the sound speed in outer medium, $\langle \cos\theta \rangle$ denotes the average of $\cos\theta$ over the scattering angles. The first term describes the momentum transferred from the beam to object, leading to positive ARF. The second term including $-\langle \cos\theta \rangle$ means the momentum transfer owing the scattering, leading to either positive or negative ARF. When the negative ARF dominates, the ARF for the object will reverse, as numerically proved in Fig. 1(c). The red solid curve is for the red pentagram with pulling force in (b), while the blue dashed curve is for the blue pentagram with positive force. The black dotted line describes the wave vector direction of Bessel beams. As shown in (c), the scattering relatively stronger in forward than backward results in the reversal of axial ARF.

The reversal of ART of a viscoelastic solid sphere is observed under the first-order Bessel beam of off-axis incidence (offset: $(x_0, y_0) = (5, 5)$), as shown in Fig. 1(e). To discuss the reversal of ART, the $ka - \beta$ curves are plotted using the equation $X = k \sin\beta R_0$ (See Eqn. 5 in Ref. [2]), with X being the roots of peaks and zeroes of cylindrical Bessel function $J_1(X)$ as plotted in (d). $R_0 = (x_0^2 + y_0^2)^{1/2}$. As observed from (e), the reversal points in (ka, β) region lie on the special curves, whose ka and β make $J_1(X)$ the peak or zero values. It is of great importance in the field of particle manipulations to find possible beam parameters to

produce axial ART reversal. A comparison of axial ART from a rigid spheroid between smooth and rough surface is made. Except for the surface, all the parameters including the incident beam and geometrical aspect ratio are same. It is found that rough surface could increase ~ 5 order of magnitude of the axial ART.

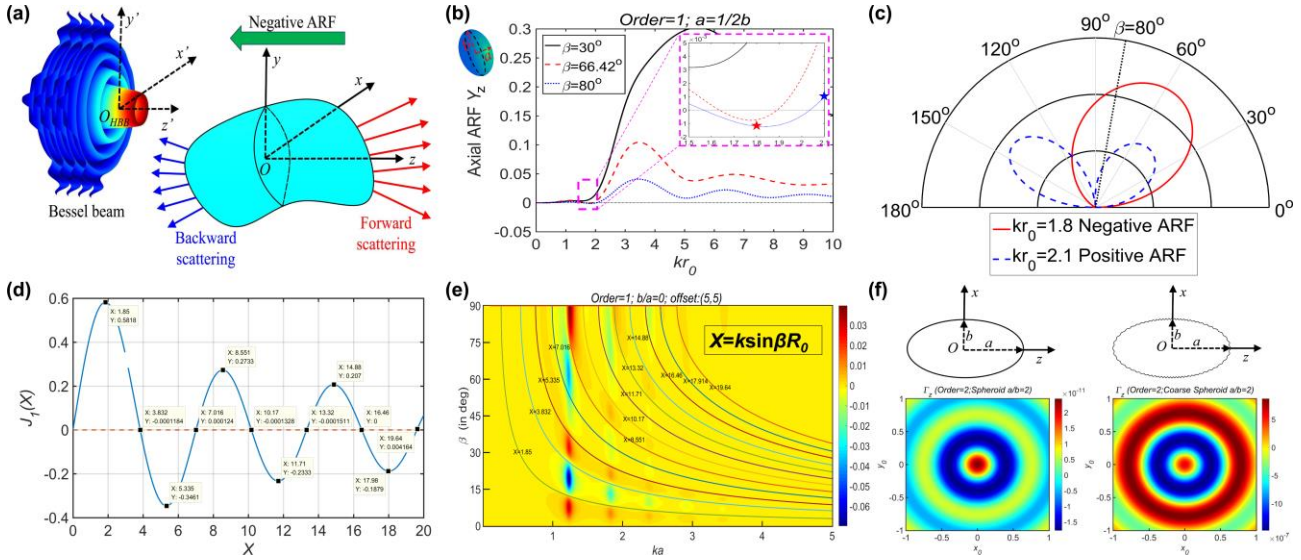


Figure 1: (a) Schematic of object in single Bessel beam; (b) Axial ARF for a rigid oblate spheroid with enlarged figure including negative ARF; (c) 2D scattering patterns at frequencies of positive and negative ARFs; (d) Roots of peak and zero values for first order cylindrical Bessel function; (e) Reversal of axial ART in 2D (ka, β) region with points lying on special curves; (f) Comparison of ART for rigid spheroids between smooth and rough surfaces.

Acoustic Tweezers Numerical Toolbox

A potential schematic of acoustic tweezers numerical toolbox is outlined as Fig. 2, which may be an alternate to optical tweezers. The three-dimensional ARF and ART could be obtained based on Eqns. (1) and (2). The known incident beam shape coefficients and scattered coefficients calculated by PWS and TMM are programmed in a vector, which could be encapsulated to compute the ARF and ART in a uniform form. Other theoretical and numerical methods may be also added into the toolbox not only for Bessel beams, but also for other waves of interest. The dynamic motions (in dashed box) are outside scope of the present work.

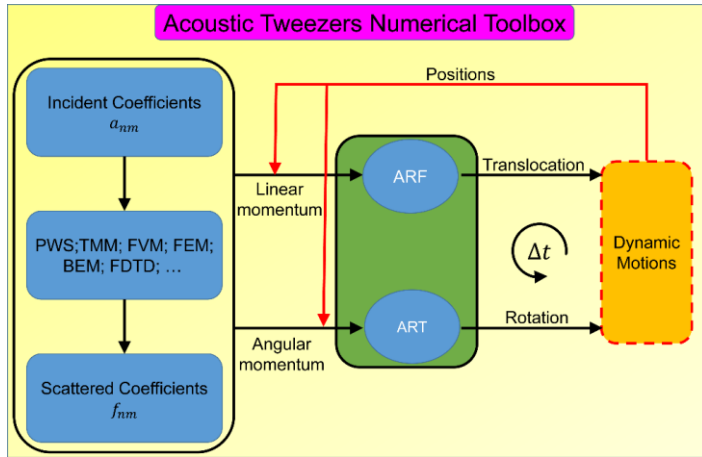


Figure 2: Potential schematic of Acoustic Tweezers Numerical Toolbox. The unknown scattered beam shape coefficients has been demonstrated by PWS and TMM for Bessel beams. Other theoretical and numerical approached may also be encapsulated into the toolbox, such as the finite volume method (FVM), the finite element method (FEM), the boundary element method (BEM), the finite-difference time domain method (FDTD). The particle dynamic motions is outside scope of the present work.

Conclusion

The acoustic radiation force and torque of spherical and nonspherical objects from a single Bessel beam are investigated using the PWS and TMM. The reversals of ARF and ART are observed and corresponding physical mechanism are revealed and discussed. A potential structure of programming is proposed to design the single-beam acoustic tweezers numerical toolbox. This work is sponsored by National Natural Science Foundation of China, China Scholarship Council and HUST.

References

- [1] P. L. Marston. J. Acoust. Soc. Am. 121, 753-758 (2007).
- [2] Z. Gong, P. L. Marston, W. Li, Y. Chai. J. Acoust. Soc. Am. 141, EL754-578 (2017).
- [3] Z. Gong, P. L. Marston, W. Li, arXiv:1710.00146v1.
- [4] L. Zhang, P. L. Marston, Phys. Rev. E 84, 035601(R) (2011).



Characterization of surface waves on water films excited by ultrasonic vibration imposed on the substrate

Amin Rahimzadeh¹, Mohammad-Reza Ahmadian-Yazdi¹, and Morteza Eslamian¹

¹ University of Michigan-Shanghai Jiao Tong University Joint Institute, Shanghai, 200240, China
E-mail: Amin.rahimzadeh@sjtu.edu.cn, URL: <http://pv.sjtu.edu.cn/index.html>

Introduction

In this paper, we report unprecedented experimental results on the propagation speed, wavelength, and frequency of surface waves induced by imposing ultrasonic vibration on the substrate of water films. Imposing horizontal or vertical vibrations to a liquid layer may destabilize the free surface and induce gravity, gravity-capillary, or capillary surface waves, depending on the liquid depth and wavelength of the disturbances. These surface waves, depending on the geometry and conditions of the problem, may be traveling or standing waves/patterns with various characteristics. The standing waves were first observed by Faraday [1], in a series of experiments, where low frequency piston-like vertical vibration was imposed on a liquid body in a vessel. Following the Faraday's instability, many theoretical and experimental studies were performed mostly in the context of the pattern formation. However, in the aforementioned works, low frequency excitation vibrations have been considered, and the regimes of the stability, formation of standing waves and patterns, and the relationship between the frequency of excitation and that of the standing waves and patterns have been established. In the case of excitation by frequencies much higher than the natural frequency of the system, such as ultrasonic vibrations, the trend may be different from piston-like low frequency vibrations and the theory is more complex. Excitation by ultrasonic transducers has several emerging applications in microfluidics, using surface acoustic waves (SAW) that hit a droplet or thin film as they travel laterally on transducer surface [2, 3], and fabrication of thin film devices by excitation of thin liquid films of electronic materials from below, using an ultrasonic transducer attached to the backside of the substrate [4, 5].

Our measurements show that an excitation frequency of the order of 10^4 Hz results in traveling surface waves with frequencies of the order of 10^2 Hz on the liquid films with thicknesses of few millimeters. Among the results, it is found that the standing waves and patterns appear only if the ratio of the imparted energy to the film thickness is large enough.

Experimental

Distilled water was used to prepare liquid films with varying millimeter range thicknesses in a shallow vessel with inner diameter of 13 cm. A CCD camera (Biolin Scientific, Sweden) was used to capture the fluid motions within the liquid films from their cross-section (camera 1 in Figure 1a). In addition, in order to observe and analyze the induced waves due to ultrasonic vibration, a high speed camera (FASTCAM SA3 Model 120K, Photron, Japan) was used (camera 2 in Figure 1a). The vibrator in Figure 1a is a metal box, inside which an ultrasonic piezoelectric transducer has been installed, to impose vertical vibration to the box and the liquid film. Three custom-made vibrators, equipped with ultrasonic transducers with frequencies of 20, 40 and 68 kHz and powers of up to 50 W were employed (Yuhuan Clangsonic Ultrasonic Co., Ltd, Zhejiang, China).

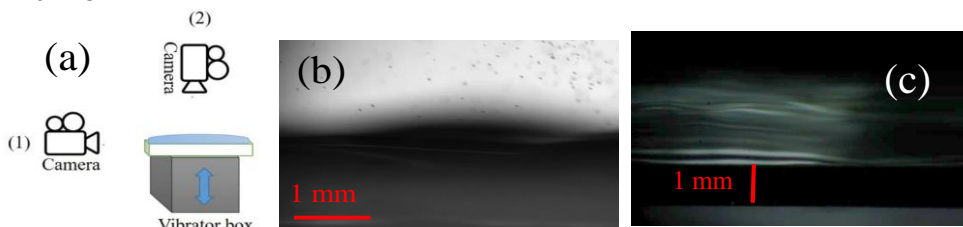


Figure 1: (a) Experimental setup for visualization of the flow motion from the side and the top of a liquid film, excited by ultrasonic vibration from below. (b) Surface waves and ultrasonic atomization. (c) Cross-sectional image showing internal waves and microstreaming.

Results and discussion

We observed that imposing ultrasonic vibration to the substrate of a large-area water film with millimeter range thicknesses, formed in a circular vessel, creates both standing and traveling waves (Figure 2a). Standing waves with different patterns formed on a laterally extended liquid film have been predicted by theory [6]. Parts a and b of Figure 2 show that at a given film thickness, with decreasing the excitation power, and therefore, the amplitude of vibration, indeed both the standing and traveling waves are attenuated. Likewise, increasing the film thickness, at constant vibration power and amplitude, results in

attenuation of the standing waves, although the attenuated traveling waves are still visible (Figure 2c, d). Therefore, all parts of Figure 2 collectively reveal that the standing waves, in particular, and the traveling waves appear on the surface, if the vibration power per film thickness is larger than a threshold. Thus, only a high intensity of imparted energy to the film can cause the formation of (visible) surface waves.

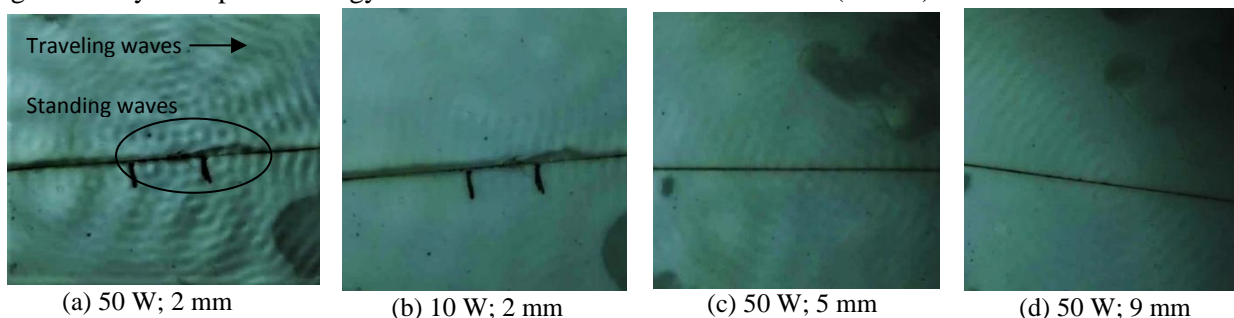


Figure 2: Standing and traveling waves on water surface in a circular container excited by 40 kHz vertical ultrasonic vibration. In (a) and (b) the thickness of the film is 2 mm, but the vibration power is 50 W in (a) and 10 W in (b). In (c) and (d), the vibration power is 50 W, but the film thickness is 5 mm in (c) and 9 mm in (d).

To gain quantitative insight, we measured the wavelengths and velocities of propagation of the surface travelling waves, for several film thicknesses and excitation frequencies for vertical vibrations. Figure 3 shows the wavelength, wave propagation velocity, and frequency (ratio of the velocity to the wavelength) of the travelling waves, due to vertical ultrasonic vibration. We observe that the wavelengths are ~ 2 mm, thus the waves are capillary waves, and only slightly vary with the film thickness and the imposed frequency. The velocity of the traveling waves is ~ 0.5 m/s, and there is no correlation between the wave velocity and the excitation frequency or film thickness. The frequency of the induced surface waves is ~ 250 Hz, while the frequency of excitation is of the order of 10^4 Hz.

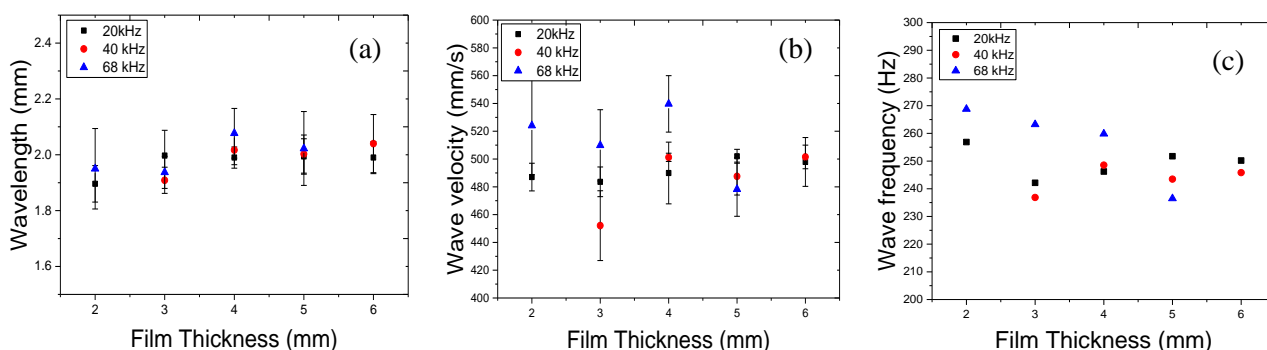


Figure 3: Measured wavelength (a) and wave propagation velocity (b), and their corresponding calculated wave frequency (c) for travelling surface waves, induced by vertical ultrasonic vibrations.

The mechanical energy of the vibration source leaked or imparted into the liquid film may cause several fluid dynamic phenomena. We have observed ultrasonic atomization on a 2.4 mm water film due to imposed ultrasonic vibration with a frequency of 40 kHz and power of 50 W (Figure 1b). In addition, figure 1c shows internal waves and microstreaming within a 2.4 mm water film under vertical ultrasonic vibration with a frequency of 40 kHz and power of 10 W.

Conclusion

In this ongoing work, various effects of ultrasonic vibration imposed on liquid films of water with millimeter range thicknesses were studied. Ultrasonic atomization, microstreaming, micromixing, and induced surface waves were visualized by imaging. In the range of the parameters studied here, the frequency of the induced surface waves is two orders of magnitude smaller than the excitation frequency.

References

- [1] M. Faraday, Philosophical Transactions of the Royal Society of London **121**, 299-340 (1831).
- [2] L. Y. Yeo and J. R. Friend, Annual Review of Fluid Mechanics **46**, 379-406 (2014).
- [3] J. Friend and L. Y. Yeo, Reviews of Modern Physics, **83**, 647-704 (2011).
- [4] A. Rahimzadeh and M. Eslamian, Chemical Engineering Science **158**, 587-598 (2017).
- [5] F. Zabihi and M. Eslamian, Journal of Coatings Technology and Research **12**, 711-719 (2015).
- [6] M. Bestehorn, Q. Han, and A. Oron, Physical Review E **88**, 023025 (2013).



Acoustofluidics in multiphase reactors

Pierre Gelin¹, Dominique Maes², Wim De Malsche²

¹ Department of Chemical Engineering, Vrije Universiteit Brussel, Brussels, Belgium
E-mail: pierre.gelin@vub.be

² Structural Biology Brussels, Vrije Universiteit Brussel, Brussels, Belgium

Introduction

The use of standing acoustic waves in microfluidic devices is explored to enhance the mass transfer rate far beyond the rate of diffusion. The effect of radiation and streaming on small and large particles is investigated in this contribution. Fast mixing of two water streams has been achieved experimentally. The displacement tracks of large (5 μm) and small (0.5 μm) particles is visualized by means of Particle Image Velocimetry. Acoustic streaming and radiation have been employed simultaneously to enable the nucleation and growth of a crystal as well as to separate the crystal from the main flow.

Mixing by acoustic streaming

In microfluidic devices low Reynold numbers dominate, ensuring predictable laminar flow. Hence, mixing only occurs by diffusion. The possibility to use bulk acoustic waves and the related phenomenon of acoustic streaming to mix two water streams inside a rectangular microfluidic channels has been investigated. Visualization was done by means of fluorescence microscopy.

The effect of the applied voltage on the mixing of the water streams was investigated for two different flow rates, 5 mm/s and 10 mm/s (Fig. 1). For low voltages (5 – 10 V_{p-p}) a strong effect of the flow rate on mixing was observed. A mixing efficiency of 0.94 was reached at a voltage of 15 V_{p-p} for both flow rates. The time needed for complete mixing at this voltage for a flowrate of 5 mm/s and 10 mm/s was 0.6 and 2.7 seconds respectively. These experimental results confirmed our CFD simulations. Mixing at this time scale of two water streams with bulk acoustic waves has to our knowledge never been achieved [1, 2].

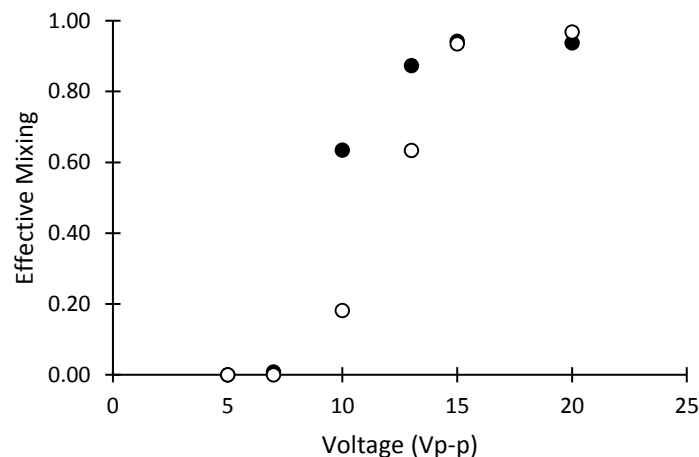


Figure 1: Mixing efficiency of two water streams in function of the applied voltage (V_{p-p}) for a total flowrate of 5 mm/s (\bullet) and 10 mm/s (\circ).

Particle tracking

Particles with a diameter of 5 μm and 0.5 μm were introduced in the microfluidic channel. The effect of the streaming drag forces and radiation forces on the small and big particles was investigated. The velocity field and amplitude was determined by 2D μPIV . As expected, focusing of the 5 μm particles on the pressure node was observed, this at a velocity around 500 $\mu\text{m/s}$ for an attenuation at 10 V_{p-p} . The 0.5 μm particles moved along with the vortices. Velocities around 100 $\mu\text{m/s}$ were observed at a voltage of 15 V_{p-p} , similar to the literature [3].

Particle maturation and crystal growth

The low mass transfer in microfluidic devices, prevents the maturation of droplets into solid particles. Acoustic streaming has been investigated to speed up the formation of solid PLGA microparticles. Next to particle maturation, a proof of concept has been obtained for the crystal formation and growth in presence of the acoustic field. Fast nucleation of a small pharmaceutical molecule was performed in the presence of acoustic streaming. The formed crystal nuclei were allowed to grow under the same conditions. Once a desired size was reached, the crystals were focussed on the pressure node and separated.

Conclusion

In this contribution very fast mixing has been achieved of two water streams. Tracking of small particles confirmed fast mass transfer in the microfluidic channel. Moreover, the phenomenon of acoustic radiation and acoustic streaming have been utilized to start the nucleation of small pharmaceutical molecules and focus the grown crystals on the pressure node.

References

- [1] K. Sritharan, C.J. Strobl, Z. Guttenberg. Applied Physics Letter **88**, 054102 (2006).
- [2] X. Shang, X. Huang, C. Yang. Experimental Thermal and Fluid Science **67**, 57-61 (2014).
- [3] P.B. Muller, M. Rossi, H. Bruus. Physical Review E **88** 023006 (2013).



A Methodology for the Quantification of Particle Separation and its Application to the Measurement of Device Effectivity and Particle Compressibility

Fabio Garofalo^{1,*}, Sander Bonestroo^{2,1}, Andreas Lenshof¹, and Thomas Laurell¹

¹Department of Biomedical Engineering, Lund University, Lund, Sweden

²Department of Applied Physics, University of Twente, Enschede, Netherlands

*email: fabio.garofalo@bme.lth.se

Introduction

Acoustophoresis separation of particles and cells has been reported quantitatively by particle counting on the separated streams, i.e. side and center outlets, in the case of blood fractionation experiments [1,2]. Despite the easiness of obtaining separation information from particle counting when this is compared to optical techniques [3,4], the former have never been used to extract quantitative information on the separation process and the sample property, e.g. acoustic energy density as function of the applied voltage and/or microparticle physical properties. The reason of this is to be found in the lack of a method that, adopting a model for the particle migration, enables to optimize the experimental separation data with respect to unknown parameters that have to be measured.

In this context, we present a method and the experimental results for (i) the measurement of the voltage-to-energy factor, here addressed as *device effectivity*, α for $E_{ac} = \alpha V_{pp}^2$, and (ii) the measurement of microparticle compressibility by analysis of particle counting experimental data.

Method

Experiments. Acoustophoretic particle separations were performed on a device operating with and without prefocusing of the streams (see Figs. 1 and 2). The total flowrate was $Q = 400 \mu\text{l min}^{-1}$ for a microchannel with cross-section of $W \times H = 375 \mu\text{m} \times 150 \mu\text{m}$ and a length of $L = 3 \text{ cm}$ (separation channel). The side/center flowrate ratios were $q_{in} = 1/3$ at the inlet and $q_{outlet} = 3/1$ at the outlet. With these flowrate ratios we estimated the inlet position for the prefocused streams at $y_{in} = 0.09 W$ and the flow-splitting abscissa at $y_{sep} = 0.4 W$. The voltage for the focusing transducer varied as to construct the curve for the separation performance. Every experiment ran for 3 min as to acquire a statistical meaningful number of beads, and each datapoint is the combination of three runs. The temperature was monitored and controlled by using a Peltier cell at $T = 25 \text{ C}$. Polystyrene microbeads with nominal diameters $5 \mu\text{m}$ and $7 \mu\text{m}$ were used for the determination of α (acoustic calibration). The compressibility of melamine beads (nominal diameter $4 \mu\text{m}$) was determined and compared with literature values [5].

Analysis Method. The method used for the analysis of the experimental data is thoroughly illustrated in [6]. It relies on the calculation of the spatial y -marginal and the side-stream recovery, namely the fraction of particles in the side stream,

$$\rho^y(y, t) = \sum_k w_k \mathcal{N}[y | m_k^y(t), s_k^{yy}(t)], \quad \text{SSR} = \sum_k \frac{w_k}{2} \text{erfc} \left[\frac{m_k^y(t_{sep,k}) - y_{sep}}{\sqrt{2 s_k^{yy}(t_{sep,k})}} \right], \quad (1)$$

where w_k , m_k^y and s_k^{yy} are the statistical properties (weight, mean and variance) associated with the k -th gaussian in the mixture model used to characterize the size distribution of the sample (we assume compressibility and density uniform for the beads' population) $\rho^r(r) = \sum_k w_k \mathcal{N}[r | m_k^r, s_k^{rr}]$. In equation (1), y_{sep} is the separation abscissa, i.e. where the flow is split toward the side and the center outlets, and $t_{sep,k}$ is the time for which the k -th gaussian reaches the outlet section, i.e. for $x = L$. The computation of the quantities in Eqs. (1) is illustrated in [6].

Results

Figure 1 shows the results for the calibration procedure in the case of prefocused streams for a PBS suspension of polystyrene microbeads with nominal diameters $5 \mu\text{m}$ and $7 \mu\text{m}$. The two experiments were performed in two different days and the estimated effectivity values were $\alpha = 4.9 \text{ J m}^{-3} \text{ V}^{-2}$ and

$\alpha = 5.0 \text{ J m}^{-3} \text{ V}^{-2}$. The small discrepancy between these two values, i.e. $\sim 1.6\%$, indicates that the method has a good reliability.

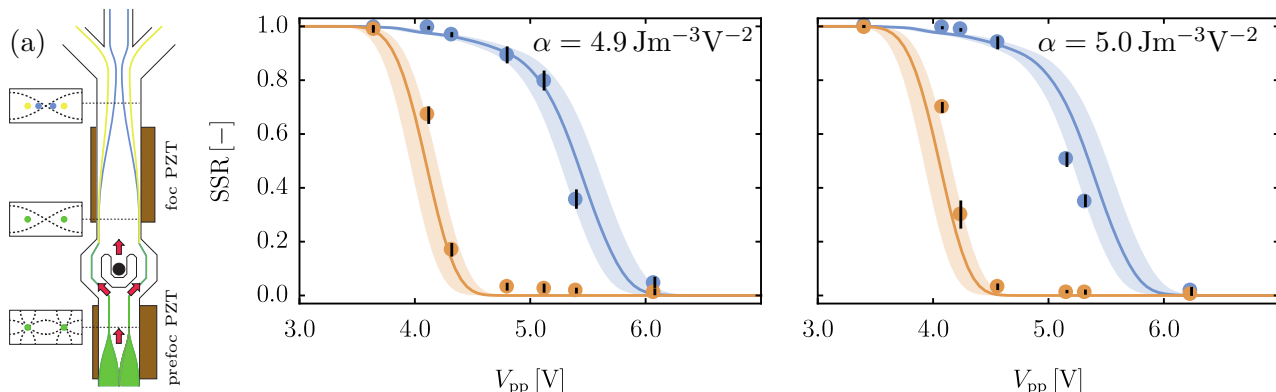


Figure 1: Results for the calibration procedure for the same chip and two separate experiments in the case of prefocused streams (a) by using PS5 μm (blue) and PS7 μm (orange) microbeads in phosphate saline buffer (PBS). Symbols are the experimental datapoints, lines are the theoretical fitting.

Figure 2 shows the results for the calibration procedure in the case of non-prefocused streams for a water suspension of polystyrene microbeads with nominal diameters 5 μm and 7 μm . The estimated device effectivity value was $\alpha = 4.4 \text{ J m}^{-3} \text{ V}^{-2}$. This value was then used to estimate the compressibility of melamine microparticles which resulted $\kappa = 125 \text{ TPa}^{-1}$. This value is in good agreement with that reported by [5] $\kappa = 124 \text{ TPa}^{-1}$, and also for this case the small discrepancy between the two values, i.e. $\sim 1.5\%$, shows that the method can be used to measure particle properties.

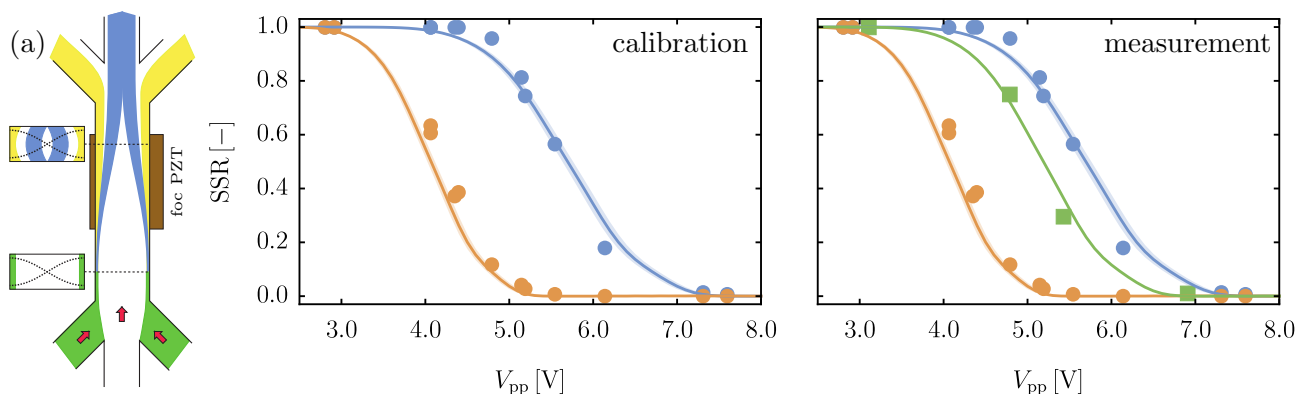


Figure 2: Results for the calibration procedure for the same chip in the case of non-prefocused stream (a) by using PS5 μm (blue) and PS7 μm (orange) microbeads in phosphate saline buffer (PBS). The compressibility measurement is performed on melamine microbeads MA4 (green). Symbols are the experimental datapoints, lines are the theoretical fitting.

Conclusion

We introduced a method for the evaluation of the separation performance in acoustophoresis by particle counting. The method has been applied to the acoustic calibration of a device by performing two identical but separate experiments of separation. For the two experiments we determined two values of the device effectivity α for $E_{ac} = \alpha V_{pp}^2$ which agreed within 2%. We also measured the compressibility of melamine microparticles by performing acoustic calibration with reference microparticles and using the unknown compressibility as fitting parameter. It agreed with a previously reported value within 2%.

References

- [1] Urbansky A, Ohlsson P, Lenshof A, Garofalo F, Scheduling S, and Laurell T, *Rapid and effective enrichment of mononuclear cells from blood using acoustophoresis*, Scientific Reports 7: 17161 (2017).
- [2] Lenshof A, Urbansky A, Scheduling S, and Laurell T, *High Performance Multiplex Acoustophoresis for WBC Subpopulation Isolation*, MicroTAS (2017).
- [3] Augustsson P, Barnkob R, Wereley ST, Bruus H, and Laurell T, *Automated and temperature-controlled micro-PIV measurements enabling long-term-stable microchannel acoustophoresis characterization*, Lab Chip 11: 4152–4164 (2011).
- [4] Augustsson P, Karlsen JT, Su H-W, Bruus H, and Voldman J, *Iso-acoustic focusing of cells for size-insensitive acousto-mechanical phenotyping*, Nature Communications 7: 11556 (2016).
- [5] Cushing KW, Garofalo F, Magnusson C, Ekblad L, Bruus H, and Laurell T, *Ultrasound Characterization of Microbead and Cell Suspensions by Speed of Sound Measurements of Neutrally Buoyant Samples*, Anal Chem 89: 8917–8923 (2017).
- [6] Garofalo F, *Quantifying Acoustophoretic Separation of Microparticle Populations by Mean-and-Covariance Dynamics for Gaussians in Mixture Models*, arXiv:1802.09790 (2018).

Copatterning of microparticles using the continuously phase-modulated standing surface acoustic waves

Chanryeol Rhyou¹, Byungjun Kang¹ and Hyungsuk Lee¹

¹ School of Mechanical Engineering, Yonsei University, Seoul, Korea
E-mail: hyungsuk@yonsei.ac.kr, URL: <http://leelab.yonsei.ac.kr>

Introduction

Microparticle manipulation such as patterning, tweezing or sorting has gained much attention in the fields of biology, chemistry, diagnostics and material science. Several techniques using surface acoustic waves have been introduced due to its label-free, biocompatible, and energy-efficient characteristics [1, 2]. Here, we developed a technique that is capable of copatterning microparticles with different dimensions. To this aim, we utilized continuously phase modulated standing surface acoustic waves (CPM-SSAW) that was previously developed in our group [3]. By obtaining the optimal rate for each particle and controlling the locations of node in a computerized manner, we demonstrated an alternative pattern of two types of microparticles.

Theory

The optimal rate of phase shift is defined as the maximum value of phase shift at which a displacement of particle by the CPM-SSAW is linear. Equilibrating two major forces, the acoustic radiation force and the drag force in acoustofluidics, we obtained the optimal rate at a given frequency and properties of particle and fluid [3]. The optimal rate depends on the particle size and the applied frequency of SAW as below.

$$\dot{\phi}_{\text{opt}} = \frac{2kF_0}{b}, \text{ where } b = 6\pi a\eta, F_0 = \frac{\pi p_0^2 V_p \beta_f}{2\lambda} \phi \text{ and } k, p_0, \lambda, V_p, \rho_p, \rho_f, \beta_p, \beta_f, \phi,$$

a , and η are the wavenumber, acoustic pressure, wavelength, particle volume, particle density, fluid density, particle compressibility, fluid compressibility, contrast factor, particle radius, and fluid viscosity respectively. In the continuous phase modulation, ϕ is a constant and is equal to the $\phi = 2\pi\Delta f$ where Δf is a frequency shift. When the optimal rate of target particle with specific size is applied, target particles are displaced linearly while the smaller particles show oscillatory motions. Eventually the difference in displacement between two particles enables the larger particles to be separated from the mixture. When the larger particles arrived at centers between nodes, the SSAW with a frequency which is two-folds of the original is applied to form the new trapping positions as shown in Fig. 1

Experiment

In order to demonstrate this strategy, we designed new piezoelectric substrate with double patterned Interdigital transducers (IDT's) to generate two frequencies, 14 and 28 MHz respectively. The former frequency was used to displace microparticles with CPM-SSAW, and the latter one was used to form new pressure nodes where the larger particles are located. We developed the software to control the frequency shift and duration of SAW application.

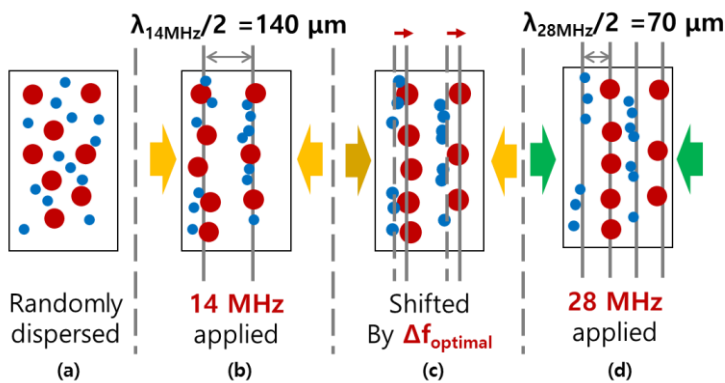


Figure 1. Steps for copatterning microparticles with two different size: (a) the mixture of two particles is randomly dispersed in a microchannel, (b) both particles are aligned by the SSAW at 14 MHz, (c) The larger particles (red) were displaced linearly and separated by using CPM-SSAW, (d) When the large particles are located between the small particles, CPM-SSAW stopped and SAW at 28 MHz was applied to form new locations of nodes.

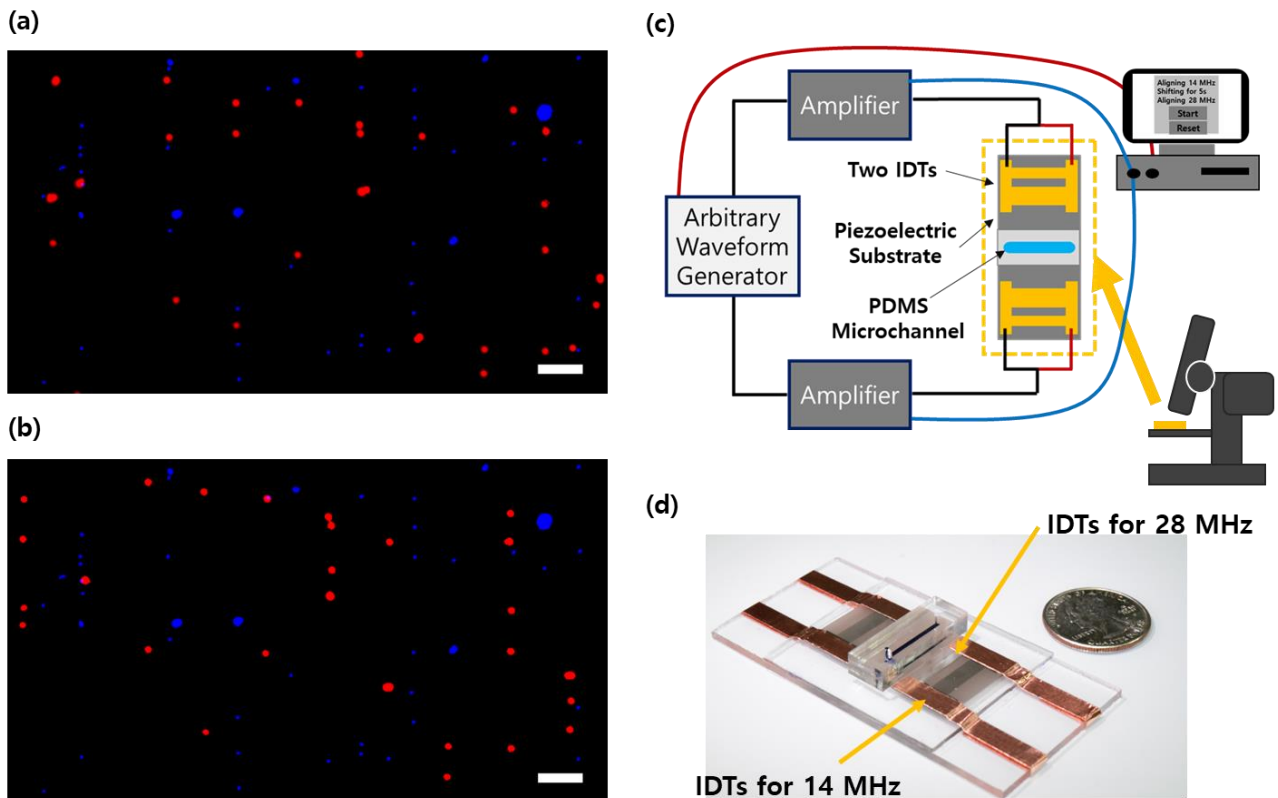


Figure 2. Images of microparticles aligned before (a) and after (b). (c) Schematic of experiment setup to show IDT substrate subject to a PC control. (d) Image of double IDTs on Lithium Niobate substrate for copatterning (Scale bars: 100 μm)

Two kinds of particles with 6 μm and 15 μm diameter were randomly dispersed in a microfluidic channel. The applied SSAW at 14 MHz had both types of particles aligned at the same pressure nodal lines as shown in Fig. 2(a). Then, using the CPM-SSAW with the optimal rate of frequency shift [3], the target particles of 15 μm (red) were displaced linearly while 6 μm particles (blue) were rarely moved with a minimal oscillation. To locate the target particles between non-target particles, when the target particles were moved at centers between the nodal lines formed at 14 MHz, the computerized program stopped the CPM-SSAW and switch the applied frequency to 28 MHz [Fig. 2(b)]. In this way, the large and small microparticles were copatterned by lines in an alternative manner. Experiment setup and the piezoelectric substrate with double IDT pattern are shown in Fig. 2(c) and Fig. 2(d) respectively.

Materials and method

PDMS micro-channel (length 23 mm) was prepared with using SU8 mold provided by the manufacturer via conventional soft lithography. PDMS mixture of prepolymer (Sylgrad[®] 184) and curing agent at a ratio of 10:1 by volume were mixed over the SU8 mold inside the petri dish ($\Phi = 150$ mm) and cured at 60 $^{\circ}\text{C}$ in dry oven overnight. The width and height of the main channel are 2000 μm and 80 μm respectively. And the PDMS wall thickness is 2 mm. The piezoelectric substrate is a 128 $^{\circ}$ rotated Y-cut X-propagating Lithium Niobate (LiNbO₃). A sinusoidal RF input was generated by an arbitrary waveform generator (Keysight, HP33522). The RF input signal was amplified by the power amplifier (Mini-Circuits, LZY-22+). Each particle was 6 μm (Polyscience BioMag[®], Bright Blue) and 15 μm (Molecular Probe FluoSphere[®], Orange). The particle mixture with the ratio 1:1 was infused by syringe pump (Chemyx, Fusion 200T) and observed via both brightfield and fluorescence microscopy (Nikon, Eclipse Ni-U)

Conclusion

We estimated the optimal rate for a target particle with a given size theoretically and experimentally. Using the obtained optimal rate and computerized control, an alternative copatterning of two particles having different sizes was demonstrated. This method can be developed further to manipulate multi-type particles with the size gradients.

References

- [1] J. Shi, D. Ahmed, X. Mao, S. C. S. Lin, A. Lawita, and T. J. Huang. Lab on a Chip **9**, 2890-2895 (2009).
- [2] X. Ding, S. C. S. Lin, B. Kiraly, H. Yue, S. Li, I. K. Chiang, J. Shi, S. J. Benkovic, and T. J. Huang. Proceedings of the National Academy of Sciences **109**, 11105-11109. (2012).
- [3] J. Lee, C. Rhyou, B. Kang, and H. Lee. Journal of Physics D: Applied Physics **50**, 165401 (2017)

Optimized LiNbO₃ cut and omnidirectional spiral surface acoustic waves for particles manipulation and multi-size particles separation in a microliter sessile drop

Naiqing Zhang¹, Tilwala Gopesh¹, Jiyang Mei¹, and James Friend¹

¹Medically Advanced Devices Laboratory, Department of Mechanical and Aerospace Engineering, University of California San Diego, San Diego, USA

E-mail: jfriend@eng.ucsd.edu, URL: <http://friend.ucsd.edu/>

Introduction

Point-of-care diagnostics has seen significant advancements in the last decade. Among various techniques, surface acoustic wave (SAW) induced mixing and separation in sessile drops has shown superiority and importance due to rapid fluid actuation, biocompatibility, and simple operating procedures. Straight interdigital transducers (IDTs) with a sessile drop located at an offset position from the center of the SAW propagation direction has been developed for fluid spinning, particle concentration and separation due to asymmetric SAW actuation. However, asymmetric material properties, difficulty in accurately locating sessile drops, and large SAW energy losses because of the offset position impede its efficiency, accuracy, and repeatability. Therefore, there is an imminent need to develop an axisymmetric SAW design for efficient transfer of energy from all directions into an accurately located sessile drop. Here, we present an optimized LiNbO₃ (LN) cut and a novel omnidirectional spiral surface acoustic wave (OSSAW) design to conduct more efficient fluid spinning and mixing. We further demonstrate accurate particle manipulation and multi-size separation in a microliter drop.

Analytical analysis of Optimized LiNbO₃ cut for omnidirectional SAWs

To generate axisymmetric omnidirectional SAWs, we first identified the optimal angle θ of Y-rotated X-propagating (YX) LN for the most efficient wave propagation in all directions of the plane. The stiffness tensor of θ YX-cut LN, c_{pqrs}^E , was obtained by a rotational transformation of LN stiffness tensor in principal axes coordinates, c_{ijkl}^E . Then 2nd-order tensor c_{3qr3}^E , showing properties of stiffness tensor in the propagation plane was compared to the planar stiffness tensor of isotropic materials, c_{iso} . As shown in Fig. 1(a), the minimum Euclidean norm between c_{3qr3}^E and c_{iso} with respect to cut angle θ showed that the 121° YX-cut has the least anisotropic properties for SAW propagation on LN.

Furthermore, the coupling coefficient of 121° YX-cut is higher than the 128° YX-cut in most propagation directions, showing its superior electromechanical effects for SAW propagation (Fig. 1(b)).

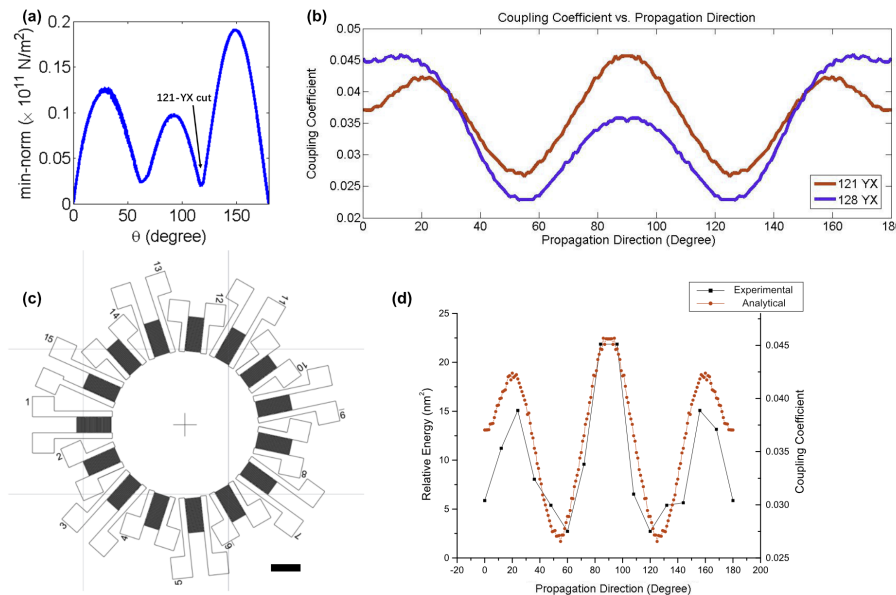


Figure 1: (a) Analytical $\min\{\|c_{3qr3}^E - c_{iso}\|_2\}$ with respect to θ degree YX-cut LN, showing the 121° YX-cut LN has the least anisotropic properties. (b) Analytical coupling coefficient of 121° and 128° YX-cut LN with respect to propagation direction using Tiersten's method [1], showing that 121° YX-cut also has high electromechanical effects for SAW propagation. (c) Experimental device for testing the coupling coefficient of 121° YX-cut LN. (d) Experimental results from laser Doppler vibrometry (UHF-120 Polytec, Germany) compared to analytical results for 121° YX-cut LN. Scale bar: 2 mm.

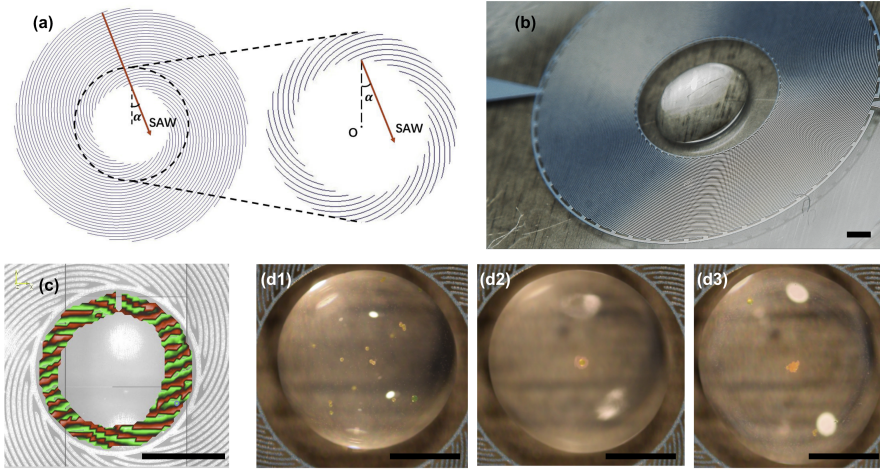


Figure 2: (a) OSSAW pattern generated in MATLAB, with rotationally symmetric SAW propagation into the inner region at a constant angle α . (b) Image of 60 MHz OSSAW device with microliter sessile drop on inner circular region. (c) LDV phase scan of OSSAW inner annular region, showing rotational waves propagating into inner region. (d1-d3) Before, during, and after the effective separation of $3.3 \mu\text{m}$ and $41.7 \mu\text{m}$ polystyrene (PS) particles in a microliter sessile drop due to different acoustic radiation (F_{AR}) and centrifugal (F_C) forces. Scale bar: 0.5 mm.

OSSAWs Design and Functionality

A novel spiral design was developed for OSSAWs such that the wave propagation directions, which are perpendicular to the spiral structure's fingers, are rotationally symmetric with a constant offset angle α relative to the inner circular region (Fig. 2(a)). The equation for one spiral line in polar coordinates (ρ, θ) is $\theta = \sqrt{A\rho^2 - 1} - \tan^{-1}(\sqrt{A\rho^2 - 1}) - \sqrt{AR_1^2 - 1} + \tan^{-1}(\sqrt{AR_1^2 - 1})$, where $A = 1/(R_2^2 \sin^2 \alpha)$; R_1 and R_2 are the outer and inner radii of the spiral IDT. The spiral pattern was used to generate a mask for standard photolithography and deposition procedures on 121° YX-cut LN (Fig. 2(b)). An LDV phase scan of inner annular region demonstrated rotational waves propagating into the inner region (Fig. 2(c)). A 60 MHz OSSAWs device performed ultrafast fluid spinning (~ 3000 rpm) and rapid uniform mixing (~ 1 s) in μl -scale sessile drops. Effective PS particle separation has also been presented, which arises from the acoustic radiation force ($\propto f^4 R^6$) [2] and centrifugal force ($\propto R^3$) (Fig. 2(d)).

Frequency-based OSSAWs for particles manipulation and multi-size separation

An integrated frequency-based OSSAW design was further developed, with 40 MHz and 100 MHz resonance frequencies for inner and outer spiral IDT patterns (Fig. 3(a)). Due to frequency-based F_{AR} (Fig. 3(b,c)), centrifugation and concentration of PS particles can be rapidly achieved (~ 1 s) with input frequencies of 40 MHz and 100 MHz respectively. Moreover, when the input signal is alternated between 40 MHz and 100 MHz at a 0.01 s time interval, the time interval scale is much smaller than the particles' dynamic motion in the fluid (~ 1 s), causing the particles to form rings with different radii where they experience equilibrium between F_{AR} and F_C . Multiple scale particle separation was performed in one μl -scale sessile drop (Fig. 3(d)) for the first time to our knowledge.

Conclusion

An optimized LN cut, a novel OSSAW design for efficient fluid spinning and mixing, and accurate particle manipulation to enable multi-size separation in μl -scale sessile drops has been presented. These advancements potentially provide an effective and powerful platform for whole blood separation and point-of-care diagnostics without need for micro or nano-scale fluidic enclosure.

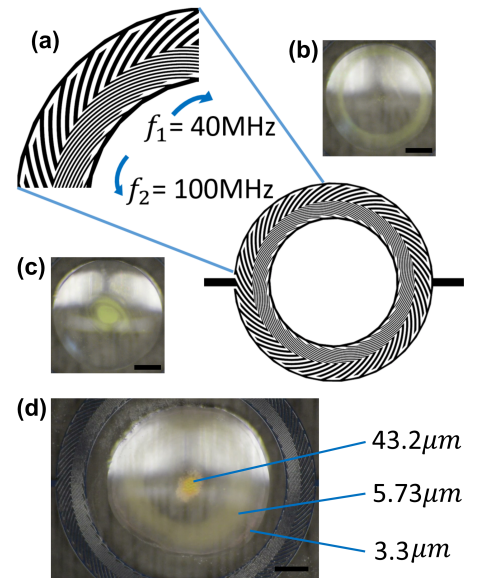


Figure 3: (a) Design of frequency-based OSSAW with resonance frequencies for the inner and outer spiral IDT patterns of 100 MHz and 40 MHz, respectively. (b) Image of outer ring formation of $5.73 \mu\text{m}$ PS particles when activating frequency $f_1 = 40$ MHz. (c) Image of concentrated middle pattern of $5.73 \mu\text{m}$ PS particles when activating frequency $f_2 = 100$ MHz. (d) Image of simultaneous separation of $3.3 \mu\text{m}$, $5.73 \mu\text{m}$, and $43.2 \mu\text{m}$ PS particles in one drop, with 0.01 s actuation time for each of the two 40 MHz and 100 MHz signals, alternating back and forth. Scale bar: 0.5 mm.

References

- [1] Slobodnik Jr, A. & Conway, E. Microwave acoustics handbook. volume 1. surface wave velocities. Tech. Rep., AIR FORCE CAMBRIDGE RESEARCH LABS HANSCOM AFB MA (1970).
- [2] King, L. V. *et al.* On the acoustic radiation pressure on spheres. *Proc. R. Soc. Lond. A* **147**, 212–240 (1934).

In situ selective manipulation and seeding of human cells in a with micro-acoustic tweezers

Antoine Riaud¹, Gabriele Pitingolo¹, Philippe Nizard¹ and Valérie Taly¹

¹INSERM UMR-S1147, CNRS SNC 5014, Paris Sorbonne Cite Universite, 75006 Paris, France
E-mail: valerie.taly@parisdescartes.fr, URL: <http://recherche.parisdescartes.fr/UMRS1147/Translational-Research-Microfluidics/Group>

Introduction

With forces five orders of magnitude larger than optical tweezers at equal power density, acoustic tweezers are foreseen as an unparalleled tool for single cell positioning and printing. Thanks to its contactless and label-free nature, it could offer an alternative to micropatterning of biomolecules and hydrodynamic traps (the former showing poor performance when using multiple cell types [1] and the latter requiring specific artificial geometries that cannot mimic well natural microenvironment. So far, most research efforts on spatial organization of cells using acoustic tweezers have focused on the mass production of suspensions of multicellular tissue constructs [2, 3] and on controlling the distance between numerous cells [4] and pairs of cells [5] in a regular array. An equally important topic is the accurate positioning of individual cells in a biomimetic environment. In this regard, the SAW trap proposed by Guo *et al.*[6] and the focused beam described by Lee *et al.*[7] offer valuable options. Nonetheless, the former is not selective which means that all the non-adherent cells are going to experience a similar force and will move together, while the latter requires a soft reflector [8] to trap cells and other particles with an acoustic impedance larger than that of water [9]. Hence, none of these methods have been successfully applied for the precise seeding of cells in a biomimetic microfluidic channel. In the present study, we experiment a recently described selective micro-acoustic tweezers [10] to manipulate HT29 human colon tumour cells and seed them in a PDMS microchannel which geometry is reminiscent of the intestinal stem cell niche.

Methods

The contactless manipulation system is shown in Fig. 1. It is composed of a swirling-SAW acoustical tweezers (Fig. 1.A,[10]) adjusted on a modified microscope stage equipped with a micromanipulator. The cells are contained in microchannel that can be displaced relatively to the tweezers by the mean of the micromanipulator. In order to minimize the friction between the channel and the spiraling IDT, we shield the transducer with a 120 μm thick PET film. The channel geometry (Fig. 1.B) is a 300 μm -wide straight channel with a series of crypts reminiscent of the intestinal stem cell niche. It includes large inlets and outlets to facilitate the introduction and removal of ethanol (sterilization),

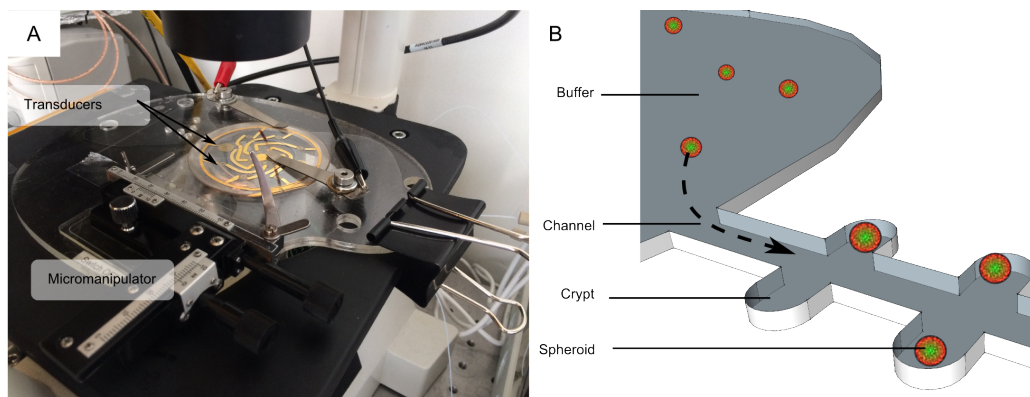


Figure 1: Experimental setup. **A.** Modified microscope stage: the micromanipulator holds the microchannel to enforce an accurate relative displacement between the acoustic tweezers and the microfluidic chip containing the cells. **B.** Biomimetic microchannel: using acoustic tweezers, cells from the buffer region are carried through the channel towards the initially empty crypts where they can be cultured.

cell medium and cell suspension. These inlets and outlets feature a wide and shallow step that acts as a buffer region to pick the cells without the interference of acoustic streaming. Indeed, when an acoustic wave propagates in a large cavity, acoustic streaming can develop and drive the cells away from the transducer[11]. The channel is placed into contact with the transducer by the mean of an oil layer that acts as a coupling gel. This allows to use disposable channels that can be placed in the biological incubator to culture the cells once the seeding process is complete.

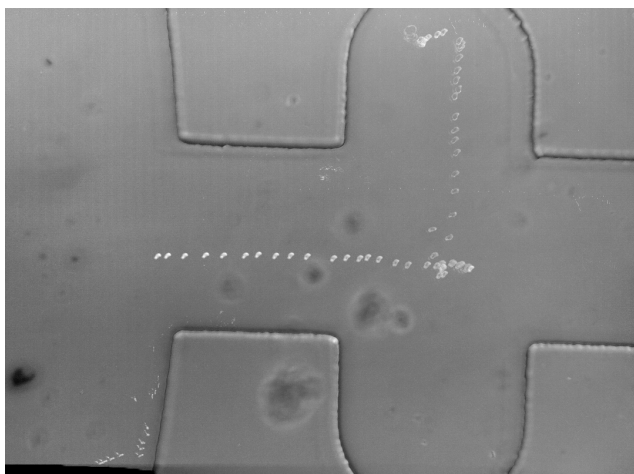


Figure 2: Manipulation of an HT29 cells in a PDMS microfluidic channel. The cell, initially introduced in the buffer region, is trapped by the acoustic tweezers and moved towards the channel crypt. This iterative process can be repeated to transport a larger number of possibly different cells to a target location. During cell culture, the medium contained in the channel has to be changed on a regular basis. The crypts geometry ensures that moderate flow velocity does not carry the cells away.

Results and discussion

We conducted a series of experiments to introduce the cells in the microchannel and culture them. In figure Fig. 2, a series of snapshots shows the capture of an individual HT29 cell in the buffer region and the seeding in a channel crypt. Eventually, a controlled number of cells can be deposited in individual crypts for further assays.

Conclusion

Cell-by-cell tissue construct remains a frontier of modern biology. Selective acoustic tweezers offer a versatile and inexpensive tool to organize biological cells in space. The method is label-free, biocompatible, and can accommodate disposable substrates. Although in the present work the throughput is relatively limited by the manual operation of a single acoustical tweezers, task automation combined with photolithography could allow patterning thousands of acoustical tweezers on a single chip and simultaneous operation of all these independent traps for an efficient massively parallel cell printing.

References

- [1] L. Lin, Y.-S. Chu, J. P. Thiery, C. T. Lim, I. Rodriguez, *Lab on a Chip* **13**, 714 (2013).
- [2] K. Chen, *et al.*, *Lab on a Chip* **16**, 2636 (2016).
- [3] J. Liu, *et al.*, *Journal of cellular biochemistry* **102**, 1180 (2007).
- [4] D. J. Collins, *et al.*, *Nature communications* **6**, 8686 (2015).
- [5] F. Guo, *et al.*, *Proceedings of the National Academy of Sciences* **112**, 43 (2015).
- [6] F. Guo, *et al.*, *Proceedings of the National Academy of Sciences* **113**, 1522 (2016).
- [7] J. Lee, *et al.*, *Applied physics letters* **95**, 073701 (2009).
- [8] Z. Hong, W. Xie, B. Wei, *Review of Scientific Instruments* **82**, 074904 (2011).
- [9] J. Lee, K. K. Shung, *The Journal of the Acoustical Society of America* **120**, 1084 (2006).
- [10] A. Riaud, M. Baudoin, O. B. Matar, L. Becerra, J.-L. Thomas, *Physical Review Applied* **7**, 024007 (2017).
- [11] A. Riaud, M. Baudoin, J.-L. Thomas, O. B. Matar, *Physical Review E* **90**, 013008 (2014).



Breakdown of acoustically levitating aggregates of fluorescent particles or living cells using specific illumination

Angelica Castro¹, Gabriel Dumy¹, Olivier Mesdjian¹, Mauricio Hoyos¹, Jean-Luc Aider¹

¹ *Laboratoire PMMH, CNRS UMR7636, ESPCI Paris, PSL Research University, 1 rue Jussieu, 75005, Paris, France*

E-mail: jean-luc.aider@espci.fr, gabriel.dumy@espci.fr, mauricio.hoyos@espci.fr, URL: <http://www.acoustofluidics.org>

Introduction

Acoustic manipulation of micro-objects (particles, cells, bacteria) can be achieved using ultrasonic standing waves in a fluidic or microfluidic resonator [1,3] as illustrated in Fig. 1. By matching proper geometrical and physical parameters it is possible to use acoustic radiation force (ARF) to gather the particles in the pressure nodal plane and thus create one or several aggregates. The axial component of the ARF maintains the particles in levitation while the radial component forces the creation of aggregate. Once the particles are very close of each other, the Bjerknes force [4,5] helps keeping the particles close together and the aggregate stable. In standard operating conditions, they can be maintained as long as needed in acoustic levitation at the equilibrium position.

In this study, we show that it is possible to force the complete breakdown of the levitating aggregate by using a proper optical wavelength and intensity. If the particles remain in acoustic levitation, they are quickly ejected from the illuminated region. We show that this phenomenon strongly depends on both the ultrasonic field and the specific illumination. Various experiments with different types of fluorescent particles and concentrations are used to discuss the possible explanations of the phenomenon. Apart from the acoustic and optical characteristics of the setup, we show that this phenomenon depends directly on the optical absorption coefficient of the particles. This phenomenon could also be applied to biological species such as red blood cells, or micro-algae, suggesting many potential applications.

Acoustic levitation and aggregation

The experiments are carried out in a simple cylindrical closed cavity. The diameter of the cavity is very large (20 mm) compared to its height (0.375 mm). The acoustic radiation force is created by matching the acoustic frequency to create an acoustic pressure node at the mid-height of the cavity (Fig. 1.i), leading to a typical acoustic frequency of 2 MHz. In standard operating conditions, the ARF forces the particles or any object with a positive acoustic contrast factor to migrate toward the pressure node and to gather to form a stable aggregate that can be maintained in levitation as long as needed (Fig. 1.ii).

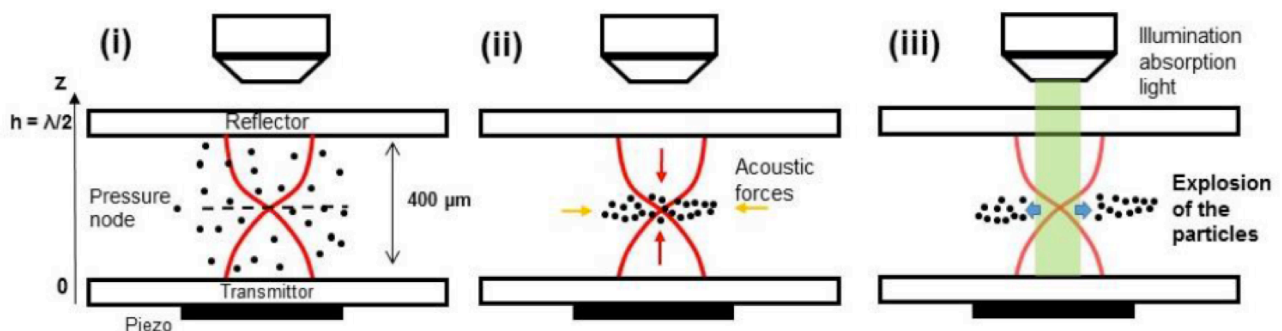


Figure 1: Sketch of the different steps of acoustic levitation and aggregation of particles in an acoustic resonator. The particles are in suspension in a resonator of 400 μm height (i). The acoustic radiation force forces the particles to gather at the pressure node and form aggregates (ii). When the aggregate is illuminated with the proper wavelength it explodes in the levitation plane.

Breakdown of the levitating aggregate using optical illumination

Once the aggregate has been formed we illuminate it with a CoolLED light source allowing the control of the wavelength. If the particles are fluorescent and if the aggregate is illuminated with the wavelength

corresponding to the peak of the absorption spectrum of the particles, then the particles are ejected from the illuminated area (Fig. 1.iii). The expulsion velocity of the particles from the aggregates v_{ej} can be very high (up to tens of $\mu\text{m}\cdot\text{s}^{-1}$ for micrometer sized particles) and scales with both the acoustic field amplitude and illumination power as :

$$v_{ej} \propto P_{light} \cdot \langle E_{ac} \rangle^{3/4}$$

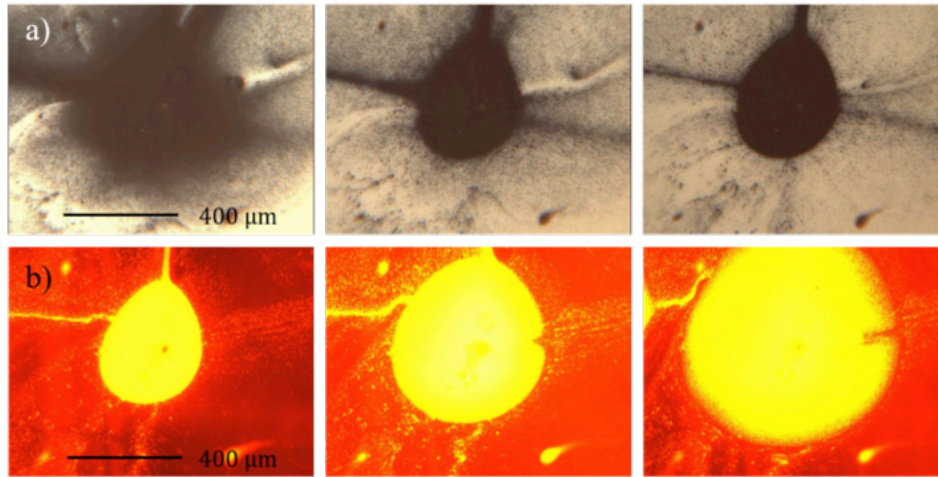


Figure 2: a) Formation of a levitating aggregate of 1.62 μm polystyrene beads absorbing green light and fluorescing in red. b) When the same aggregate, maintained in stable acoustic levitation, is illuminated with a strong green light, the particles are ejected from the illuminated area while still remaining in acoustic levitation.

Potential for highly selective separation

The same experiments have been carried out with various particles, confirming the phenomenon. The same process has been applied to a binary mixture of particles each absorbing the light at different wavelengths. When the aggregate has been illuminated with the absorption wavelength of one of the species, we observed the ejection of the given particles from the aggregate, leaving the other particles in stable acoustic levitation. It is then possible to quickly and efficiently separate a mixture of particles as a function of their absorption wavelength. It demonstrates the potential of this new process as a highly selective and efficient separation technique.

Finally this technique has also been applied to various living cells. It has been shown that red blood cells could also be ejected from the illuminated area, confirming that only the absorption coefficient plays a role in the process. The same result has been obtained with micro-algae (phacodactylum).

Conclusion

We have shown in this study that it is possible to reverse the aggregation process of particles under acoustic levitation. It means that the aggregating and attractive acoustic forces, which are responsible for the formation of large aggregates in acoustic levitation, can be cancelled out and even reversed. It suggests the creation of a repulsive force when the objects in acoustic levitation absorb a sufficiently large amount of energy. More experiments are needed to explain the physical mechanisms involved in this phenomenon. Nevertheless, our results confirm the robustness of this coupled optic and acoustic manipulation. It also opens interesting perspective for new highly selective separation processes in various application fields.

References

- [1] W. T. Coakley and J. F. Spengler, *Analytical scale ultrasonic standing wave manipulation of cells and microparticles* Ultrasonics, vol. 38, pp. 638-641, 2000.
- [2] J. Nilsson, M. Evander, B. Hammarström, and T. Laurell, *Review of cell and particle trapping in micro-fluidic systems*, Analytica chimica acta, vol. 649, pp. 141-157, 2009.
- [3] O. Dron and J.-L. Aider, *Varying the agglomeration position of particles in a micro-channel using acoustic radiation force beyond the resonance condition*, Ultrasonics vol. 53, no. 7, pp. 1280-1287, 2013
- [4] V. F. K. Bjerknes, *Fields of Force*, Columbia University Press, 1906
- [5] A. Garcia-Sabaté, A. Castro and M. Hoyos, *Experimental study on inter-particle acoustic forces*, The Journal of the Acoustical Society of America, vol. 135, 1056, 2014.



Size-dependent steady-state motion of microparticles in acoustophoresis

Wei Qiu¹, David van Assche², Henrik Bruus¹, and Per Augustsson²

¹Department of Physics, Technical University of Denmark, Kongens Lyngby, Denmark
E-mail: weiqiu@fysik.dtu.dk, URL: <http://www.fysik.dtu.dk/microfluidics>

²Department of Biomedical Engineering, Lund University, Lund, Sweden

Introduction

In acoustophoresis induced by a standing-wave field, suspended microparticles in a microchannel are subject to both the acoustic radiation force and the Stokes drag force from the acoustic streaming. The relative magnitude of the two forces depends on the size of the microparticles and the material of the solvent. For polystyrene particles in water at 2 MHz, theoretical studies have predicted a critical diameter of 2 μm for the cross-over, where the two forces are equal [1-3]. Here, using 3D tracking, we explore experimentally this cross-over for particle diameters ranging from 0.5 to 3.1 μm . We find that the particles become confined to particle-size-dependent rolls close to the channel floor and ceiling, and furthermore that large regions of the channel are depleted, even for particles far below the critical radius.

Materials and experimental methods

The measurements of particle trajectories were performed using an aqueous 2.5 wt% Ficoll PM70 solution in a standard 130- μm -high and 375- μm -wide long straight channel in a silicon-glass chip with a PZT transducer bonded underneath, as illustrated in Figure 1. The motion of the polystyrene beads (diameters 0.5, 1.0, 1.9, and 3.1 μm) was recorded using a general defocusing particle tracking (GDPT) [4]. The measurements were conducted after stopping the flow in a half-wavelength standing wave field with an input ac voltage on the transducer of 1.6 V_{p-p} and with a frequency sweep ranging from 1.95 to 2.05 MHz. The microparticles were initially uniformly distributed in the channel and the particle motions were recorded for 60 s after the onset of ultrasound. The experiment was repeated at least 16 times for each particle size to improve the statistics.

Results

The positions of microparticles with different sizes in the initial and the steady states are shown in Figure 2. The particle positions in the two intervals from 0 to 10 s and from 50 to 60 s are overlaid separately to illustrate the initial and the steady state positions of the particles. For 0.5- μm -diameter particles, the initial state and the steady state do not differ: in both cases the particles follow the streaming rolls, occupying the whole area of the channel cross section, see Figure 2(a). For 1- μm -diameter particles, depleted regions appear in the steady state at the horizontal and vertical center planes and close to the sidewalls, see Figure 2(b). The depleted regions further expand for 1.9- μm -diameter and 3.1- μm -diameter particles, see Figures 2(c) and (d).

Discussion

At first glance it may be counterintuitive that increasing the relative radiation component leads to a depletion of particles at the pressure minima. But, as illustrated in Figure 3, by overlaying streaming rolls with a particle trajectory, when the radiation is orthogonal to the streaming component the particle shifts streamline inwards the center. A larger particle will experience a longer sideways shift, leading to larger depleted areas at mid height and mid width. The mechanism results in the depleted regions shown in Figures 2(b) and (c). If the particles are sufficiently small, the radiation force never dominates in any position in the channel, hence

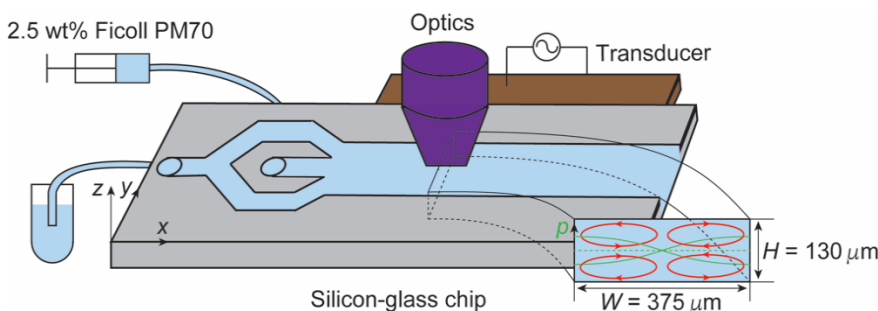


Figure 1. Sketch of the experimental system consisting of a long straight channel with a rectangular cross section of height 130 μm and width 375 μm . The half-wavelength pressure field and streaming rolls (inset, green and red) are excited by a piezoelectric transducer at 2 MHz. The motion of polystyrene beads with different diameters are recorded through the optical system (purple).

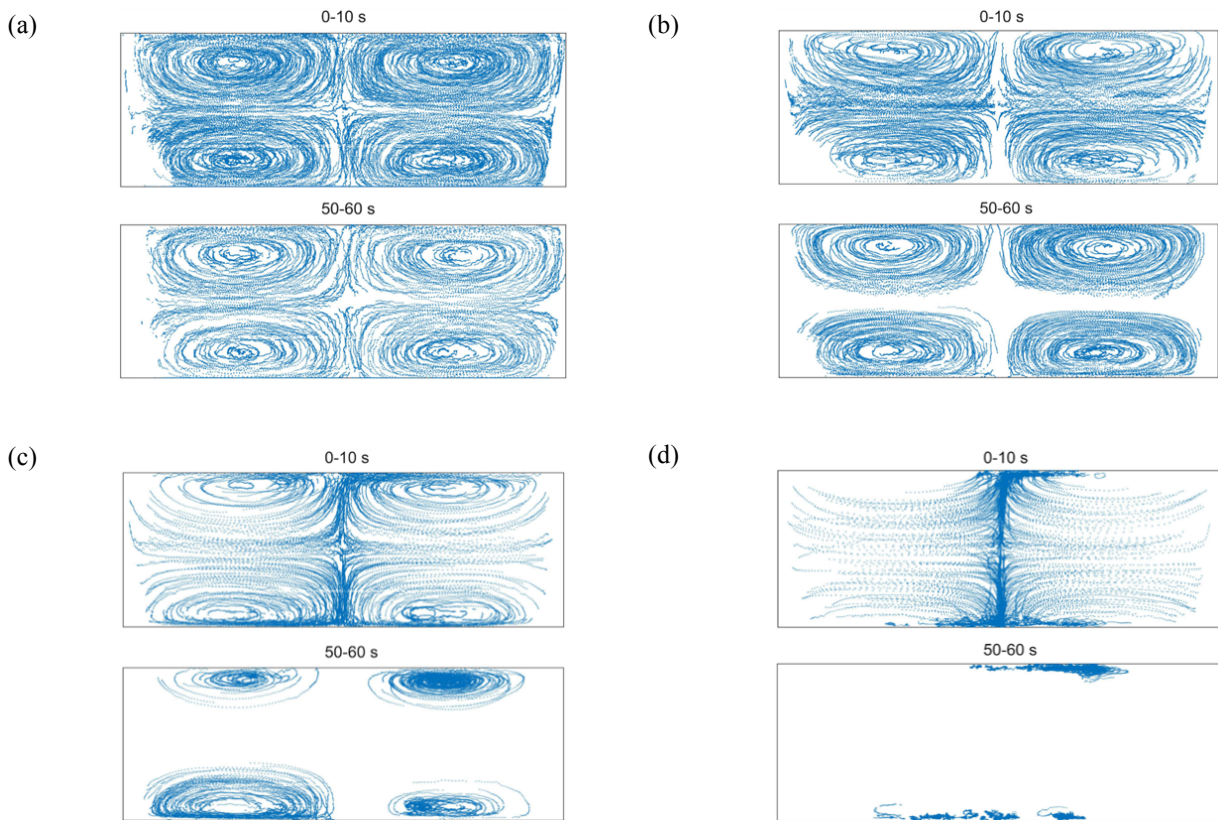


Figure 2: Overlaid particle positions in the two intervals from $t = 0$ to 10 s and from $t = 50$ to 60 s for four different particle diameters: (a) $0.5 \mu\text{m}$, (b) $1.0 \mu\text{m}$, (c) $1.9 \mu\text{m}$, and (d) $3.1 \mu\text{m}$.

no depleted region is formed, Figure 2(a). The initial motion of $3.1\text{-}\mu\text{m}$ -diameter particles exhibits focusing due to the large radiation force. After streaming has brought the particles to the ceiling or floor, they are further dragged away by the streaming (the radiation force close to the nodal plane is close to zero) instead of staying close to the pressure nodal plane, and then they are pushed back by the radiation force. The resulting motion of the particles forms a loop, which is closely confined to the walls, and the farthest position the particles can reach away from the pressure node is around the quarter of the channel width, where the radiation force is the maximum. The steady state of large particles indicates that the streaming-induced drag force is increased, when the particles are closer to the walls, and thus dominates over the radiation force.

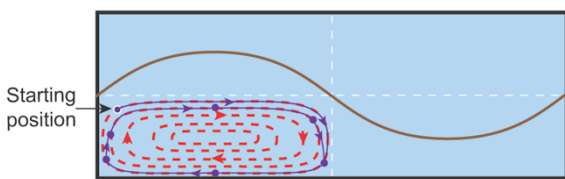


Figure 3: Schematic diagram of the formation of the depleted regions. The streaming rolls and the particle trajectories are indicated by red dashed lines and purple solid lines, respectively. The brown solid line indicates the acoustic radiation force along the channel cross section. The particles are indicated by purple solid circles, and the starting position is indicated by an arrow.

Conclusion

We have found that acoustophoresis of particles near the critical diameter leads to unexpected and strongly size-dependent trajectories. A preliminary physical explanation of this phenomenon has been given, and it is our intention that further details of the underlying physics will be understood after performing numerical simulations as well as further experimental investigations of wall interactions near the floor and ceiling. Prior to Acoustofluidics 2018, we will further extend our study to include also fluids of spatially inhomogeneous density and compressibility where acoustic streaming can be greatly suppressed [5]. This study will be useful to better understand microparticle manipulation using acoustophoresis near and below the critical diameter.

References

- [1] R. Barnkob, P. Augustsson, T. Laurell, and H. Bruus, *Phys. Rev. E* **86**, 056307 1-11 (2012).
- [2] P.B. Muller, R. Barnkob, M.J.H. Jensen, and H. Bruus, *Lab Chip* **12**, 4617-4627 (2012).
- [3] P.B. Muller, M. Rossi, A.G. Marin, R. Barnkob, P. Augustsson, T. Laurell, C.J. Kähler, and H. Bruus, *Phys. Rev. E* **88**, 023006 1-12 (2013).
- [4] R. Barnkob, C.J. Kähler, and M. Rossi, *Lab Chip* **15**, 3556-3560 (2015).
- [5] J.T. Karlsen, W. Qiu, P. Augustsson, and H. Bruus, *Phys. Rev. Lett.* **120**, 054501 1-6 (2018).



Ultrasound Manipulation of Bacteria in Drinking Water for Attenuated Total Reflection Infrared (ATR-IR) Spectroscopy

Stephan Freitag, Andreas Schwaighofer, Stefan Radel, Bernhard Lendl

Institute of Chemical Technologies and Analytics, Technische Universität Wien,
Getreidemarkt 9/164, A 1060 Vienna, Austria
E-mail: Stephan.Freitag@tuwien.ac.at

Introduction

Freshwater is a finite resource, essential for agriculture, industry and even human existence [1]. Different types of pathogenic bacteria can be present in water sources. For example, *Escherichia coli* (*E.coli*) is an indicator for fecal contamination of drinking water [2]. Therefore, fast, effective and sensitive monitoring of microbiological pathogens is needed to evaluate the presence of waterborne diseases or contamination.

In the food and pharmaceutical industries, infrared (IR) spectroscopy is applied for analysis of microorganisms for rapid identification and screening of life-threatening pathogens, biotechnological process control and microbiological quality control [3]. It provides qualitative and quantitative information in a non-destructive and label-free manner, because inherent vibrations of molecular vibrations are detected [4]. For measurements in water, which is a strong absorber in the mid-IR region and thus allows only interaction lengths in the range of a few micrometers, attenuated total reflection (ATR) configurations are the most commonly employed. Using this technique, the light is totally reflected within the optically denser ATR element, forming an evanescent field that interacts with the sample at typical penetration depths of approximately 1 to 2 μm . To improve sensitivity of ATR-IR experiments, bacteria could be enriched in the evanescent field for example through sedimentation [5]. As an alternative, ultrasound (US) particle manipulation as a mighty tool for separating suspended particles from their host liquid [6] has shown potential in biomedical analytic tasks like cell separation [7], bead-based bioassays [8] and concentration of bacteria in water [9]. Moreover, the formation of conglomerates, due to ultrasonic excitation of yeast suspension enabled US enhanced IR spectroscopy for in-line monitoring of yeast in a bioreactor [10,11].

Our current work aims at developing a device based on ultrasonic particle manipulation and ATR-IR spectroscopy for measuring bacteria in drinking water.

Experimental

We developed an acoustofluidic cell made out of aluminum, equipped with an ultrasound composite transducer consisting of a 10 mm PZT disc (lead zirconium titanate, type PIC 181, PI Ceramics, Lederhose, Germany) with wraparound silver electrodes glued to a Macor cylinder with a two-component epoxy resin (Polytec EP 630, Polytec PT GmbH, Karlsbad, Germany). This cell was mounted on a custom-built ATR fixture (US-ATR-IR Sensor; cf.: Figure 1) and embedded in a Fourier-transform (FT)-IR spectrometer (Bruker, Tensor 27, Ettlingen, Germany). ZnS was chosen as material for the ATR crystal due to its refraction index of 2.35 and VIS transparency, which enables observation of the US experiments by a conventional camera. The US transducer was operated at a frequency of approx. 2.6 MHz.

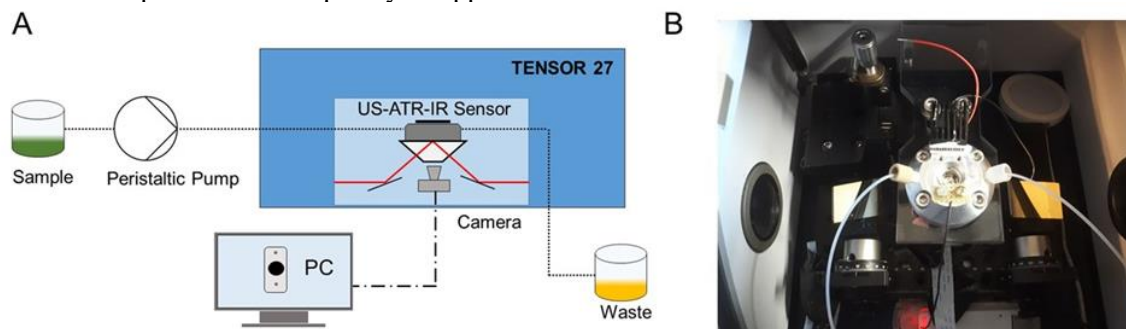


Figure 1: (A) Schematic of the experimental setup. (B) Picture of the custom-made ATR setup incorporated in the sample compartment of the Tensor 27 FT-IR spectrometer.

Results

The acoustofluidic cell of the US-ATR-IR sensor was filled with a 5 mg/ml *E.coli* suspension using a peristaltic pump. When US was turned on, the formation of *E.coli* conglomerates could be observed through the ATR element via a camera (cf.: Figure 2A,B). After 15 min of US exposure, a spectrum was recorded featuring no absorption bands (Figure 2C, black solid line) of *E.coli*, indicating that bacteria agglomeration takes place above the sensitive region of the ATR element. Turning the US off followed by 12 minutes of sedimentation time, an IR spectrum was recorded featuring the typical absorption bands of bacteria, indicating the presence of *E.coli* in the evanescent field (Figure 2C, red solid line). Subsequently, the US transducer was reactivated and an IR spectrum was recorded, which did not show typical IR bands of bacteria (Figure 2C, green dashed-dotted line). After turning off the US transducer again and 12 minutes of sedimentation time, the recorded IR spectrum depicts characteristic IR features of bacteria again (Figure 2C, blue dashed-dotted line). The recorded spectra indicate that our US-ATR-IR sensor is capable of manipulating *E.coli* suspensions via US.

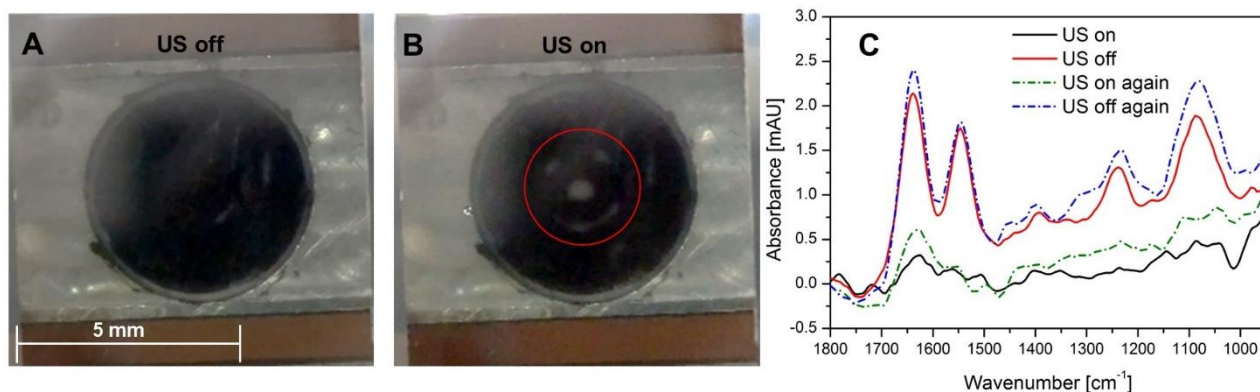


Figure 2: (A) Acoustofluidic cell filled with *E.coli* suspension when US is turned off. (B) Acoustofluidic cell filled with *E.coli* suspension when US is turned on, *E.coli* conglomerates are encircled in red. (C) IR spectra of *E.coli*, black line US turned on, red line US turned off, green dashed-dotted line US turned on again, blue dashed-dotted line US off again.

Conclusion

In this preliminary work, we present our efforts towards developing an US-ATR-IR sensor for monitoring of bacteria in drinking water. We demonstrated that our system is now capable of trapping *E.coli*. By turning off the US, we showed that the bacteria subsequently settled into the evanescent field of the ATR element making them feasible for IR measurements. Furthermore, we are also capable of lifting the bacteria back into the cavity between transducer and the ATR element to clean the sensitive region.

Our next steps will focus on the miniaturization of our acoustofluidic cell and actively push the bacteria conglomerates into the evanescent field.

Acknowledgement

This work was performed in the course of the WaterSpy project and has therefore received funding from the European Union's Horizon 2020 research and innovation programme under the grant agreement no.: 731778.

- [1] Bartram, J. and Ballance, R., *Water quality monitoring: a practical guide to the design and implementation of freshwater quality studies and monitoring programmes*, CRC Press, (1996).
- [2] Edberg, S., Rice, E., Karlin, R. and Allen, M. *Journal of Applied Microbiology* **88**, 106S-116S (2000).
- [3] Naumann, D. *Encyclopedia of analytical chemistry*, (2000).
- [4] Steele, D. *Handbook of Vibrational Spectroscopy*, (2006).
- [5] Schnoller, J. and Lendl, B. *Proceedings of IEEE*, 742-745, 2004.
- [6] Gröschl, M. *Acta Acustica united with Acustica* **84**, 432-447 (1998).
- [7] Barani, A., Paktinat, H., Janmaleki, M., Mohammadi, A., Mosaddegh, P., Fadaei-Tehrani, A. and Sanati-Nezhad, A. *Biosensors and Bioelectronics* **85**, 714-725 (2016).
- [8] Wiklund, M., Radel, S. and Hawkes, J. *Lab on a chip* **13**, 420-451 (2014).
- [9] Carugo, D., Octon, T., Messaoudi, W., Fisher, A. L., Carboni, M., Harris, N. R., Hill, M. and Glynne-Jones, P. *Lab on a Chip* **14**, 3830-3842 (2014).
- [10] Koch, C., Brandstetter, M., Lendl, B. and Radel, S. *Ultrasound in Medicine and Biology* **39**, 1094-1101 (2013).
- [11] Koch, C., Brandstetter, M., Wechselberger, P., Lortantfy, B., Plata, M. R., Radel, S., Herwig, C. and Lendl, B. *Analytical chemistry* **87**, 2314-2320 (2015).



3D simulations of an acoustofluidic immersed-IDT SAW device

Nils Refstrup Skov¹, Prateek Sehgal², J.S. Bach¹, Brian J. Kirby², and Henrik Bruus¹

¹Department of Physics, Technical University of Denmark, Kongens Lyngby, Denmark
E-mail: nilsre@fysik.dtu.dk, URL: <http://www.fysik.dtu.dk/microfluidics>

²Sibley School of Mechanical and Aerospace Engineering, Cornell University, Ithaca, New York, USA

Introduction

To go beyond the proof-of-concept stage in acoustofluidics and design devices for clinical use, a thorough understanding of the basic working principles is necessary. This goal is best obtained by using a feedback loop combining experiments and design with theory and simulation. This reduces cost and time consumption, while giving insights into those physical properties of a given device that are hard to obtain by purely experimental methods. Previously, 3D simulations have been scarce, and most numeric models have been restricted to 2D cross-sectional representations of long, straight channels. For devices that are not invariant in the lateral direction, it is necessary to perform full 3D simulations. Here, we present a full 3D model of a complex device and compare its predictions with experiments. The model takes into account the piezoelectric substrate, the metal electrodes, and the fluid domain embedded in an elastic solid.

The previous device and experiments

Our numeric model is based on the device by Sehgal and Kirby [1], where a microchannel is defined in a PDMS-slab, which is bonded onto a lithium niobate substrate as shown in Fig. 1. Surface acoustic waves (SAWs) are generated by applying a MHz ac voltage to a metal interdigitated transducer (IDT) electrode patterned on the substrate, placed inside the microchannel, and oriented at an angle of 10° relative to the fluid flow direction. The IDT is bounded by a set of Bragg reflectors, also placed inside the channel, designed to reflect outgoing waves back towards the IDT, thereby creating a standing wave field in between the reflectors. The device enables separation of 100 and 300 nm particles, as the acoustic radiation force is 27 times larger on the latter than on the former. Some of the experimental findings related to the innermost electrodes have been explained using a unit-cell 2D simulation [2], while others related to particle positioning and in-planing streaming effects at the electrode edges, have not yet been explained.

Current device and 3D model

The numeric model is a full representation of a test device similar to the one in Fig. 1, including fluid and solid mechanics as well as the piezoelectric effect. The model consists of a lithium niobate substrate, metal electrodes, a fluid domain embedded in an isotropic linear elastic solid bonded onto the substrate, as shown in Fig. 2(a). The model includes a first-order velocity vector field \mathbf{v}_1 in the solids, a second-order velocity vector field \mathbf{v}_2 as well as first- and second-order pressure scalar fields p_1 , p_2 in the fluid, and an electric potential scalar field ϕ in the substrate. The forcing boundary condition applied on the device is a harmonically oscillating potential $\phi = V_0 e^{-i\omega t}$ applied to the charged IDT electrode driving the piezoelectric effect. The model uses previously presented simplification steps [3], namely (1) perfectly matched layers to prevent reflection of outgoing waves and (2) symmetry

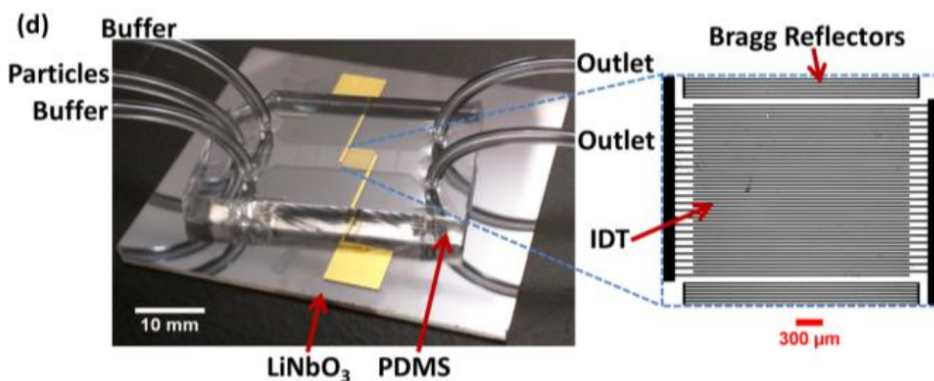


Figure 1: The previous SAW device [2] with its channel defined in PDMS placed on top of a LiNbO₃ substrate [2]. The actuation takes place inside the channel through a central IDT emitting waves that are partially reflected by surrounding Bragg reflectors leading to a standing wave field in the fluid.

planes to eliminate redundancies. This allows us to keep the numeric model down to a manageable computational cost in 3D, while capturing effects not present in 2D models.

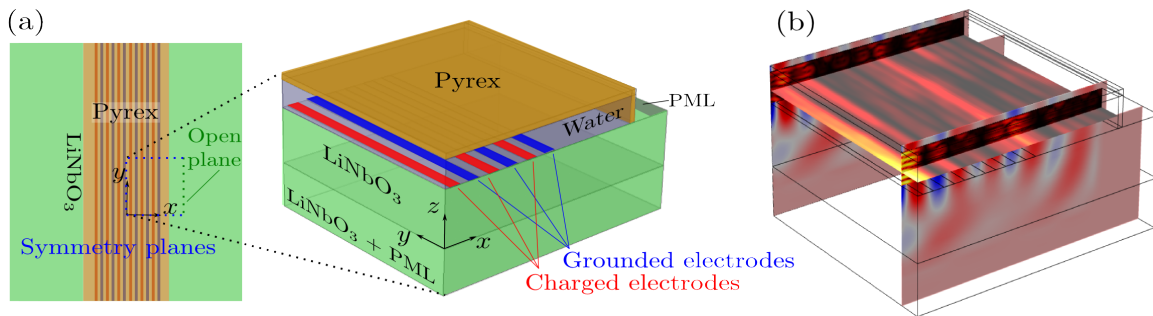


Figure 2: (a) Schematic of an experimental test device similar to the one in Fig. 1, but larger and with a Pyrex lid instead of PDMS. The corresponding COMSOL model is reduced by letting three of the four vertical boundary planes be symmetry planes and the last one a free boundary condition. To further reduce computational costs, only 3 out of 24 IDT electrode pairs are included, and perfectly matched layers are used to reduce the height and length of the LiNbO₃, as the surface acoustic waves are evanescent vertically and are absorbed horizontally past the reflectors. (b) Color plot of the COMSOL simulation of the magnitude of the acoustic radiation force on a 100 nm polystyrene sphere [from 0 (black) between the electrodes to 16 fN (yellow) above the electrodes] in the water domain and the vertical displacement [from -4 \AA (blue) to 4 \AA (red)] in the LiNbO₃ and Pyrex domains. Particles will migrate from areas of large radiation force magnitude (yellow) to regions of low/no force (black), as observed in the test device.

Results on the energy radiation

Because the electrodes are immersed in the microchannel of the present device, the acoustic waves are generated in direct contact with the water. Consequently, only a small portion of the wave propagates along the substrate, and so we find that the Bragg reflectors have little effect on the device performance.

Results on the acoustophoretic motion

Using our model, we find a good agreement between our numerical predictions and the experimentally observed particle motion. In a test device, suspended particles have been experimentally observed to focus above IDT electrodes, which is in agreement with the stable acoustophoretic equilibria predicted by our model Fig. 2(b). Regarding second-order fields, four large scale streaming rolls have been observed in the horizontal plane at the vertical center of the experimental testing device. Fig. 3(a) shows an image of the upper half of one such roll in the experimental device visualized using $1.7 \mu\text{m}$ polystyrene beads. In Fig. 3(b) a similar half-roll is seen in a preliminary numerical 3D simulation using effective boundary conditions for streaming [4]. Although the numeric model is not a one-to-one replica of the test device due to computational restrictions, there is a qualitative agreement between experiment and model. Notice in particular the positioning of the rolls above the end of the electrodes.

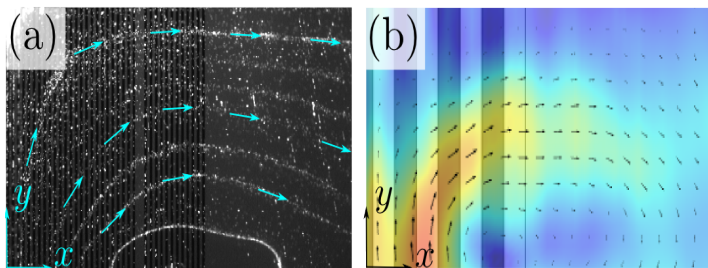


Figure 3: Large-scale horizontal streaming rolls in the xy -plane at the vertical center of the channel. (a) Experimental image of streaming rolls observed in the test device, using $1.7 \mu\text{m}$ polystyrene particles. (b) Color plot of the second-order streaming velocity field magnitude $|\mathbf{v}_2|$ from 0 (blue) to $80 \mu\text{m/s}$ (red) found in our simulations, with the field components overlaid as arrows. The black lines indicate IDT electrode positions on substrate below.

Conclusion

We have fully modeled a SAW device in 3D, taking into account the piezoelectric effect along with solid and fluid mechanics. Using this model, we have taken steps towards investigating effects not captured by 2D simulations, such as streaming rolls in the lateral direction, and acoustic fields near IDT edges. Prior to Acoustofluidics 2018, we plan to expand our numeric model beyond the testing device, to represent the actual experimental device.

References

- [1] P. Sehgal and B.J. Kirby *Procs. pp. 93-94, Acoustofluidics 2017*, San Diego, 28 - 29 August 2017.
- [2] P. Sehgal and B.J. Kirby *Anal. Chem.* **89**, 12192-12200 (2017).
- [3] N.R. Skov and H. Bruus *Procs. pp. 97-98, Acoustofluidics 2017*, San Diego, 28 - 29 August 2017.
- [4] J.S. Bach and H. Bruus *submitted* (2018), <https://arxiv.org/abs/1804.05802>



Spatial characterization of the acoustic field in a standing wave cavity to control the aggregate shape

Nathan Jeger-Madiot, Gabriel Dumy, Mauricio Hoyos, and Jean-Luc Aider¹

¹PMMH (UMR 7636 CNRS-ESPCI-Paris 6-Paris 7) ESPCI, 1 rue Jussieu, 75005, Paris
E-mail: nathan.jeger-madiot@espci.fr, URL: <https://pmmh.spip.espci.fr/?Acoustofluidic-425>

Introduction

Acoustophoresis in micro-channel is commonly used to form particles or cells aggregate. In a standing wave cavity, different forces act on particles. The knowledge of the acoustic energy density and its space distribution, directly related to the Acoustic Radiation Forces (ARF)[1], is required to thoroughly understand the aggregate geometry. A new method is presented. This method measures the acoustic pressure in free field with a needle hydrophone and gives a large scale representation of the acoustic field. Thus, the aggregate distribution patterns can be explained by the spatial acoustic heterogeneities caused by the effect of the transducer confined into the micro-cavity.

Relation between the ARF and the acoustic field in a standing wave cavity

To achieve acoustic manipulation of particles and build aggregate, we use a standing wave cavity. This is a powerful acoustic resonator [3]. The resonances occur when the emitted frequency f matches with the cavity geometry : $f_n = n \frac{c}{2h}$ with n the mode number, c the ultrasound velocity and h the cavity height. In our setup, the first mode is chosen, which leads to $h = 500 \mu m$ for a $1,5 MHz$ working frequency. A piezoelectric transducer (PZT) generates the ultrasound wave in the fluid. Thereby, the suspensions in the fluid will be brought in the acoustic pressure node (with a particle density ρ_p greater than the fluid density ρ_f). This study focuses on the primary effect of a standing wave cavity called ARF although there are other effects like acoustic streaming or Bjerkness Forces. The Yosioka model [1] is used to depict the ARF effect on spherical particles. The primary ARF responsible of the particle acoustic levitation is defined by :

$$\vec{F}_{AC} = \frac{\pi}{4} \langle E_{AC} \rangle k d_p^3 F_Y \sin(2kz) \vec{e}_z$$

With $\langle E_{AC} \rangle$ is the time averaging acoustic energy density inside the cavity, d_p is the particles diameter, k the wave number and F_Y the contrast factor which depends on the physics properties of the fluid and the particles. The transverse component of the ARF appears once the particles are in the nodal plane ($\vec{F}_{AC} = \vec{0}$). Indeed, the transverse component is two orders of magnitude smaller than the primary one. The formula is given by Whitworth [4] for a radially symmetric acoustic wave in the nodal plane :

$$F_T = d_p^3 \frac{3(\rho_p - \rho_f)}{\rho_f + 2\rho_p} \nabla \langle E_{AC} \rangle$$

To conclude this section, the first ARF effect on the fluid suspension will be the axial movement of particles toward the nodal plane. Then, the transverse effect will cluster particles in aggregate (see Fig 1). The knowledge of the acoustic energy density magnitude and its space distribution provides information on the axial force applied on the particle and the shape of aggregate caused by the transverse component.

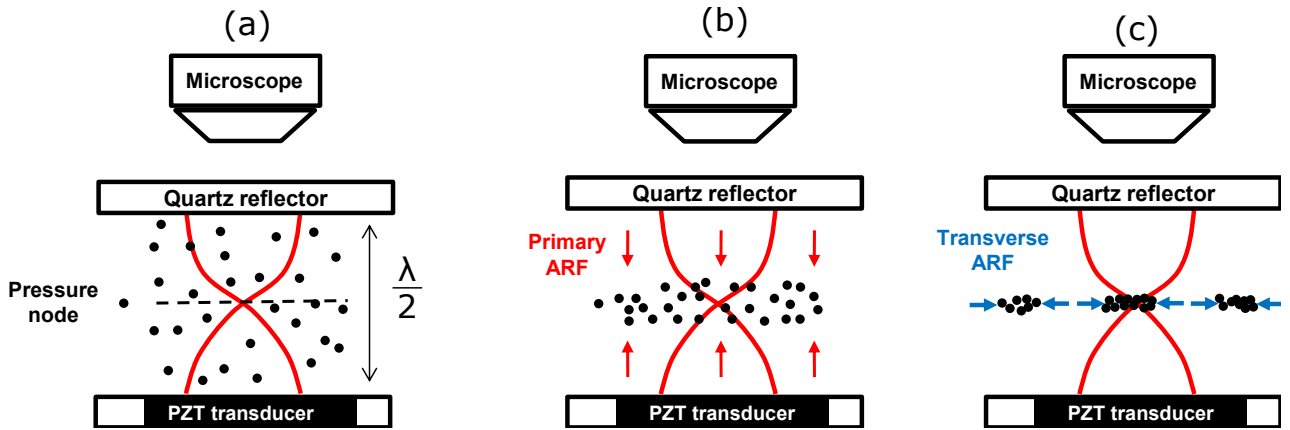


Figure 1: (a) The acoustic emission is turned on. The particles suspension begins to feel the acoustic effects. (b) The primary acoustic radiation force (ARF) brings particles to the nodal plane with its axial component. (c) Once the particles have reached the nodal plane, the transverse ARF (with a lower magnitude about two orders compared to the primary one) clusters them and creates aggregates. Aggregate patterns depend on the acoustic energy gradient.

Setup presentation and preliminary results

The first experiment aims to characterize the emitting transducer (2MHz probe from SignalProcessing SA) with an external hydrophone (needle hydrophone from Precision Acoustics Ltd) in free field. To do this, we have used a water tank and two motors to achieve a 2D scan of the pressure acoustic field (see Fig 2). For a first assessment of the spatial acoustic field inside the cavity, we have averaged the pressure on each profile (with a $500\mu m$ pixel thickness) in the axial (z) direction. This average gives the pressure magnitude and its spatial distribution along the cavity width. Thereby, the pressure gradient and the transverse ARF can be deduced from this spatial organization.

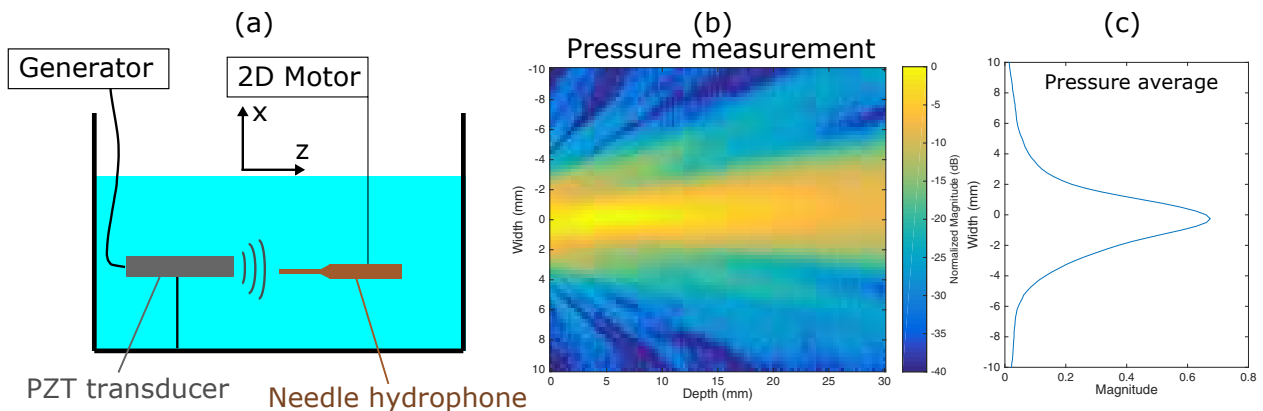


Figure 2: (a) Experimental Setup. (b) 2D scan of the acoustic pressure for a 1,5MHz frequency (c) Pressure average in the axial direction (z) to model the acoustic profile into the cavity.

Conclusion

In this conference, we will show a new acoustic method to assess the spatial acoustic field inside the cavity. This knowledge is fundamental to understand the aggregate behaviour. Indeed, the acoustic energy density and its spatial distribution directly affect the Acoustic Radiation Forces (ARF). In the future, this method will be compared with another one which uses optical information on local area to estimate the acoustic energy in the standing wave cavity [2].

References

- [1] K. Yosioka and Y. Kawasima. *Acta Acust. united with Acust* **vol. 5**, no. 3, pp. 167 173, 1955.
- [2] O. Dron and J.-L. Aider. *EPL Europhysics Lett.*, vol. 97, no. 4, p. 44011, Feb. 2012.
- [3] H. Bruus. *Lab Chip*, 2012,12,20.
- [4] G. Whitworth, M.A. Grundy, W.T. Coakley. *Ultrasonics Procs.*, 1991, 29, 439 444,



Investigation of Particle Interaction Forces in a standing acoustic wave field

Davood Saeidi^{1,2}, Mohsen Saghafian¹, Björn Hammarström², and Martin Wiklund²

¹Department of Mechanical Engineering, Isfahan University of Technology, Isfahan, Iran
E-mail: davoods@kth.se

²Biomedical and X-ray Physics, Royal Institute of Technology, KTH-AlbaNova, SE-106 91 Stockholm, Sweden

Introduction

In recent years, the implementation of primary acoustic forces in devices for cell and particle separation, manipulation [1], and trapping [2] has widely increased. However, in the case of accurate cell and particle manipulation, particle interaction force can also be effective. This force is generated due to scattering effects of particles in the acoustic field, and may be comparable with primary forces in the case of bubble manipulation. Several investigations have been done to theoretically extract this force by Bjerknes [3], Weiser and Apfel [4], and Doinikov [5]. The phenomenon has also been investigated theoretically by Silva and Bruus [6]. In addition, Garcia-Sabate et al. [7] experimentally studied the inter-particle force between latex particles of size between 5-15 μm in the nodal pressure plane in the standing acoustic field.

In the current paper we propose the use of particle tracking algorithms to study the inter-particle forces experimentally. We show that this force can cause deflection in the particle movement in an acoustic field, enabling characterization of secondary forces outside of the nodal pressure plane and at relevant inter-particle angles.

Materials and Methods

All the experiments were performed in a silicon glass micro channel with rectangular cross section $375 \times 100 \mu\text{m}^2$ having a resonance frequency of 1.95 MHz. Acoustic fields were generated by using a signal generator with an output voltage of 10 V_{pp} and without any amplification. A PZT piezo with a nominal 2.5 MHz resonance frequency was used.

In order to experimentally investigate the interaction force between particles two different polystyrene beads were used, 4.8 μm and 25 μm . The larger beads were fixed in the channel, while the smaller ones were initially located close to the 25 μm diameter particles but free to move when exposed to the acoustic field. To control the location of the small particles a stop-valve was used, and in this way any fluid flow in the channel was eliminated. Particle movement was recorded by using a monochromatic camera.

Data Analysis

Particle movement was recorded at the speed of 13 frame per second (fps) and velocity measurement was done by implementing the free video analysis tool Tracker [8] – allowing tracking in the perpendicular and parallel direction of wave propagation.

Results and discussion

Fig. 1 and 2 show the particle trajectory for two different cases. By exposing the particles to the acoustic field the 4.8 μm diameter bead starts moving straight towards the nodal line but when getting close to the 25 μm diameter bead its motion is distorted from the main pathway. This interaction force between the two particles can be either attractive or repulsive based on the particle and fluid properties and the angle between the two particles. When the two particles lined up perpendicular to wave propagation direction the force is attractive while it is repulsive in parallel direction [4]. The results show that by decreasing the initial distance between two particles the inter-particle force is more pronounced. Fig. 3 shows the force ratio between the perpendicular and parallel directions of wave propagation in different dimensionless distance from the nodal pressure point for two cases. In Case 2 the initial horizontal distance between the moving object and the fixed one is larger than in Case 1 by about 20% and thus, reduction in the force in the horizontal direction in Case 2 can be seen related to the Case 1.

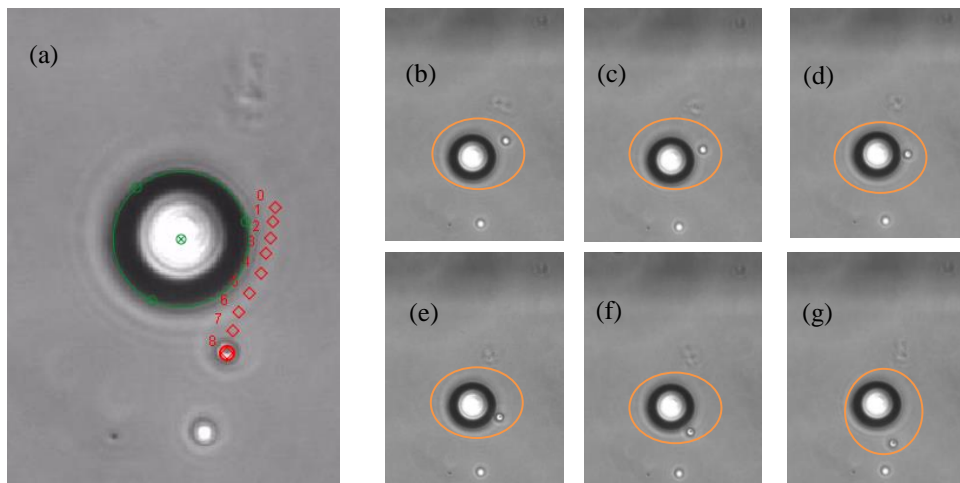


Figure 1: Case 1. Particle motion exposed to standing acoustic field.

The moving particle is 4.8 μm in diameter and the fixed particle is 25 μm in diameter (a).

Trajectory of the moving particle (b-g) with equal time steps of 1 second.

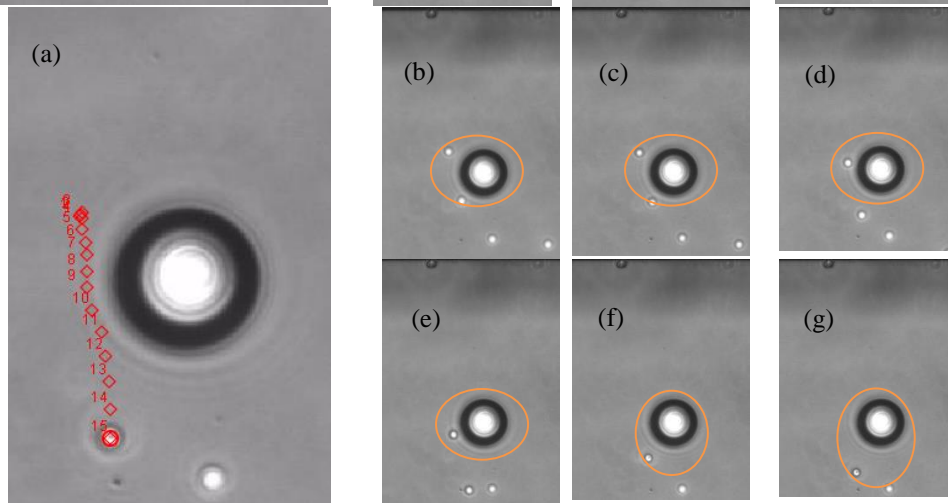
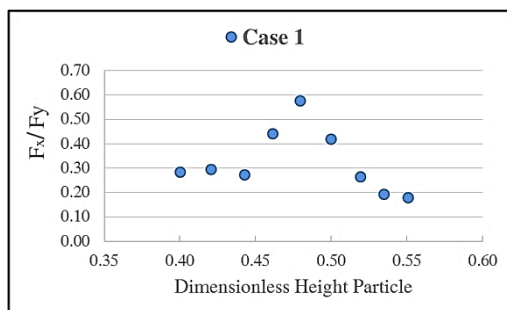


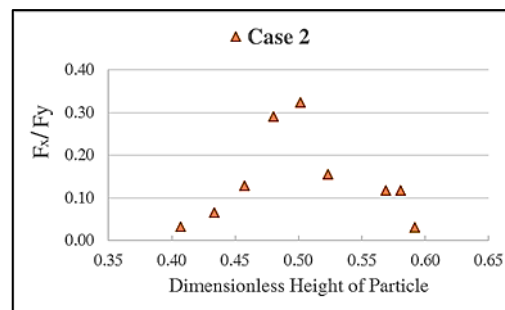
Figure 2: Case 2. Particle motion exposed to standing acoustic field.

The moving particle is 4.8 μm in diameter and the fixed particle is 25 μm in diameter (a).

Trajectory of the moving particle (b-g) with equal time steps of 2 seconds.



(a)



(b)

Figure 3: Force ratio in perpendicular and parallel directions of wave propagation. (a) Case 1, (b) Case 2.

Conclusion

In the current study we investigated the inter-particle force between two polystyrene particles with different diameter size, 4.8 and 25 μm outside the pressure nodal line. The results show that this force would be effective in the case that the particles are close to each other and can easily change the particle moving direction, and reach magnitudes of about half the force parallel to the wave propagation direction. These findings show that inter-particle force in the acoustic separating devices can cause reduction in the purity of separated cells and play an important role in particle aggregation.

References

- [1] A. Lenshof, C. Magnusson and T. Laurell. *Lab Chip* **12**, 1210 (2012).
- [2] M. Evander and J. Nilsson. *Lab Chip*, **12** 4667-4676 (2012).
- [3] V. F. K. Bjerknes, *Fields of Force* (Columbia University, New York, 1906).
- [4] M. A. H. Weiser, R. E. Apfel and E. A. Neppiras. *Acta Acust.* **56**, 114 (1984).
- [5] A. A. Doinikov. *J. Acoust. Soc. Am.* **111**, 1602 (2002).
- [6] G. T. Silva and H. Bruus. *Phys Rev. E* **90**, 063007 (2014).
- [7] A. Garcia-Sabate, A. Castro, M. Hoyos and R. Gonzalez-Cinca. *Am. J. Phys.* **135**, 1056 (2014).
- [8] D. Brown. Tracker 4.11.0, Free video analysis and modeling tool for physics education. Online open source: <https://physlets.org/tracker/index.html>, (Sep 2017).



Acoustophoretic focusing in a microfluidic chip for rapid label-free identification of harmful microbial in water

Jing Bo Zhang¹, Xin Li², Patricia Yang Liu² and Sha Xiong²

¹Advanced Environmental & Biology Centre, Nanyang Environmental & Water Research Institute, Nanyang Technological University, 1 Cleantech Loop, Cleantech One #06-08, Singapore 637141
E-mail: zhangjingbo@ntu.edu.sg

²School of EEE, Nanyang Technological University, 50 Nanyang Avenue, Singapore 639798

Rapid detection and identification of harmful microbial in water source is significant to prevent parasitic infections and outbreaks. Oocyst/Cysts stage of protozoa is of primary importance for dispersal and infectivity of parasites and thus is of the utmost importance for rapid and reliable detection and alarming. The conventional practice for inspection of oocysts is a series of time-consuming bio-laboratory processes including filtration, immunomagnetic separation, fluorescent antibody staining and examination/counting under a microscopic. It is vital to discover physical finger prints of oocysts/cysts and focus them effectively in the microfluidic channel if we want to adapt advanced microfluidic technology for automatic and label-free detection. On the other hand, using an acoustophoretic means for spatial control and manipulation has become well developed in the last two centuries. This presentation reports our successful application using standing wave focusing for suspended oocysts in a microfluidic channel.

Methodology

The acoustophoretic focusing is experimentally realized by an ultrasonic standing wave field which generates acoustic radiation forces on suspension particles and acoustic streaming in the fluid. The acoustic radiation forces push particles to the pressure node position, while the fluid exerts a viscous Stock drag force on particles which drags particles away from the pressure node position. According to the well-known equations, the acoustic radiation force is proportional to cubic radius of a particle, while the drag force is linear to the radius [1]. Therefore the axial radiation force is dominant for large particles and easy to achieve tight focusing. Considering the 4 ~ 6 μm dimension of the species of oocysts; we selected the channel width of 375 μm and the depth of 340 μm . Then the lowest order nominal frequency to generate an ultrasonic standing wave field inside the channel is determined. The standing wave is realized by gluing one or more Piezoelectric transducer(s) (PZT) on one side of a microfluidic chip bounded with glass (Fig. 1).

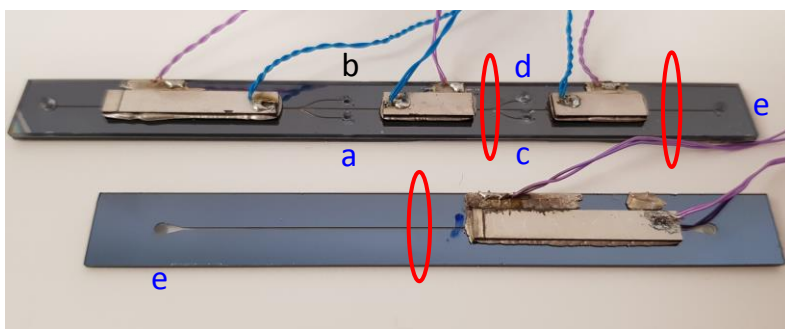


Fig. 1 Acoustopheratic chips with 5 outlets (upper) and one outlet (bottom).

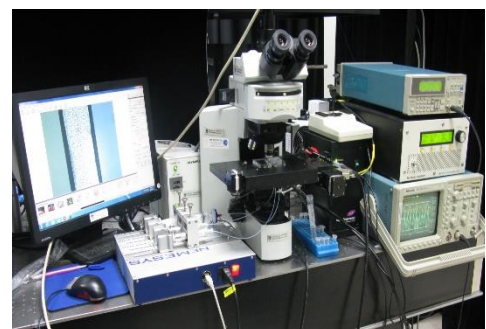


Fig. 2 The setup for monitoring of the effects of acoustopheratic focusing.

The focusing monitoring test of each individual chip is performed with the setups shown in Fig. 2. After it, we mount one chip onto an optical detection module composed of a low power laser diode and a high speed mono-color CMOS camera. For every test run, 10 ~15 ml of water sample spiked with oocysts flow through the microfluidic channel at a stable speed regulated by syringe pump(s). The optical patterns of individual oocysts and large numbers of unknown particles, which exist in various water samples, were captured for identification.

Results and analysis

Firstly, we will fine tune the RF signal generator to find the lowest driven oscillation frequency for stable standing wave field. For both types chips, the frequency is in the range of 1.8725 ~ 1.850 MHz at 30V. For both chips, the focused sample particles are flow out from the outlet e. Once the oocysts are well focused in the central stream of less than 40 μm^2 cross section, there would be no oocysts flowing away from outlets a, b, c and d. However practically, as there exist large amount of unknown particles in water, it is not always stable, this result in some losses from these outlets. To examine such losses, we compared the recovery rates of the 5 and one outlet chips.

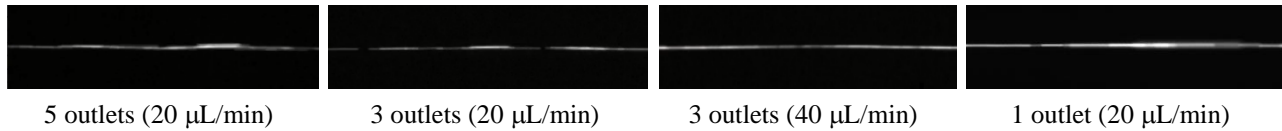


Fig. 3 Images of focused flow stream of 5 μm polystyrene beads with the first 3 obtained from the 5 outlet chip and the last one from the one outlet chip. When testing the focusing of a 3 outlet structure, we monitor in the area circled with red before outlets c and d while keeping them blocked. For beads, all focusing stream are within 20 μm width along the axis of the channel.

Figure 3 displays the focusing results of the two chips using low cost 5 μm polystyrene beads. Real time monitoring showed that with more PZTs, the focusing is tighter with the stream width less than 20 μm . Due to difference in density, non-uniformity and different surface features, oocysts are more difficult to focus than 5 μm polystyrene beads and hence have lower recovery rate. Therefore, we designed a series of tests to monitor the focusing results under microscope at the two positions of the 5 outlet chip (Fig. 1 upper) highlighted in red rings. To imitate infection outburst cases with trace amount of harmful microbial, we spiked small numbers of oocysts with the stain of FITC in our water sample. As trace amount of oocysts cannot form a continuous central stream, we took videos and counted the focused and unfocused oocysts to find the optimum structure and flow rate for this application. Focusing results are tabulated in table 1.

Table 1: Focusing test results:

Chip type	Inlet speed ($\mu\text{m}/\text{min}$)	Speed of all 5 outlets ($\mu\text{m}/\text{min}$)	Monitored before outlets c and d (equivalent to a 3 outlet chip)	Monitored before outlet e (with full function of 5 outlets)	Analysis & future optimizations
5 outlet chip	100	20	Tight focusing in both axial (< 25 μm) and depth directions.	Excellent focus in both axial (< 25 μm) and depth directions	Recovering rate: 96% With more PZTs, focusing is better than one PZT chip.
5 outlet chip	150 (for 3 outlet test, 90)	30	Tight focusing. No change compares with 20 $\mu\text{m}/\text{min}$ speed	Tight focusing in both directions, no visible changes.	Recovering rate: 95% When speed of all 5 outlets increase, more PZTs better
One outlet chip	20	20		Good focus in axial (< 60 μm) but not very good in depth direction	Recovering rate: 69% Focusing is not as good as the case of using of 3 PZTs.
One outlet	30	30		No visible difference with speed 20 $\mu\text{m}/\text{min}$	Recovering rate: 66%

Conclusions

We have achieved ultrasonic standing wave focusing for the oocyst stage of protozoa. With full cycle test runs including ultrasonic standing wave focusing and finger print pattern identification, a 50~60% identification rate can be achieved.

References

- [1] P. B. Muller, M. Rossi, Á. G. Marín, R. Barnkob, P. Augustsson, T. Laurell, C. J. Kähler and H. Bruus, *Physical Review E* 88, 023006-1 (2013).
- [2] H. Bruus, *Lab on a Chip* 12, 1014-1021 (2014).

Particle Separation Using Bulk Angled Standing Waves

Kedar C. Chitale, Bart Lipkens, Walter Presz, Jr., Benjamin Ross-Johnsrud

Flodesign Sonics, Wilbraham MA USA

Email: k.chitale@fdsonics.com, URL: <http://www.fdsonics.com>

Introduction

Tilted or angled standing waves have been used at MEMS scale to separate out particles of various sizes very effectively [1,2]. In this work, we propose a universal analytical solution for such a problem and study its physics. The mathematical formulation is validated with numerical simulations and experiments. Separation experiments are performed to determine the efficiency of macro scale angled wave system. The system shows 90+% efficiency in separating Jurkat T-cells from 30-micron beads. An advantage of such a macro-scale system is higher throughputs (several ml/min)

Analytical Model

Consider a standing wave at an angle (γ) to the flow direction of a particle with radius. Assuming an ideal standing wave with sinusoidal pressure distribution, an integral equation can be obtained for a particle's time of flight in the standing wave, neglecting the inertial forces. Solving this equation, one obtains an analytical solution to particle's deflection angle ($\Delta\theta_m$) inside an angled standing wave. A non-dimensional parameter (M) can be defined as given by Eq. (1) and represents the ratio of acoustic radiation force to the viscous drag force. This parameter plays a key role in determining particle deflection.

$$M = \frac{\pi r_p \beta_f P_o^2 X}{3\lambda\mu V} \quad (1)$$

In Eq. (1), r_p is particle radius, β_f is fluid compressibility, P_o is acoustic pressure amplitude, X is particle contrast factor, λ is wavelength, μ is fluid viscosity, and V is fluid velocity. The equation for particle deflection angle is given by Eq. (2).

$$\theta_M = \begin{cases} \tan^{-1}\left(\frac{1}{\tan \gamma \sqrt{1 - \left(\frac{M}{\sin \gamma}\right)^2}}\right) - \frac{\pi}{2} + \gamma & \text{if } \frac{M}{\sin \gamma} < 1 \\ \gamma & \text{if } \frac{M}{\sin \gamma} \geq 1 \end{cases} \quad (2)$$

Detailed derivation is given in Chitale [3]. The particle deflection depends on wave angle, γ , and the M parameter. This analytical model can be used to obtain universal curves for particle deflection based on its properties. Figure 1 shows these analytical curves.

Model Validation

The analytical model has been validated using numerical trajectory calculations and experiments with known sized beads. Figure 2(a) shows experimental results for particle deflection angle for beads of known size and acoustic contrast with variation in electrical power supplied to the transducer. Figure 2(b) shows comparison of these results with the universal curve of M parameter.

Separation Results

Figure 3 shows experimental results of separation of Jurkat T-cells from 30-micron beads.

References

[1] X. Ding, S. C. Lin, M. I. Lapsley, S. Li, X. Guo, C. Y. Chan, I. K. Chiang, L. Wang, J. P. McCoy, T. J. Huang, "Standing surface acoustic wave (SSAW) based multichannel cell sorting." Lab Chip 12(21), pp. 4228-4231, (2012).

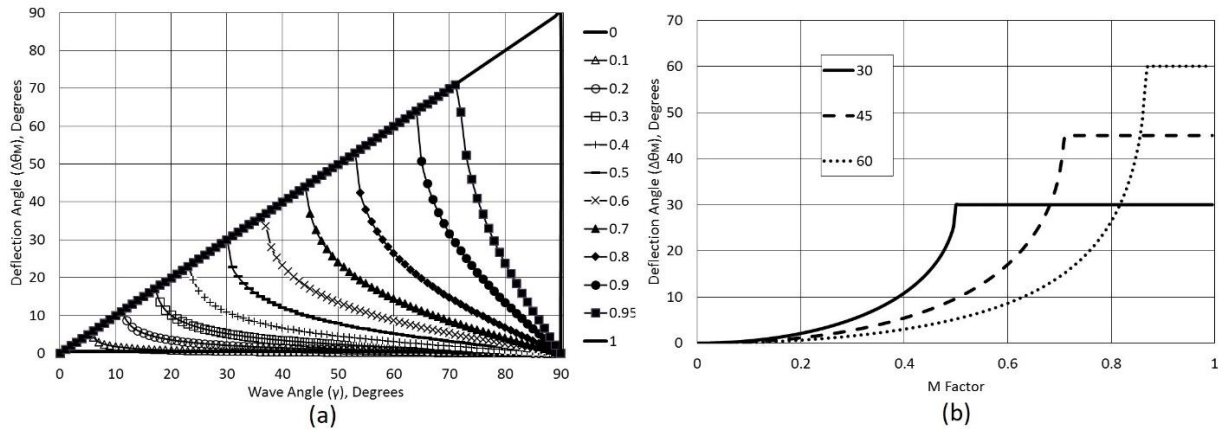


Figure 1: Universal deflection curves obtained from the analytical model for particle deflection angle, with respect to (a) wave angle, (b) M parameter.

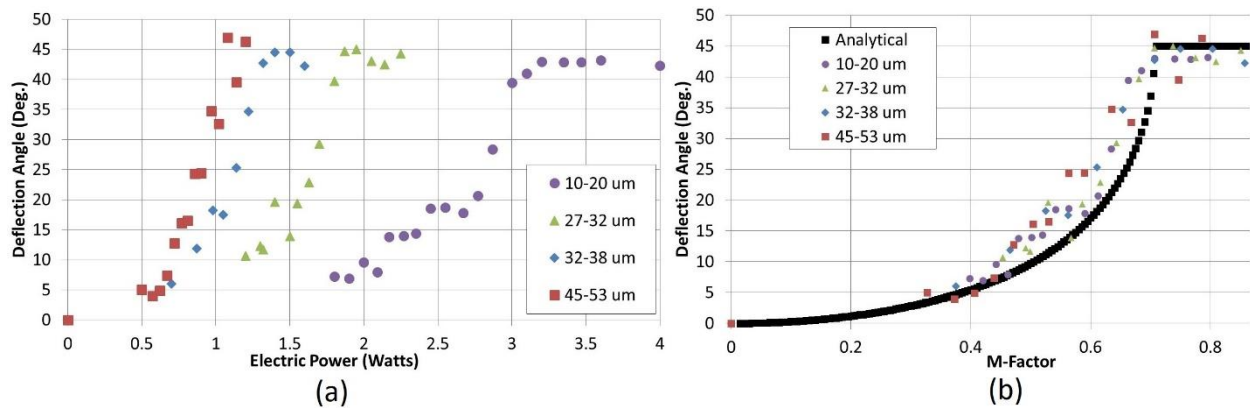


Figure 2: Experimental results of particle deflection angle for various sized beads, with respect to (a) electrical power, (b) M parameter.

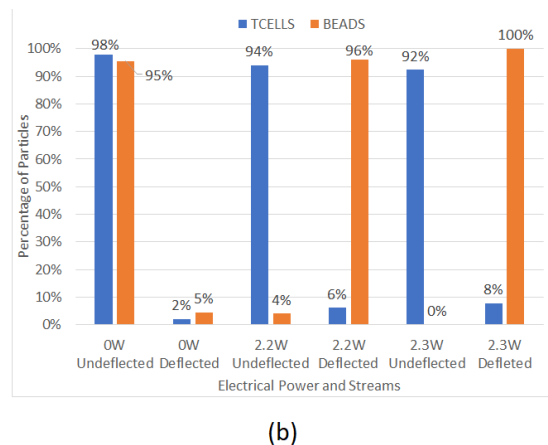
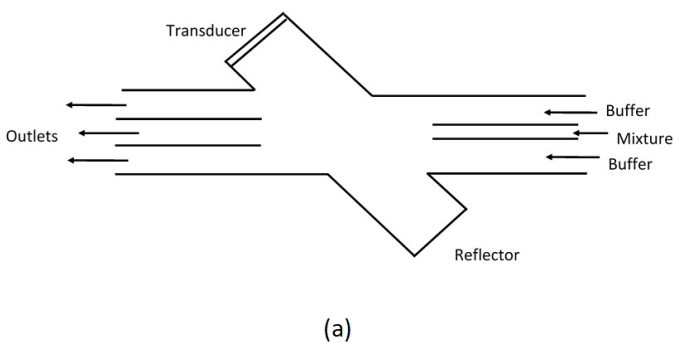


Figure 3: (a) Typical setup of the angled wave system, (b) experimental results for T-cell and 30-micron bead fractionation

[2] P. Li, Z. Mao, Z. Peng, L. Zhou, Y. Chen, P. Huang, C. I. Truica, J. J. Drabick, W. S. El-Deiry, M. Dao, S. Suresh, T. J. Huang, "Acoustic separation of circulating tumor cells.", 12.16, Proc. Natl. Acad. Sci., pp. 4970-4975, (2015).

[3] Chitale, K. C., Presz W. Jr., Ross-Johnsrud B., Hyman M., Lamontagne M., Lipkens B., "Particle manipulation using macroscale angled ultrasonic standing waves", Proc. Mtgs. Acoust. 30, 045004 (2017).

Experimental study of acoustic induced streaming around sharp edges in a Y-type mixing channel

Chuanyu ZHANG¹, Xiaofeng GUO¹, Philippe BRUNET² and Laurent ROYON¹

¹Univ Paris Diderot, Sorbonne Paris Cité, LIED, UMR 8236, CNRS, F-75013, Paris, France
E-mail: chuanyu.dream@gmail.com

²Univ Paris Diderot, Sorbonne Paris Cité, MSC, UMR 7057, CNRS, F-75013, Paris, France
E-mail: philippe.brunet@univ-paris-diderot.fr

Introduction

Acoustic streaming is a constant, second-order flow generated by periodic acoustic excitation. In the Navier-Stokes equation, this phenomenon is originated from the time-averaged second order inertia terms. In acoustic waves of frequency < 1 MHz, streaming is typically generated within the viscous boundary layer [1]. This could be used in heat and mass transfer enhancement in fluid channels to accelerate the mixing process, for instance. Recently, several studies have shown that more intense streaming flows can be produced around sharp structures such as edges or needles [2,3]. However, the underlying mechanisms have to be better understood. The purpose of our study is a quantitative characterisation of the streaming flow.

Acoustic streaming is visualized around a sharp edge in a PDMS channel stick on a glass slide. A piezoelectric transducer coupled to the slide, is used to produce vibration. A pair of vortices is observed around the sharp structures, See Fig. 2. The size and intensity of vortices are dependent on frequency, acoustic displacement, edge angle and advection flow-rate. Larger streaming vortices are observed with no flow but it their size significantly reduces when flow rate becomes non-zero.

Experiment setup

Fig.1 shows the configuration of our experimental setup comprising: i) two syringe pumps used to push the fluid into the channel; ii) signal generator to provide acoustic signal with frequency adjustment; iii) amplifier to adjust the input voltage (thus power) of the piezo transducer; and at finally a binocular microscope and a fast camera together with fluorescent particles for flow visualization. The Y-type mixer has been lithographed using PDMS curing against a previously-prepared SU8 mould. The PDMS is then sealed against a glass slide using oxygen plasma treatment. We also characterize the frequency-response of the transducer in order to operate close to resonances, between 1 and 20 kHz. A calibration of the acoustic displacement versus voltage, for the different fixed frequencies, is also under way.

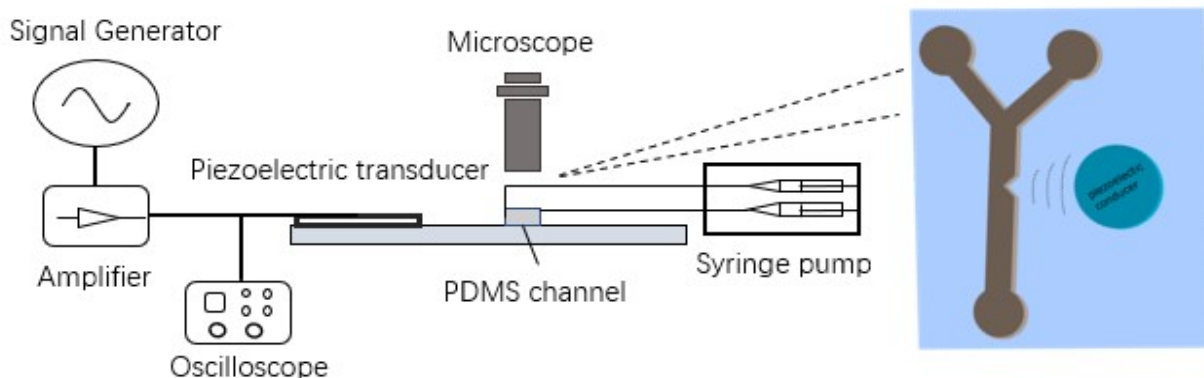


Fig.1 Schematic of the experimental setup

Results and discussions

Without advection, vortices pairs are almost symmetrical on both sides of the edge. Following the trajectory of particles around the sharp edge, one observes a strong jet in the area ahead of the tips. When injecting liquid from inlets at a certain flow-rate, the two vortices are influenced by the main flow and become asymmetric. The flow jetting from the upper stream follow the main stream and cannot go backwards. The downstream vortex shrinks. Still, vortices can bring some disturbance to the main flow.

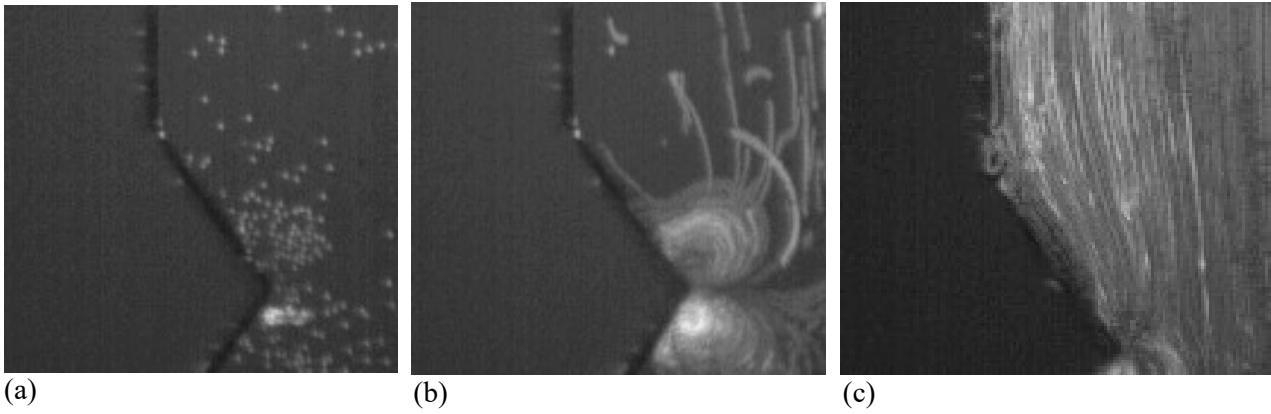


Fig.2 Experimentally observed trajectories of fluorescent particles without (a) and with (b) acoustic vibration (3.1 kHz, 50 V) with no directional flow, and with vibration (3.1 kHz, 50 V) at 2ul/min flowrate (c)

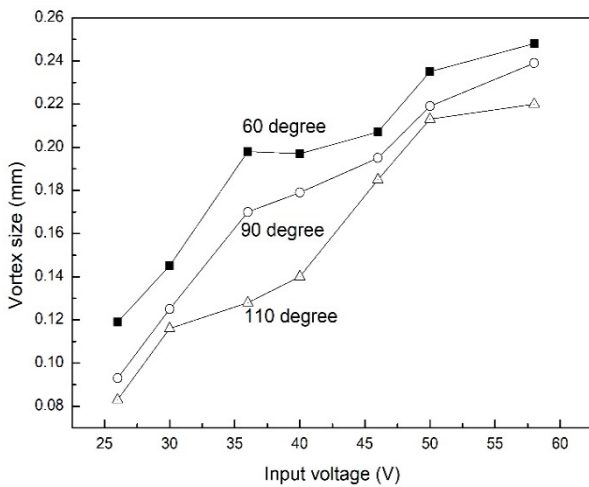


Fig.3 Vortex size vs. input voltage on the transducer

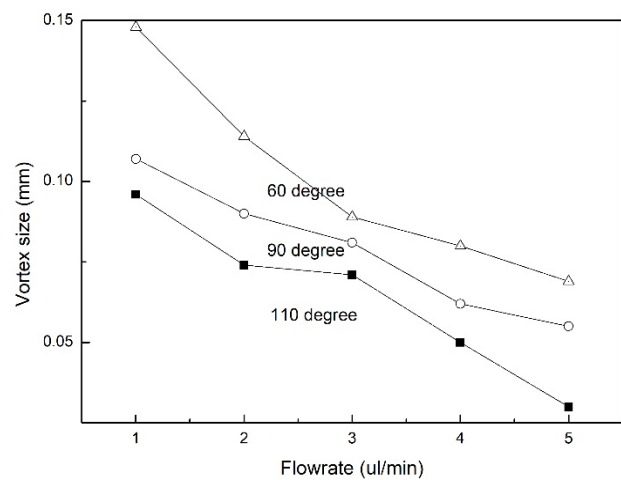


Fig.4 Variation of the vortex size with flow-rate

The vortex size is defined as the longest distance of the particles jetted from the tip of the sharp edge in the horizontal direction. Fig.3 and Fig.4 show the vortex size versus input voltage and versus flow-rate. In Fig.3, the experiment is conducted at zero flow-rate. It shows that with increasing voltage, the vibration amplitude of the channel becomes stronger and the corresponding vortex size becomes larger. Thus under these conditions, the acoustic streaming gives rise to larger disturbance on the main stream. Especially at 58 V, the vortex size can reach around 0.24 mm, i.e., half of the channel width (0.5 mm). Besides, it is observed that sharper edges (e.g., 60°) can help produce larger vortex than blunt ones (e.g., 110°).

Fig.4 shows the vortex size variation with respect to the channel throughput. The experiment is conducted at 50 V and 3.1 kHz. It shows that the vortex size greatly decreases under higher flow rates. At 5 ul/min, the vortex size is compressed to less 0.07 mm and there is only a very small vortex appearing on the downstream of the sharp edge. In such situations, the acoustic streaming has only limited influence on the main flow.

Conclusion

Acoustic induced vortex is observed experimentally around sharp edges. The vortex size depends highly on acoustic field (input voltage and frequency) as well as flowing conditions mainly flow-rate. Larger vortices is observed with higher activating voltage and lower flow-rate. The angle of the sharp edge can also have an influence on the vortex size and this will be studied by our future experimental and numerical investigations.

References

- [1] Sir James Lighthill (1978), *Acoustic streaming*, Journal of Sound and Vibration **61**, 391-418.
- [2] N. Nama, P-S. Huang, T.J. Huang and F. Costanzo (2014), *Investigation of acoustic streaming patterns around oscillating sharp edges*. Lab. Chip **14**, 2824-2836.
- [3] Ovchinnikov, M., Zhou, J., & Yalamanchili, S. (2014). *Acoustic streaming of a sharp edge*. The Journal of the Acoustical Society of America, **136**(1), 22–29.



Aluminium-foil chip for ultrasonic particle manipulation

Itziar González¹, Ivan Camilo Navarrete², Abelino Vargas², María Marcela Camacho²

¹Department of Ultrasounds, ITEFI, CSIC Spanish National Research Council, Madrid (Spain)
E-mail: iciar.gonzalez@csic.es URL: <http://www.itefi.csic.es/en/research-departments/>

²Department of Health, Faculty of Biology, National University of Colombia, Bogotá (Colombia)

Introduction

We present a novel ultra-low-cost (less than 10 cents) microfluidic chip to perform particle manipulation. It has a simple design and its extremely low cost of fabrication. It consists of an Aluminium foil (Al-foil chip) with a channelization glued to a microscope slide and actuated by a piezoelectric ceramic resonating in thickness mode at a frequency close to 1MHz. This device design proceeds from our previous microfluidic polymeric separators in which we introduced changes in their geometrical and structural properties to optimize their performance of particle/cell manipulation [1,2]. The experimental results of our Al-foil chip show that our device can successfully collect micron-sized particles

Experimental Setup

The *Al-foil Chip* consists of a rectangular adhesive Aluminium sheet with a channelization glued to a glass microscope slide and covered by a transparent film (Figure 1.a).



Figure 1: a) Image of the Chip and Schematic illustration of the fabrication process of the polymer film chip. b) polystyrene beads collected along the central axis of the main channel of acoustic treatment.

The main channel had a rectangular cross section of 600 μm (width) \times 100 μm (height) and a length of 50 mm. The chip was actuated by a small piezoelectric ceramic Ferroperm pz26 (Ferroperm, Krisgard, Denmark) of a rectangular area (10 \times 5 \times 1.5 mm³) with a thickness-mode resonance at 1 MHz. It was attached to the chip top covering an area partially occupied by the channel. The piezoelectric ceramic was activated by a function generator (Agilent 33220A, Agilent Technologies Inc., Santa Clara, CA, USA) equipped with a power amplifier (E&I RF linear broad Amplifier 240 L, Research Blvd. Rochester, NY, USA). The voltage supplied to the

transducer was measured and controlled by an oscilloscope (Tektronix TDS 3034B, Tektronix UK Ltd., Bracknell, UK).

The thickness of the chip was 1.3mm, including the glass, aluminium foil and polymeric sheet thicknesses. The high velocity of sound established within the glass slide (of approximately 5500m/s) provided a wavelength of almost 3mm at the frequency close to 1MHz, almost three times larger than its thickness. The geometrical configuration of the chip associated to a very large surface/volume ratio together with its thickness slightly larger than a quarter of the wavelength at the frequency of work, provided a plate-like actuation of the whole structure of the chip [1]. This configuration fulfills the theoretical conditions of the models developed first by Mindlin and later by other authors to study free and forced vibrations of thick and moderately thick rectangular plates with different boundary conditions and thicknesses [4].

The actuation of our chip is based on the principle of plate acoustic waves PAW and shows the advantages of other previous microfluidic devices developed before [1], such as a simple design versatility of actuation in frequency and fabrication with a extremely low-cost.

The plate vibratory behaviour of the chip allowed a frequency close to that of the piezoelectric actuator generating a pressure node along the central axis of the channel, where particles collected (see figure 1.b).

Conclusion

The experimental results show that our Al-foil device can successfully drive and collect micron-sized particles along the central axis, proving the potential availability of this novel chip for biomedical or environmental applications requiring low-cost mass production.

Our experimental results demonstrate for the first time the ability of a paper-based chip to manipulate micron-sized particles as a conventional microseparator with the advantage of a extremely low cost fabrication.

References

- [1] González, I.; Fernández, L.J.; Gómez, T.; Berganzo, J.; Soto, J.L.; Carrato, A. A polymeric chip for micromanipulation and particle sorting by ultrasounds based on a multilayer configuration. *Sens. Actuators B Chem.* **144**, 310–317. (2010)
- [2] González, I.; Tijero, M.; Martín, A.; Acosta, V.; Berganzo, J.; Castillejo, A.; Bouali, M.M.; Soto, J.L. Optimizing polymer Lab-on-Chip platforms for ultrasonic manipulation: Influence of the substrate. *Micromachines*, **6**, 574–591 (2015)
- [3] I. González, J. Earl, L.J. Fernández, B. Sainz Jr., A. Pinto, R. Monge, S. Alcalá, A. Castillejo, J. L. Soto and A. Carrato, A Label Free Disposable Device for Rapid Isolation of Rare Tumor Cells from Blood by Ultrasounds, *Micromachines*, **9**, 129; doi:10.3390/mi9030129 (2018)
- [4] Mindlin, R.D., Schacknow, A., Deresiewicz, H., 1956. Flexural vibration of rectangular plates. *ASME Journal of Applied Mechanics* **23**, 430–436.



Whole-system resonances enabling acoustophoresis in all-polymer microfluidic devices

Rayisa P. Moiseyenko and Henrik Bruus

Department of Physics, Technical University of Denmark, Kongens Lyngby, Denmark
 E-mail: bruus@fysik.dtu.dk, URL: <http://www.fysik.dtu.dk/microfluidics>

Introduction. During the past two decades, several devices based on acoustically hard materials, such as glass and silicon, have been fabricated and successfully tested for acoustophoretic particle handling in microscale acoustofluidic devices using MHz bulk acoustic waves (BAW) [1]. In this context, a hard material is one for which the acoustic impedance is about one order of magnitude, or more, larger than that of water. In contrast, the development of similar devices based on acoustically soft polymer materials has been much slower. Surface acoustic waves (SAW) have been successfully used in PDMS devices [2], but creating good all-polymer devices based on BAW has proven more difficult. Among the few reports of BAW-handling of suspended microparticles in all-polymer devices are focusing of polymer beads [2–6], lipids [3], and red blood cells [4,7], as well as blood-bacteria separation [8], however providing little theory.

One obstacle to the advancement of polymer-based acoustofluidic system is of physical nature, namely the low acoustic contrast factor as the acoustic impedance for polymers is only about 1.5 times that of water, and as a consequence acoustic resonances are less pronounced in water cavities embedded in polymers as compared to glass or silicon. Another obstacle is the lack of thorough theoretical analysis of the polymer-based acoustofluidic systems. In this work, we present a theoretical analysis of the whole-system-resonance principle and use it to identify good acoustophoresis capabilities in all-polymer devices at specific ultrasound resonances.

The physical principle of whole-system acoustic resonances. For acoustically hard systems such as Pyrex, it is a good approximation to assume that the hard-wall boundary condition applies to the water-domain, and then by tuning the frequency, pressure BAW resonances can be found, typically standing half-waves as in Fig. 1(a). Similarly, for a SAW resonance, the boundary-condition may be set as the given SAW-velocity, see Fig. 1(b). For an all-polymer device such as a PMMA device, one must apply a more complete model, where all parts of the coupled solid-fluid system contribute to the whole-system resonance, see Fig. 1(c). Here, the fundamental principle is that the high acoustic contrast between the polymer and the surrounding air, involving impedance ratios larger than 10^4 , spawns pronounced resonances.

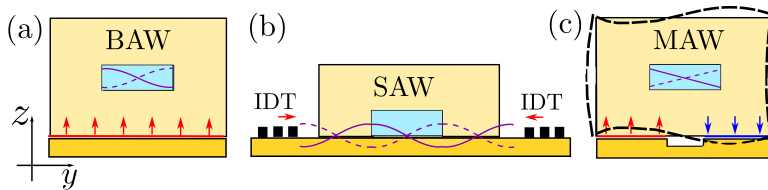


Figure 1: Sketch of a water channel (blue) in a solid (beige) placed on a MHz actuator (orange). Models for the pressure field in the water due to (a) bulk acoustic waves (BAW), (b) surface acoustic waves (SAW), and (c) a whole-system resonance in the fluid-solid system leading to a mixed acoustic wave (MAW).

Theory of acoustics in coupled fluid-solid systems. We apply the theory of pressure acoustics at frequency ω , Ley and Bruus [9]. The fields are the pressure p of water, with density $\rho_0 = 998 \frac{\text{kg}}{\text{m}^3}$ and sound speed $c_0 = 1497 \frac{\text{m}}{\text{s}}$, and the displacement \mathbf{u} of the isotropic PMMA, with density $\rho_{\text{sl}} = 1170 \frac{\text{kg}}{\text{m}^3}$ and longitudinal and transverse sound speeds $c_{\text{lo}} = 2706 \frac{\text{m}}{\text{s}}$ and $c_{\text{tr}} = 1105 \frac{\text{m}}{\text{s}}$. The governing acoustics equations and boundary conditions are

$$\text{Solid: } -\rho_{\text{sl}}\omega^2\mathbf{u} = \nabla \cdot \boldsymbol{\sigma}_{\text{sl}}, \text{ with } \boldsymbol{\sigma}_{\text{sl}} = \rho_{\text{sl}}c_{\text{tr}}^2[\nabla\mathbf{u} + (\nabla\mathbf{u})^T] + \rho_{\text{sl}}(c_{\text{lo}}^2 - 2c_{\text{tr}}^2)(\nabla \cdot \mathbf{u})\mathbf{I}, \quad (1a)$$

$$\text{Fluid: } \nabla^2 p = -\frac{\omega^2}{c_0^2} p, \text{ with fluid velocity } \mathbf{v} = -\frac{i}{\omega\rho_0} \nabla p, \quad (1b)$$

$$\text{Fluid-solid boundary: } \mathbf{v} = -i\omega\mathbf{u}, \quad -p\mathbf{n} = \boldsymbol{\sigma}_{\text{sl}} \cdot \mathbf{n}. \quad \text{Air-solid boundary: } \mathbf{0} = \boldsymbol{\sigma}_{\text{sl}} \cdot \mathbf{n}. \quad (1c)$$

Results from COMSOL simulations on a 2D PMMA device. We consider a rectangular PMMA domain of width 3 mm and height 1.4 mm. It contains a rectangular water domain of width 0.38 mm and height 0.16 mm, centered 0.4 mm below the PMMA-air surface. The bottom-surface actuation with displacement amplitude $u_0 = 10$ nm is shown in Fig. 1(c). In Figs. 2(a) and (b) are shown two resonances in the PMMA device consisting of mixed longitudinal and transverse waves in the PMMA and compressional waves in the water. In Figs. 2(c), the method is validated by using it to compute the known resonance $f_{\text{res}} = \frac{c_0}{2W} = 1.97$ MHz of a conventional Si-Pyrex device. In Figs. 2(c) and (d) the acoustic radiation force is calculated for the Si-Pyrex device (with $u_0 = 0.1$ nm) and the PMMA device (with $u_0 = 10$ nm), and we see comparable results, thus demonstrating that the whole-system-resonance principle works.

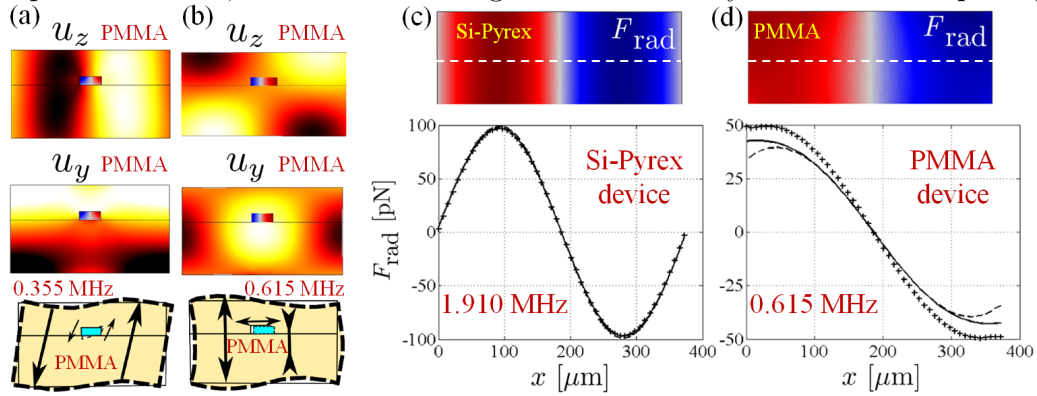


Figure 2: (a) Color plots from the PMMA device at the resonance $f = 0.355$ MHz: the PMMA displacement $\mathbf{u}_1 = (u_y, u_z)$ from -20 nm (black) to 20 nm (white) and of the water pressure p_1 from -0.1 MPa (blue) to 0.1 MPa (red). The mode is sketched at the bottom. (b) The same as (a) but at the resonance $f = 0.615$ MHz. (c) Color and line plots (bottom, at the white dashed line, top) of the radiation force \mathbf{F}^{rad} in a conventional Si-Pyrex device at resonance $f = 1.910$ MHz. (d) Same as (c) but for a PMMA device at resonance $f = 0.615$ MHz.

Results from COMSOL simulations on a 3D PMMA device. A more realistic test of the whole-system-resonance principle is shown in Fig. 3 for a 4 cm long microchannel embedded in a 5 cm long PMMA chip and actuated along the entire bottom surface with amplitude $u_0 = 3$ nm as sketched in Fig. 1(c). The resulting acoustic radiation force is shown in Fig. 3(d).

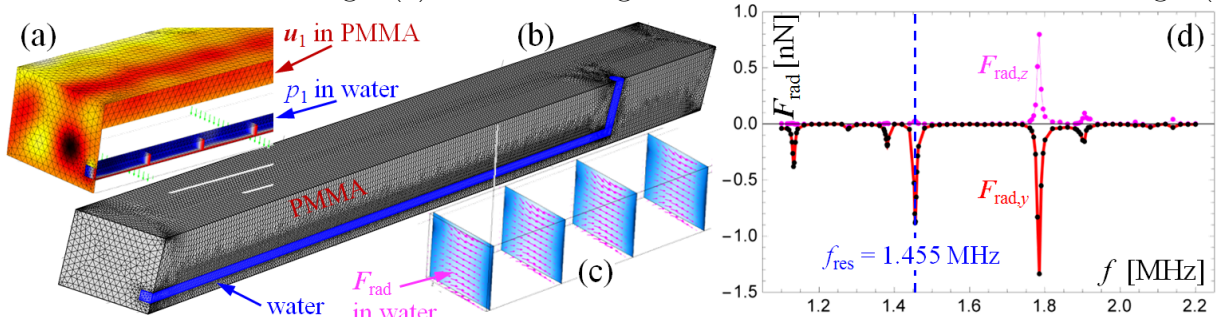


Figure 3: Numerical results for a water-filled micro channel ($0.15 \times 0.375 \times 40$ mm³) embedded in PMMA ($1.34 \times 3.0 \times 50$ mm³) and actuated at resonance 1.455 MHz. (a) Color plots of displacement and pressure near the center. (b) The finite-element mesh. (c) The radiation force \mathbf{F}^{rad} on a 10- μ m-diameter polystyrene bead in the channel. (d) \mathbf{F}^{rad} plotted versus frequency. At resonance 1.455 MHz, $\mathbf{F}_{\text{rad},y} \approx -1$ nN and $\mathbf{F}_{\text{rad},z} \approx 0$ nN.

Conclusion. The whole-system-resonance principle is introduced for all-polymer devices, and it is used to identify resonances in coupled polymer-water systems. The corresponding acoustic radiation forces enable microparticle acoustophoresis, as verified by preliminary experiments.

References

- [1] A. Lenshof, C. Magnusson and T. Laurell. *Lab Chip* **12**, 1210 (2012).
- [2] M. Gedge and M. Hill. *Lab Chip* **12**, 2998 (2012).
- [3] N. Harris, M. Hill, A. Keating, and P. Baylac-Choulet. *J. Appl. Biomed. Eng.* **5**, 20 (2012).
- [4] A. Mueller, A. Lever, T.V. Nguyen, J. Comolli, and J. Fiering. *J. Micromech. Microeng.* **23** 125006 (2013).
- [5] I. González, M. Tijero et al. *Micromachines* **6**, 574 (2015).
- [6] C. Yang, Z. Li, et al. *IEEE Ultrasonics Symposium 2017*, <http://dx.doi.org/10.1109/ULTSYM.2017.8092245>
- [7] W.J. Savage, J.R. Burns, and J. Fiering. *Transfusion* **57**, 1818 (2017).
- [8] R. Silva, P. Dow, et al. *Biomed Microdevices* **19**, 70 (2017).
- [9] M.W.H. Ley and H. Bruus. *Phys. Rev. Appl.* **8**, 204020 1-15 (2017).



Acoustic Affinity Cell Selection for CAR T-Cell Manufacturing

Rui Tostoes, Kyunghoon Lee, Shirae Leslie, Jack Saloio, Bart Lipkens
Flodesign Sonics, Wilbraham MA USA
Email: b.lipkens@fdsonics.com, URL: <http://www.fdsonics.com>

Introduction

Acoustic Cell Processing utilizing a macro-scale acousto-fluidics technology platform provides a shear-free manipulation of cells using ultrasonic standing waves. The platform has broad applications in the field of cell and gene therapy, e.g., cell concentration and washing, cell expansion, microcarrier/cell separation, acoustic affinity cell selection and label-free cell selection. The acoustic radiation force exerted by the ultrasonic standing wave on the suspended cells in combination with fluid drag forces and gravitational forces is used to manipulate the cells and achieve a certain cell processing unit operation, e.g. cell concentration and washing. The technology is closed, single-use, continuous, and can be scaled up, down or out. It therefore allows for a flexible and modular approach that can be customized to process a desired cell count, cell culture volume or cell concentration within a given required process time.

Acoustic Affinity Cell Selection

Acoustic affinity cell sorting has been utilized at the MEMS acousto-fluidics scale. Urbansky *et al.* [1] used a MEMS acousto-fluidics platform to sort CD8 lymphocytes from peripheral blood progenitor cell (PBPC) products by affinity-bead-mediated acoustophoresis using anti-CD8-coated magnetic beads. Cushing *et al.* [2] demonstrated a proof of concept for continuous flow acoustophoretic negative selection of white blood cells (WBCs) from cancer cells using negative acoustic contrast elastomeric particles activated with CD45-antibodies that specifically bind to WBCs. Faridi *et al.* [3] present a microfluidic-based microBubble-Activated Acoustic Cell Sorting method that relies on the specific binding of target cells to microbubbles conjugated with specific antibodies on their surface for continuous cell separation using ultrasonic standing wave in a MEMS device.

We have developed an Acoustic Activated Cell Selection (AACS) platform at the macro-scale for positive or negative cell selection processes typically employed in cell and gene therapy applications. A unique and patented acoustic standing wave edge effect fluidized bed system has been developed for AACS. A schematic of the device and process is shown in Figure 1. In a first application, the device is used for a TCR+ T-cell depletion step as part of an allogeneic CAR-T process. The mixed cell population, typically 70% TCR- and 30% TCR+ T-cells, flow into the fluidized bed, which is filled with 50 μm PMMA beads coated with monomeric avidin. The TCR+ T-cells bind to the affinity beads. The acoustic standing wave is used to retain all the PMMA beads with the attached TCR+ T-cells in the fluidized bed. The unbound TCR- T-cells pass freely through the acoustic standing wave field. The small-scale prototype device has a fluidized bed column volume of 5ml, and operates at flow rates of 2-5 ml/min. In a typical experiment, 10 ml of a cell culture containing about 10^6 T-cells per ml, of which 30% are TCR+, flow into the fluidized bed. After passage through the fluidized bed, the measured purity of the harvest cell stream exceeds 99%, i.e., depletion of TCR+ T-cells to less than 1%. The TCR- T-cell recovery exceeds 80% indicating a loss of 20% of the TCR- target T-cells. The process times is less than two hours. Current

efforts are focused on scaling up of the technology to accommodate affinity cell depletion of at least 10 billion TCR+ T-cells.

The AACS technology is a scalable acoustic affinity cell selection method using a non-paramagnetic clinical-grade affinity bead for positive or negative cell selection. AACS is a powerful acoustic-based cell processing technology that lowers cost and risk while enabling a modular, automation-friendly manufacturing process for cell and gene therapy manufacturing.

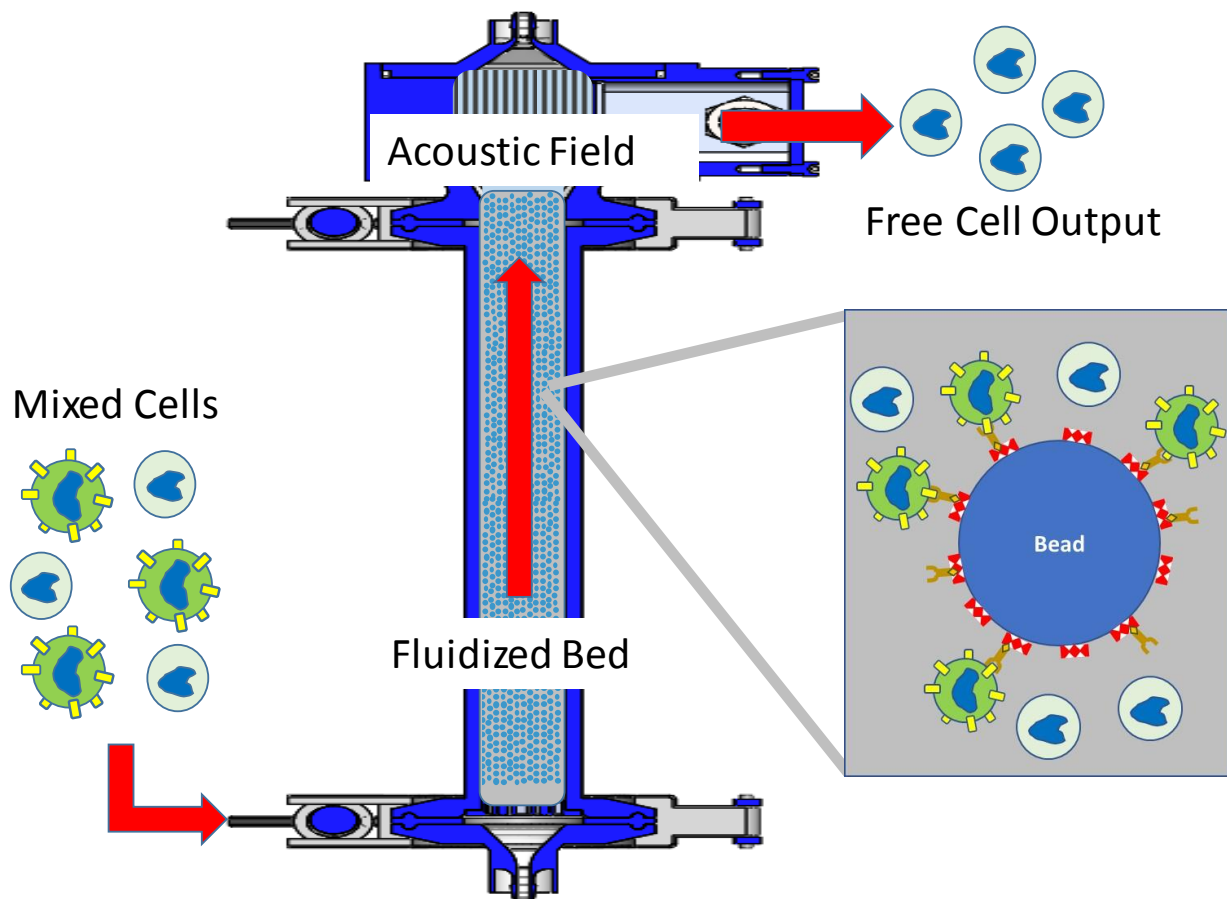


Figure 1: Schematic diagram of an acoustic fluidized bed setup. The fluidized bed is loaded with the affinity beads. A mixed cell population of TCR+ and TCR- T-cells flow into the fluidized bed column. The TCR+ cells bind to the affinity bead. The affinity bead/TCR+ cell complexes are retained by the acoustic standing wave field. The unbound TCR- target cells flow through the acoustic field and are harvested.

References

- [1] Affinity-Bead-Mediated Enrichment of CD8+ Lymphocytes from Peripheral Blood Progenitor Cell Products using Acoustophoresis, *Micromachines* 2016, 7, 101; doi:10.3390/mi7060101
- [2] Reducing WBC background in cancer cell separation products by negative acoustic contrast particle immuno-acoustophoresis, Kevin Cushing, Eva Undvall, Yvonne Ceder, Hans Lilja, Thomas Laurell, *Analytica Chimica Acta* 2018 Feb 13;1000:256-264. doi: 10.1016
- [3] MicroBubble activated acoustic cell sorting, M. A. Faridi, H. Ramachandraiah, I. Iranmanesh, D. Grishenkov, M. Wiklund, and A. Russom, *Biomed Microdevices* (2017) 19:23 DOI 10.1007/s10544-017-0157-4

Building resonant cavities from multiple Lamé resonator units

Jeremy J. Hawkes¹ and Bart Lipkens²

¹Acoustic Machines, Liverpool L25 4TQ, UK JeremyJHawkes@gmail.com

²FloDesign Sonics, 380 Main St Wilbraham, MA 01095, USA

Introduction Nodes and antinodes in the structural elements of a cavity are responsible for the local sound intensity in the adjacent fluid. This is seen when the fluid is at resonance and contains suspended particles, the pattern of nodes and antinodes in the structural element is mirrored in a pattern of particle clumps at the fluids nodal planes. For many structural mode types the position of the nodes and antinodes cannot be accurately predicted. However the resonant frequency of the Lamé mode can be predicted to 6 significant figures this makes it an interesting mode to observe structural interactions with resonant fluids. The first step is to design the structure which resonates in the Lamé mode.

Why choose the Lamé mode?

A violin string is half a wavelength long when resonating at its fundamental frequency. For structures with more dimensions the axis and the speed of sound governing each resonance are not always so obvious and for most modes the resonant frequency changes as the number of half-wavelengths and length increases. However, multi-wavelength systems formed by stepwise length increases using squares resonating in the Lamé always resonant at exactly the same frequency. A square plate is the smallest (fundamental) unit for Lamé mode its resonant frequency depends on the longest in-plane axis, the corner-to-corner distance. A further advantage of the Lamé mode is that it can be held at its corners where there is no movement or stress, see Figure 1a.

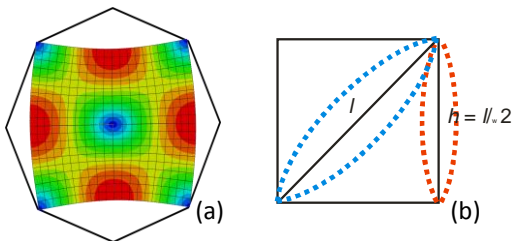


Figure 1: (a) FE model of the Fundamental Resonant Unit of the Lamé mode held at its corners where stress and displacement are zero, Colours here indicate displacement. (b) The wavelength along the side shorter than the diagonal wavelength. (The 2D FE model give the illusion of a whole wavelength corner to corner because it combines U1 and U2).

Agreement between modeling methods

Pythagoras: Figure 1b shows two different half wavelengths in the square that the corner to corner half wavelength l and height half-wavelength h . Using the Pythagoras theorem equation 1 gives the resonant frequency f .

$$f = c/2l = c/2h\sqrt{2} \quad \text{Equation 1}$$

Here the speed of sound c is the bulk speed of sound if Poisson's ratio ν is 0.33. If $\nu \neq 0.33$ the speed of sound is calculated from the Young's Modulus E and the density ρ with ν set to 0.33.

$$c_{Solid} = \sqrt{\frac{E(1-\nu)}{\rho(1+\nu)(1-2\nu)}} \quad \text{Equation 2}$$

Therefore the general equation for the speed of sound along one side of the fundamental resonant unit is:

$$c_{fru} = \sqrt{\frac{3E}{4\rho}} \quad \text{Equation 3}$$

And the resonant frequency of the Lamé mode is given by equation 4 and b¹

$$\text{Lamé mode } f = \frac{1}{2l} \sqrt{\frac{3E}{4\rho}} = \frac{1}{l} \sqrt{\frac{G}{2\rho}} \quad \text{Equation 4 a and b}$$

Dispersion curves

The Lamé mode lies on the S0 (plate thickness) mode dispersion curve. The resonant square is formed when the mode's half wavelength is equal to the thickness of the plate. To find the frequency and phase velocity at this point we calculated the wavelength along the mode's frequency : phase-velocity curve. The points where the wavelengths are the same in two dimensions (the resonant frequency of the squares) are shown in figure 2.

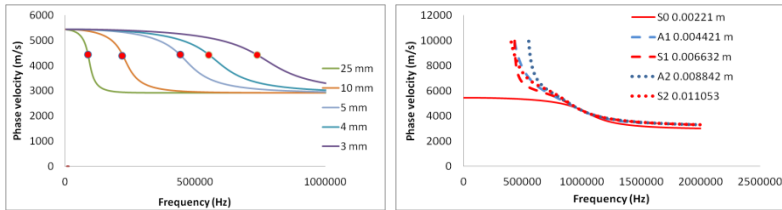


Figure 2.(a)S0 dispersion curves for aluminium plates. Red dots =point where plate thickness and half wavelength are equal. (b)The Lamé mode lies on all dispersion curves. For a square of material they touch at one frequency and phase velocity.

Since the curvature of the wave is the same on all sides of the squares, when two squares are combined to produce a rectangle the curves will fit and vibrates at the same frequency as the single square but with an symmetric S0 mode on the short axis and an anti-symmetric A1 mode on the long axis. The rectangle can be extended by adding squares, additional squares do not change the resonant frequency but change the mode following the series S0, A1, S1, A2, S2 etc. shown in figure 2b and figure 3.

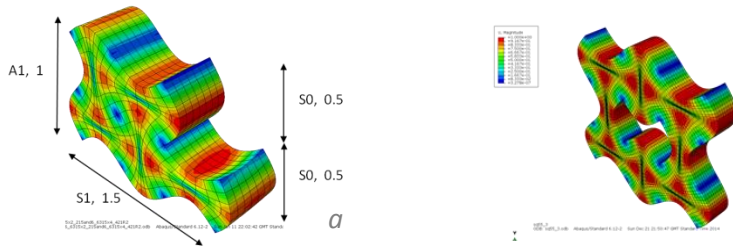


Figure 3. (a)When the thickness of the plate is increased in increments of the fundamental resonant unit the resonance frequency and sound velocity do not change but the modes increase (S0, A1, S1, A2, S2 etc).shown (b) A duct formed from fundamental resonant units.

Experimental examples of the particle clump patterns produced will also be given.

The methods and analytical equations described here were derived after “discovering” the Lamé mode while producing FE models using Abaqus

References

[1] S.A. Bhawe, D. Gao, R. Maboudian, and R.T. Howe. *18th IEEE International Conference on Micro Electro Mechanical Systems*, pp.223-226, 2005



Tunable control of atomized droplet size in a single thickness-mode acoustic device via signal modulation

William Connacher¹, Shuai Zhang¹, and James Friend²

¹Materials Science and Engineering Program, University of California, San Diego, USA
E-mail: wconnach@eng.ucsd.edu, URL: <http://www.fysik.dtu.dk/Acoustofluidics2018>

²Department of Mechanical and Aerospace Engineering, University of California, San Diego, USA

Introduction

Atomization, the generation of a large number of small fluid droplets, is already useful in many technologies and industrial processes and has several promising potential applications in microfabrication[1,2], evaporative cooling[3], and drug delivery[4]. All these technologies rely on a known range of droplet sizes in order to function properly. At the moment, a given application is limited to a set of fluids and atomization methods capable of producing the desired size. Previous work in our group has determined that thickness-mode acoustic vibration is capable of atomizing a large range of fluids at high flow rates. We seek to impose control over the droplet size distribution in the context of this atomization method by various modulations of the input signal.

Attempts have been made to understand atomized droplet sizes from SAW devices by utilizing Kelvin's equation and relying on Faraday wave theory to predict capillary wave frequency. Recently Qi and Collins have confirmed that, in fact, Faraday wave theory does not apply in the high frequency case and that a mechanism based estimate for capillary wave frequency yields better predictions [5,6]. They also revealed the importance of fluid meniscus geometry in atomization. Collignon provided a good predictor of the onset of atomization for a given fluid and actuation parameters in the form of an atomization Reynolds number [7]. Despite this research there is no prescription for device operation parameters given desired droplet sizes and fluids.

It is well known that droplet size is inversely proportional to driving frequency in SAW devices. Using thickness-mode vibration we are able to access multiple frequencies (limited by the increasing power required to achieve atomization) in a single device due to the presence of higher harmonics across the thickness of the piezoelectric material.

Thus we can produce frequency dependent changes in droplet size in a single device. To allow further control we have applied signals that combine two frequencies as illustrated in Fig. 1.

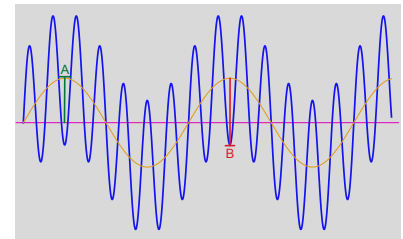


Figure 1: A multi-frequency sinusoidal waveform with amplitude of the 6.8 MHz component equal to 'A' and that of the 21.3 MHz component equal to 'B'.

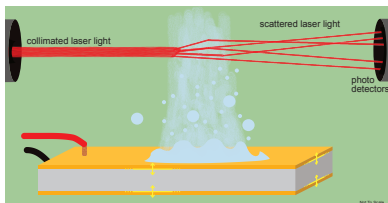


Figure 2: A droplet being atomized from a thickness-mode device while the resulting droplets are measured by laser diffraction.

Experimental methods and signal modulation

Thickness-mode devices were fabricated by depositing 1 micron thick gold layers on each side of 500 micron thick single crystalline lithium niobate wafers via electron-beam evaporation. Devices were diced from these wafers into 10mm by 5mm pieces. The first and third harmonics of the devices are 6.8 MHz and 21.3 MHz and these were confirmed to be thickness-mode resonances via laser Doppler vibrometry. Experiments were conducted with water, but it will be useful in the future to map out the viscosity parameter space by experimenting with glycerol/water mixtures. The amplitudes of each frequency component of the signal were varied using a signal generator (NF) and a 2W amplifier (Minicircuits) while measuring the voltage and current into the device.

Experiments consisted of atomization events during which a 1.5 microliter sessile drop was actuated with a multi-frequency signal until no liquid remained on the surface (see Fig.2). The droplet size distribution during each atomization event was recorded for the duration of the event using a laser diffraction system (Malvern, Spraytec).

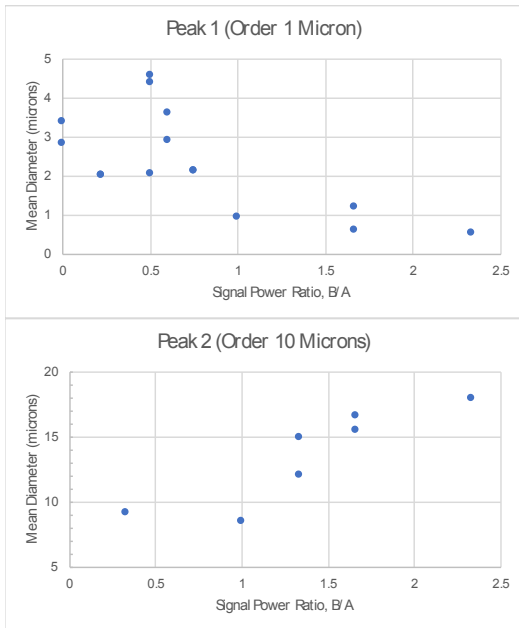


Figure 3: The mean droplet diameter in the 1st peak (containing droplets of order 1 micron) is seen to decrease with greater contribution from the 21.3 MHz signal while that of the 2nd peak (order 10 microns) is seen to increase.

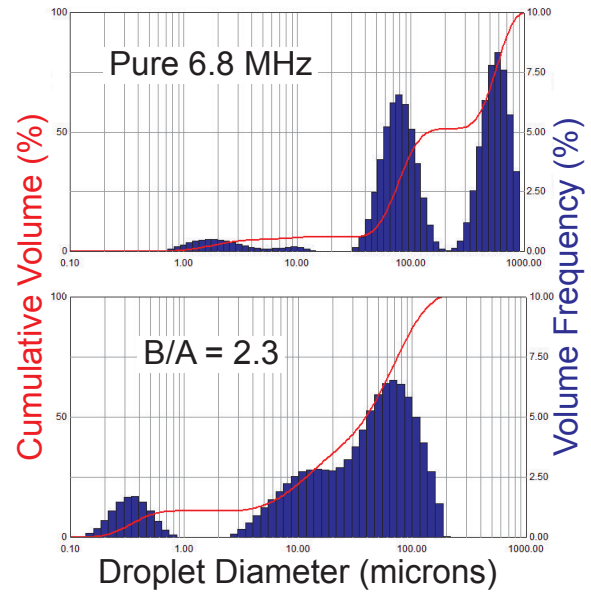


Figure 4: A comparison between droplet size distributions from a pure 6.8 MHz signal and a multi-frequency signal dominated by the 21.3 MHz component. Notice both a shift in peak location and the absence of the 4th peak in the case where $B/A = 2.3$.

Preliminary results and discussion

It is well known that acoustofluidic atomization using SAW devices tends to produce three mode droplet size distributions. In our experiments we have observed 4 distinct peaks in the distributions, though not every signal produces each peak. The mean size of droplets in the first and second peaks, with characteristic orders of magnitude of 1 micron and 10 microns respectively, for the various signals are given in Fig.3. The mean size of droplets in the third and fourth peak were not sensitive to frequency variations, though the existence of these peaks in a given distribution was correlated with frequency. Fig.4 illustrates a typical droplet size distribution a pure 6.4 MHz signal as compared to that of a multi-frequency signal dominated by 21.27 MHz.

Conclusion

Our investigation suggests that the desired order of magnitude droplet size can be selected by choosing a multi-frequency signal that tends to produce peaks with the desired size range. Further it appears that signals that favor the higher frequency tend to produce smaller droplets within the first peak and larger droplets within the second peak (i.e. the peaks shift).

We also plan to present work to be completed in the interim. Further meaningful data remains to be collected on the flow rates obtained during actuation as well as size variation with increased power input.

References

- [1] Gilissen, et al. "Ultrasonic spray coating as deposition technique for the light-emitting layer in polymer LEDs." *Org Elect* 20 (2015): 31-35.
- [2] Friend, et al. "Evaporative self-assembly assisted synthesis of polymer nanoparticles by surface acoustic wave atomization." *Nanotechnology* 19.14 (2008): 1-6.
- [3] Ang, et al. "Nozzleless spray cooling using surface acoustic waves." *J Aerosol Sci* 79 (2015): 48-60.
- [4] Cortez-Jugo, et al. "Pulmonary monoclonal antibody delivery via a portable microfluidic nebulization platform." *Biomechanics* 9.5 (2015): 052603.
- [5] Qi, Yeo, and Friend. "Interfacial destabilization and atomization driven by surface acoustic waves." *Phys Fluids* 20.7 (2008): 074103.
- [6] Collins, et al. "Atomization off thin water films generated by high-frequency substrate wave vibrations." *Phys Rev E* 86.5 (2012): 056312.
- [7] Collignon, Manor, and Friend. "Improving and Predicting Fluid Atomization via Hysteresis-Free Thickness Vibration of Lithium Niobate." *Adv Func Mats* 28.8 (2018): 1704359.

Boundary-layer streaming in viscoelastic fluids

S. Amir Bahrani^{1,2}, Nicolas Périnet³, Maxime Costalonga^{1,2,*}, Laurent Royon² and Philippe Brunet¹

¹Lab. Matière et Systèmes Complexes, UMR 7057 CNRS, Univ. Paris Diderot, Paris, France.
E-mail: seyed-amir.bahrani@univ-paris-diderot.fr

²Lab. Interdisciplinaire des Energies de Demain, UMR 8236 CNRS, Univ. Paris Diderot, Paris, France.

³Dept. de Física, Fac. de Ciencias Físicas y Matemáticas, Univ. de Chile, Casilla, Santiago, Chile.

* Present address : Department of Mechanics, Massachusetts Institute of Technology, 77 Massachusetts Avenue Cambridge MA 02139-4307.

Introduction

Oscillations of immersed bodies are known to generate a steady streaming flow, originating from Reynolds stress within the viscous instantaneous boundary layer in the vicinity of the object [1,2]. This phenomenon is very similar to acoustic streaming generated by sound or ultrasound waves within a fluid [3]. These phenomena have recently found a renewal of interest due to the development of microfluidics and the requirement to induce mixing in confined and viscosity-dominated flows. In the classical situation of an oscillating cylinder of diameter d , oscillating with amplitude A and frequency f , and providing that $\frac{A^2 f}{\nu} > 1$ (but $A \ll d$), the steady streaming flow is decomposed into two main zones : (1) an inner recirculation zone of typical thickness $\delta_s = \sqrt{\frac{2\nu}{\omega}}$ around the cylinder, where ν is the kinematic viscosity and ω the oscillations frequency, and (2) an external flow, with two pairs of outer vortices of typical size comparable to the diameter of the vibrating cylinder. The frame of our study is that of a low-viscous fluid, with $\delta_s \ll d$. We recently revisited such a streaming flow under two-dimensional confinement (Hele-Shaw) [4] or at high forcing ($A \simeq d$) [5], which showed unexpected influence of viscosity as well as stretching of the outer vortices along the axis of vibration. For non-newtonian fluids, especially those exhibiting viscoelasticity, the experimental and theoretical studies of streaming are scarce [6]. Still, streaming flows could be potentially of great interest to induce mixing in non-newtonian liquids. In particular, one can ask the question about the steady flow if the fluid responds with significant importance of elasticity to the oscillations.

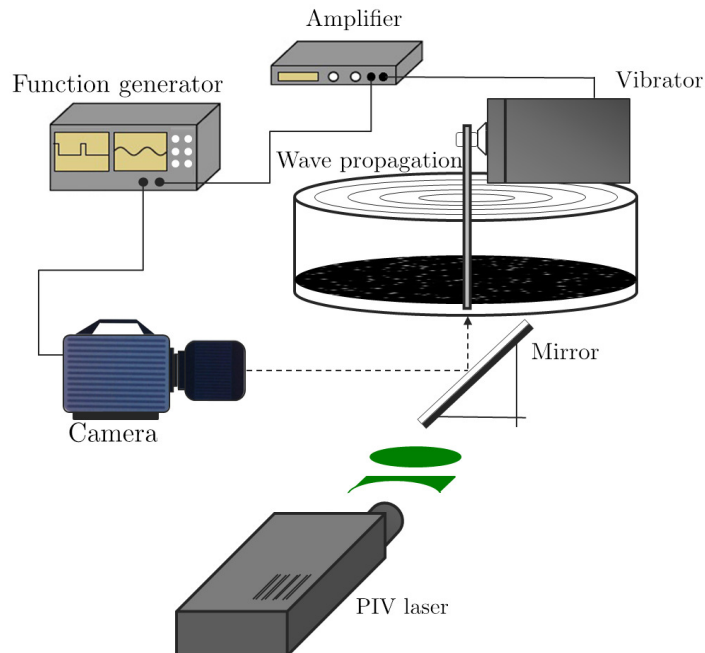


Figure 1: Experimental setup.

Experimental study

Hence, the main intention of this work is to investigate experimentally the effect of viscoelasticity on the steady streaming. The setup is described in Fig. 1. It consists of a cylinder immersed within a fluid layer of thickness much larger than its diameter, and oscillating perpendicularly to its axis. A periodic sinusoidal voltage, generated by a function generator, is transmitted to the vibrator via a power amplifier. It allows one to finely tune the amplitude and frequency of the vibrations, which are the two main control parameters here. The evolution of the structure and flow patterns with various frequencies (5 to 90 Hz) and amplitudes, was determined from measurements of the velocity field using particle image velocimetry (PIV), thanks to a high-speed camera (taking 10 images per period), an appropriate zoom lens and a 2D laser sheet.

The viscoelastic fluid used is polyethylene oxide (PEO) with two molecular weights (2 MP and 4 MP) and various concentrations, which enables to change both the critical shear rate for which elastic effects can appear, and the elongational viscosity. Elongational viscosity cannot be measured with usual shear rheometers, hence we used a home-made method, visualising the dynamics of a stretched polymer filament over several orders of magnitude in length and time, with a high-speed camera and a microscope zoom. A systematic comparison with a purely Newtonian fluid has been carried out and results showed several qualitative differences. First, when the elasticity is significant enough, we observe that the inner boundary layer, i.e. the recirculating vortices near the object, are much larger than for a newtonian fluid of the same viscosity, see Fig. 2-(a). Actually, a similar behavior would appear for a very viscous newtonian fluid (or at very low frequency), for which $\delta_s \gg d$. Hence, a new type of mechanism here has to be invoked to explain the dramatic size enlargement of the inner vortices. We propose that elongational viscosity is a potential mechanism. Indeed, the stretching of vortices by elongational viscosity has been observed in various other types of flows [7]. This was already observed by Chang and Schowalter [6] but remained ill-explained. We hope that our systematic measurements, will be able to propose a robust and quantitatively validated mechanism.

Second, for high enough forcing, the streaming flow loses its initial symmetry of the four-vortices usual structure. Instead, the pairs of vortices can become uneven, i.e. they are not image-mirror of each others with respect to the axis of vibration and that perpendicular to the vibration, see Fig. 2-(b) and (d). Finally, a more complex structure can appear where each initial vortex can split into two smaller ones, showing a steady eight-vortices structure, see Fig. 2-(c). To the best of our knowledge, these phenomena were unobserved so far.

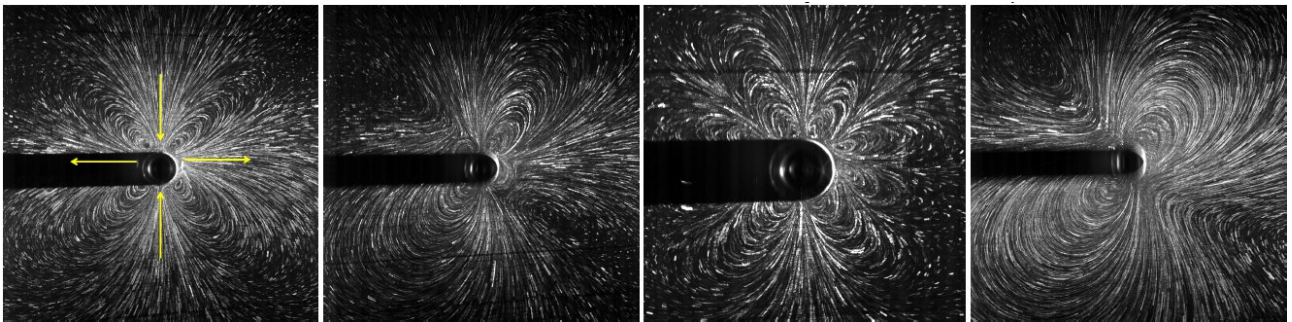


Figure 2: Different flow structures obtained with viscoelastic fluids. The cylinder, located in the center of each image, is vibrated vertically. The dark shadow to the left of the cylinder is due to the fact that the light comes from the right. From left to right : (a) inner boundary layer streaming, with four large vortices, replacing the usual outer flow. Arrows show the flow direction, (b) Loss of reflection symmetry of the flow, (c) regime with 8 vortices, (d) very large flow structure with uneven vortices pairs.

References

- [1] H. Schlichting, *Boundary-Layer Theory*, Springer.
- [2] W.L. Nyborg, *J. Acoust. Soc. Am.* **30**, 329-339 (1958).
- [3] Sir J. Lighthill, *J. Sound. Vib.* **61**, 391-418 (1978).
- [4] M. Costalonga, P. Brunet, and H. Peerhossaini, *Phys. Fluids* **27**, 013101 (2015).
- [5] S. A. Bahrani, N. Périnet, M. Costalonga, L. Royon, and P. Brunet. *In preparation*.
- [6] C.F. Chang and W.R. Schowalter, *Nature* **252**, 686(1974).
- [7] J.P. Rothstein and G. H. McKinley, *J. Non-Newtonian Fluid Mech.* **98**, 33-63 (2001).



Mesure de la force de pression de radiation exercée par une pince acoustique (Measurement of the radiation pressure force exerted by an acoustic gripper)

Dan Zhao, Jean-Louis Thomas, Régis Marchiano

(French)

La pince acoustique est un dispositif permettant de déplacer une sphère élastique dans les trois directions de l'espace à partir d'un faisceau ultrasonore unique. Le mécanisme physique utilisé est la pression de radiation qui est une interaction non linéaire entre le champ ondulatoire et l'objet insonifié. Une difficulté majeure est l'évaluation des composantes de cette force tri-dimensionnelle et notamment de la composante axiale qui est faible comparée aux composantes transverses. Une étude récente a montré que la force peut être reliée au champ acoustique incident seul si on connaît sa décomposition dans une base d'harmoniques sphériques. Dans ce travail nous proposons d'évaluer la force à partir de la mesure du champ acoustique incident. Pour cela plusieurs méthodes sont présentées et comparées. La première consiste à mesurer le champ sur des surfaces sphériques centrées sur la position théorique de l'objet et à calculer la décomposition en harmoniques sphériques par des quadratures adaptées. La seconde repose sur la mesure du champ en des points aléatoires et la résolution du problème inverse par une méthode parcimonieuse avec l'algorithme d'orthogonal.

(English)

The acoustic clamp is a device for moving an elastic sphere in the three directions of space from a single ultrasonic beam. The physical mechanism used is the radiation pressure which is a nonlinear interaction between the wave field and the insonified object. A major difficulty is the evaluation of the components of this three-dimensional force and in particular of the axial component which is weak compared to the transverse components. A recent study has shown that the force can be related to the incident acoustic field alone if we know its decomposition in a base of spherical harmonics. In this work we propose to evaluate the force from the measurement of the incident acoustic field. For this, several methods are presented and compared. The first is to measure the field on spherical surfaces centered on the theoretical position of the object and to calculate the decomposition in spherical harmonics by adapted quadratures. The second is based on the measurement of the field at random points and the resolution of the inverse problem by a parsimonious method with the orthogonal algorithm.



Unstationnary contact-lines and oscillating drops

Philippe Brunet¹, Maxime Costalonga^{1,*}, Michael Baudoin²

¹Lab. Matière et Systèmes Complexes, UMR 7057 CNRS, Univ. Paris Diderot, Paris, France

²International Associated Laboratory LEMAC, IEMN, CNRS UMR 8520, Université des Sciences et Technologies de Lille and EC Lille, 59652 Villeneuve d'Ascq Cedex, France

*Present address : Department of Mechanics, Massachusetts Institute of Technology, 77 Massachusetts Avenue Cambridge MA 02139-4307.

Introduction

The spreading and dewetting of liquids on substrates is generally ruled by a subtle balance between surface tension forces and viscous shear, which is the main source of dissipation. The classical situation is that of a drop sliding on an incline plane, or a liquid plug moving along a capillary tube. The inner flow and free-surface shape generally reach a steady state, leading to a selection of dynamical contact-angles given by the Cox-Voinov's law [1,2] :

$$\theta_d^3 - \theta_s^3 = 9 \frac{\eta U}{\gamma} \log \left(\frac{\mathcal{L}_M}{l_m} \right) \quad (1)$$

where U is the contact-line velocity, η the viscosity, γ the surface tension. This relationship reflects the viscous bending effect. The dynamical angle θ_d can be considered either at the front or the rear part of the drop, depending on the sign of U . The static angle θ_s is within the range of hysteresis $[\theta_r, \theta_a]$, and it was shown experimentally that θ_s should be equal respectively to θ_r or θ_a for receding or advancing contact-lines. Finally, \mathcal{L}_M and l_m are respectively macroscopic and microscopic (molecular) length scales. This hydrodynamic model, supposing the existence of a liquid wedge of almost constant slope, can be refined by including local variations of the slope or by combining it with other effects including mesoscopic slip length, the existence of a precursor film due to disjoining pressure or thermally-activated jumps at molecular scale [1,2].

To what extent equation (1) remains valid if fluid inertia is not negligible anymore ? This situation can occur in various situations, like the during the first steps of wetting [4], in a drop sliding inclines at high enough velocity [5] or in liquid meniscii or droplets subjected to oscillating forces from a vibrating substrate [6,7].

The importance of inertia can be quantified by the ratio between the thickness of a viscous boundary layer and the drop height ($\frac{\delta}{h}$). If this ration is larger than or close to one, the inner flow is considered in a steady state and Eq. (1) should hold. For drops excited at frequency ω , from a vibrating substrate, $\delta = \sqrt{\frac{2\nu}{\omega}}$ is the typical thickness of an unstationnary boundary layer, where ν is the kinematic viscosity. With typical values of $\omega = 50$ Hz and $\nu = 10^{-5}$ m².s⁻¹, $\delta \simeq 600$ μ m, hence smaller than the typical drop height $h \simeq 1$ to 3 mm.

Historically, the influence of periodic shaking on drops or meniscii has been partly motivated by the seek for a way to induce a directional motion and to overcome the pinning forces due to substrate imperfections [6,7]. Indeed, it was shown that such vibrations could remove partly or completely the pinning forces [7,8] on a rough and chemically inhomogeneous substrate.

When plotting the dynamical contact-angles at the rear and the front of the drop, versus instantaneous velocity $U(t)$ of the respective contact-lines, one generally obtains a hysteretic behavior that departs from Eq. (1) [6,7]. Therefore, a question arising is how to explain this hysteretic behavior what which ingredients have to be added in the dynamics to include the influence of fluid inertia ? Various theoretical studies addressed this question in order to add a correction to Eq. (1) with a contribution of the Reynolds number [9,10].

We addressed this question by carrying out experiments on sessile drops actuated with Surface Acoustic Waves (SAWs) with frequency $f_{ac} = 20$ MHz. The actuation here is modulated at a frequency f between 10 and 200 Hz, close to the first inertio-capillary eigen modes of the drops, enabling an optimal response of the drop free-surface and oscillations of the drop contact-

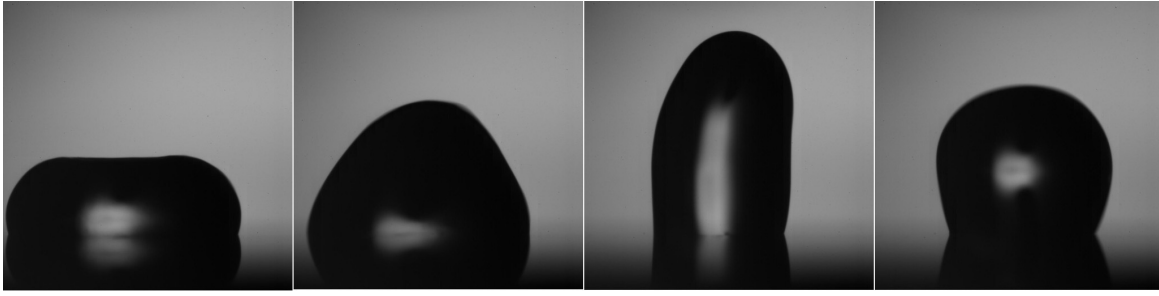


Figure 1: Successive shapes taken by a sessile drop excited by 20 MHz surface acoustic waves (SAWs) modulated at low frequency f . The drop response combines both directional motion to the right (the direction of SAWs propagation) and free-surface oscillations.

lines [11]. The experimental setup is detailed in [11], and the resulting dynamics is depicted in figure 1. Under the SAWs excitation, the drop acquires both an average velocity $\langle V \rangle$ and oscillations of its free-surface and basal radius at the frequency of modulation f . We recorded the dynamical contact-angles and the position of the contact-line versus time, with high speed imaging and we plotted the dimensionless velocity Ca versus the left and right dynamical angles.

Results

Figure 2 shows an example of this response, at several f , and a similar acoustic power. We notice an hysteretic behavior, especially for positive velocities (advancing angles), that cannot be captured by Eq. (1) and that remains to be explained.

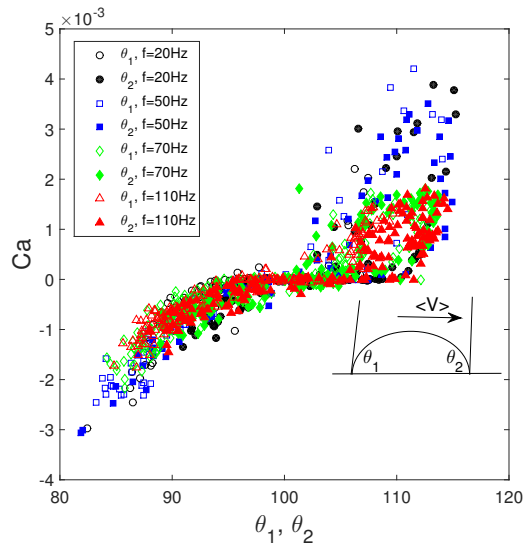


Figure 2: Dimensionless oscillating velocity $Ca = \eta U / \gamma$ of rear and front contact lines, versus the respective dynamical angles at the rear (left) and the front (right) of a sessile drop actuated by 20 MHz- surface acoustic waves modulated at frequency f . The drop moves with an average velocity $\langle V \rangle$ towards the right.

References

- [1] D. Bonn, J. Eggers, J. Indekeu, J. Meunier, E. Rolley, Rev. Mod. Phys. **81**, 739-805 (2009).
- [2] J.H. Snoeijer and B. Andreotti, Ann. Rev. Fluid. Mech. **45**, 269-292 (2013).
- [3] E. Rio, A. Daerr, B. Andreotti, and L. Limat, Phys. Rev. Lett. **94**, 024503 (2005).
- [4] A. Eddi, K.G. Winkels and J.H. Snoeijer, Phys. Rev. Lett. **111**, 144502 (2013).
- [5] B. A. Puthenveetil, V. K. Senthilkumar and E. J. Hopfinger, J. Fluid Mech. **726**, 26-61 (2013).
- [6] C-L. Ting and M. Perlin, J. Fluid Mech. **295**, 263-300 (1995).
- [7] P. Brunet, J. Eggers and R.D. Deegan, Phys. Rev. Lett. **99**, 144501 (2007).
- [8] E.L. Decker and S. Garoff, Langmuir **12**, 2100-2110 (1996).
- [9] R.G. Cox, J. Fluid Mech. **357**, 249-278 (1998).
- [10] L.M. Hocking and S.H. Davis, J. Fluid Mech. **467**, 1-17 (2002).
- [11] M. Baudoin, P. Brunet, O. Bou Matar and E. Herth, Appl. Phys. Lett. **100**, 154102 (2012).



Plug-and-actuate on demand: Fluid Actuation in 96-Well Plate using Hybrid Acoustic Waves

Amgad Rezk¹, and Leslie Yeo¹

Micro/Nanophysics Research Laboratory, RMIT University, Melbourne, VIC 3000, Australia
E-mail: amgad.rezk@rmit.edu.au

Introduction Acoustic waves are commonly defined as either surface or bulk type. We have discovered that a combination of surface and bulk type wave shows an order-of-magnitude improvement in microfluidic manipulation efficiency. This talk, mainly presenting experimental data with some numerical support, will introduce these hybrid waves and some of their new applications with a particular emphasis on their integration with standard 96-well plates. Integrating these hybrid waves with 96 independent electrical inputs, we demonstrate the potential for true simultaneous and/or sequential well addressability. The proposed platform is highly reconfigurable to accommodate other well plate formats and is capable of driving a range of microfluidic processes including mixing, particle concentration and drop ejection, all in a solid-state configuration without any moving parts.

Previous attempts incorporating acoustics with microwells

Acoustic means have been proposed as an efficient technology for liquid handling, especially for small liquid sample transfer down to the nanolitre range while interfacing with standard laboratory technologies, such as well plates. However, existing bulk transducer based applications are limited to liquid jetting which constitutes only one of the many processes routinely carried out in pharmaceutical industries. More significantly, current bulk transducers technologies, such as LabCyte Inc. (San Jose, CA, USA) are designed to mechanically slide beneath well plates to address one particular well at a time which mechanically limits their overall sample actuation speed, increasing the equipment cost and complexity.

High Frequency mega-hertz order surface acoustic waves (SAWs) have been used for the last decade as an extremely efficient platform in driving a wide range of fluid actuation processes in droplets.^[1] However, most research to date has been demonstrated only on *chip-scale* because SAW technology is fundamentally *incompatible* with the familiar industry standard equipment used in drug discovery laboratories, such as 96 and 384 well plate format. The conflicting requirements between miniaturising the acoustic chips to match a single well size while accessing the electrodes to trigger the SAW presents an obvious limitation and hence, the SAW has been demonstrated to drive mixing in an entire well plate row,^[2] in a technology that has been introduced by Advalytix. Previous work utilising SAW to drive particle and cell concentration in a single well has eluded to the potential of addressing an entire well plate array, but this has never been demonstrated, whereas, other bulk MHz transducers were limited to large 24 well array platform and have not demonstrated an entire well addressability either.

Our Proposed platform

Here, utilising our recently discovered hybrid acoustic waves wave (i.e., HYDRA)^[3] we propose a novel modular acoustic platform allowing for chip miniaturisation to match 96 well plate format, whilst allowing for electrode accessibility (from the back of the chip) without loss in efficiency. Using printed circuit board (PCB) platform, we embedded traces for each individual well to ultimately connect to edge connectors at the periphery of the PCB, where the edge connectors can be manually or digitally triggered by an Arduino environment. Subsequently, 96 pin pairs were soldered and self-aligned with hot air gun. The technological contrast between SAW technology and HYDRA is demonstrated in Figure 1. As shown in Figure 1a, the interdigital transducers (IDTs) protrude outside the well dimension and overlap with neighbouring wells, thus jeopardising single well addressability, whereas, in Figure 2b, it is clear how the proposed HYDRA platform fundamentally allows for both miniaturisation and practical acoustic actuation. In the latter, the chips are partially enclosed in a 3D printed housing and snap fitted to interface with protruding pin from a PCB for electrical excitation.

Uniquely, we demonstrate a variety of actuation processes such as sequential mixing, particle and cell concentration in addition to liquid jetting from single and multiple wells. For example, as shown in Figure 2, addressable single well mixing was carried out, where the letters "96" were patterned by mixing the fluids in the corresponding wells. Pink coloured dye was used to half fill the entire 96 well plate array and traces of blue coloured dye was carefully added to the side end of each well. The targeted wells were excited externally

with manual switches soldered to the edge connectors. It is important to note that we have minimal crosstalk between the wells thus minimising any acoustic transfer from the concerned well to the others. In addition, we demonstrate, using the same platform, particle/cell agglomeration as well as drop ejection.

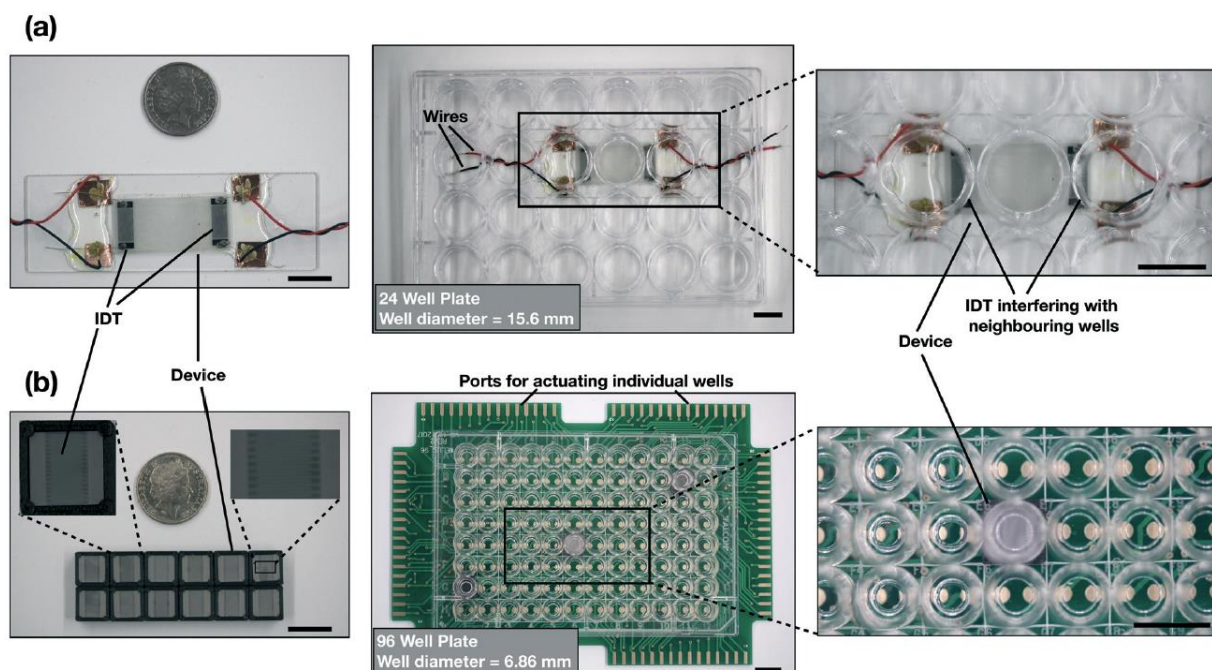


Figure 1: (a) Previous SAW integration attempts. (b) Our proposed Plug-and-actuate platform utilising Hybrid acoustic waves. The magnified view on the right shows the possibility for individual addressability of each well or even simultaneous addressability of multiple wells on demand since the devices are not only matched in dimension so that they only transmit acoustic energy into the well that is directly above them, but are also isolated from neighbouring devices by the 3D printed housing that encases them. The scale bars denote a length of 10 mm.

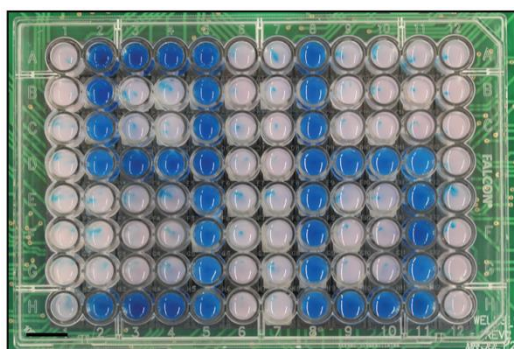


Figure 2: Simultaneous on-demand mixing in individual wells of a 96-well plate driven using the modular HYDRA platform. Prior to the excitation of the SRBW under select wells, each well contained the same amount of pink-dyed solution (100 μ l) into which an equal amount of blue dye (1 μ l) was placed. The scale bars represent a length of 10 mm.

Conclusion

We have demonstrated a versatile modular plug-and-actuate concept that is truly compatible with the microarray titre plate. This novel platform is capable of efficiently driving a range of microfluidic actuation processes from mixing, sample preconcentration and external liquid transfer—all of which comprise critical steps in the drug discovery workflow—on demand, with the possibility of addressing individual, multiple or all wells on the plate sequentially or simultaneously, thus constituting a significant step towards improving the functionality associated with existing laboratory protocols and processes. Looking forward to presenting for the international acoustofluidics community at *Acoustofluidics 2018* at sunny Lille, Universite de Lille, Lille, France on 29–31 August 2018.

References

- [1] L. Y. Yeo and J. R. Friend, *Annual Review of Fluid Mechanics*, 2014, 46, 379–406.
- [2] J. Comley, *Drug Discovery World*, 2007, 8, 35–46.
- [3] A. R. Rezk, J. K. Tan and L. Y. Yeo, *Advanced Materials*, 2016, 28, 1970–1975



Microfabrication of Continuous Stable patterns Using Standing Surface acoustic waves in microfluidic systems

Haim Sazan, Silvia Piperno, and Hagay Shpaisman

Department of Chemistry, Institute for Nanotechnology and Advanced Materials, Bar Ilan University, Ramat Gan, 5290002, Israel
E-mail: sazanh@biu.ac.il

Introduction

Directed-assembly by applying external forces can result in temporary alignment of particles in a state of local equilibrium with complex spatial organization. Acoustic-based alignment techniques only require a difference in compressibility and/or density between the particles and the surrounding medium (acoustic contrast) and is therefore highly attractive. While previous studies demonstrated only arrangement of particles with surface acoustic waves (SAWs) and Standing surface acoustic waves (SSAWs), [1,2] this research [3] present a new approach for directed-assembly where SSAWs are used to deposit in predetermined locations the products of an ongoing chemical reaction such as Polydimethylsiloxane (PDMS) polymerization. [4] This method provides, in a single step, well-ordered and continuous polymeric micro-structures. This technique could conceptually be implemented for directed assembly of many other products of ongoing chemical reactions, as the acoustic standing waves will influence almost all dispersed systems.

Experimental

The acoustic waves were generated by a pair of interdigital transducers (IDTs) that were fabricated on a lithium niobate (LiNbO_3) piezoelectric substrate. Once a radio frequency (RF) signal is applied to both IDTs, two series of surface acoustic waves propagate in opposite directions and their constructive interference results in the formation of a SSAW. The distance between the electrodes of the IDTs is $100 \mu\text{m}$. A PDMS microfluidic channel was attached to a cover glass and positioned between the two IDTs. The emulsion was prepared by a mixed solution of ammonia, dimethyldiethoxysilane (DMDES) and trimethoxysilane (MTES). Na_2SO_4 was added to screen charges. **Figure 1** describe a schematic image of the arrangement process.

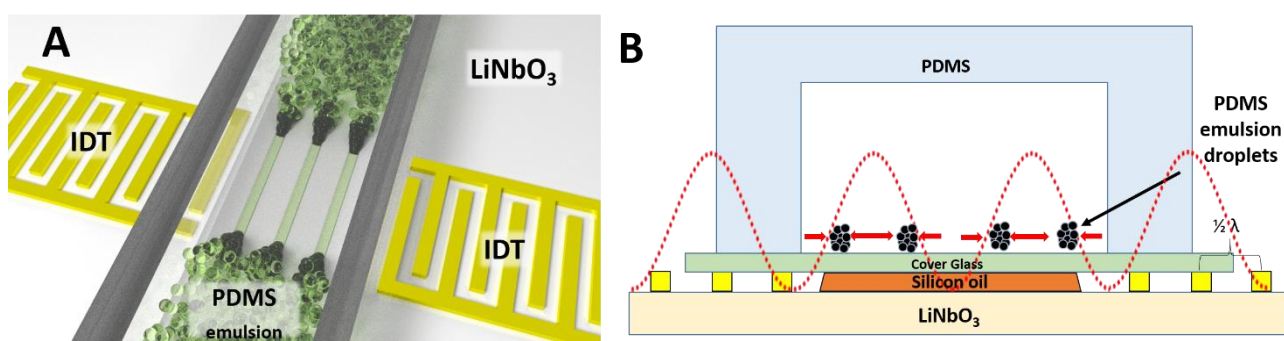


Figure 1: Illustration of polymeric microstructure formation from a solution undergoing polymerization while applying SSAWs. A) The comb-shaped metal electrodes (IDTs) deposited on top of a LiNbO_3 substrate convert electric signals to surface acoustic waves. Emulsion droplets are arranged inside a PDMS microfluidic channel along the pressure nodes. B) Cross-section of the microfluidic system showing the primary acoustic force (red arrows) that drives the droplets towards the pressure nodes of the SSAWs.

The process can be divided into two main steps: 1) the nucleation sites are directed to node positions and coalesce (minimizing surface tension) to larger spherical micron-sized droplets. 2) The droplets wet the glass substrate along the pressure nodes and merge due to the acoustic force leading to formation of continuous

micro-structures. These steps are shown in **Figures 2A-2C** for a 12.5 wt% emulsion solution with 80% cross-linker.

After ~10 minutes from the time of solution preparation, sub-micron nucleation sites become visible inside the microchannel using bright-field microscopy. Once the SSAWs are generated, patterns appear within less than 30 seconds (**Figure 2A**). The nucleation sites and droplets continue to accumulate until, after 3 additional minutes, they merge to form a continuous microstructure that is permanently attached to the bottom surface (**Figure 2B**). Only a few droplets are positioned along the polymerized lines that have not yet merged. After 7 additional minutes, the droplets along the nodes have fully merged (**Figure 2C**).

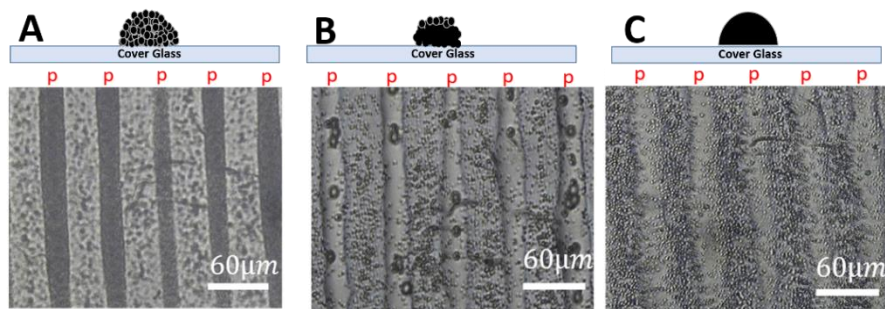


Figure 2: Assembly over time (in-situ bright field microscopy images, and illustration of a cross-section of a single line). A) 30 seconds after turning on the SSAWs. B) After 3 minutes, particles coalesce forming continuous lines. C) After 10 minutes, droplets have fully merged. The letter "p" in red is shown above the location of the PDMS lines.

The dependence of the forming structure on the cross-linker ratio is shown in **Figure 3**. This ratio influences the polymerization rate that plays a central role in the assembly and polymerization of the structure. Solutions with varying cross-linker concentrations were prepared and infused into the microchannel once nucleation sites started forming (at the first signs of turbidity). This correlates to 10, 10, 60, 120 minutes (± 2 minutes) for 90%, 80%, 60% and 40% cross-linker ratios, respectively. **Figure 3** shows the forming structures for the different cross-linker ratios (1 hour after infusion).

80% cross-linker ratio (**Figure 3b**) results in the formation of well-defined and continuous lines. In this case, the colliding droplets wet the surface along the nodes, and their high viscosity results in merging without

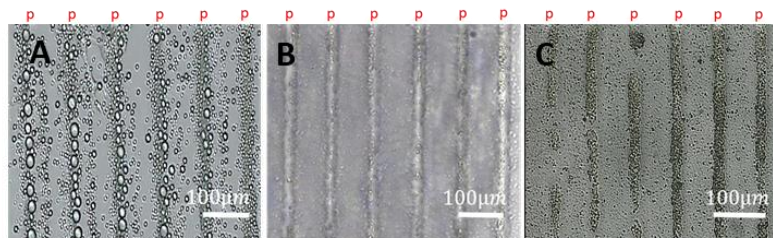


Figure 3: Bright-field images (in situ) for different concentrations of cross-linker: a) 40% b) 80% and c) 90%. Continuous structures are only formed at 80% cross-linker. The letter "p" in red is shown above the location of the PDMS lines.

breakup into individual hemispheres thus forming well connected continuous lines

Conclusion

We have demonstrated directed deposition of emulsion droplets undergoing polymerization into ordered PDMS microstructures by SSAWs. This is the first realization of SSAWs being used to manipulate and spatially direct the products of an ongoing chemical reaction, rather than preformed materials. Acoustic forces can influence almost all dispersed systems, require only low power densities and can be easily scaled up. Combining chemical synthesis with the patterning processes as shown here (a one-step procedure), can therefore be beneficial for various applications.

References

- [1] J. Shi, H. Huang, Z. Stratton, Y. Huang, T.J. Huang, Continuous particle separation in a microfluidic channel via standing surface acoustic waves (SSAW), *Lab. Chip.* 9 (2009) 3354–3359. doi:10.1039/B915113C.
- [2] M. Sesen, T. Alan, A. Neild, Microfluidic on-demand droplet merging using surface acoustic waves, *Lab. Chip.* 14 (2014) 3325–3333. doi:10.1039/C4LC00456F.
- [3] S. Piperno, H. Sazan, H. Shpaisman, One-step Acoustic Directed Assembly: From Emulsion Droplets to Polymeric Microstructures, Submitted, second revision
- [4] G. Gillies, C.A. Prestidge, P. Attard, An AFM Study of the Deformation and Nanorheology of Cross-Linked PDMS Droplets, *Langmuir.* 18 (2002) 1674–1679. doi:10.1021/la011461g.

Velocity field analysis of acoustophoretic focusing in a single-cell printing system

Clara Siber¹, Fabian Stumpf^{1,2}, Jonas Schöndube¹, Stefan Zimmermann^{1,2}, Peter Koltay², Lena Lautscham¹

¹cytena GmbH, Freiburg, Germany

E-mail: siber@cytena.com, URL: www.cytene.com/home.html

²Department of Microsystems Engineering, Albert-Ludwig University, Freiburg, Germany

Introduction

Single-cell isolation is of major importance for cell line development and recently has raised increasing interest in newer fields such as single-cell analysis. In this fields gentle cell isolation and consequently high clonal recovery rates play a key role. This can be achieved by single-cell printing, a technology based on an ink-jet like operating principle [1]. Successful single-cell printing depends on reliable single-cell detection and isolation and, especially in the case of samples containing a small number of rare cells, on minimum cell loss. Integrating acoustophoretic cell focusing into the printing process was shown to significantly improve these two aspects by lining-up the cells in the center of the dosage chamber of the cartridge used for printing [2]. In single-cell printing it is crucial to work with disposable cartridges to avoid cross-contaminations. Therefore, we extended our previous work by developing a non-permanent contact between the piezoelectric transducer and the disposable cartridge that allows for effective coupling of the acoustic field into the cartridge. With this approach, the excitation of a resonance mode that results in the alignment of cells on the center line of the cartridge chamber was achieved. The corresponding velocity field of the particles generating the alignment was measured by means of μ PIV.

The single-cell printer and the benefit of acoustophoresis

As illustrated in Figure 1 the isolation of single-cells by the single-cell printer is achieved by generating free flying droplets of a cell suspension and simultaneously imaging the nozzle to detect cells and predict the number of cells each droplet will contain. A vacuum shutter removes all droplets containing more than one or no cell. If a droplet contains exactly one cell, the vacuum shutter is turned off and the droplet is deposited onto the substrate. However, the cell detection in the region of interest is impeded by shadows of the microfluidic structure close to the channel walls (cf. Figure 1). As a result some cells may not be detected which can lead to cell loss or in a more severe case to multiple cells per well. This issue can be avoided by controlling the position of the cells in the chamber and directing them away from the shadowed areas at the channel walls by lining them up in front of the nozzle orifice by acoustophoretic radiation force.

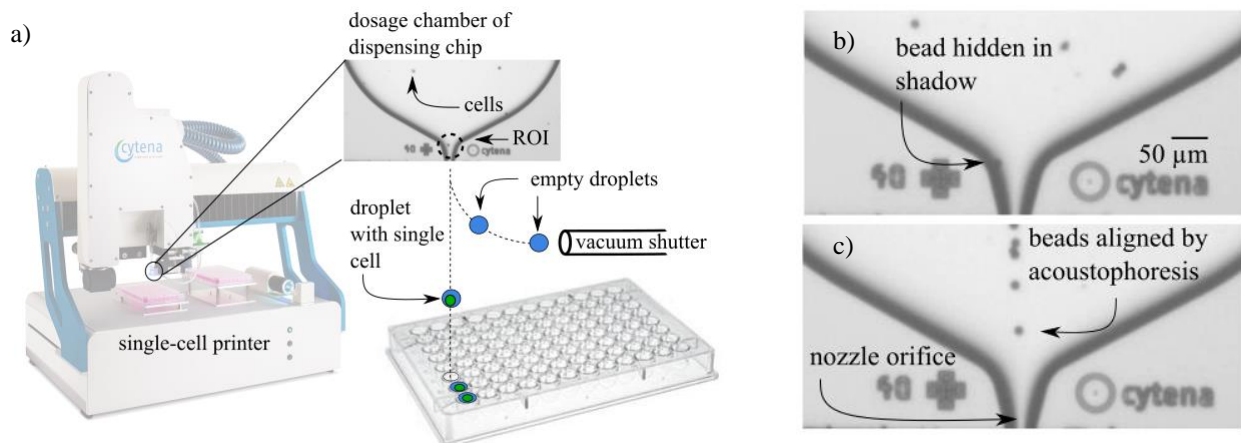


Figure 1: Single-cell isolation by ink-jet like single cell printing a) Schematic of the printing process (not to scale). A cell or bead suspension is filled into a cartridge hosting a microfluidic dispenser chip. The membrane of the dispenser chip is deflected by a piezo stack actuator resulting in ejection of a picoliter-sized droplet of the suspension. A detection algorithm determines the number of cells resp. beads present in the volume to be ejected with the next droplet (i.e. the region of interest, ROI). Only droplets that are predicted to contain a single cell resp. bead are deposited onto the substrate. b) Random distribution of beads inside the chip close to the nozzle. Here one bead is hidden in the shadow and remains undetected. c) Beads lined-up in the center of the chip by acoustophoresis approach the nozzle in a well ordered.

The acoustic field inside the dispenser chip

The printing cartridge consists of a silicon dispenser chip, featuring an inlet, a dosage chamber bound by a membrane and a nozzle. The chip is sealed by a transparent Pyrex lid and assembled into the cartridge together with the chip holder made from PMMA featuring a cell suspension reservoir. This cartridge acts as the acoustic resonator and essentially determines the different resonance modes and their corresponding frequencies. For our application the $\lambda/2$ -mode in lateral direction with its pressure node directly at the central line of the dosage chamber is of the highest interest. However, it has an oval shape that is needed for the droplet generation, making it difficult for a standing wave to form inside the cavity of the dosage chamber. Nonetheless, the excitation of a static field in the $\lambda/2$ -mode is possible with a frequency of 555 kHz (cf. Figure 2). For long channels the acoustophoretic radiation force acting on the particles can be described by $F^{rad} = 4\pi\Phi ka^3 E_{ac} \sin(2kz)$, where Φ is the acoustophoretic contrast factor, k the wave number, a the particle radius and E_{ac} the acoustic energy density. Balancing it with the Stokes drag force $F^{drag} = -6\pi\eta a v_p$ leads to an expression for the particle velocity $v_p = (2\pi\Phi ka^2 E_{ac} / 6\pi\eta) \sin(2kz)$ [3]. In the middle, where the chamber structure can be compared to a short channel with parallel walls, the horizontal velocity can be described by this sinusoidal velocity curve (cf. Figure 2b). Besides this $\lambda/2$ -mode also other resonances were found and e.g. a ring pattern or lateral lines were observed. Especially these might be of use to control the spacing between the cells approaching the nozzle.

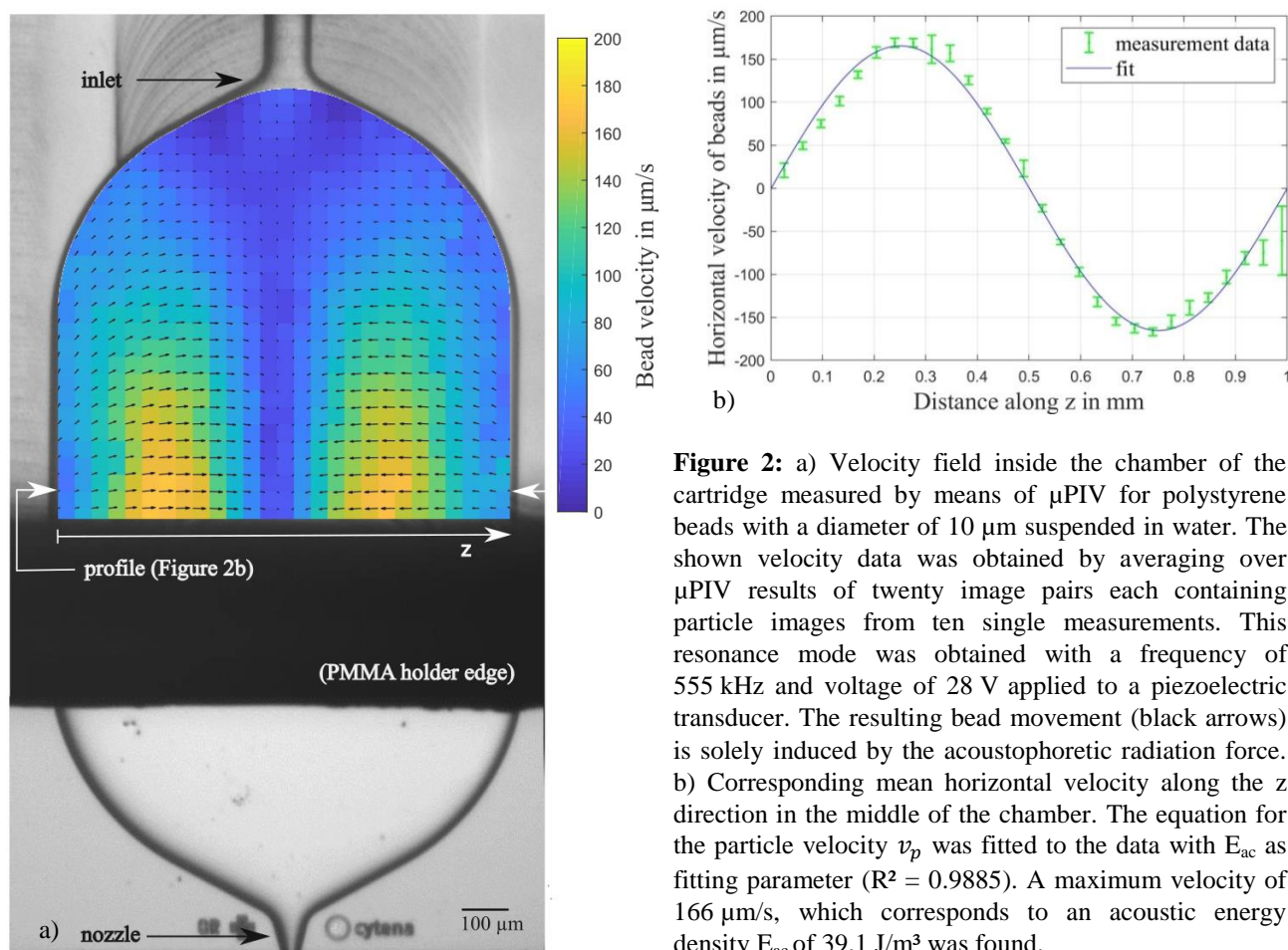


Figure 2: a) Velocity field inside the chamber of the cartridge measured by means of μ PIV for polystyrene beads with a diameter of 10 μ m suspended in water. The shown velocity data was obtained by averaging over μ PIV results of twenty image pairs each containing particle images from ten single measurements. This resonance mode was obtained with a frequency of 555 kHz and voltage of 28 V applied to a piezoelectric transducer. The resulting bead movement (black arrows) is solely induced by the acoustophoretic radiation force. b) Corresponding mean horizontal velocity along the z direction in the middle of the chamber. The equation for the particle velocity v_p was fitted to the data with E_{ac} as fitting parameter ($R^2 = 0.9885$). A maximum velocity of 166 μ m/s, which corresponds to an acoustic energy density E_{ac} of 39.1 J/m³ was found.

Conclusion

In this study, we have shown that acoustophoresis can align single beads inside a printing cartridge by centering the beads inside the dispenser chip. Using μ PIV we characterized the velocity field inside the chip. The $\lambda/2$ -mode desired for our application was achieved to be induced inside the printing cartridge with an estimated acoustic energy density of 39.1 J/m³, which moves 10 μ m beads with a velocity of up to 166 μ m/s towards the center line. Furthermore, we were able to implement the technology within a small disposable cartridge using a detachable piezoelectric transducer that was not glued to the cartridge like in previous works.

References

- [1] A. Gross, J. Schöndube, S. Niekrawitz, W. Streule, L. Riegger, R. Zengerle, P. Koltay. *Journal of Laboratory Automation* **18**(6), 504-418 (2013).
- [2] I. Leibacher, J. Schöndube, J. Dual, R. Zengerle, P. Koltay. *Biomicrofluidics* **9**, 024-109 (2015).
- [3] H. Bruus. *Lab on a Chip* **12**, 1014 (2012).